SYNTHESIS AND BIOFUNCTIONALIZATION OF NANOPARTICLES FOR BREAST CANCER DIAGNOSIS AND TREATMENT

SYNTHESIS AND BIOFUNCTIONALIZATION OF NANOPARTICLES FOR BREAST CANCER DIAGNOSIS AND TREATMENT

Miriam Colombo

Matr. 725231

TUTOR: Dr. Davide Prosperi

COTUTOR: Prof. Fabio Corsi

December, 2011

Abstract

The early identification of the insurgence of a malignant cancer and the selective targeting of the tumor with specific drugs are still an open frontier for cancer diagnosis and treatment. The ultimate goal is to improve the therapy efficiency and to reduce the side effects usually encountered with conventional chemotherapy. Worldwide, mammary carcinoma represents the second most recurrent type of malignant tumor in adult women and the fifth cause of death among cancer types. In the context of this thesis, I have designed and developed multifunctional hybrid nanoparticles consisting of an inorganic iron oxide core, useful as source of signal for magnetic resonance imaging (MRI), and an organic shell, including bioactive ligands for the pharmacological effect combined with specific cell targeting, and a molecular dye as fluorescence signal emitter. The nanoparticle characteristics were optimized in terms of size, morphology, surface charge, stability, fluorescence emission and capability to enhance the MRI contrast. In addition, specific biomolecular ligands based on anti-HER-2 monoclonal antibody have been developed and novel strategies for their conjugation to nanoparticles were explored. The resulting hybrid nanocomplexes were tested both in vitro and in vivo to evaluate their toxicity, endocytosis, degradation pathways, and the efficient recognition of cell-surface biomarkers. Next, these nanoparticles proved to be highly effective in selectively targeting breast cancer cells in transplanted mice bearing HER-2-positive tumors. A multifaceted bioanalytical approach, combining fluorescence, magnetic relaxivity, transmission electron microscopy, and histological experiments in vivo and ex vivo, has demonstrated that these nanoprobes prevalently accumulated at the tumor by an active targeting route. The nanoparticles were endocytosed by the tumor cells following a lysosomal pathway of degradation, while did not result in permanent damage of healthy tissues. The principal outcome of this work was the development of a versatile and reliable biotechnological platform based on finely structured, multifunctional nanosized probes useful for the interrogation of biological systems.

List of publications

During the course of this project, a number of publications have been made, which are based on the work presented in this thesis. All of them are listed here for reference, while those that are directly related to the content of this work are included in the last section of the thesis.

1. L. Polito, M. Colombo, D. Monti, S. Melato, E. Caneva, D. Prosperi. Resolving the structure of ligands bound to the surface of superparamagnetic iron oxide nanoparticles by high-resolution magic-angle-spinning NMR Spectroscopy. *J. Am. Chem. Soc.* **2008**, *130*, 12712–12724.

2. M. Colombo, S. Ronchi, D. Monti, F. Corsi, E. Trabucchi, D. Prosperi. Femtomolar detection of autoantibodies by magnetic relaxation nanosensors. *Anal. Biochem.*, **2009**, *392*, 96–102.

3. F. Corsi, C. De Palma, M. Colombo, M. Nebuloni, S. Ronchi, G. Rizzi, R. Allevi, A. Tosoni, E. Trabucchi, E. Clementi, D. Prosperi. Towards ideal magnetofluorescent nanoparticles for bimodal detection of breast cancer cells. *Small*, **2009**, *5*, 2555–2564.

4. G. Prencipe, S. Maiorana, P. Verderio, M. Colombo, P. Fermo, E. Caneva, D. Prosperi, E. Licandro. Magnetic Peptide Nucleic Acids for DNA targeting. *Chem. Commun.*, **2009**, 6017–6019.

5. M. Colombo, F. Corsi, D.Foschi, E. Mazzantini, S. Mazzucchelli, C. Morasso, E. Occhipinti, L. Polito, D. Prosperi, S. Ronchi, P. Verderio. HER2 targeting as a two-sided strategy for breast cancer diagnosis and treatment: Outlook and recent implications in nanomedical approaches. *Pharmacol. Res.* **2010**, *62*, 150–165.

6. C. Morasso, M. Colombo, S. Ronchi, L. Polito, S. Mazzucchelli, D. Monti, T. Bellini, D. Prosperi. Towards a universal method for the stable and clean functionalization of perfluoropolymer nanoparticles: exploiting photopolymerizable amphiphilic diacetylenes. *Adv. Funct. Mater.*, **2010**, *20*, 3932–3940.

7. S. Mazzucchelli,† M. Colombo, † C. De Palma, P. Verderio, M. D. Coghi, E. Clementi, P. Tortora, F. Corsi, D. Prosperi. Single-domain protein A-engineered magnetic nanoparticles: towards a universal strategy to site-specific labeling of antibodies for targeted detection of tumor cells. *ACS Nano*, **2010**, *4*, 5693–5702.

8. E. Occhipinti, P. Verderio, A. Natalello, E. Galbiati, M. Colombo, S. Mazzucchelli, P. Tortora, S. M. Doglia, D. Prosperi. Investigating the structural biofunctionality of antibodies conjugated to magnetic nanoparticles. *Nanoscale*, **2010**, *3*, 387–390.

9. S. Ronchi, M. Colombo, P. Verderio, S. Mazzucchelli, F. Corsi, C. De Palma, R. Allevi, E. Clementi, D. Prosperi. Magnetofluorescent nanoparticles for bimodal detection of breast cancer cells. *AIP Conf. Proc.*, 1275, 102–105.

10. M. Piazza,† M. Colombo,† I. Zanoni, F. Granucci, P. Tortora, J.Weiss, T. Gioannini, D. Prosperi, F. Peri. Uniform LPS-loaded magnetic nanoparticlesfor the investigation of LPS/TLR4 signaling. *Angew. Chem., Int. Ed.*, **2011**, *50*, 622–626.

11. L. Rizzi, M. Braschi, M. Colombo, N. Vaiana, G. Tibolla, G. D. Norata, A. L. Catapano, S. Romeo, D. Prosperi. Novel biotinylated bile acid amphiphiles: micellar aggregates formation and interaction with hepatocytes. *Org. Biomol. Chem.*, **2011**, *9*, 2899–2950.

12. F. Corsi, L. Fiandra, C. De Palma, M. Colombo, S. Mazzucchelli, P. Verderio, R. Allevi, A. Tosoni, M. Nebuloni, E. Clementi, D. Prosperi. HER2 expression in breast cancer cells is downregulated upon active targeting by antibody-engineered multifunctional nanoparticles in mice. *ACS Nano*, **2011**, *8*, 6383–6393.

13. S. Mazzucchelli, P. Verderio, S. Sommaruga, M. Colombo, A. Salvadè, F. Corsi, P. Galeffi, P. Tortora, D. Prosperi. Multiple presentation of Scfv800E6 on silica nanospheres enhances targeting efficiency toward HER-2 receptor in breast cancer cells. *Bioconjugate Chem.*, **2011**, *22*, 2296–2303.

14. M. Colombo,† S. Sommaruga,† S. Mazzucchelli, L. Polito, P. Verderio, P. Galeffi, F. Corsi, P. Tortora, D. Prosperi. Site-specific conjugation of Scfvs to nanoparticles by bioorthogonal strain-promoted alkyne-nitrone cycloaddition. *Angew. Chem., Int.* **2011** EPub. DOI: 10.1002/anie.201106775

† contributed equally

Acknoledgements

My special gratitude is devoted to Prof. Emilio Trabucchi for his continuous support to my work. I gratefully acknowledge Prof. Paolo Tortora for his essential contribution in discussing the biological features of this work, and Prof. Wolfgang J. Parak for giving me the opportunity to spend six months of my PhD in his Lab at the Department of Physic, Phillips University of Marburg, where I could become familiar with the most advanced technologies for nanoparticle manipulation.

My doctoral fellowship associated with this project was funded by "Fondazione Romeo ed Enrica Invernizzi" and "Centro di Microscopia Elettronica per lo sviluppo delle Nanotecnologie applicate alla medicina" (CMENA, University of Milan).

Introduction

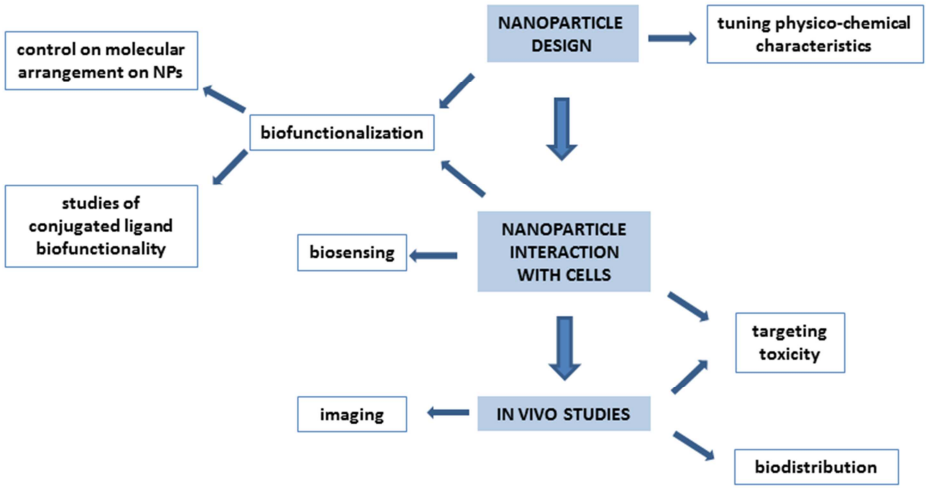

The growing impact of nanotechnology on biomedical science in view of a potential routine clinical application has raised numerous questions, which will require the joint efforts of interdisciplinary research groups to be adequately faced. Of course, when using nanoparticles for targeted cancer diagnosis, one of the main issues to be considered concerns the design and optimization of effective functionalization strategies to achieve a reliable receptor/cell targeting. However, the first step consists in the evaluation of those factors related with the interaction of the cell with heterogeneous nanomaterials before, during and after their adhesion and incorporation. For this reason, we have designed a nanotechnology platform using different complementary technologies capable of providing compelling evidence on many of these key factors, including the mechanisms of adhesion and internalization, the degradation pathways, cytotoxicity, capability of nanomaterials of providing suitable diagnostic signals useful for biomedical purposes, and more. As a leading case to assess the utility of our multitask approach, we chose the mammary carcinoma, a metastatic solid tumor, which threatens millions of adult women every year worldwide.

An attractive possibility to detect mammary carcinomas in the early stages of their development in a noninvasive way can be envisaged in developing tracing agents that can be delivered and detected via magnetic nanoparticles. Thanks to their unique magnetic properties, magnetic nanoparticles now find large application in many fields of biomedical research, including use as magnetic resonance imaging contrast agents, heating mediators for cancer thermotherapy, magnetic-force-based drug and gene delivery systems, and tools for selective separation and detection of biomolecules.

In the past, major concerns about magnetic nanoparticles have been cellular toxicity, tendency to a rapid clearance after delivery in the circulatory system, and low intracellular labeling efficiency. In particular, these nanoparticles need to fulfill several criteria in order to be used as diagnostic materials in humans, including high resolution, accuracy and sensitivity of detection, which may be provided by using magnetic nanoparticles coated with protein-targeting biomarkers overexpressed by breast cancer cells, *e.g.,* the human Epidermal Growth Factor Receptor 2 (HER-2) receptor. In addition, they must be nontoxic and able to interact in a physiological way with biological tissues without aggregating while being delivered. Eventually, since membrane receptors are endocytosed as part of their normal response to ligand binding, magnetic nanoparticles have to follow physiological pathways when internalized by the cell. So far, only preliminary evidence has been reported about these latter factors, which are critical for clinical use.

A further fundamental feature concerns the nanoparticle capability to be confined at the diseased site. When a sharp tissue distribution is desired, targeted contrast agents are designed in such a way that they localize to specific cell types through active binding mechanisms, which exploit the conjugation of the signal enhancer with suitable molecular ligands. Among them, most used are folate, small peptides, and antibodies, which stimulate specific recognition with the associated tumor cell receptor. When ligands are complex molecules, such as proteins, their proper orientation on the surface of nanoparticles becomes a crucial factor for maximizing the affinity for their molecular counterparts. Thus, the ultimate challenge is represented by the development of reliable

strategies for the conjugation of targeting biomolecules, especially monoclonal antibodies (IgGs), to magnetic nanoparticles. The available approaches can be collected in three general categories: 1) passive/electrostatic physical adsorption, 2) tight immobilization exploiting the selective recognition of biological counterparts, and 3) the formation of covalent chemical connections. Although these approaches may offer different solutions and all have been successfully employed in several circumstances, they share the same basic limitation, that is a non-site-specific binding to IgG molecule, which affects the targeting efficiency of the antibody. As a matter of fact, the actual conservation of the targeting bioactivity of immobilized IgGs is not obvious and remains a crucial issue, which must be addressed in designing a successful targeted nanoprobe. Most of the current approaches directed to the conjugation of antibodies to nanoparticles are usually designed to answer to the specific requirements of the experiment of interest. However, in view of clinical translation of a new generation of nanoscale targeted diagnostics, versatile multitask nanoprobes would be highly desired to improve and simplify sample handling and reduce the costs of Public Health.

Finally, in view of a potential application in the treatment of human cancer, several capital questions, mostly concerning toxicity, biodistribution and targeting efficacy of nanoconjugates in vivo, remain open, as documented by the large number of papers on this topic appeared in the last years in top journals. In particular, antibody-functionalized nanoparticles, sometimes referred to as the second generation targeted nanoconjugates, while being universally recognized as a powerful tool for the investigation at the cellular level, have been seriously questioned as regard to their effective potential in vivo. Indeed, it is commonly believed that alternative factors, including opsonization, macrophage-mediated transport and passive delivery in general, might strongly affect the targeting efficiency and final destiny of nanoparticles and, in most cases, become the predominant factor. The last step of the present work was focused on the optimization of a IgG-nanoconjugate to perform an accurate study of nanoparticle-membrane receptor in vivo. Our results strongly supported the assumption that active targeting is indeed possible in vivo, allowing for tumor localization, and can induce

receptor downregulation, interfering with cell-signaling processes, and thus opening the possibility to utilize IgG-conjugated nanoparticles for adjuvant and neoadjuvant therapy accompanying chemical treatments and/or surgical intervention.

In summary, the general scope of this thesis was to develop a comprehensive approach for the investigation of the different crucial aspects involved in the interaction of hybrid bioinorganic nanoparticles with biological systems for potential biomedical applications. Several issues, including nanoparticle synthesis, biofunctionalization, toxicity and use as diagnostic and therapeutic agents both in vitro and in vivo, have been thoroughly examined and optimized. By taking advantage of the interdisciplinary view offered by synergistic chemical, physical and biochemical approaches, we have designed a new generation of multifunctional hybrid nanosystems suitable to explore new frontiers in the diagnosis and therapy of cancer disease, as illustrated in the representative scientific platform depicted in the above block diagram. Of course, the clinical application in human treatments is the final goal of this and related research. However, to reach such objective is necessary not only to design a suitable system for practical use, but also to assess and optimize the essential characteristics for specific effects such as safety, capability to get to the specific target, to provide useful signal amplification and to avoid the immunogenic system. For this reason, in order to have a feedback on the diagnostic and therapeutic potential of the developing nanosystems and to focus the research on a specific purpose, this project has been planned and developed in collaboration with groups of medical doctors working at Sacco Hospital, Milan.

Contents

Chapter 1

Background

Contents

In recent years, nanoparticles have played an increasing role in biomedical research and clinical applications. The use of nanotechnology is gaining interestin biology and medicine and the unique chemical/physical properties of nanomaterials are being exploited in the field of nanomedicine for basic research investigations as well as in clinical practice for both diagnosis and treatment of several diseases. Possible applications include drug delivery nanosystemsand cell targeting, magnetic resonance imaging (MRI) contrast enhancement, gene therapy, biomarker identification, targeted hyperthermia and many others.[1-5]

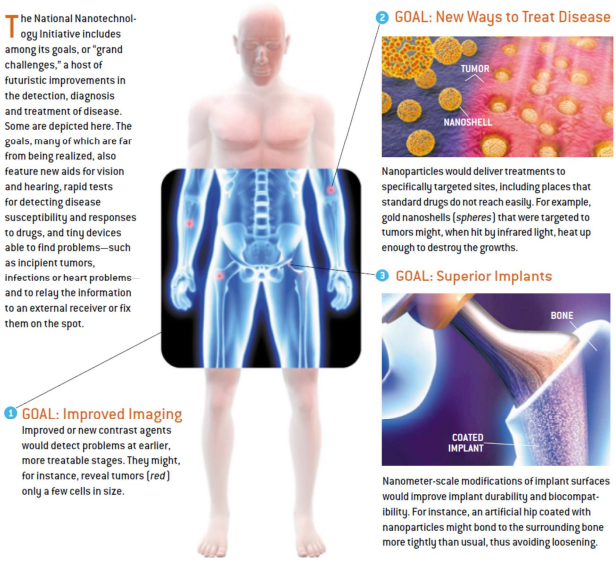

Figure 1. Potential of nanomedicine.[6]

1. Nanotechnology and medical applications

Nanotechnology is defined as the intentional design, characterization, production, and application of materials, structures, devices, and systems by controlling their size and shape at the nanoscale (1 to 100 nm).[7] Because nanomaterials are similar in scale to biological molecules and systems, yet can be engineered to have various functions, nanotechnology is potentially useful for medical applications. The field of nanomedicine aims to use the properties and physical characteristics of nanomaterials for the diagnosis and treatment of diseases at the molecular level. Nanomaterials are now being designed to aid the transport of diagnostic or therapeutic agents through biological barriers, to gain access to specific functions, to mediate molecular interactions, and to detect molecular changes in a sensitive and highthroughput manner. In contrast to atoms and macroscopic materials, nanomaterials have a high ratio of surface area to volume as well as tunable optical, electronic, magnetic, and biological properties. In addition, they can be engineered to have different sizes, shapes, chemical compositions, surface chemical characteristics, and hollow or solid structures. These properties are being incorporated into a new generation of drug delivery vehicles, contrast

agents, and diagnostic devices, some of which are currently undergoing clinical trials or have been approved by the Food and Drug Administration (FDA) for use in humans, others are in the proof-of-concept stage in research laboratories.

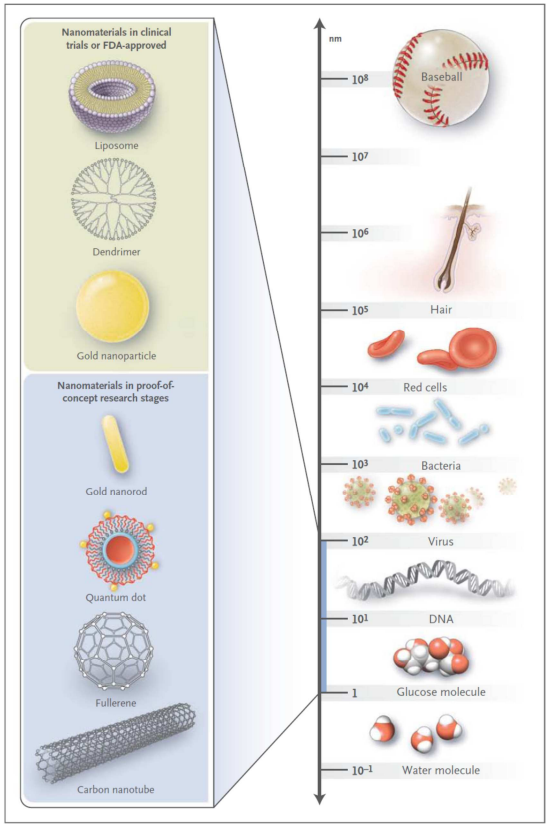

Figure 2. Nanomaterials commonly used in medicine. **Liposomes** contain amphiphilic molecules, which have hydrophobic and hydrophilic groups that self-assemble in water. **Dendrimers** are branched nanostructures; each terminus contains reactive chemical functional groups that allow the addition of multiple monomers to increase the size of the nanostructure. **Gold nanoparticles** are solid metal particles that are conventionally coated with drug molecules, proteins, or oligonucleotides. **Quantum dots** are semiconductor nanocrystals endowed with strong photoluminescence usually consisting of a core-shell structure (*e.g.*, CdSe coated with zinc sulfide with a stabilizing molecule and a polymer layer coated with a protein). **Fullerenes** and **carbon nanotubes** have only carbon-to-carbon bonds. These nanostructures are commonly named according to the number of carbon atoms that form the structure (*e.g.*, a C60 fullerene contains 60 carbons).[1]

Nanomaterials generally consist of metal atoms, nonmetal atoms, or a mixture of metal and nonmetal atoms, commonly referred to as metallic, organic, or semiconducting nanostructures, respectively. The surface of nanomaterials is usually coated with polymers or biorecognition molecules to achieve an improved biocompatibility and selective binding with biological molecules. The final size, composition, shape (spherical, rod-like, star-like, wires, octahedral, cubic, etc.) and morphological characteristics (full, hollow, porous, etc.) of nanomaterials depend on the salt and surfactant additives, reactant concentrations, reaction temperatures, and solvent conditions used during their synthesis. A common feature of all nanomaterials is their large ratio of surface area to volume, which may be orders of magnitude greater than that of macroscopic materials. For example, cutting a 1 cm cube into 10^{21} cubes that are each 1 nm on a side will result in the same overall volume and mass, but the surface area will be increased by a factor of 10 million. Thus, the advantage of using nanomaterials as carriers is that their surface can be coated with a large number of active molecules, which can be delivered using only small volumes of formulation.[8]

1.1 Nanomaterials for in vivo investigation

A handful of nanomaterials are being studied in clinical trials or have already been approved by the FDA for use in humans,[9-11] and several proof-of-concept studies of nanomaterials in cell culture and small animal models for medical applications are under way.[12-14] A number of these nanomaterials are designed to target tumors in vivo and are intended for use either as drug carriers or as contrast agents for molecular imaging. Nanomaterials infused into the bloodstream can accumulate in tumors owing to the “enhanced permeability and retention” (EPR) effect, as the vasculature of immature tumors presents fenestrations with pores ranging from 200 to 600 nm, allowing for the extravasation of nanoparticles from the blood into the tumor tissue.[15] The infusion of antineoplastic drugs exploiting nanomaterials as carriers results in an increased accumulation of drugs at the tumor, as compared with conventional administartion. In addition, the high ratio of surface area to volume favors high surface loading of therapeutic agents; when using

organic nanomaterials, their hollow or porous core allows the encapsulation of hundreds to thousands of drug molecules within a single carrier nanoparticle. As the carrier degrades to some extent, the drug molecules are released, and the rate of degradation can even be controlled and finely tuned according to the polymer or coating composition. These delivery nanovehicles can also be coated with polymers, such as polyethylene glycol, to increase their half-life in the blood circulation, to prevent opsonins from adhering to the nanomaterial surface, and reduce the rapid metabolism and clearance of the nanoparticulate. Moreover, the use of nanomaterials for drug delivery may minimize adverse effects by preventing the nonspecific uptake of therapeutic agents from healthy tissues.[16,17] Nanoparticles are further attractive as sensitive contrast agents for cancer imaging. For instance, in magnetic nanoparticle-enhanced MRI, a contrast can be observed between tissues with and those without having captured superparamagnetic iron oxide nanoparticles, owing to a difference in the precession frequency of the water protons in proximity of paramagnetic nanodipoles. The use of magnetic nanoparticles as contrast agents for MRI, as compared with conventional MRI, was associated with substantial increases in both diagnostic sensitivity (90.5% vs. 35.4%) and specificity (97.9% vs. 90.4%) in the detection of metastatic tumors.[18] Magnetic nanoparticles are also being studied in clinical trials for imaging of hyperplasia, adenoma, and more specifically, primary lung cancer, in which a decrease in the function of the reticuloendothelial system affects the amount of nonspecific phagocytic uptake.

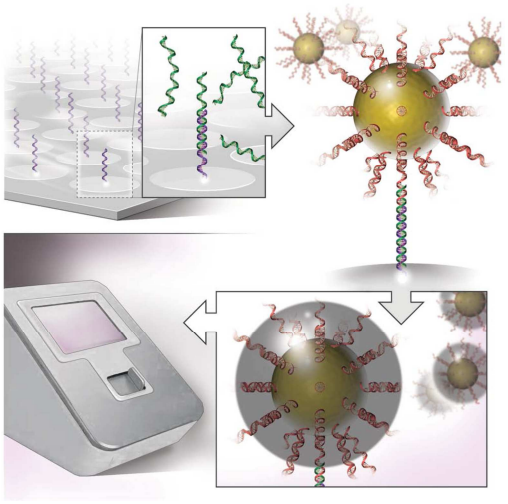

Figure 3. Nanomaterials used as labels to amplify detection signals in diagnostic devices. Nanomaterials such as gold nanoparticles can be coated with biorecognition molecules to target either a patient's DNA or a protein sample. In this picture, gold nanoparticles are coated with a complementary oligonucleotide (single-stranded DNA) that recognizes the variant gene sequence captured on a surface. Once nanoparticles are bound to the surface, the detected signal (*e.g.*, RAMAN absorption) associated to bimolecular counterparts is amplified by means of a silver nitrate reduction reaction. This technique, commonly referred to as Surface Enhanced Raman Scattering (SERS),[19] has been reported to have sensitivity equivalent to that of the polymerase chain reaction assay for genic analysis.[1]

Nanoparticles can be also employed as labels for measuring molecules of interest in biological samples. To this aim, nanomaterials can be used to either simplify/amplify the readout or to lower substantially the detection threshold of a diagnostic device. Nanoparticles are used in lateral-flow in vitro diagnostic assays (LFA), such as the urine pregnancy test, for detecting protein markers (*e.g.*, human chorionic gonadotropin [hCG]).[20] This allows an easier readout of the signal at the point of care without the need for a more complex instrumentation. A number of FDA-approved LFAs for measuring human immunodeficiency virus (HIV), malaria, and cardiac markers are also available. Although this technique is simple to use and can be carried out rapidly (one complete assay takes less than 1 h), it suffers from poor detection sensitivity (millimolar to micromolar, depending on the biomarker). Gold nanoparticles are also

used in highthroughput genomic detection devices without the need for polymerase chain reaction (PCR) amplification but with a sensitivity on the same order of that of PCR-based assays (Figure 3).[21] This technology has been approved by the FDA for genetic screening to determine drug sensitivity and to detect genetic mutations. This approach does not suffer from the problems often associated with conventional fluorescent probes for microarray labeling, such as photobleaching (a loss of signal after exposure to light), and can detect multiple markers with a high sensitivity (95%) and low detection threshold (down to 10^{-18} M). A modification of this approach called the bio-barcode assay is currently being validated for the detection of proteins associated with prostate cancer.[22]

1.2 Nanomaterials for theranostics

The term "theranostic" defines the combination of diagnostic and therapeutic capabilities into a single agent, and identifies the ongoing efforts in clinics to develop more specific and personalized therapies for various diseases.[23] The rationale arose from the fact that several diseases are broadly heterogeneous and all existing treatments are effective for only limited patient subpopulations and at selective stages of disease development. The close marriage between diagnosis and therapy could provide therapeutic protocols that are more specific to individuals and, therefore, more likely to offer improved prognoses. The emergence of nanotechnology has offered an unprecedented opportunity to draw diagnosis and therapy closer. Nanoparticle-based imaging and therapy have been investigated separately, and understanding of them has now evolved in nanoplatforms that can codeliver therapeutic and imaging functions. These nanoparticles possess unique optical or magnetic properties and have been previously studied in the imaging setting and have achieving successful outcomes in several circumstances. These have laid the foundation for the current exploits, since the imaging probes can be easily upgraded when loaded with appropriate therapeutics. It has been shown that various kinds of therapeutics, including those based on small molecules, proteins and nucleotides can be conveniently tethered onto nanoplatforms. The large capacity even allows for the loading of a

second or third functionality, a feature that encourages the formation of an all-in-one nanosystems with comprehensive features (Figure 4).

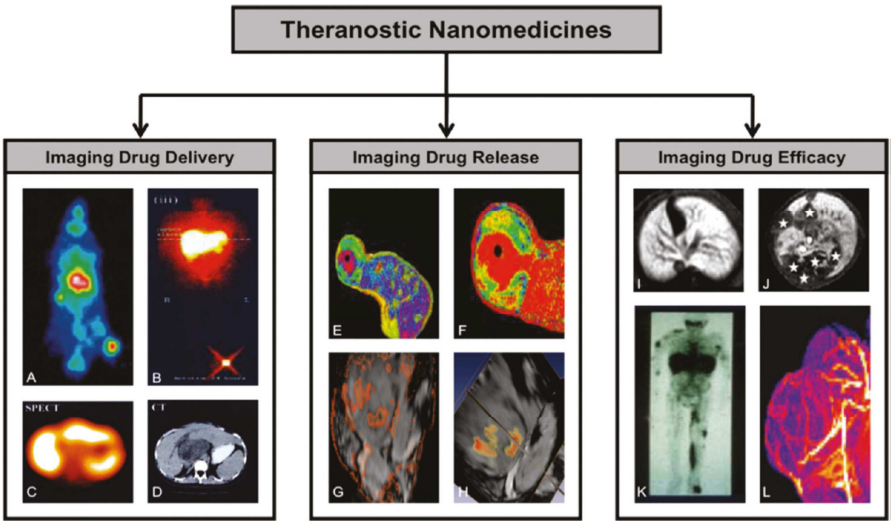

Figure 4. Applications of theranostic nanomedicine formulations. Theranostic nanomedicines can be applied for various different purposes, most notably for imaging drug delivery (A-D), drug release (F-H), and drug efficacy (I-L). (A) Gamma camera imaging of biodistribution and tumor accumulation of a passively tumor-targeted iodine^{131}-labeled HPMA copolymer in a Copenhagen rat bearing a Dunning AT1 tumor in its right hind limb. (B) Gamma camera image showing effective active drug targeting to the liver using an iodine^{123}-labeled galactosamine-modified HPMA copolymer containing doxorubicin *(i.e.,* PK2) in a patient suffering from hepatocellular carcinoma. (C,D) Functional SPECT imaging (C) of the tumor and liver localization of iodine^{123}-labeled PK2 combined with anatomical CT imaging (D), exemplifying that the majority of the liver-targeted polymeric prodrug does not localize to the (dark) tumorous region in the middle of the SPECT and CT image. (E,F) MR-based visualization and quantification of manganese and doxorubicin release from temperature-sensitive liposomes (TSL). The color-coded Mn2þ-enhanced T_1 map obtained at 45 min after the i.v. injection of TSL into a rat bearing a preheated fibrosarcoma tumor is shown in (E). (F) Amount of released doxorubicin calculated and correlated on a pixel-by-pixel basis from the image in (E), exemplifying release in the periphery of the tumor. (G,H) Release of Gd-DTPA from PLGA-based nanoparticles containing iron oxide, Gd-DTPA and 5-FU. (G) Subtraction image of precontrast minus postcontrast T_1-map (in red; showing Gd-DTPA release; note that the Gd-DTPA-signal is quenched in close proximity to iron oxide), overlaid on a T_2*-weighted image, showing the tumor accumulation of the particles (in black). (H) A 3D image depicting T_2*-weighted signals overlaid with quantitative T_1 values (yellow, 50 μM; red, 500 μM), enabling quantification of drug release. (I,J) Accumulation of Gd-labeled polypropylene diaminobutane dendrimers in a healthy mouse liver (I) and in a liver containing several

metastatic lesions (J), exemplifying the suitability of these particles to visualize liver metastases. (K) Biodistribution of indium^{111}-labeled PEGylated liposomes in a Kaposi sarcoma patient. Localization to a large tumorous mass in the lower left leg and to several metastatic lesions can be clearly observed, exemplifying the possibility of such formulations for predicting and monitoring treatment responses. (L) Maximal intensity projection of an MR angiography scan of a Dunning AT1 tumor obtained at 30 min after the i.v. injection of a 25 kDa sized gadolinium-labeled HPMA copolymer. Such MR angiography-based approaches are considered to be highly useful for noninvasively assessing the efficacy of nanomedicine based antiangiogenic interventions.[23]

2. Magnetic nanoparticle design for medical diagnosis and therapy

In the last decade, several investigations with different types of crystalline iron oxides have been carried out in the field of nanosized magnetic particles (mostly single domains of about 5-20 nm) in diameter of maghemite (γ-Fe_2O_3), and magnetite (Fe_3O_4), among which magnetite is a very promising candidate since its biocompatibility has already been established.[24] With proper surface coating, the magnetic nanoparticles can be dispersed in suitable solvents, forming homogeneous suspensions, called ferrofluids.[25,26] Such a suspension can interact with an external magnetic field and be positioned to a specific area, facilitating magnetic resonance contrast enhancement. Nanosized crystals exhibit unique physical and chemical properties that are not found neither at atom nor at bulk level. Quantum size effects and the large surface area of magnetic nanoparticles dramatically change some of the magnetic properties and exhibit superparamagnetic character and quantum tunneling of magnetization, because each particle can be considered as a single magnetic domain.[27] Based on their unique mesoscopic physical, chemical, thermal, and mechanical properties, superparamagnetic nanoparticles offer a high potential for a broad spectrum of biomedical applications:

- cellular therapy, including cell labeling and targeting, tools for cell-biology basic research to separate and purify cell populations
- tissue repair
- drug delivery

- magnetic resonance imaging
- hyperthermia
- magnetofection
-

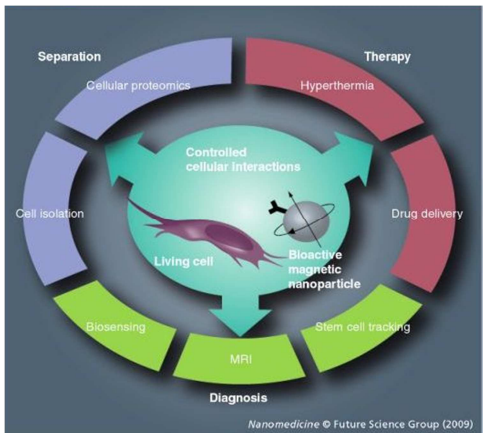

Figure 5. Biomedical applications of magnetic nanoparticles.

For these applications, nanoparticles must have combined properties of high magnetic saturation, biocompatibility and interactive functions at the surface. The surfaces of these particles could be modified through the creation of few atomic-thick layers of organic polymer or inorganic metallic (*e.g.,* gold) or oxide surfaces (*e.g.,* silica or alumina), suitable for further functionalization through the attachment of various bioactive molecules.[28] As magnetic nanoparticles accumulate at the target site, *e.g.,* in a tumor tissue, they can play an important role in the detection of malignancies through MRI or electron microscopy imaging to localize them and measure their binding or as drug carrier for anti-cancer drugs. Magnetic nanoparticles having suitable surface characteristics have a high potential for use in a lot of in vitro and in vivo applications. In all these cases, superparamagnetism is the key feature because magnetic nanoparticles do not retain any magnetism after removal of the external magnetic field. Thus, the utility of this class of nanoparticles depends upon several parameters, including high superparamagnetic

susceptibility for an effective magnetic enrichment,[29] magnetic core size, which should be possibly monodisperse in the range 6-15 nm, superparamagnetic behavior,[30] tailored surface chemistry.

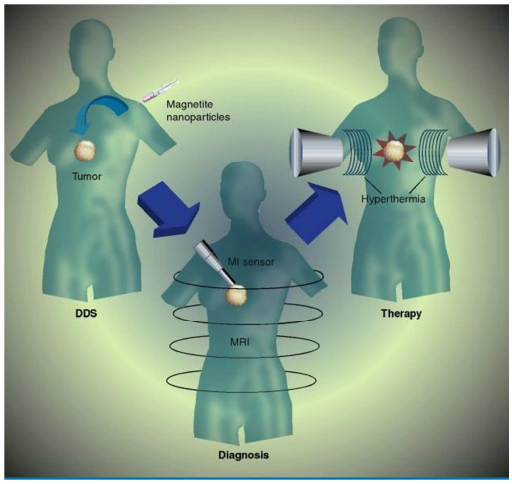

Figure 6. Therapeutic strategies using magnetic nanoparticles. Functionalized magnetic nanoparticles accumulate at the tumor tissues via drug delivery system (DDS). Magnetic nanoparticles can be used as a tool for cancer diagnosis by MRI. Hyperthermia can then be induced by exposure to an alternating magnetic field. Hence, magnetic nanoparticles can be used for simultaneous cancer therapy and diagnosis.[31]

2.1 Chemical synthesis of superparamagnetic iron oxide nanoparticles

The wet chemical strategy for preparing monodisperse nanoparticles involves the separation of nucleation step from growth of nanocrystals. A burst nucleation event first occurs when the monomer concentration quickly increases over a critical supersaturation without further formation of nuclei afterwards. The produced nuclei then grow at the same rate, resulting in monodisperse nanosized crystals. Once formed, these nanoparticles have a high surface area and agglomerate rapidly to minimize their surface energy. Thus, a suitable capping agent has to be used to stabilize these nanoparticles and prevent them by forming aggregates. Numerous synthetic methods have been developed to

synthesize magnetic nanoparticles, including coprecipitation,[32] sol-gel synthesis,[33] microemulsion synthesis,[34] sonochemical reaction,[35] hydrothermal reaction,[36] thermal decomposition,[37] electrospray synthesis,[38] and laser pyrolysis.[39] Coprecipitation of Fe^{3+} and Fe^{2+} ions is a classical method used to prepare iron oxide nanoparticles on a large scale by aging a stoichiometric mixture of inorganic salts in aqueous solution. A set of experimental parameters, such as pH, reaction temperature, and precursor, have been studied to control nanoparticle morphology, size, and yeld. The solvothermal process exploits a high-pressure reaction to obtain highly crystalline magnetic nanoparticles. However, when using these two methods, it is difficult to produce magnetic nanoparticles with a narrow size distribution. High temperature decomposition of metal complexes is now routinely applied to prepare magnetic nanoparticles with better-controlled size and morphology.[40] A typical thermal decomposition method requires the presence of a metal complex and a surfactant in an organic solvent with a high-boiling point. In the reaction, the precursors are either added via a hot-injection process or directly heated up from a homogeneous mixture.[41] In the hot-injection process, the thermally unstable metal complexes are rapidly injected into a hot solution in the presence of surfactants to create an instantaneous nucleation event, followed by a controlled growth process. In the heating up procedure, all the precursors are mixed and heated, magnetic nanoparticles are made by tailoring reaction temperature and precursors concentration. Oleic acid and oleylamine are two surfactants commonly used for nanoparticle stabilization and for the control of nanoparticle size and morphology. The metal precursors are usually metal acetylacetonates and metal oleates. For example, iron(III) acetylacetonate, $Fe(acac)_3$, was mixed with 1,2-hexadecanediol, oleic acid, and oleylamine in dibenzyl ether and the mixture was heated up to 300 °C to make monodisperse Fe_3O_4 nanoparticles with a narrow size distribution in the range 4-8 nm with 5-10% dispersity. Iron(III) oleate was used to prepare monodisperse iron oxide nanoparticles on a large scale. The first example of synthesis of size-controlled monodisperse Fe_3O_4 nanoparticles obtained through a heating up procedure of $Fe(acac)_3$ in the presence of oleic acid and oleylamine, was reported in 2002 by Sun et al.[42] Rockemberger et al.

demonstrated for the first time the applicability of hot injection approach to the synthesis of γ-Fe_2O_3 nanoparticles in 1999.[43]

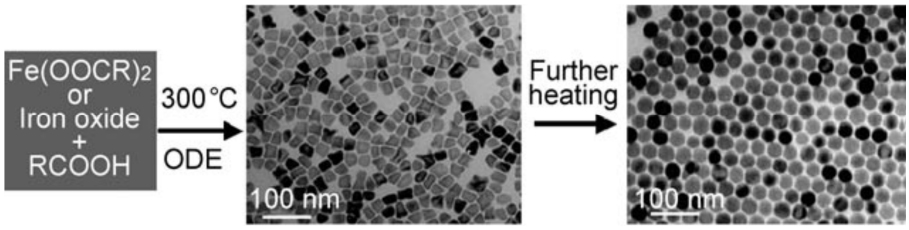

Figure 7. The formation of Fe_3O_4 nanocrystals. The middle and right panels are TEM images of the as-synthesized nanocrystals taken at different reaction times.44

2.2 Surface modification of magnetic nanoparticles

In the preparation and storage of nanoparticles in colloidal form, the stability of the colloid is of utmost importance. Ferrofluids are colloidal suspensions of magnetic particles which possess a unique combination of fluidity and aptitude to interact with a magnetic field. In the absence of any surface coating, magnetic iron oxide nanoparticles have hydrophobic surfaces with a large surface area to volume ratio. Due to colloidal interactions between the particles, these particles agglomerate and form large clusters, resulting in increased particle size. Hence, these clusters, exhibit strong magnetic dipole–dipole attractions between them and show ferromagnetic behavior.[45] The adherence of magnetic nanoparticles causes a mutual magnetization, resulting in increased aggregation properties. For effective stabilization of iron oxide nanoparticles, often a very strong requirement of density for coating is desirable. Stabilizers such as a surfactant or a polymer are usually added at the time of preparation to prevent aggregation of the nanoscale particulate. Most of these polymers adhere to the surfaces in a substrate-specific manner.[46] Monodisperse nanoparticles with controlled shapes and sizes are usually coated with a long-chain hydrocarbon, leading to a hydrophobic surface. To make these nanoparticles biocompatible for biological applications, their surface needs to be functionalized, which is usually accomplished by two alternative approaches, 1) surfactant addition or 2) surfactant

exchange. Surfactant addition is achieved by means of the adsorption of amphiphilic molecules that contain both a hydrophobic segment and a hydrophilic component. The hydrophobic segment forms a double layer structure with the original hydrocarbon chain anchored to the nanoparticle surface, while the hydrophilic groups are exposed to the outer layer of the nanoparticle, conferring it water solubility. In contrast, the surfactant exchange approach involves the direct replacement of the original surfactant with a new bifunctional surfactant. This bifunctional surfactant has one functional group available for binding to the nanoparticle surface tightly via a strong chemical bond and the second functional group at the other end has a polar character so that the nanoparticle can be dispersed in water or be conjugated to a further molecule.

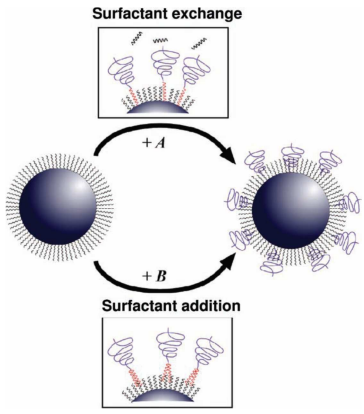

Figure 8. Strategies for NP surface modification.[47]

There are various kinds of materials that can be chosen for coating nanoparticles.[48,49] Polymer coating materials, including lipids, proteins, dendrimers, gelatin, dextran, chitosan and PEG are often chosen for this purpose.[50] Bifunctional molecules, such as dimercaptosuccinic acids (DMSA), dopamine, and silanes, were also investigated for use in nanoparticle functionalization. For example, dopamine was found to be a stable anchor on the Fe_3O_4 nanoparticle surface. In 2007, Messersmith and coworkers published an approach inspired by the adhesive proteins

secreted by mussels for attachment to wet surfaces.[51] Mussels are promiscuous fouling organisms and have been shown to attach to virtually all types of inorganic and organic surfaces, including classically adhesion-resistant materials such as poly(tetrafluoroethylene) (PTFE). Clues to mussels adhesive versatility may lie in the aminoacid composition of proteins found near the plaque-substrate interface, which are rich in 3,4-dihydroxy-L-phenylalanine (DOPA) and lysine amino acids. In addition to participating in reactions leading to bulk solidification of the adhesive, DOPA forms strong covalent and noncovalent interactions with substrates. DOPA and other catechol compounds behave as binding agents for coating inorganic surfaces, including the electropolymerization of dopamine onto conducting electrodes; however, coating of organic surfaces has proven much more elusive. Silanes were employed to exchange the hydrophobic ligands on ferrite magnetic nanostructures. The end group of silanes, including isocyanine, acrylate, thiol, amino, and carboxylic groups, offer extensive chemistry for the modification of nanostructures. The use of dopamine and saline as stabilizers often need to be combined with PEG or other polymers to offer long-term nanoparticle stabilization in biological solutions. Besides PEG, chitosan, alginate, and dextran can also be utilized to disperse the nanostructures and offer them long-term stability and biocompatibility. A shell does not only serve to stabilize and protect the magnetic nanoparticles against degradation, but can also be used for further functionalization with specific components, such as catalytically active species, drugs, specific binding sites, or other functional groups.

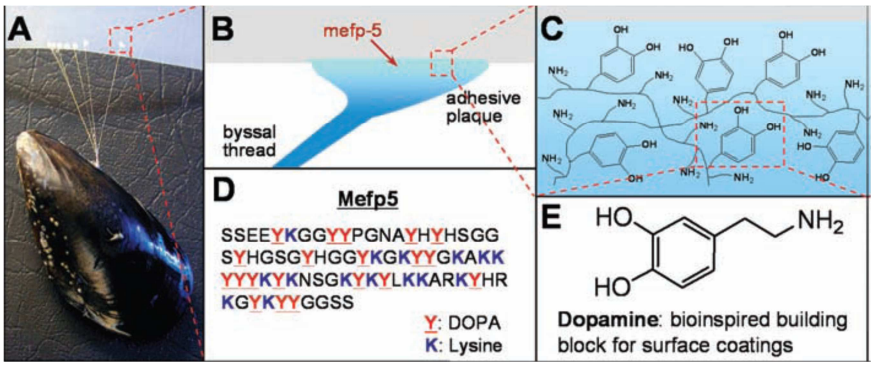

Figure 9. (A) Photograph of a mussel attached to commercial PTFE. (B, C) Schematic illustrations of the interfacial location of Mefp5 and a simplified molecular representation of characteristic amine and catechol groups. (D) The amino acid sequence of Mefp5. (E) Dopamine contains both amine and catechol functional groups found in Mefp5 and was used as a molecular building block for polymer coatings.[51]

2.3 Targeted nanoparticles

It is obvious that future developments of magnetic nanoparticles will be in the direction of active targeting through molecular imaging and cell tracking. Therefore in the case of cancer diagnosis, the next challenge resides in the generation of suitably functionalized surfaces of these particles. The development of long-circulating nanoparticles is the first requirement for active targeting. The most satisfactory strategy consists in using macrophage-evading nanoparticles, with long plasma half-life in order to increase the probability of attaining the desired target. The design of such "stealth" nanoparticles requires the consideration of a multitude of physico-chemical and physiological factors, affecting circulation time. In particular, their surface protection by a barrier of hydrophilic oligosaccharide groups is thought to prevent the opsonin adsorption and therefore to avoid the macrophage recognition. Among the physico-chemical factors, which are known to have an effect on the opsonization process, the size, the surface charge density and the hydrophilicity/hydrophobicity balance have been widely investigated, either in liposome or in polymeric nanoparticle systems.[52] The main conclusion is that the smaller, the more neutral and the more hydrophilic

the carrier surface, the longer its plasma half-life. Concerning the size effect, the available data suggest that surface curvature changes may affect the extent and/or the type of opsonin adsorption. It is generally assumed that surface features are more important than those related to the core, because the surface is in direct contact with blood and organs. For hydrophobic carriers, many studies have concerned the development of core-corona structures where the corona is made of hydrophilic macromolecules for creating polymer brushes, acting as a steric surface barrier and reducing opsonin adsorption. Among the natural or artificial macromolecules, linear dextrans, PEG and their derivatives are widely used. Linear dextrans have been used frequently as plasma expanders in medicine: drugs conjugated to dextran remain in the blood circulation for extended periods of time, proportional to the average molecular weight of the macromolecule. The clearance rate of dextran-coated liposomes is dependent on the density of dextran molecules. Other biological macromolecules have been investigated, *e.g.,* polysialic acid, heparin and heparin-like polysaccharides, but, because of their high cost and/or the possible immunological consequences associated with bacterial-made macromolecules, efforts have been directed to the design of synthetic hydrophilic macromolecules, including "block copolymers". The strength of polymer adsorption and the resultant polymer conformation is dependent on the proportion and on the size of the hydrophobic block (*e.g.*, polypropylene oxide, PPO) that is flanked on both sides by two hydrophilic chains of polyethylene oxide (PEO) block.[53] In addition, the physico-chemical properties and the curvature of the nanoparticle surface play a role. The nanoparticle stealth behaviour is believed to be a function of the thickness and of the density of the PEO layer. Nevertheless, in order to avoid the possible depletion of copolymers in the blood compartment, great efforts have dealt with the covalent anchorage of PEO macromolecules onto the carrier surface. Such a route is well known in galenical pharmacology, where drugs (small molecules, peptides, proteins, antibodies and oligonucleoides) are conjugated to PEO macromolecules in order to improve their circulation lifetime and bioavailability and decrease their immunogenicity, renal clearance rate and dosing frequency. This process is so widely used that it is called PEGylation. Polyethylene glycol (PEG) is the α,ϖ-dihydroxyl derivative of PEO and is a flexible polyether, hydrophilic (but also soluble in some

organic media), not biodegradable and easily excreted from living organisms by physiological routes. Its functional end-groups are available for derivatization leading to numerous possibilities for covalent attachment onto preformed functional surfaces or anchoring during the synthesis of polymeric particles. PEG has been shown to be the most effective polymer for suppressing protein adsorption, the optimal molecular weight varying between 2000 and 5000 Da. Lastly, regardless of the active targeting strategy, long circulating carriers present also a great interest as circulating reservoirs for drugs or therapeutic agents with short elimination half-lives or for blood-pool imaging in nuclear medicine. Moreover, long-circulating particles escape from the circulation is normally restricted to sites where the capillaries have open fenestrations, such as in the sinus endothelium of the liver, or when the integrity of the endothelial barrier is perturbed by inflammatory processes (*e.g.,* rheumatoid arthritis, infarction, infections) or by some kinds of tumors. Therefore the idea of exploiting such vascular abnormalities for extravasating and accumulating nanoparticles in these inflammatory sites or tumors is particularly attractive. Such a strategy can be considered both as an active and a passive targeting strategy, as it is independent of the mononuclear phagocyte system mediation.

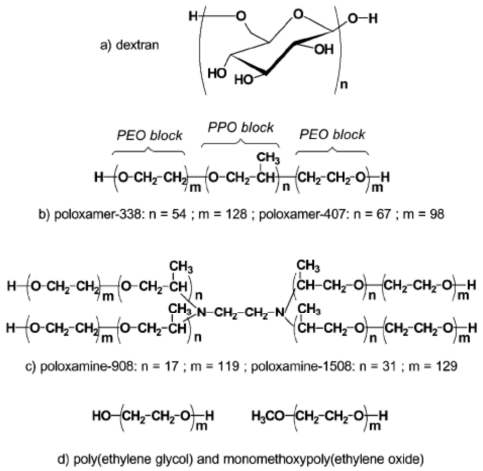

Figure 10. Typical macromolecules used as hydrophilic coating for mononuclear phagocyte system-evading nanoparticles.[54]

Ligand conjugation is the second requirement for active targeting. To increase the probability of redirecting long-circulating nanoparticles to the desired target site, their surface has to be modified with ligands that specifically bind to surface epitopes or receptors present on the target cells, for istance, by molecular recognition processes involving antibody-antigene interactions. In principle, these ligands have to be not macrophage-recognizable and coupled to the surface of stealth carriers. Such a strategy should open the possibility of targeting specific cell types or subsets of cells within the vasculature and even elements of vascular emboli and thrombi. In cancer therapy, active targeting could allow for the selective destruction of cancer cells. Among these ligands, often recurring are oligosaccharides, oligopeptides, folic acid, antibodies and their fragments. Due to the unique specificity of monoclonal antibodies for their molecular counterparts and to the possibility to produce immunoglobulins for almost every known marker receptor, this class of proteins is usually considered the preferred choice for active targeting and grate effort has been devoted to the development of antibody-functionalized nanocarriers. However, antibody coupling has at least two drawbacks: 1) the overall size of the antibodies (typically in the range 15-20 nm), which cause particles to diffuse poorly through biological barriers, and 2) their immunogenicity, *i.e.* the property of being able to elicit an immune response within an organism. For this reason, the coupling of small non-immunogenic ligands to polymeric carriers has been also investigated. Therefore, for tumor targeting, folic acid, antibodies or peptides could be grafted to PEGylated nanoparticles in order to take advantage of the frequent overexpression of the specific receptors onto the surface of human cancer cells. Interestingly, nanoparticles conjugated with antibodies appeared to interact more efficiently with their receptors than free antibodies. Thus, not only do nanoparticles conjugated with biological molecules selectively target cancer cells, but they could also improve the internalization of the encapsulated drugs into the targeted cancer cells.

2.4 Biomedical applications of magnetic nanoparticles

2.4.1 Magnetic Resonance Imaging

Superparamagnetic iron oxide nanoparticles can play an important role as MRI contrast agents, to better differentiate healthy and pathological tissues.[55] In vivo molecular imaging has been identified by the National Cancer Institute of the United States of America as an outstanding opportunity for studying diseases noninvasively at the molecular level.[56] The aim is to visualize molecular characteristics of physiological or pathological processes in living organisms before they manifest in form of anatomic changes. MRI offers several advantages over alternative techniques, including lack of irradiation, possibility to generate 3D images, excellent spatial resolution with optimal contrast within soft tissues, and a very good signal-to-noise ratio. Paramagnetic (*e.g.,* gadolinium, europium, neodynium, and manganese-containing materials) and superparamagnetic (iron oxide nanocrystals in the form of γ-Fe_2O_3,and Fe_3O_4) compounds can be used as MR contrast materials. A first important difference between these two classes of contrast enhancers is that while paramagnetic species enhance the signal in T_1-weighted images resulting in a positive contrast, magnetic nanoparticles provide strong signal enhancement in T_2-weighted images (negative contrast), owing to a different contrasting mechanism.[57,58] Unfortunately, in most cases, antibody-conjugated gadolinium complexes proved to be largely unsuccessful due to the relatively low sensitivity of MRI and the low density of cell target receptors, thus requiring administration of excessive gadolinium doses. However, Gd-contrast materials may induce severe adverse effects with lethal outcome that have been observed in patients with compromised renal function and subsequent deposition in different organs/tissues and release of highly toxic Gd^{3+} leading to a nephrogenic systemic fibrosis. This drawback can be partially overcome by using magnetic nanoparticles based on iron oxide, which have been demonstrated to induce large increments in transverse relaxation rate upon binding with a 10^6 signal amplification over Gd-DTPA.[59] For this reason, superparamagnetic iron oxide nanoparticles are gaining much attention in view of their usefulness as contrast agents for MRI. The first and major prerequisite of targeted contrast agents is the identification of cell- and/or disease- and/or function-specific biomarkers. Ideally, the

biomarkers should be solely and abundantly expressed on the desired cell types. Furthermore, disease-specific biomarkers should be clearly different from healthy status. Biomarkers for targeted contrast agents are cell surface receptors, phospholipids of the outer leaflet of the cell membrane, and enzymes. Targeted magnetic nanoparticles are composed of at least two components: 1) the magnetic iron oxide core represents the imaging or sensing component and 2) the attached molecules represent the targeting or affinity component. Magnetic nanoparticles without targeting components are rapidly engulfed by monocytes and macrophages. Thereby, they can be used to image monocytes and macrophages and their phagocytic aptitude in vivo.

2.4.2 Monitoring stem cell migration and tissue repair

Stem cells transplants is expected to have tremendous potential for the treatment of many degenerative diseases because of their capability to perform multiple cell cycle divisions and of their differentiation efficiency.[60] Several clinical trials are ongoing with different types of stem cells. Mesenchymal stem cells are used for the reparation of damaged tissues, regeneration of bone defects and spinal cord injury, stroke and myocardial infarction, while neural stem cells are investigated for the neural lineages generation of the nervous system. On this basis, one important issue is to identify and track the stem cells after their injection in the body, to monitor their motility and to follow their localization and expansion thereafter. Among the available in vivo imaging techniques useful for stem cell monitoring, MRI is particularly promising since it can provide high spatial resolution images without compromising the patient care. T_2 contrast agents based on iron oxides offer a powerful labeling for the in vivo visualization of stem cells. Magnetic nanopaticle sizes for utilization in stem cell labeling can vary from ultrasmall (within 35 nm) to micron-sized. The nanoparticles can be coated by different polymers, including polyethylene glycol, silica, dextran and polystyrene, to increase the stability of the suspension avoiding the cell toxicity caused by the formation of large aggregates. Different preparations may affect the labeling efficiency of nanoparticles, which determines the interactions between nanoparticles and cells. The

typical nanoparticle uptake follows an endocytosis pathway that can be induced by mere incubation of the nanoparticle suspension in the cell medium, which, in turn, can be improved by application of an external magnetic field. The addition of adjuvants as transfection agents or nanoparticle functionalization with antibodies exploiting a ligand-receptor specific interaction, could be of help with some cell types. In alternative, it is possible to induce a temporary membrane permeability by electroporation or ultrasound pulses. Several magnetic nanoparticle-based contrast enhancers were successfully applied to in preclinical trials.[61]

2.4.3 Drug delivery

Most pharmacological approaches to cancer therapy are based on chemotherapeutic substances, which generally exhibit high cytotoxic activities but poor specificity for the intended biological target. This practice mostly results in a systemic distribution of the cytotoxic agents leading to the occurrence of well-documented side effects associated with chemotherapy. Besides magnetic force delivery, two alternative "physiological" routes can be followed by magnetic nanoparticles, which are common to all kinds of nanoparticulates. The passive targeting route takes advantage of the biological function of the reticuloendothelial system (RES), a cell family of the immune system comprising circulating monocytes, bone marrow progenitors and tissue macrophages, which is deputed to the first clearance activity in mammalian organisms. Once unprotected particles are immersed in the blood stream, an array of plasma proteins recognizes them as invading entities and immediately adsorb on their surface. The parameters affecting the extent of opsonization are essentially related to the physical properties of the nanoparticle surface, including size, shape, charge and aggregation state. Large objects are rapidly cleared and highly charged particles have a tendency to attract opsonins. Consequently, magnetic nanoparticles coated by these plasma proteins are rapidly endocytosed by the RES cells, resulting in their removal from circulation and accumulation in organs with high phagocytic activity, such as liver and spleen. Particle size is a key parameter as magnetic particles smaller than 4 μm

accumulate in the liver (70-90%) and spleen (3-10 %) quickly. Particles larger than 250 nm are usually filtered to the spleen; particles in the range 10-100 nm are mainly phagocytosed through liver cells, while nanoparticles below 5.5 nm can be cleared by renal route.[62] Therefore the optimal particle size for drug delivery treatments ranges between 10 to 100 nm, as these will have the longest blood circulation time. It has been suggested that also the shape can play a role.[63] Hence, passive nanocarriers can be used to deliver drugs for the treatment of hepatic diseases, such as liver metastases, and to favor the internalization of antibiotics by phagocytic cells of the RES for the treatment of intracellular infections. Magnetically assisted targeting will have the advantage of increasing the local concentration of the administered drug, while the overall dose can be reduced. The movement of magnetic nanoparticles inside a matrix or fluid depends directly on a multitude of factors such as the external magnetic field, the temperature and the viscosity of the medium, the fluid flow, the interaction between nanoparticles and fluid components and the size and shape of the nanoparticles. The dynamics of nanoparticle transport in vivo through a vein or artery to an area of interest are far from being fully understood and modeled but there are nowadays several studies in this direction. In contrast with the passive delivery route, active targeting has the advantage of improving the accumulation of chemotherapeutics at the tumor site, but requires multiple synthetic steps to tailor the chemical properties of nanoparticles in order to achieve a suitably bioengineered magnetic nanocarrier. In principle, it is always necessary to stabilize the nanoparticle dispersion in the aqueous environment. As described in Paragraph 2.3, coating the nanoparticles with a suitable polymer shell, including organic (PEG, dextran, chitosan, polyethyleneimine, and phospholipids) or inorganic (silica) is the first step. Whatever the stabilizer, the next requirement is to reduce significantly the possible interactions with opsonins and with the RES, by conjugating the magnetic nanoparticles with an appropriate protein-repellent molecular species, such as PEG. The final step consists in functionalizing such long-circulating nanoparticles with targeting ligands having high selectivity for specific cancer cell receptors. The full-armed magnetic drug delivery nanosystem is obtained by loading a cytotoxic cargo at some stage of the above synthetic steps.[64]

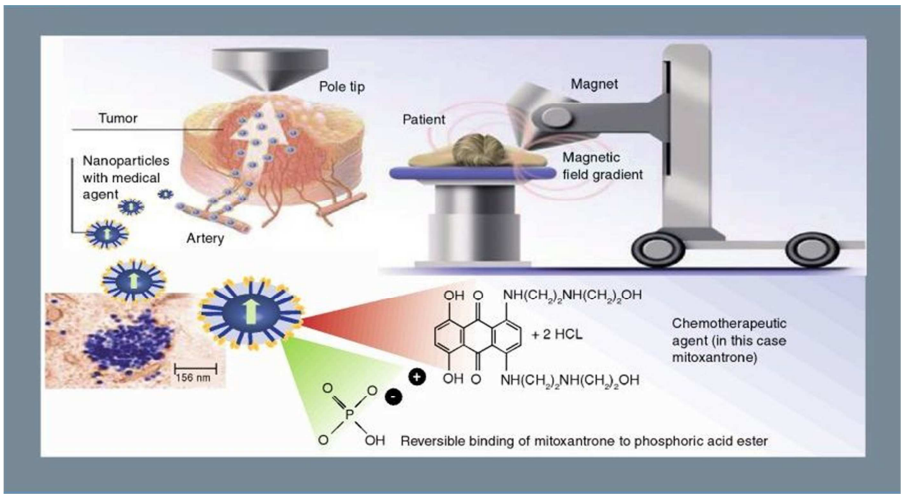

Figure 11. Magnetic drug targeting. Magnetic drug nanocarriers decompose in the target zone and release the drug.[65]

2.4.4 Cellular labeling and cell separation

Cell labeling with ferro/paramagnetic substances is an increasingly common method for cell separation.[66] Current techniques utilize either of the following two approaches: attaching magnetic particles to the cell surface or internalizing biocompatible magnetic particles by fluid phase endocytosis, receptor-mediated endocytosis or phagocytosis. One strategy for the efficient and specific cell labeling with magnetic particles is to modify the nanoparticle surface with a ligand that is efficiently taken up by the target cells via receptor-mediated endocytosis. A variety of potential ligands have been conjugated to the nanoparticle surfaces to facilitate receptor-mediated endocytosis of the nanoparticles. Targeting agents have been demonstrated to preferentially target cell surface, because the receptors for these ligands are frequently overexpressed on the surface of mammalian cells. Many of these ligands are stable, and generally poorly immunogenic. In the absence of any system to inhibit endocytosis, most nanoparticles are endocytosed by cells and eventually sequestered in digestive vacuoles inside the cell. Once the particles are endocytosed, they are probably removed from the contact with specific cell surface receptors and become ineffective. As a result of these events,

the cells are at high risk of apoptosis from overload with particles. If the particles can be prevented from leaving the cell surface, they remain in contact with their specific receptors and are expected to leave the cell in a state of prolonged stimulation while protecting the cells from damages triggered by endocytosis.

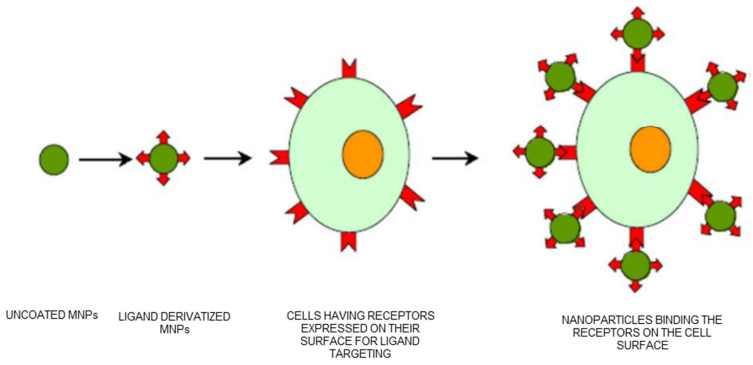

Figure 12. Schematic representation of derivatization of superparamagnetic iron oxide nanoparticles with targeting ligands and their adhesion to cells. The derivatized nanoparticles act as cellular labels that are targeted at the membrane receptors expressed on cells surface without being internalized.[24]

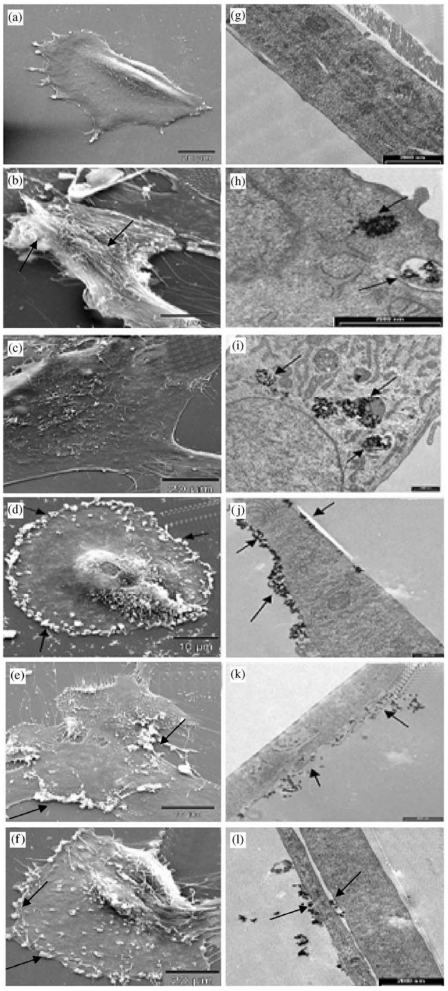

Figure 13. Scanning electron microscopy (SEM) (a-f) and transmission electron microscopy (TEM) (g-l) images of human fibroblasts (a,g, control) and incubated with (b,h) uncoated magnetic nanoparticles, (c,i) PEG-coated nanoparticles, (d,j) lactoferrin-derivatized nanoparticles, (e,k) ceruloplasmin-derivatized nanoparticles and (f,l) insulin-conjugated nanoparticles. Uncoated magnetic particles show vacuoles in cell body and distorted cell membranes. PEG-coated nanoparticles were internalized in huge amounts without being toxic, while protein-coated nanoparticles were not endocytosed and were found at the cellular membranes (see arrows).[23]

2.4.5 Hyperthermia

Another interesting application of magnetic nanoparticles is in cancer thermotheraphy, which is considered as a supplementary treatment associated with chemotherapy, radiotherapy, and surgery.[67] The idea of using magnetic induction hyperthermia is based on the fact that when magnetic nanoparticles are exposed to a variable magnetic field, heat is generated by the magnetic hysteresis loss. The amount of heat generated depends on the nature of magnetic material and of magnetic field parameters. Magnetic particles embedded around a tumor site and placed within an oscillating magnetic field will heat up to a temperature dependent on the magnetic properties of the material, the strength of the magnetic field, the frequency of oscillation and the cooling capacity of the blood flow in the tumor. Cancer cells are sensitive to temperature increase and are killed when the temperature raises above 43 °C, whereas the normal cells can survive at higher temperature values. Heat could be generated by applying an appropriate magnetic field. The size of the magnetic crystals commonly employed in hyperthermia is submicrometric, thus the powders or bulk of these biomaterials have comparable properties. These materials are not only biocompatible, but also bioactive and could be useful for bone tumors. Choosing high-power magnetic nanocrystals combined with appropriate external magnetic field, very small amounts of nanoparticles in the order of tenth of milligram may easily be used to raise the temperature of biological tissue locally up to cell necrosis. It has been shown that hyperthermia greatly enhances cytotoxicity of radiation and drug treatment with brain tumor cell lines, which were also confirmed in vivo by multimodel hyperthermia studies with rat, rabbits and dogs.[68] Concomitantly, Yanase M. et al. have suggested that hyperthermia produced by magnetic nanoparticles can activate the immune response against cancer cells triggered by massive release of heat shock proteins from those treated cells. (Figure 14).

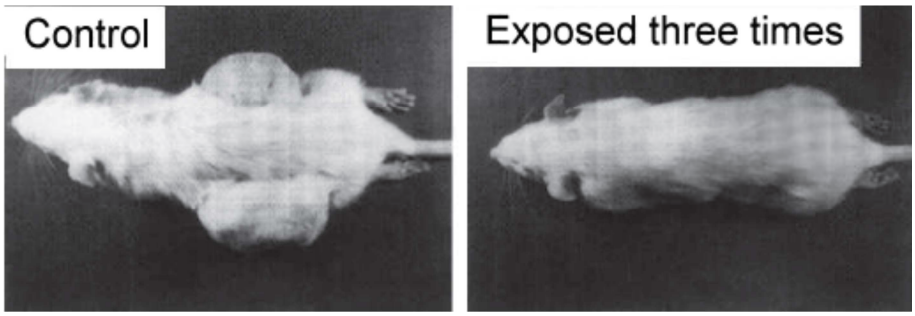

Figure 14. Antitumor immune response induced by hyperthermia using magnetite nanoparticles. (A) Rats photographed at the 28th day after the magnetic cationic liposomes injection. Rat glioma T-9 cells (1×10^7 cells) were transplanted subcutaneously into the left femoral region of F344 rats. On the 9th day after transplantation into the left side, another aliquot of the T-9 cell suspension (1×10^7 cells) was transplanted subcutaneously into the right femoral region. The magnetic cationic liposomes were injected into the left tumor only, on the 11th day after the first transplantation. When hyperthermic treatment was repeated three times at 24 h intervals, both tumors had disappeared by the 28th day after the magnetic cationic liposomes injection.[69]

The efficiency of this type of thermotherapy has been demonstrated on several types of cancers including brain cancer,[70,71] prostate cancer,[72,73] and breast cancer.[74,75] Research in this area has also led to industrial developments. In addition to the company Nanobacterie, there are at least three companies that develop cancer therapy using the heat generated by magnetic nanoparticles when the latter are exposed to an alternative magnetic field (AMF).[76] The patents that have been published by these companies describe various ways of using the heat generated by chemically synthesized magnetic nanoparticles to carry out AMF cancer therapy.[77]

2.4.6 Magnetofection

Magnetofection is a method in which magnetic nanoparticles associated with vector DNA are transfected into cells under the influence of an external magnetic field. For this purpose, magnetic nanoparticles might be coated with a polycationic polymer, such as polyethyleneimine which readily associates with negatively charged DNA since the magnetic

particles are positively charged due to polyethyleneimine coating. Whether viral or nonviral vector is exploited, magnetofection has been shown to enhance the efficiency of delivery up to several thousand times. For magnetically assisted nucleic acid transfection, magnetofection is unusually rapid, simple and yields transfection level saturation at low doses in vitro. Furthermore, since these magnetic particles do not rely on receptors or other membrane-bound proteins for cell uptake, it is possible to transfect cells that normally are non-permissive.

3. Final considerations

Most of the work included in this thesis exploits a new generation of targeted magnetic nanoparticles. The preferred molecular receptor investigated is the Human Epidermal Growth Factor Receptor 2 (HER2), which is considered one of the most relevant biomarkers for the diagnosis of metastatic breast cancer. Mammary carcinoma is the second most common type of malignant tumor in adult women after lung cancer, as more than one million women are diagnosed with breast cancer every year. Despite the advances in diagnosis and treatment, which have resulted in a decrease in mortality in recent decades, breast cancer remains a major public health problem. Among the most significant unresolved clinical and scientific problems are the occurrence of resistance to clinical treatments, their toxicity, and how to predict, prevent and overcome them. However, the heterogeneity of human breast cancer in terms of genetic features, molecular profiles and clinical behavior represents a constraint obstructing the discovery of a resolution to the disease. It is currently considered that the chances of success of a therapy may increase if the tumor cells are selectively removed before they can evolve to their mature stages up to metastases production. A rationale for this resides in the common development story that has been recently generalized for solid tumors.[78] A typical cell in the human body is 10 μm in diameter. Hence every 1 cm^3 of solid tissue contains approximately 10^9 cells; the entire human body is estimated to contain approximately 10^{14} cells. Because a malignant clone evolves from a single cell, theoretically one would need a sensitivity of 10^{-14} to detect the genesis of a tumor. However, solid tumors typically display Gompertzian

kinetics, with a first phase starting from the single cell stage characterized by a slow growth profile up to 10^5 cells, where a sudden rise of the curve slope occurs in correspondence of a switch from a diffusion-limited nutrition to a neovascularization. This threshold is usually termed "angiogenic switch". Finally, a second lag phase culminates in death of the patient at approximately 10^{12} cell (see Figure 15). The goal of cancer imaging should be to detect and/or image the smallest possible number of tumor cells, ideally early then the angiogenic switch. Unfortunately, the present detection threshold for solid tumors is approximately 10^9 cells (1 g ≈ 1 cm^3) growing as a single mass. Hence from an imaging standpoint, the term remission literally means that there are somewhere between zero and 10^9 malignant cells in the patient body. This level of uncertainty is unacceptable to both the patient and the radiologist.

Therefore, novel and more sensitive diagnostic tools are being developed, with the aim of improving the early and noninvasive detection of rising malignancies and the accuracy of tumor tissue localization. Meanwhile, there is an emerging use of targeted therapies in oncology, depending on the expression of specific proteins or genes present in the tumor cells. In current studies, various types of nanoparticles conjugated with the anti-HER2 monoclonal antibody (mAb), the so-called Trastuzumab (Tz), are investigated extensively due to promising results in biological and preclinical applications. In the review paper from our group included in the publication section, we present a critical insight into the preparation and use of different kinds of Tz-functionalized nanoparticles, with an emphasis on the therapeutic and diagnostic (theranostic) potential of this generation of hybrid nanoparticles, exploiting the multifaceted mechanisms of action of Tz against malignant cells. (**ARTICLE 1**) The state-of-the-art reported in such critical review article represents a starting point from which I moved the first steps of my work.

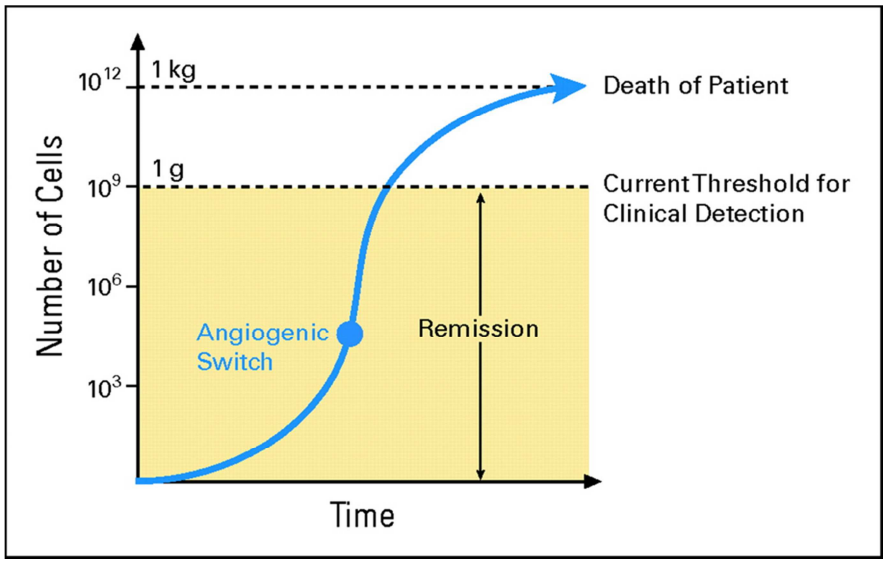

Figure 15. Gompertzian growth curve of a solid tumor and its relationship to cancer detection and imaging. Number of malignant cells (ordinate) as a function of time (abscissa). The transition from first lag to log phase of growth, associated with the transition from diffusion-limited nutrition to neovascularization, is labeled "angiogenic switch." Remission is shown as the uncertainty of cell number ranging from zero to the current clinical threshold for cancer detection (approximately 10^9 cells growing as a single mass).[78]

Chapter 2

Research work

Contents

1. Design and synthesis of magnetofluorescent nanoparticles and preliminary studies on labeling of cancer cells

The first approach of my study consisted in the investigation of toxicity, mechanism of endocytosis, and degradation pathways of multifunctional nanoparticles for possible clinical translation as tumor diagnostics. Three different models of nanoscale magnetofluorescent particle (MFN) systems were designed and fabricated in a multilayer fashion. The magnetic core consisted of a magnetic nanoparticle (MNP) cluster prepared by conventional approaches either as a water dispersion of bare magnetite nanocrystals (MNP1, 7 ± 3 nm) or as surfactant-coated, highly monodisperse 5 nm magnetite nanoparticles (MNP2) obtained by solvothermal decomposition. The MNP cluster was embedded in a silica shell of tunable thickness and coated by a fluorescent layer, which also provided surface amino groups ready for further conjugation. In order to obtain quite uniform MFNs, two main strategies were followed: 1) a sol-gel process using an aqueous dispersion of as-synthesized uncoated Fe_3O_4 nanoparticles (MFN1) and 2) a reaction confinement within the submicrometer domain of a water-in-oil microemulsion system using

hydrophobic monocrystalline Fe_3O_4 nanoparticles as the starting material (MFN2).

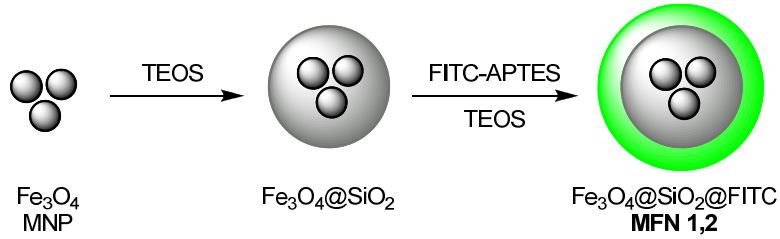

Scheme 1.

Both MFN1 and MFN2 nanoparticles were evaluated in terms of size, morphology, zeta potential, fluorescence efficiency, capability of enhancing T_2 relaxivity of water protons, and stability in water suspension.

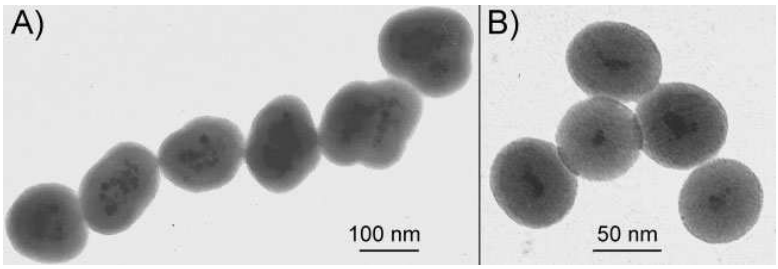

Figure 16. TEM images of A) MFN1 and B) MFN2 in ethanol. In both cases, an outer, less contrasted shell is visible, attributable to the presence of an external silica layer that incorporated the organic fluorophore.

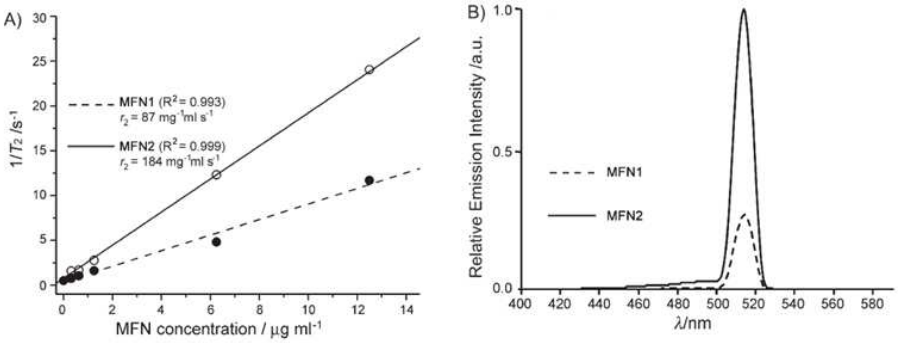

Figure 17. Magnetic and optical properties of as-synthesized MFNs. A) Relaxometric analysis of MFN1 (full dots) and MFN2 (empty dots). The inverse of experimental T_2 values obtained at different MFN concentrations are plotted versus μg mL^{-1} MFNs. Both MFN1 and MFN2 are fitted by a line and the T_2 relaxivities are given by the respective line slopes. B) Relative fluorescence emission of MFN1 (dashed line) and MFN2 (continuous line).

Combining the magnetic, fluorescence, colloidal stability, and morphological characteristics, we selected MFN2 as the best candidate for biological evaluation. The mechanism of internalization, the intracellular fate, and the toxicity in MCF7 adenocarcinoma cells were studied. Besides the well-documented size effect,[79] the anionic charge proved to be a crucial factor for particle internalization, as nanoparticle penetration through the cell membrane could be modulated by surface charge. Ultrastructural analysis of transmission electron micrographs combined with evidence from confocal microscopy suggested that nanoparticles could be internalized by clathrin-mediated endocytosis and macropinocytosis.

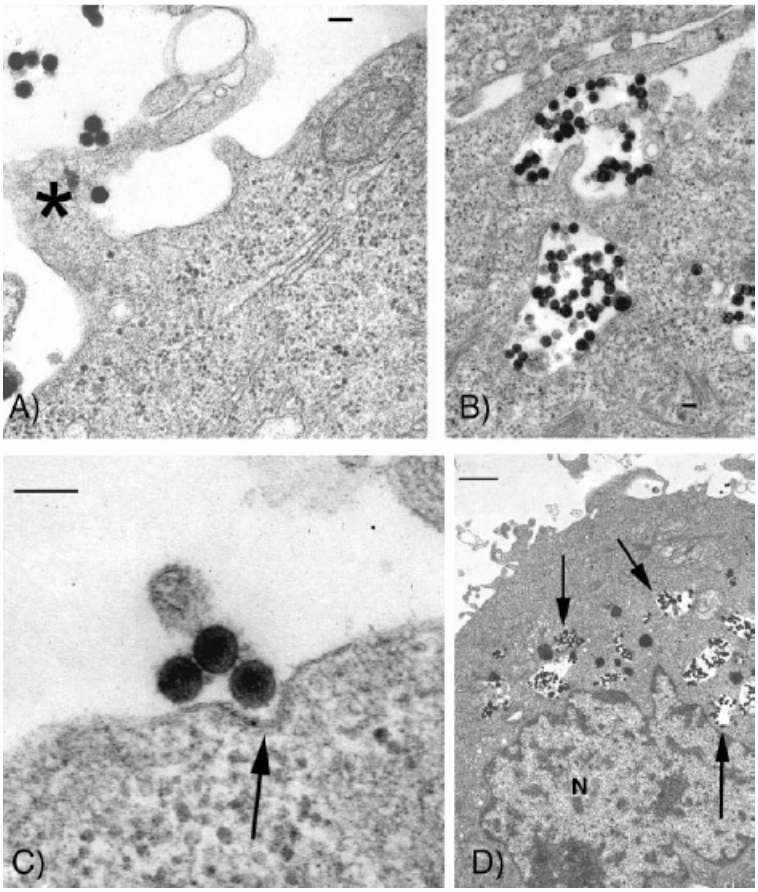

Figure 18. Ultrastructural images of MCF7 MFN2 interaction. A) Nanoparticles adhere to the cytoplasmic membrane at 30 min incubation and initial macropinocytosis is demonstrated by extension of plasma membrane (star symbol) surrounding nanoparticles. B,C) After 1 h, nanoparticle uptake takes place by processes consistent with macropinocytosis (B) and clathrin-coated, vesicle-mediated internalization (C, arrow). D) At 5 h, a large amount of vacuoles (arrows) containing non-clustered nanoparticles are present in the cytoplasm of MCF7 cells (N = nucleus). Scale bars A-C: 100 nm, D: 1 μm.

Moreover, the endocytic pathways of MFN2 was characterized by investigating colocalization of the particles with different markers of endocytic compartments, namely the recycling endosome marker transferrin receptor, the early endosome marker EEA1, the Golgi marker GM-130, and the lysosomal marker cathepsin D. Nanoparticles were

found in EEA1-positive endosomes and in lysosomes, indicating that they followed a physiological pathway of endocytosis.

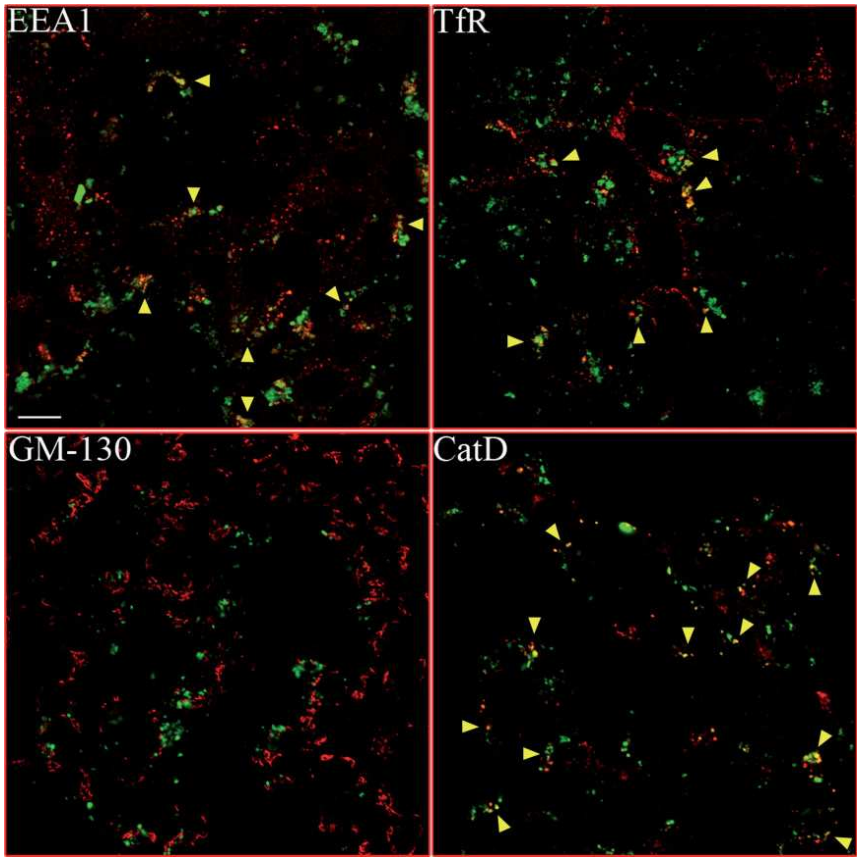

Figure 19. Intracellular localization of MFN2 in MCF7 cells. Images reveal the localization of MFN2, identified by their green fluorescence versus that of the early endosome marker EEA1, the recycling endosome marker TfR, the lysosomal protein Cat D, and the Golgi marker GM-130, labeled using secondary, TRITC-conjugated Abs (red). Scale bar: 10 μm.

Magnetorelaxometric analysis demonstrated that nanoparticles enable the detection of 5×10^5 cells mL^{-1} after treatment with particle dosages as low as 30 mg mL^{-1}. In summary, nanoparticles appeared to be a valuable and safe bimodal contrast agent that can be developed for noninvasive diagnosis of breast cancer. (**ARTICLE 2**)

Table 1. Relaxivity measurements on labeled MCF7 cells[a]

	T_2 (ms) [b]			
Concentration [cells mL^{-1}]	**MCF7** unlabeled	**MFN2** [30 μg mL^{-1}]	**MFN2** [50 μg mL^{-1}]	**MFN3** [50 μg mL^{-1}]
5.0×10^6	2153 ± 16	851 ± 12	616 ± 10	1091 ± 15
1.0×10^6	2408 ± 21	1832 ± 15	1793 ± 14	2248 ± 22
5.0×10^5	2622 ± 23	1983 ± 14	1969 ± 16	2338 ± 22
2.5×10^5	2646 ± 29	2630 ± 27	2603 ± 24	2656 ± 32

[a] Data are the mean ± SD of three different relaxivity measurements. [b] T_2 values correspond to progressive dilutions of an initial cell concentration after incubation with different concentrations and kinds of nanoparticles.

2. Magnetic nanoparticles for biomarker detection in biological samples

Along with the physico-chemical characterization of the above mentioned magnetic nanoparticles, we studied in depth their magnetic properties looking forward to their potential application as contrast agents for MRI. To assess their capability to offer a robust contrast agent diagnostic device, we measured the spin–spin relaxation time (T_2) induced by our core-shell magnetic nanoparticles on the adjacent water protons in aqueous suspension. These biocomposite nanomaterials can provide a powerful tool for the investigation of biointeractions, which are fundamental for cell functionality as well as for modern diagnostic techniques and new therapeutic outlooks. In this context, we have focused on the development of a novel biosensor (magnetic switch nanosensor, MNS) based on the use of the same kind of magnetic nanoparticles suitably functionalized with surface ligands selective for recognition of plasma proteins. The interaction of specific ligands conjugated to magnetic nanoparticles with soluble protein markers induce a reversible alteration of nanoparticle microaggregation state, which can be sensitively measured as changes in T_2 relaxation time of water protons of the medium in which the recognition occurs. In addition, as this detection method does not involve optical readout, the measurement does not require optically purified samples and, for this reason, it might be applied directly to extracted sera. The technique sensitivity and the efficiency of the as-synthesized silica-encapsulated magnetic nanoparticles (SMNP, Scheme 2) suggested their potential application for the rapid and sensitive detection of a biological analyte in solution. To assess the minimal useful SMNP concentration for biosensing analysis, we first evaluated the range of concentrations within which the signal was suitably stable. (Figure 20)

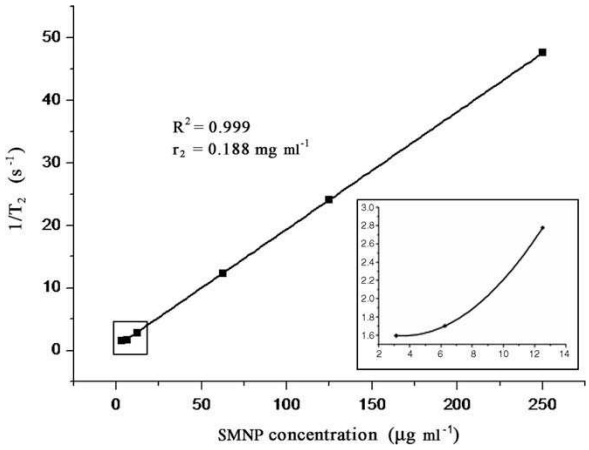

Figure 20. T_2 relaxometry analysis of SMNP. The inverse of experimental T_2 values obtained at different SMNP concentrations is plotted versus particle concentration (μg mL^{-1}). The experimental data are fitted by a line in the range of 20-250 μg mL^{-1}. The T_2 relaxivity is indicated by the line slope. Inset: magnification of the selected region, point fitting in the range of 3-13 μg mL^{-1}.

As a proof of concept of the efficiency and reliability of MNS, we examined the accurate detection of anti-HSA (human serum albumin) antibodies in fluid samples by protein-functionalized magnetic nanospherical probes. HSA is the most abundant serum protein in the human circulatory system. It is well documented that a few largely widespread diseases consist of anomalous concentrations of anti-HSA antibodies as a consequence of pathological changes of the systemic condition that cause the extracellular proteins to become antigenic. The alterations in the conformation and the biological properties of HSA are usually triggered by protein oxidation due mainly to the undesired presence of reactive oxygen species. Indeed, protein oxidation phenomena are generally associated with cellular functional disruption along with many other protein conformational changes. There are several studies that provide evidence that such protein oxidation is often associated with cellular disorder observed during aging and age-related neurodegenerative diseases, including Alzheimer and Parkinson diseases.[80] Although the circulating autoantibodies exhibit reactivity against both native and modified proteins, modified HSA appears to be highly immunogenic compared with native HSA.[81] A number of studies

point to type 1 diabetes mellitus, familial dysautonomia, and liver failure as the main pathologies in which a remarkable occurrence of anti-HSA Abs is observed, with the concentration of anti-HSA Abs in diabetic patients being 5–20 times greater than in healthy subjects. For this reason, the application of a method, such as MNS, for the rapid, sensitive, and selective detection of anti-HSA Abs in solution could be highly beneficial for clinical practice.

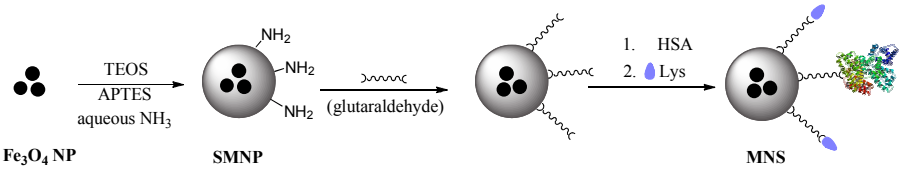

Scheme 2.

HSA molecules were covalently conjugated to amino functionalized SMNP, via glutaraldehyde cross linking and the residual CHO terminal groups were saturated with lysines. First, we performed a set of measurements to evaluate the temporal changes of water T_2 relaxation time induced by MNS in the presence of 100 pM target complementary polyclonal Ab (pAb).

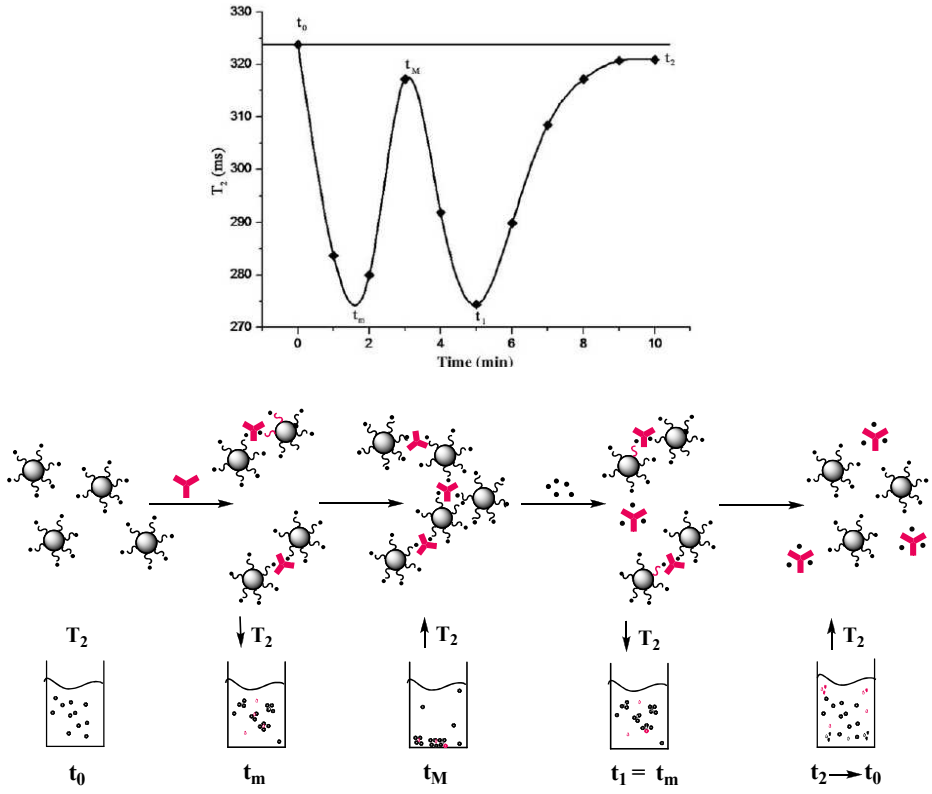

Figure 21. Time course of changes in water T_2 using MNS in the presence of 100 pM anti-HSA pAbs and schematic of the particle aggregation sequence in response to the addition/subtraction of anti-HSA pAbs.

Once the optimal parameters were adjusted, the method proved to be very sensitive, providing concentration- and time-dependent responses. Furthermore, we demonstrated that the developed immunoassay was able to quantitatively determine the biomarker concentration from the T_2 linear correlation, thereby supplying a rapid, yet accurate, assay with sensitivity in the femtomolar range (Figure 22).

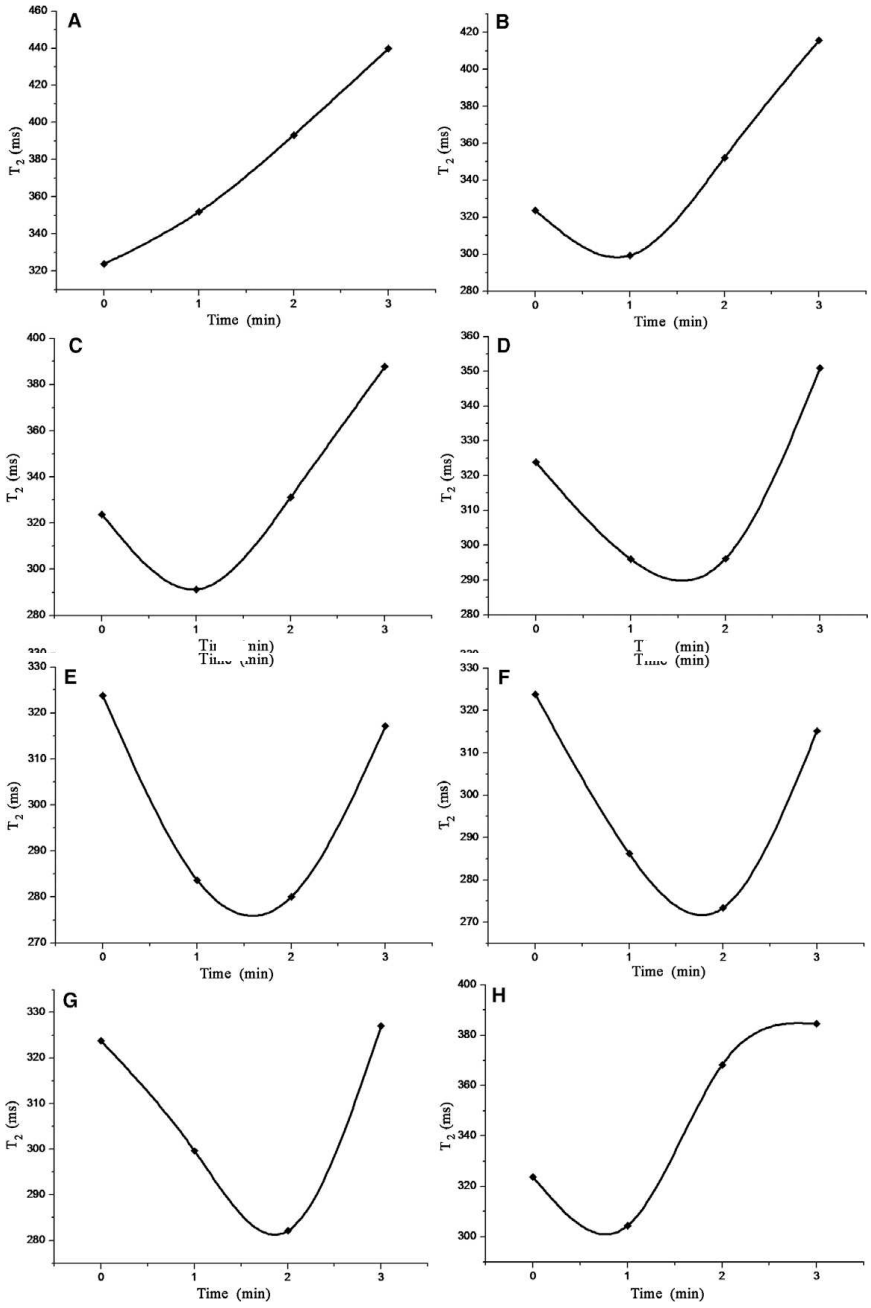

Figure 22. Time-dependent changes in T_2 resulting from the aggregation states induced by different anti-HSA concentrations: (A) 1 μM; (B) 100 nM; (C) 10 nM; (D) 1 nM; (E) 100 pM; (F) 10 pM; (G) 1 pM; (H) 100 fM.

A further major advance of our MNS-based method is that the T_2 relaxometry experiment can be used to determine concentrations of a specific target quantitatively when its concentration is not known a priori. We obtained a standard calibration curve by plotting $\log(T_2-T_{2_0})$ vs. log[Ab], where the Ab concentration is expressed in μg mL^{-1} and T_{2_0} is a fitting parameter useful for linearization. The high susceptibility and stability of these magnetic nanoparticles, as well as their accessible synthetic preparation, make these nanosensors a promising new tool for versatile and effective analysis of biological samples. (**ARTICLE 3**)

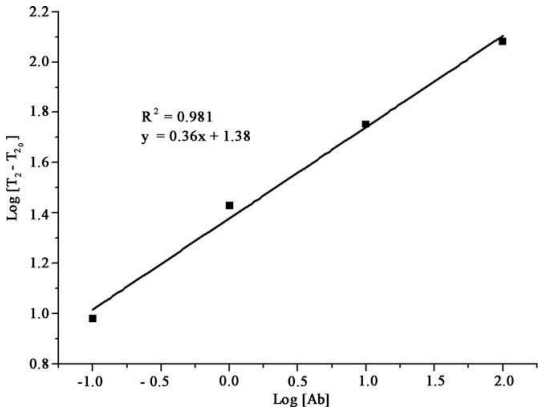

Figure 23. Logarithmic plot of relaxometric analysis of MNS incubated with different concentrations of anti-HSA pAb.

3. Antibody functionalization of nanoparticles for selective targeting of cancer cells

After the toxicity investigation and the interaction/internalization studies of the nanoparticles with cells, the subsequent step was the nanoparticle functionalization with biomolecules in order to achieve a selective targeting to the cancer cells. We optimized the characteristics of the magnetic nanoparticle hybrid system in order to present the lowest molecular weight, reduce the nanoparticle overall size and increase the stability in aqueous medium. Highly monodisperse magnetite nanocrystals were synthesized in organic media and transferred to the water phase by ultrasound-assisted ligand exchange with an iminodiacetic phosphonate (PMIDA). The resulting water soluble magnetic nanoparticles were characterized by transmission electron microscopy (TEM), dynamic light scattering (DLS), and magnetorelaxometry, which suggested that this method allowed us to obtain stable particle dispersions with narrow size distribution and unusually high magnetic resonance T_2 contrast power (Figure 24).

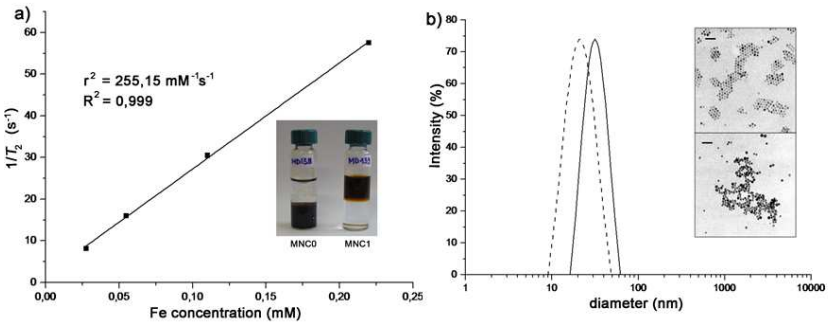

Figure 24. (a) T_2 relaxometry analysis of newly synthesized magnetic nanoparticles. Inset: nanoparticle phase transfer from organic solvent (MNC0 in chloroform) to aqueous solution (MNC1). (b) Hydrodynamic size distribution histograms of oleic-coated Fe_3O_4 nanoparticles (dashed line) and after ligand exchange (continuous line). Diameters were measured by DLS in chloroform and water, respectively. Inset: TEM images of as synthesized nanoparticles in hexane (top) and after the surfactant exchange in PBS (bottom). Scale bars 50 nm.

These nanoparticles were conjugated to a newly designed recombinant monodomain low molecular-weight fragment of protein A (spaBC3), which exhibited a convincingly strong affinity for human and rabbit IgG molecules (we used Tz). SpaBC3, designed to present a terminal cysteine tripod, was produced in *E. coli*, purified by combined His-tag and GST technologies (Figure 25).

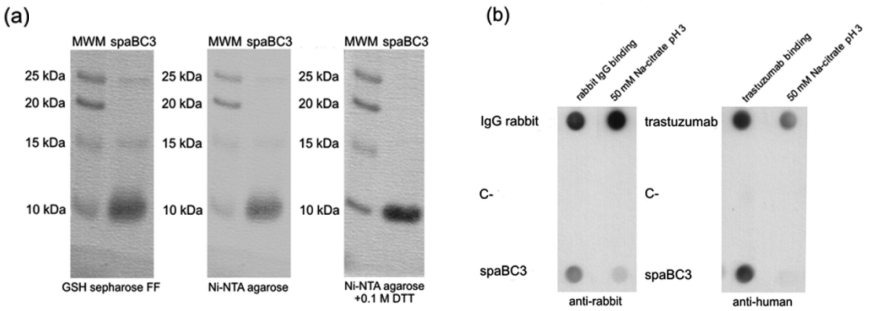

Figure 25. a) SDS-PAGE of spaBC3 purified fractions. Purified protein (4 μg) was loaded after elution with PreScission protease (left). After purification with Ni-NTA agarose to remove GST contaminants, the same amount of spaBC3 was loaded on SDS-PAGE with or without 0.1 M dithiothreitol (DTT) in running buffer (right and middle, respectively). (b) SpaBC3 binding assay. SpaBC3 (250 ng) was filtered through PVDF membrane and incubated with rabbit IgG or Tz. IgG removal was obtained by Na-citrate incubation. GST protein (C^-, 250 ng), as negative control, and rabbit IgG or Tz (250 ng), as positives, were used. The presence of rabbit IgG or Tz was revealed by antirabbit or antihuman secondary antibodies conjugated to HRP, respectively.

SpaBC3 was conjugated to MNC1 through an appropriate protocol: carboxylate functionalities were converted into amine ends by reaction with a bifunctional diamino-linker; the amino functionalities on the particle surface allowed the conjugation with N-succinimidyl-3-[2-pyridyldithio]-propionate (SPDP) resulting in the thiol-reactive pro-functional MNC3 (Scheme 3). MNC3 were the ideal building block for bioconjugation with thiol-engineered protein A variant, as PDP functionality is very reactive toward sulfhydryl ends of organic and biological thiol-containing molecules by formation of stable disulfide bridges. Owing to the nature of antibody-protein A binding, tight antibody immobilization occurred through the Fc fragment thus taking full advantage of the targeting potential of bound IgGs.

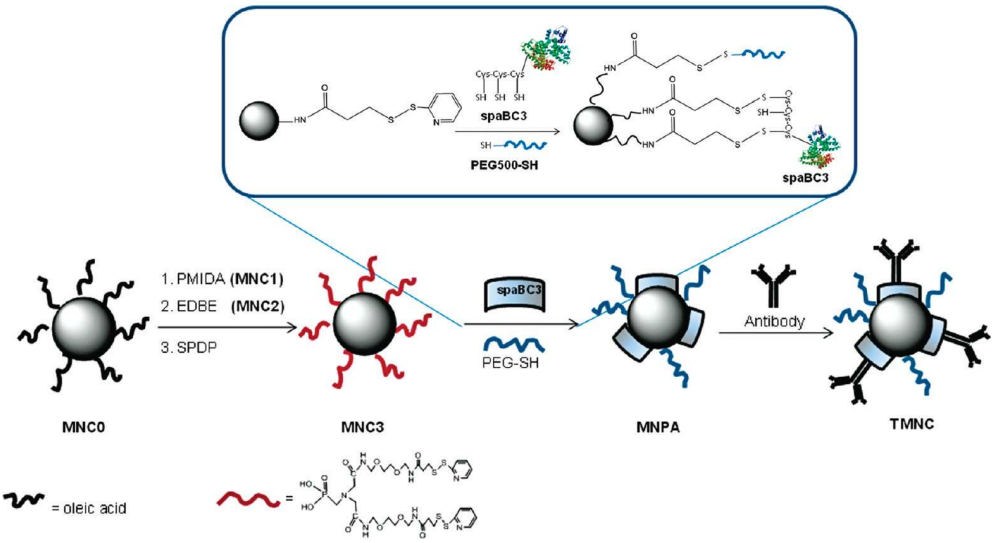

Scheme 3.

As a proof of concept of the utility of our paramagnetic labeling system of human IgGs for biomedical applications. Tz was immobilized on hybrid magnetic nanoparticles (TMNC). TMNC and the supernatant (unbound, ub) were analyzed by western blotting with anti-HER-2 antibody in order to reveal HER-2 binding to TMNC (Figure 25b). The nanoparticles were then assessed by immunoprecipitation assay (Figure 26).

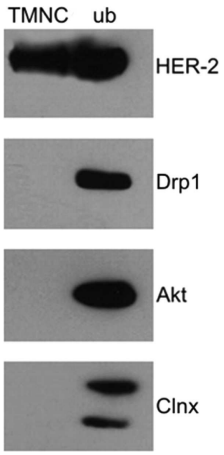

Figure 26. HER-2 receptor is selectively recognized by TMNC. Bound and unbound proteins were then eluted in SDS-PAGE application buffer, electrophoresed, and immunoblotted using either anti-HER-2, anti-Drp1, anti-Akt, and anti-Clnx antibodies.

To validate the immunoprecipitation data, the specificity of binding between TMNC and HER-2 was observed by confocal laser scanning microscopy. Indeed, as HER-2 is a transmembrane receptor, TMNC were expected to accumulate in correspondence of the external surface of HER-2-overexpressing cells. TMNC were observed in HER-2 positive MCF7 cell surfaces, but not in MDA negative control cells, demonstrating that they localized selectively in correspondence of transmembrane receptors owing to the presence of the specific targeting agent. **(ARTICLE 4)**

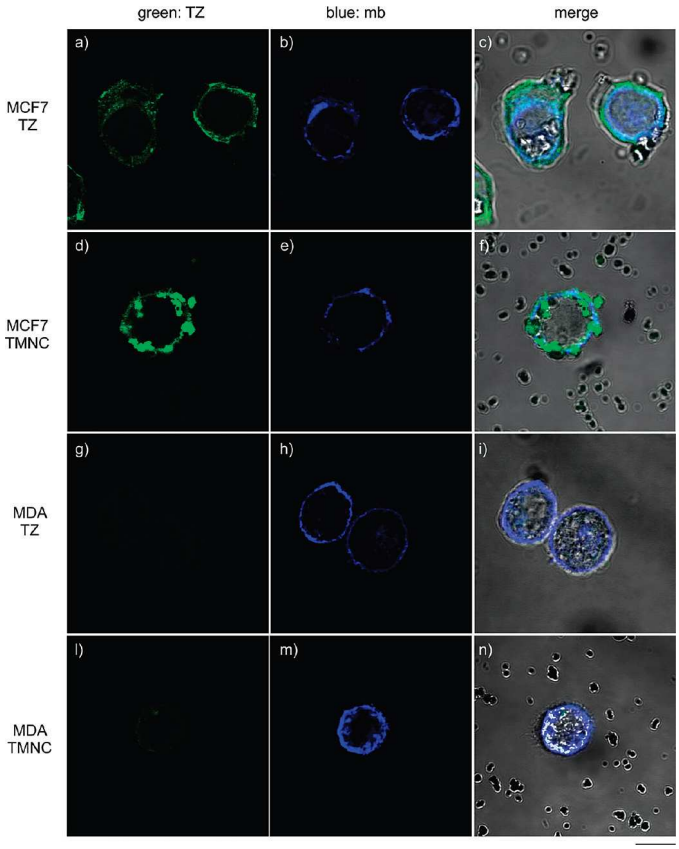

Figure 27. Confocal laser images of MCF7 and MDA cells cultured with TMNC or free Tz. MCF7 and MDA were incubated for 15 min with TMNC (150 μg mL^{-1}; panels d-f and l-n, respectively) and Tz (15 μg mL^{-1}; panels a-c and g-i, respectively). Cell membranes were stained with DiD oil (blue). TMNC and Tz were labeled with antihuman FITC secondary antibodies. Scale bar = 10 μm.

4. Biofunctionality of protein ligands conjugated to nanoparticles

Despite the huge interest for monoclonal antibody nanoconjugates, only poor evidence is available on the actual conservation of the protein biofunctionality at the molecular structural level, once Tz has been covalently conjugated to the nanoparticle. Such difficulty mainly resides in the lack of reliable methods capable of providing exhaustive information on structural/conformational features sustaining the protein functionalities of nanobioconjugate systems. This is indeed a crucial point, which urgently needs to be addressed. We investigated the possibility to provide a direct evidence on the extent of preservation of the structural bioactivity of IgGs immobilized onto the surface of iron oxide nanoparticles deduced by accurate analysis of the essential folding features obtained by Fourier-transform infrared (FTIR) spectroscopy. As a model for this study, PEG-stabilized, Tz-modified magnetite nanoparticles (TMNP) were developed. Bare monodisperse magnetite nanoparticles were obtained by a coprecipitation approach in water and modified on the surface with PEG600 diacid, exploiting the high affinity of carboxylate functionality for iron oxide, for ready conjugation with amine-containing biomolecules by amide coupling. To examine their potential in mAb conjugation, purified Tz was covalently bound via amine-bearing lysine residues.

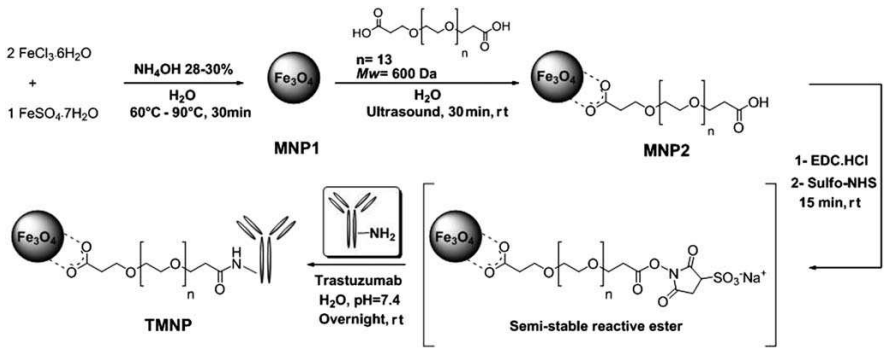

Scheme 4.

In order to explore the structural properties of the conjugated antibody, we applied FTIR spectroscopy to obtain information on protein secondary structure (Figure 28). This method in some circumstances has been exploited to investigate protein molecules physically adsorbed onto nanoscale surfaces.[82,83]

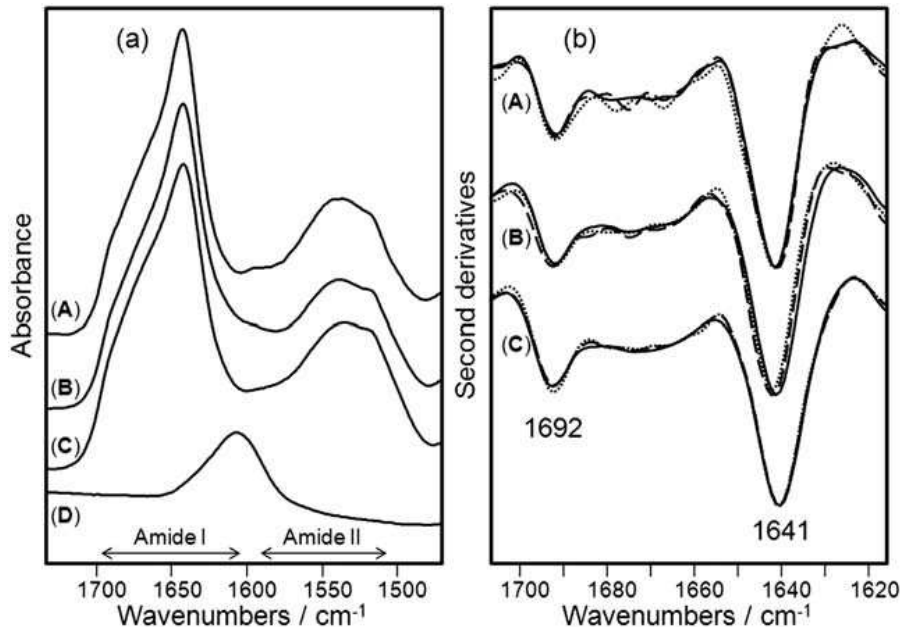

Figure 28. Structural characterization of Tz, TMNP and MNP2 by FTIR spectroscopy. (a) FTIR absorption spectra in the amide I and amide II regions of (A) free Tz, (B) a mixture of free Tz and free MNP2, (C) TMNP, and (D) MNP2. In this spectral region, MNP2 (D) displayed only a broad absorption around 1606 cm^{-1}, while TMNP (C) showed the protein amide I and amide II bands confirming the success of the bioconjugation. (b) Second derivatives of the spectra reported in (a). Spectra were collected at time 0 (continuous lines), after 24 h (dashed lines), and after 96 h (dotted lines). The spectra are dominated by two components at 1692 cm^{-1} and 1641 cm^{-1} assigned to the native β-sheet structure of Tz that were found to be stable both in the free and in the bioconjugated protein.

The amide I and amide II bands in the TMNP spectrum, due to the absorption of the C=O stretching and N–H bending vibrations, respectively, of the protein backbone, confirmed that the conjugation reaction occurred successfully. Indeed, unconjugated MNP2 displayed a completely different profile in this spectral region. Information on the

secondary structure of the protein can be obtained through the analysis of the amide I band, as it is the spectral region most sensitive to the structural conformation changes of the protein. To check whether TMNP were indeed able to maintain the specific targeting capability of Tz for HER-2-positive breast cancer cells, we investigated the TMNP binding to HER-2 in HER-2-overexpressed MCF7 cells. Immunoprecipitants (IP) and the supernatants (unbound) were first analyzed by western blotting with anti-HER-2 antibody in order to reveal TMNP binding to HER-2 receptor. The comparison between TMNP and MNP2 confirmed that the conjugation with Tz was necessary to immunoprecipitate HER-2 membrane receptor in MCF7 whole cell extract (Figure 29).

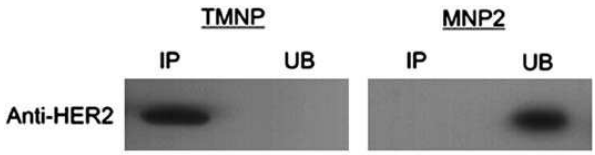

Figure 29. Immunoprecipitation of HER-2 in MCF7 cells. Immunoprecipitation was performed using anti-HER-2 antibodies crosslinked to TMNP and MNP2 (as negative control). Bound (IP) and unbound (UB) proteins were eluted in SDS-PAGE application buffer, electrophoresed and immunoblotted.

The immunoprecipitation data were confirmed by relaxivity measurements, which provided evidence on iron oxide capture by MCF7, and by immunofluorescence after TMNP incubation with living cells. TMNP were observed in MCF7 cell surfaces, demonstrating that they localized selectively in correspondence of transmembrane receptors (Figure 30). (**ARTICLE 5**)

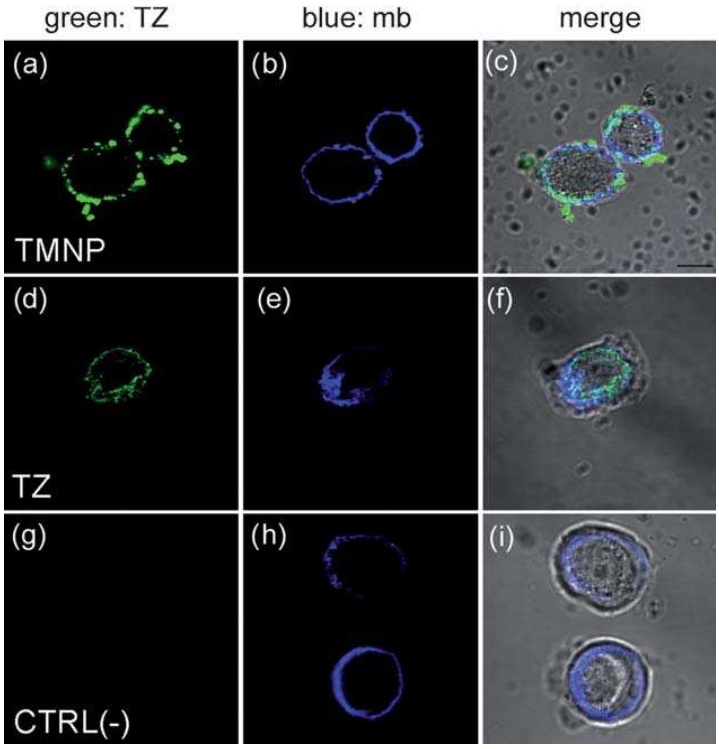

Figure 30. Confocal laser images of MCF7 cells cultured with TMNP or free Tz. MCF7 were incubated for 20 min with TMNP (a-c) or Tz (d-f). As negative control, MCF7 were stained with secondary antibodies anti-human FITC (g-i). Cell membranes (mb) were stained with DiD oil (blue). TMNP and Tz were labeled with anti-human FITC secondary antibodies. Scale bar = 10 μm.

5. Enhancement of targeting efficiency of immunoconjugates by multiple presentation of scFv fragments on silica nanospheres

The experiments reported in paragraphs 3 and 4 highlight the importance of ligand arrangement on nanoparticle surface to achieve an optimal molecular recognition. Next, we moved to the assessment of a further parameter, namely multivalency, which is usually responsible of enhancing the overall affinity of a molecular species for its biological counterpart. Indeed, multiple presentation of ligands on a 3D nanoscale surface is expected to result in an increase of binding affinity due to a cooperative effect.

In the context of our breast cancer model, we found that monoclonal antibodies are often less effective toward solid tumors, because only a small amount of mAbs can indeed accumulate at the tumor tissue, due to their high immunogenicity and low penetration. Moreover, mAbs remain circulating for an extended time because their large size prevents excretion by renal clearance. Recently, recombinant antibodies with modified properties have been designed in order to improve tissue penetration and biodistribution. Among them, small antibody fragments consisting of the variable heavy chain (V_H) and light chain (V_L) regions connected through a synthetic loop, called single-chain fragment variable recombinant antibodies (scFv), hold great promise. ScFv display has improved biodistribution compared to intact IgGs due to small size (typically in the 20-30 kDa range) and absence of a highly immunogenic stem. However, a poor retention time and a decreased affinity and specificity caused by their monovalent binding strongly limit their application in cancer immunotherapy.[84] Hence, while immunogenicity is remarkably weakened and scFv clearance is accelerated, the binding efficacy is often reduced compared to their parent mAb resulting in a remarkably lower affinity for the receptor. Multimerization has been recently envisaged as a strategy to enhance the functional affinity (avidity) of scFv increasing the k_a by 2-3 orders of magnitude relative to the monovalent fragment. We developed a strategy to enhance scFv target binding efficacy that makes use of silica nanoparticles (SNPs) as a multimerization scaffold. Uniform 60 nm spherical SNP were synthesized and scFv was linked to SNP by two alternative strategies: 1) by His-tagged affinity-oriented immobilization (SNP-HT), 2) covalently

attached via glutaraldehyde crosslinking resulting in functional SNP-UT (Figure 31).

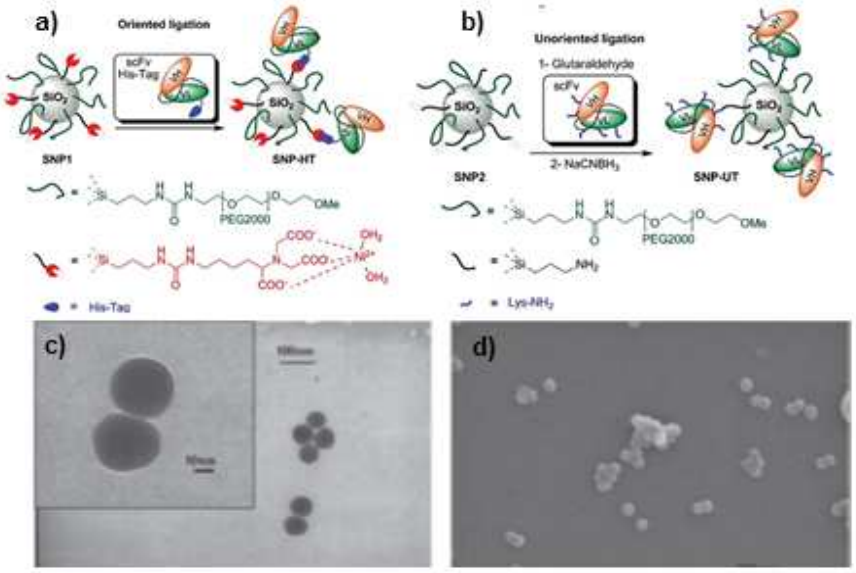

Figure 31. a) Method 1: SNP functionalized with Ni-NTA groups tightly and specifically interact with scFv histidine tag leading to an oriented protein immobilization (SNP-HT). b) Method 2: the available amino groups of lysine residues of scFv bind to SNP via the aldehydic groups, which have been generated on the surface of nanoparticles by glutaraldehyde addition, resulting in a random ligation (SNP-UT). c) TEM (Inset: magnification) and d) SEM images of as-synthesized SNP.

To assess the effect of multivalent presentation of scFv on silica nanoparticles, SNP-HT and SNP-UT binding toward HER-2 receptor in breast cancer cells was evaluated by flow cytometry, which evidenced a right-shift of fluorescence signal accounting for an increase in scFv binding efficacy upon multimerization due to SNP conjugation (Figure 32). Moreover, scFv multimerized on SNP via glutaraldehyde crosslinking (SNP-UT) exhibited a mean fluorescence intensity value very close to that of intact Tz, indicating that there was a significant improvement in receptor binding capability, which can be attributed to avidity effect. However, the conjugation strategy exploited for scFv

multimerization on SNP surfaces (method 1 vs. method 2) did not prove to be crucial in enhancing scFv binding efficiency in this case.

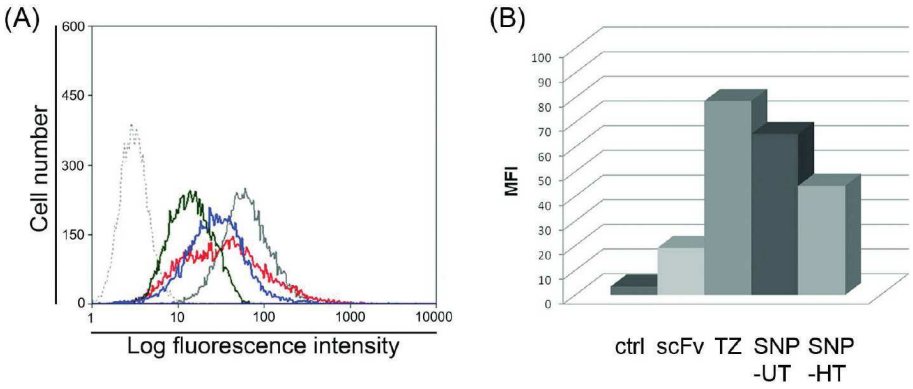

Figure 32. Multivalent presentation of scFv onto SNP-HT and SNP-UT enhances binding avidity toward HER-2 receptor. (A) MCF7 cells were incubated with scFv (black), SNP-HT (blue), SNP-UT (red), or trastuzumab (Tz; gray continuous) and processed by flow cytometry. ScFv incubation with HER-2 cells as negative control (gray dashed line). (B) Mean fluorescence intensity (MFI).

The specificity of binding between SNP-HT or SNP-UT and HER-2 was assessed by confocal laser scanning microscopy. We expected an accumulation of SNP-HT and SNP-UT at the level of the cell membrane of HER-2 positive cells only, which would confirm that nanoparticle capture occurs via specific membrane receptor-mediated internalization. SNP-HT and SNP-UT (Figure 33) were indeed observed on HER-2-positive MCF7 cell surface but not on HER-2-negative MDA cells, which demonstrates that they were both actually capable of specifically targeting their transmembrane receptor. Images show that SNP-UT and SNP-HT were mostly localized on cell membrane after 1 h incubation, although a small amount of nanoparticles were already internalized.

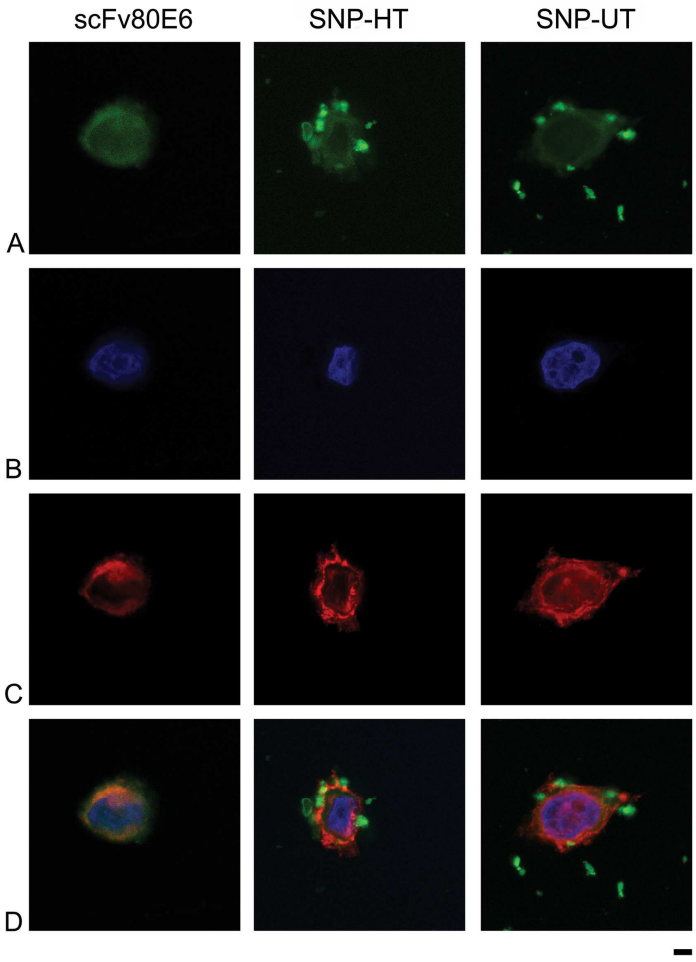

Figure 33. Assessment of targeting efficacy of SNP-HT and SNP-UT on HER-2 positive cells. Free scFv was used as a positive control. ScFv, SNP-HT, and SNP-UT were revealed with FITC-labeled anti-whole mouse secondary antibodies (green, A). Nuclei were stained with DAPI (B), membranes (MB) with DiD oil (C). Merge images are shown in D. Scale bar: 10 µm.

These results suggest that the use of size- and shape-controlled inorganic nanoparticles as a multimerization scaffold is capable to improve scFv target binding efficacy, reaching an affinity value very close to that of native IgG. (**ARTICLE 6**)

6. Reversible immobilization of biomolecules on hydrophobic nanoparticles for the investigation of signaling mechanisms

In our ongoing studies on possible new strategies for the orientation-controlled immobilization on nanoparticles, we focused on another class of non-peptidic molecules of biomedical interest, namely lipopolysaccharide (LPS), of Gram-negative bacteria. These potent proinflammatory molecules include a hydrophilic oligosaccharide chain of variable length and a hydrophobic, membrane-anchoring moiety, termed lipid A. The interaction of LPS with cells of the innate immune system leads to the formation and release of endogenous mediators, which initiate inflammatory and immune responses essential for optimal antibacterial defense. Such a cascade of events is triggered by activation of the Toll-like receptor 4 (TLR4) by LPS.

The design of metal-based nanoparticles that possess a suitable rigid size-controlled support for the reversible anchorage of a limited number of LPS molecules suggests a novel approach to the development of nanoscale vectors for delivery of TLR4 agonists. To provide nanoparticles that would more likely make possible the stable and reversible binding of a monolayer of LPS monomers, we designed a hydrophobic brush nanoparticle (HBNP) system with an outer layer of exposed hydrocarbon chains at the surface. A biphasic mixture of HBNPs resuspended in hexane and of an aqueous dispersion of LPS, was mildly warmed (40 °C) and sonicated to cause the slow evaporation of the organic solvent while mixing. This process promoted the formation of LPS-coated magnetic nanoparticles (LMNPs, Figure 34).

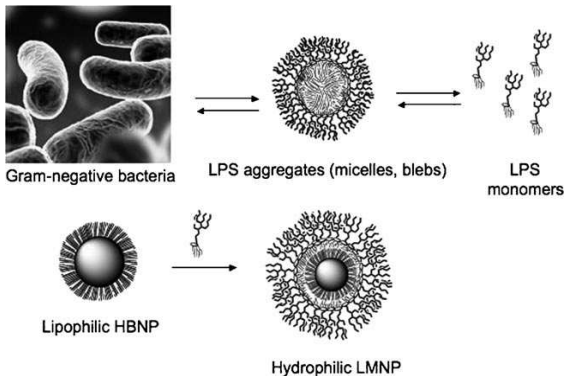

Figure 34. LPSs extracted and purified or spontaneously released from Gram-negative bacteria form large aggregates (micelles, membrane blebs) in an aqueous environment. LPS-coated magnetic nanoparticles (LMNPs) mimicking LPS aggregates are obtained by coating a hydrophobic brush nanoparticle (HBNP) with LPS.

DLS analysis and TEM images of LMNPs in water confirmed that the recovered hybrid nanoparticles retained their shape and were generally organized as small clusters of individual particles.

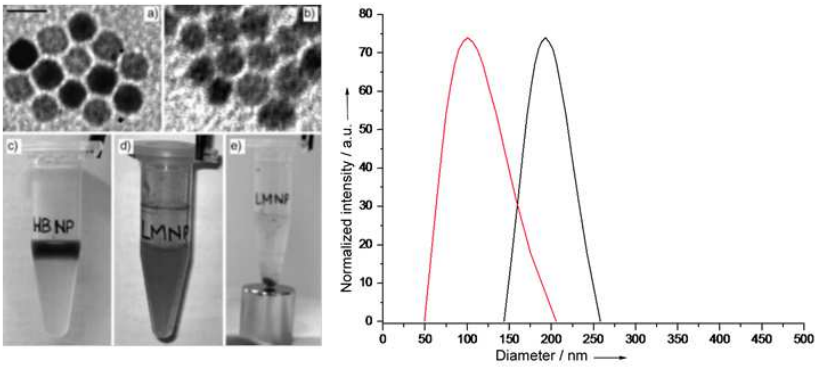

Figure 35. On the left, TEM images of a) HBNPs in hexane and b) LMNPs in distilled water. Scale bar: 10 nm. c) The upper colored phase is a HBNP dispersion in hexane, while the lower colorless phase is 16.7 μm LPS in Tris–EDTA. d) LMNP aqueous dispersion after phase mixing and evaporation of the organic solvent. e) Purification of LMNPs by magnetic decantation. On the right, hydrodynamic size distribution of LPS micelles (red line) and of purified LMNPs (black line) in PBS buffer obtained by DLS. The micelles were recovered in the supernatant solution after magnetic sequestration of LMNPs from the reaction mixture.

The bioactivity of LPS bound to LMNPs was assessed by measuring the ability of LMNPs to stimulate TLR4-dependent cell activation. Increasing concentrations of LMNPs induced a dose-dependent activation of transformed HEK293 cells expressing CD14, MD-2, and TLR4, as manifested by extracellular accumulation of interleukin-8 (IL-8) from treated "HEK-TLR4" cells (Figure 36a) and of secreted embryonic alkaline phosphatase from treated "HEK-Blue" cells (Figure 36b).

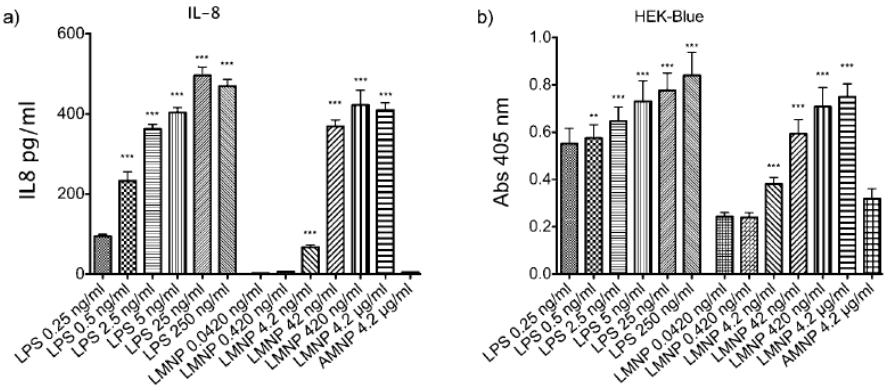

Figure 36. a) LMNP-dependent IL-8 production in HEK-TLR4 cells. b) Measurement of LMNP-induced activation of the transcription factor NF-kB level in HEK-Blue cells.

To further define the ability of LMNPs to stimulate TLR4-dependent cellular responses, LMNP-induced activation of cells of the innate immune system was investigated using wild-type (wt), $CD14^{-/-}$, and $TLR4^{-/-}$ murine bone-marrow derived dendritic cells (BMDCs) and bone-marrow derived macrophages (BMDMs). Cell activation was monitored by the accumulation of extracellular tumor necrosis factor a (TNF-α) during incubation for 24 h. As shown in Figure 37, LMNPs produced dose-dependent activation of both cell types derived from wt mice. To verify that the biological activity observed for LMNPs was exclusively related to the immobilized LPS and not influenced by the inorganic core, we tested LPS-free, watersoluble magnetic nanoparticles as a negative control.

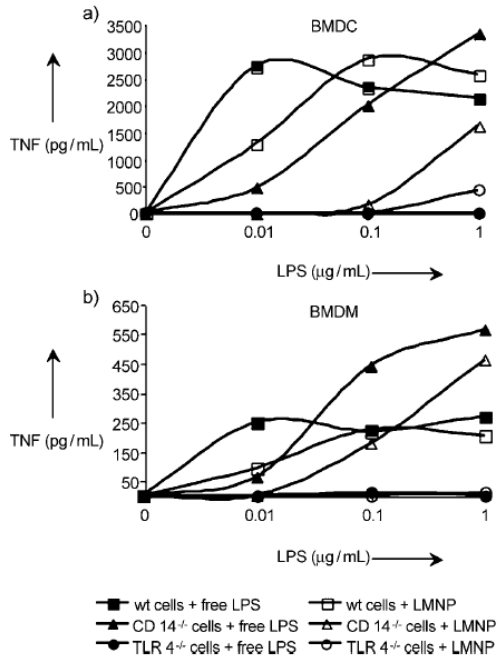

Figure 37. LMNP- and free LPS-mediated activation of BMDCs (left) and BMDMs (right). Cells of the innate immune system were activated with LMNPs and the corresponding amounts of free LPS and the release of TNF-α were measured in the supernatant 24 h later. Data are means of at least three independent experiments.

Finally, we compared of the dose-dependent activation by LMNPs and by LPS of HEK-TLR4 and HEK-Blue cells (Figure 36) and of wt and CD14$^{-/-}$ murine BMDMs and BMDCs (Figure 37). It was revealed that the LMNPs were about tenfold less potent than LPS when normalized for the amount of LPS added. Even at the highest dose tested (4.2 nM), LMNPs had no detectable cytotoxic effect, which indicated that the reduced potency of LMNPs in inducing TLR4-dependent cell activation was most likely due to reduced efficiency of delivery of LPS from LMNPs (versus aggregates of LPS) to CD14 and to MD-2-TLR4 and not a general cytotoxic effect of the LMNPs. (**ARTICLE 7**)

7. Active targeting of antibody-engineered multifunctional nanoparticles in mice and downregulation of HER-2 expression in breast cancer cells

TMNC used for HER-2 labeling in MCF7 cell cultures were further assessed as to their capability of targeting breast cancer cells in vivo and of imaging their localization in living animals. To this aim, we have improved the preparation of the hybrid nanocomposites for in vivo application. The original procedure for the synthesis of TMNC, presented in paragraph 2, involved a nanocrystal controlled nucleation and growth by solvothermal decomposition in the presence of oleic acid followed by ligand exchange, which led to a dispersion soluble in the aqueous phase. However, when we explored the possibility of using TMNC for intravenous administration, they invariably exhibited a tendency to accumulate at the mouse tail, in correspondence to the site of injection. After having thoroughly checked each step of the synthetic procedure in terms of particulate stability, we found that the critical step was the ligand exchange. Hence, we improved the phase transfer by an intermediate reaction with tetramethylammonium hydroxide (TMAOH, Scheme 5), which led to the same final antibody nanocomplex dramatically reducing the TMNC accumulation at the site of injection, as it was capable of diffusing quickly in the bloodstream. Moreover, Tz was labeled with Alexa Fluor 688 for fluorescence imaging purpose.

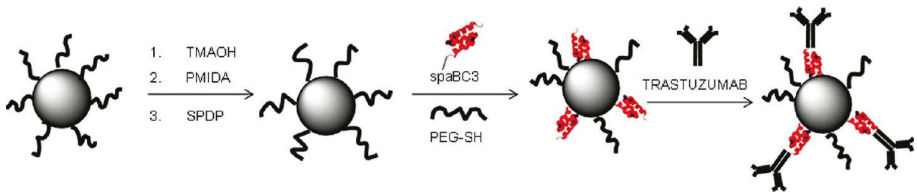

Scheme 5

We carefully investigated the TMNC targeting efficiency and biodistribution by combining MRI monitoring, highly sensitive epifluorescence (Epf) tracking of nanoparticles in mice bearing MCF7 cells, and accurate tissue analyses. These nanoparticles proved to be

highly effective in selectively targeting the tumor mass, resulting in a detectable increase in contrast by MRI. Indeed, a remarkable decrease in T_2-weighted axial maps was observed in the tumor region at 24 h.

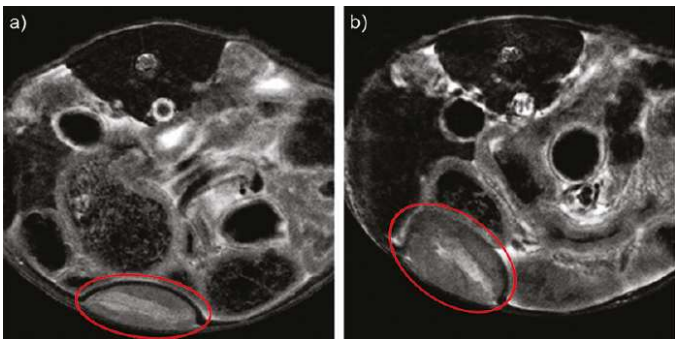

Figure 38. Monitoring of TMNC uptake in vivo by MRI. The axial T_2-weighted MR images have been obtained from MCF7 tumor-bearing mice (a) before and (b) 24 h after the injection of nanocrystals.

Epf images of supine mice, obtained with a CCD camera at 5 h, 24 h, and 1 week after injection, confirmed a localization of TMNC in correspondence of the HER-2-positive tumors (Figure [39]). We observed the same behavior with perfused mice, which suggested that TMNC diffused in the extravascular region of the tumor tissue.

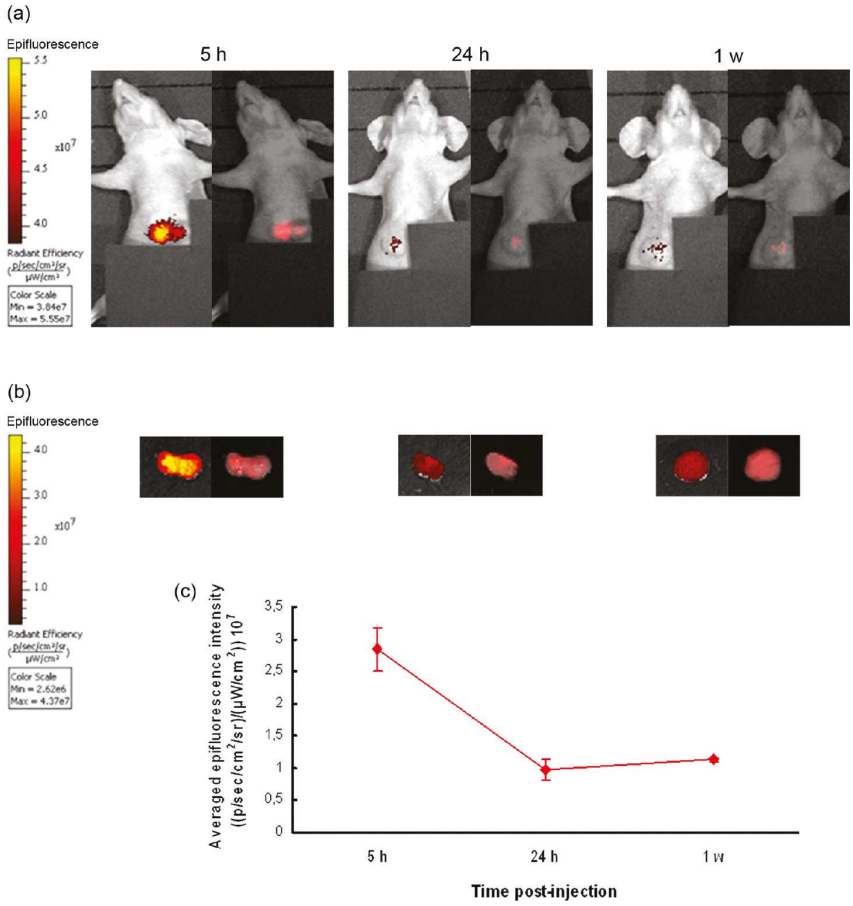

Figure 39. CCD camera images of (a) mice bearing MCF7 xenografts and (b) of the isolated tumors at 5 h, 24 h, and 1 week postinjection of TMNC. Epifluorescence intensity images and spectrally unmixed fluorescence images are reported on left and right, respectively. (c) Averaged epifluorescence intensity of isolated tumors. Mean ± SE (standard error) of three different samples for each experimental time.

The maximal Epf emission in xenografts, as confirmed by isolated tumors, was observed at 5 h, while the signal intensity in the tumor unexpectedly decreased after 24 h. The fall of fluorescence observed by CCD images reflected the degradation of the organic corona, subsequent to the receptor-mediated TMNC internalization. Therefore, we predicted that fluorescence signal associated with the presence of Tz in TMNC would rapidly decrease, while in contrast, iron oxide would progressively accumulate inside the tumor tissue (Figure 40).

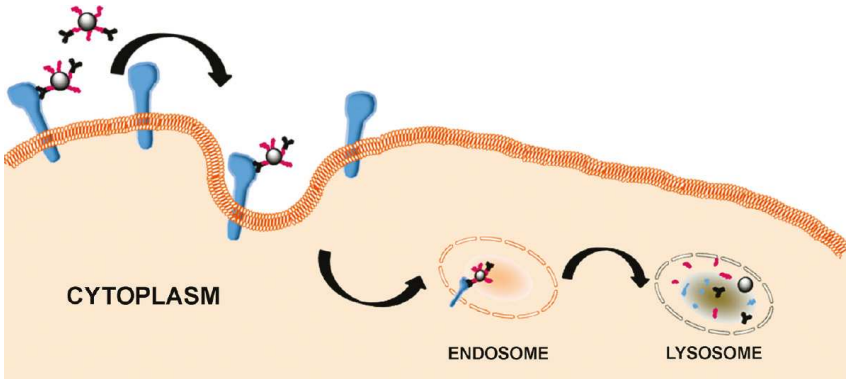

Figure 40. Mechanism of TMNC internalization and degradation in HER2-positive MCF7 cells. In a first step, TMNC binds to HER-2 membrane receptors, inhibiting homodimer formation. Next, the TMNC-HER2 complex formation triggers the local membrane invagination, followed by the complex incorporation within internal early endosomes, which evolve in late endosomes and, eventually, in lysosomes, where the organic corona is rapidly degraded. This process results in a reduced surface expression of HER-2 receptor.

Spectrofluorimetric assays performed on lysates of the same tumors analyzed by the CCD camera provided support to the latter interpretation, as tissue depth was not an issue in this case. Fluorescence intensity, normalized to the overall mass of proteins in each lysate, once again was maximal at 5 h and progressively decreased over time. The same samples were also analyzed by magnetic relaxation measurements to assess the relative amount of iron due to the presence of magnetic nanocrystals incorporated in the tumor tissue. The gradual increment in relaxivity ($1/T_2$)over time was an index of the progressive accumulation of iron in the tumor (Figure 41).

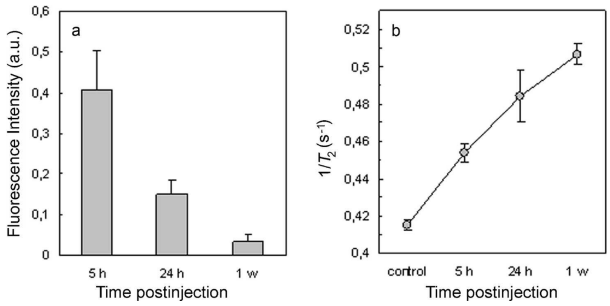

Figure 41. Fluorescence intensity (a) and inverse relaxation time (b) of MCF7 lysates, at 5 h, 24 h, and 1 week postinjection of TMNC.

In accordance with the putative mechanism of TMNC internalization illustrated in Figure 40, immunohistochemical analysis provided evidence that nanoparticles were able to saturate HER-2 monomers expressed on cell surface of the tumor tissue, thus eliciting the rapid receptor degradation, which is expected to strongly interfere with signaling processes promoted by this receptor accounting for a direct involvement of HER-2 in the mechanism of TMNC internalization (Figure 42).

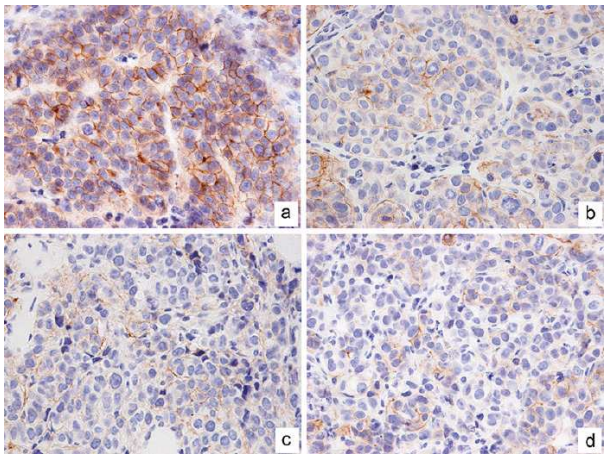

Figure 42. Immunohistochemistry of tumor section extracts (a) before and (b-d) after treatment with TMNC. (a) Strong and diffuse membrane c-erb-2 immunostaining in all of the neoplastic cells. (b-d) No c-erb-2 expression is recovered in most of the neoplastic elements, with only a few c-erb-2-positive cells with diffuse (panel b) or focal (panels c and d) weak pattern of distribution in the tumor at 5 h, 24 h, and 1 week, respectively

A confocal microscopy examination of tumor cryosections indicated that TMNC came into contact with the plasma membrane of cells to be subsequently internalized (Figure 43). Within 24 h, TMNC was endocytosed by tumor cells, as indicated by the presence of labeled spots deep in the cytoplasm and nearby the nucleus. Fluorescence intensity appeared strongly reduced in tumors isolated after 1 week.

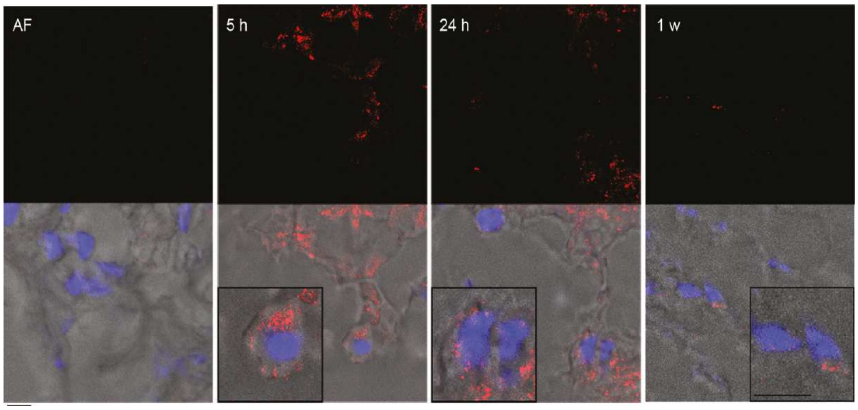

Figure 43. Confocal laser scanning micrographs of cryosections obtained from MCF7 tumors at 5 h, 24 h, and 1 week postinjection of TMNC, and then counterstained with DAPI for nuclei detection. Autofluorescence sample (AF) is a MCF7 tumor from noninjected mice. The confocal images of nanocrystals (red) have been overlaid on the corresponding bright-field images reporting nuclei (blue). A high magnification of representative cells can be observed in the insets. Scale bars = 10 μm.

TEM images provided compelling evidence that TMNC was captured by the plasma membrane of MCF7 cells within the first 5 h followed by membrane invagination, which likely reflects the binding to the target receptors activating the process of internalization (Figure 44). After 24 h, TMNC was recovered inside the cytoplasm, compartmentalized in endosomes and lysosomes, suggesting that it was subjected to a typical endocytic pathway upon incorporation by the cell.

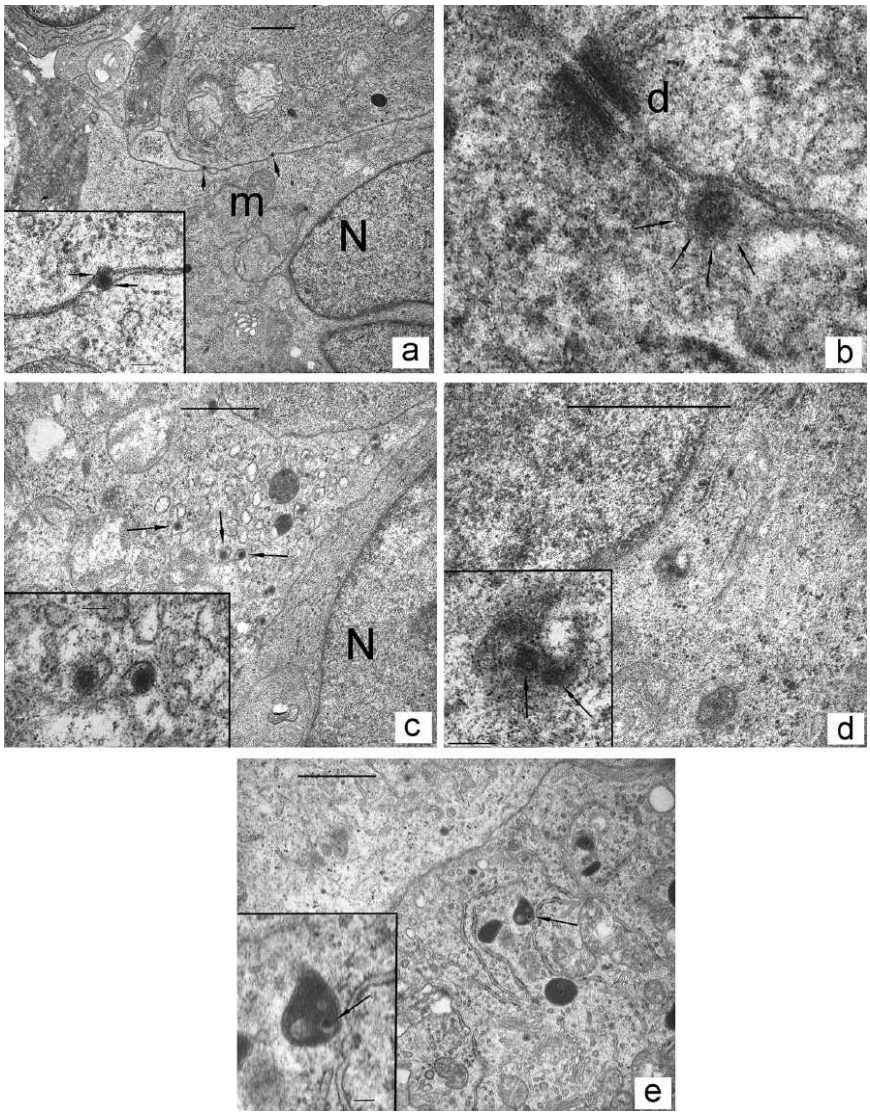

Figure 44. TEM images of MCF7 tumors isolated at (a,b) 5 h, (c,d) 24 h, and (e) 1 week postinjection of TMNC. At 5 h, two nanocrystals (arrows) are interposed between the membranes of two adjacent cells. At a higher magnification (inset), it is evident the close interaction of nanocrystal with membrane (arrows), which invaginates at the binding site level. At 24 h, nanocrystals are compartmentalized (arrows) in endosomes (c) and lysosomes (d) and, after 1 week, only in lysosomes (e). m, mitochondria; N, nucleus; d, desmosome. Scale bars = 1 μm (a,c,d,e), 100 nm (b and insets).

To evaluate the biodistribution of injected TMNC in mice, some model organs have been monitored by a CCD camera (Figure 45). The Epf images of liver, kidneys, spleen, and lungs were determined 5 h, 24 h, and 1 week after TMNC injection. The results obtained confirmed a preferential distribution of TMNC in liver and kidneys after 5 h, and an appreciable fluorescence was also recovered in lungs, although no significant labeling was observed in ex vivo imaging, probably due to a deeper penetration of labeled nanocrystals in this tissue. We observed the progressive decrease of intensity in liver and kidneys: after 1 week from TMNC injection, the fluorescence intensity of liver and kidneys was reduced to about one-third and one-fifth, respectively, of the values recorded at 5 h.

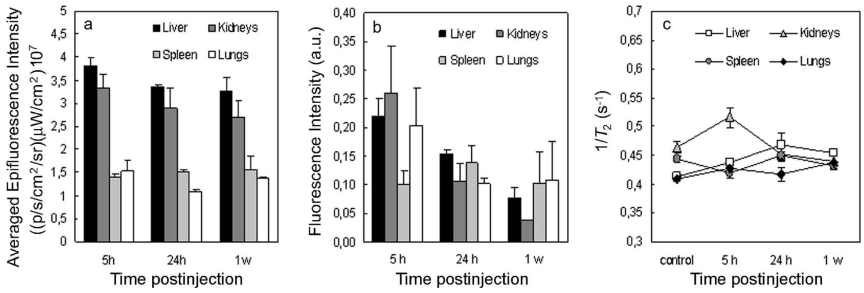

Figure 45. (a) Averaged epf intensity of isolated liver, kidneys, spleen, and lungs. (b) Fluorescence intensity and (c) inverse relaxation time of organ lysates at 5 h, 24 h, and 1 week postinjection of TMNC.

Finally, in order to investigate the possible toxic effects of TMNC on non-target organs, we performed a histopathological examination of liver, kidneys, spleen, and lungs isolated 5 h, 24 h, and 1 week after TMNC injection. No histological lesions were found in liver, kidneys, and spleen at all observed times, while in lungs an initial inflammation process was recovered, which reversed rapidly afterwards (Figure 46). (**ARTICLE 8**)

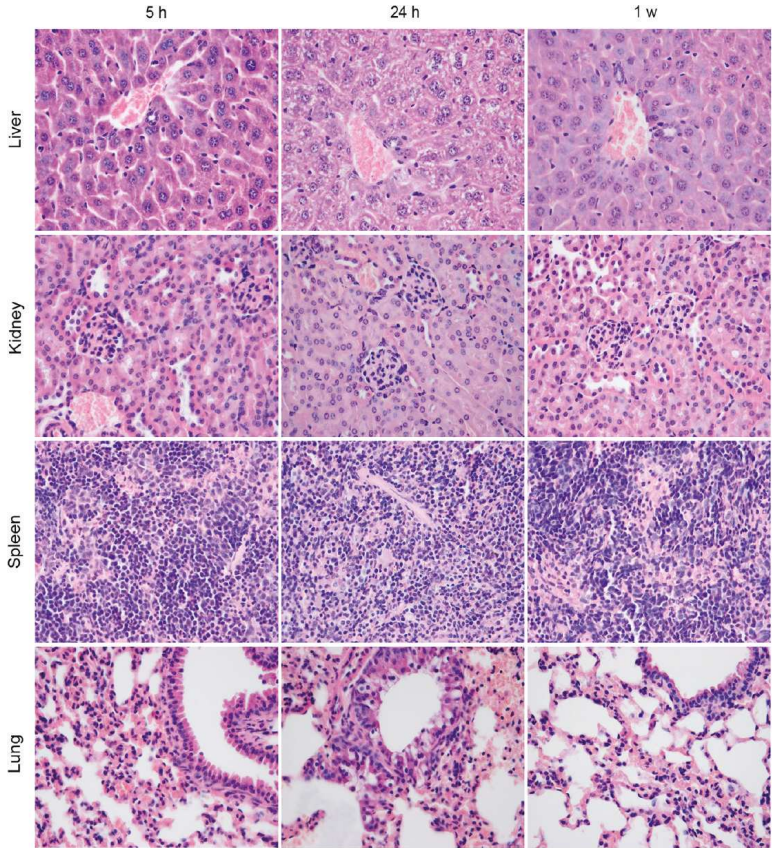

Figure 46. Histopathological analysis of tissue samples. No histological lesions in liver, kidneys, and spleen. A mild inflammatory interstitial infiltrate in all lung samples; a mild hyperplastic reaction of the bronchial epithelium is observed in 24 h lung sample.

Chapter 3

Outlook

Contents

The design of ideal targeted nanoparticles needs careful optimization of fundamental features including uniform size and shape, surface charge, optical and magnetic properties, and efficient functionalization with suitable homing ligands to improve the signal amplification and target selectivity toward malignant cells. We devoted great effort to the development of novel strategies for the biofunctionalization of nanoparticles with proteins to improve the targeting efficiency of nanoparticles toward cell receptors. Protein orientation on the surface of nanoparticles becomes a crucial factor for maximizing the affinity for their molecular counterparts. We reasoned that the bioorthogonal ligation approach could be particularly promising for this purpose, as it involves two different active chemical functionalities placed on the respective ligand pairs, which are joined together. In this light, we are focusing on the investigation of different models based on the interaction between recombinant proteins made by a molecule of biomedical interest (protein, antibody, antibody fragment, etc.) in fusion with a small peptide sequence (capture module) which covalently and selectively binds the nanoparticle functionalized with a substrate analogue or inhibitor in order to generate an oriented and stable functionalization. The advantages of this approach are:

- stable and highly specific binding

- attachment of protein with uniform orientation

- reduced risk of protein degradation or denaturation because of the occurrence of a spontaneous biological interaction instead of a chemical coupling

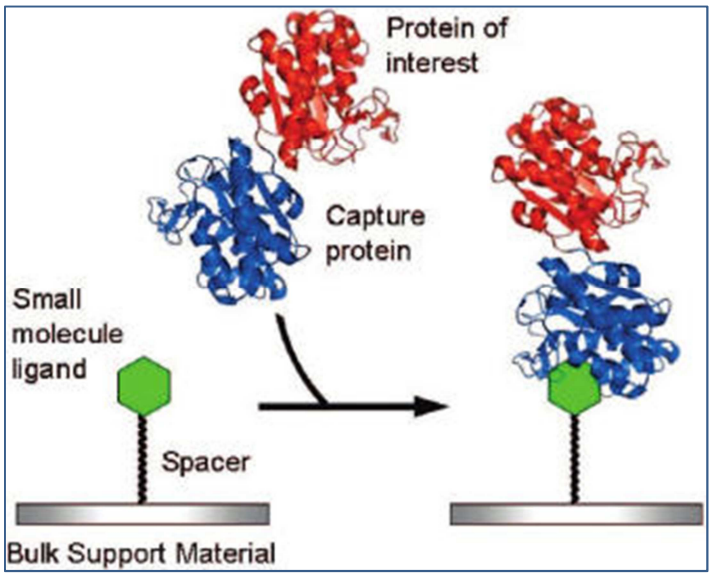

Figure 47. Covalent immobilization via enzymatically active fusion protein

In the course of the last part of this project, we have just finished two works focusing on this protein conjugation strategy. In this section, the results of these works are presented, the first exploiting an alkyne-nitrone cycloaddition reaction, while the second taking advantage of the SNAP-tag technology.

1. Site-specific conjugation of scFvs to nanoparticles by bioorthogonal strain-promoted alkyne-nitrone cycloaddition

We have explored a new method based on a single-step bioorthogonal reaction as an efficient variant of the copper-free "click" cycloaddition, for the reliable surface functionalization of magnetofluorescent nanoparticles with proteins. This approach has several advantages compared with other methods: 1) the reaction is fast and versatile, 2) a complete control on the site of conjugation of the protein (and consequently on the protein orientation on the nanoparticle) can be achieved with a precision of a single aminoacid, 3) the reaction works best in a biocompatible environment and 4) the reaction is byproduct-free, thus each step of purification is simple and efficient. We validated the method using a scFv mutant of the anti-HER2 antibody against breast cancer cells, demonstrating that the resulting scFv-functionalized nanoparticles were able to selectively bind to the specific membrane receptors expressed on target-positive cancer cells.

Copper catalyzed azide-alkyne cycloaddition (CuAAC), which has been exploited for protein immobilization on iron oxide nanoparticles is versatile,[85] but requires metal catalysts that are toxic for cells and unsuited for several kinds of proteins, which strongly limits its applicability.[86] The strain-promoted nitrone-alkyne cycloaddition (SPANC) modification of CuAAC, in which the terminal alkyne is replaced by a highly reactive cyclooctyne, does not require Cu(I) catalysis and has provided excellent results. The reaction requires an N-terminal serine residue in the peptide sequence, which can be easily converted to reactive nitrone and in situ reacted with a ring-strained cyclooctyne-bearing ligand. The kinetics of the reaction can be improved by introducing electron-withdrawing substituents adjacent to the triple bond of the ring-strained cyclooctyne.

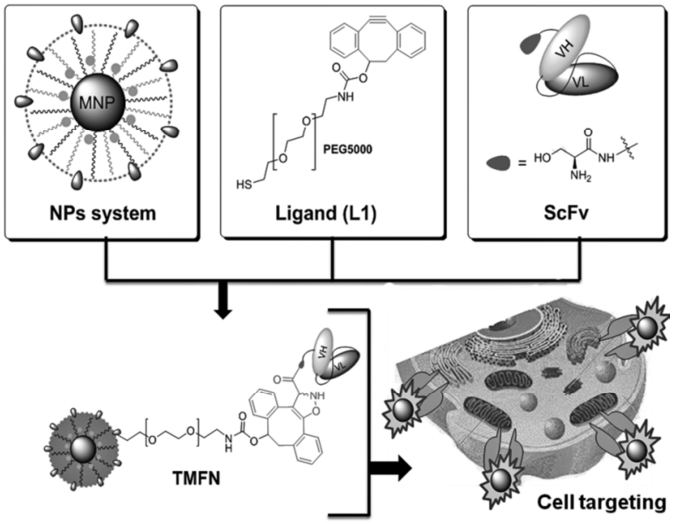

Scheme 6. Synthetic strategy and cell labeling.

Nanoparticles, obtained by solvothermal decomposition in organic solvents, were transferred to water phase by mixing with an amphiphilic polymer, which was previously reacted with fluoresceinamine. These highly stable nanoparticles were functionalized with amino groups for the reaction with a SH-terminated PEG5000 carbamate linker, reactive for the scFv1 previously oxidated on the n-terminal serine.

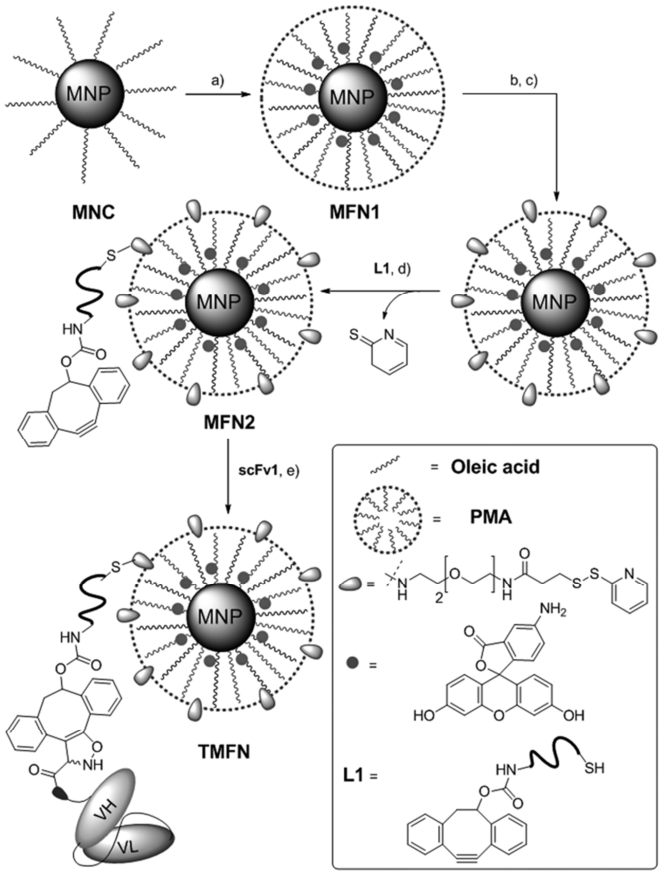

Scheme 7. Synthesis of scFv-functionalized nanoparticles. a) FITC-PMA; b) EDBE, EDC·HCl, 2 h, c) SPDP, 4 h, r.t. ; d) **L1**, 2 h, r.t. ; e) scFv1, 1 h, r.t., 14 h at 4 °C

The functionalized nanoparticles were assessed by flow cytometry to evaluate their affinity and target selectivity in labeling MCF7 breast cancer cells expressing HER-2 membrane receptors. We have evidence of a remarkable right-shift of fluorescence signal for both nanoparticles concentrations with HER-2$^+$ cells, which was not observed with MDA cells. These results suggest that nanoparticles accumulate selectively on MCF7 cells and that nanoparticle-HER-2 recognition is concentration-dependent (Figure 48).

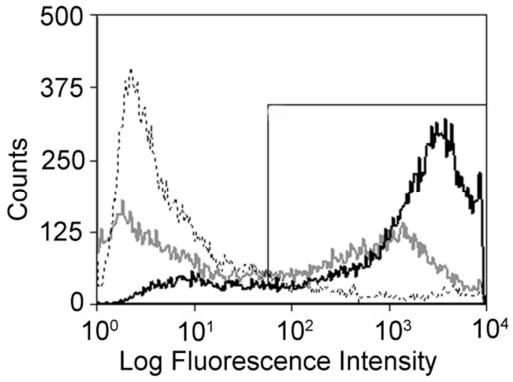

Figure 48. MCF7 cells were incubated 1 h at 37 °C with 20 µg mL^{-1} (gray line) and 100 µg mL^{-1} (black line), respectively, of nanoparticles. As a negative control, MDA cells were treated with nanoparticles (dashed line).

The specificity of binding between nanoparticles and HER-2 was validated by confocal laser scanning microscopy. We observed an accumulation of nanoparticles and scFv1 at the cell membrane of HER-2^+ cells only, which confirmed that nanoparticle capture by cells was actually mediated by specific membrane receptor interaction.

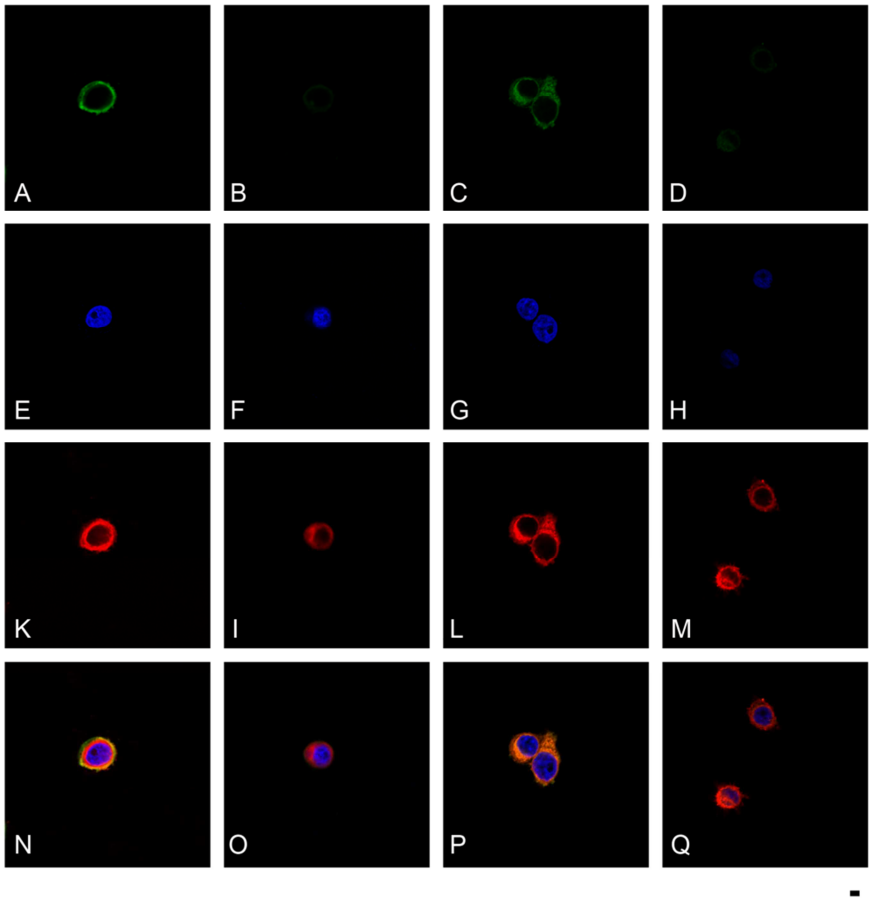

Figure 49. HER-2^{+} cells (MCF7; A, E, K, N) and HER-2^{-} cells (MDA; B, F, I, O) were incubated 1 h at 37 °C with nanoparticles (100 µg mL^{-1}). ScFv1 incubation with MCF7 and MDA cells was used as positive (C, G, L, P) and negative controls (D, H, M, Q), respectively. ScFv1 was revealed by a FITC-conjugated antibody to whole murine IgG (C, D). Nuclei were stained with DAPI (E, F, G, H) and membranes were stained with DiD oil (K, I, L, M). Merge images were showed in panels N, O, P and Q. Scale bar = 10 µm

To evaluate the potential of the synthesized nanoparticles as magnetic contrast agents in living cells, we performed a set of T_2 relaxation experiments on MCF7 and MDA cells. The treated samples as well as unlabeled MCF7 and MDA cells (controls) were analyzed by relaxometric measurements. All the treated MCF7 cells exhibited a significant dose-dependent fall in T_2 compared to the control, confirming the capture of

paramagnetic iron by cultured. In contrast, MDA cells did not provide evidence of T_2 decrease attributable to the interaction with nanoparticles at all the concentration tested.

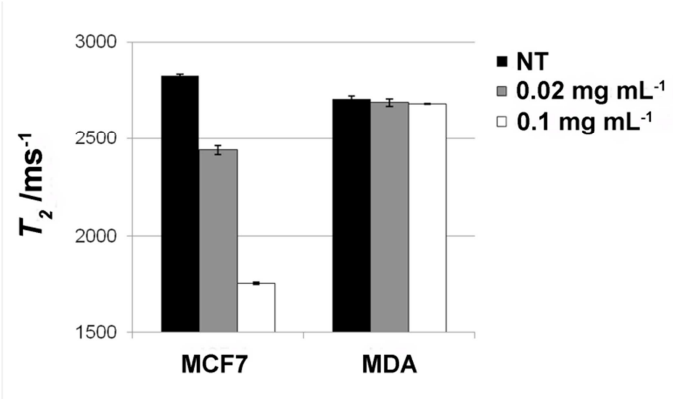

Figure 50. Relaxivity measurements on treated and untreated (NT, controls) MCF7 and MDA cells. Data are the mean ± S.E. of three different relaxivity measurements. T_2 values refer to 5×10^5 cells after incubation with different concentrations of nanoparticles.

Finally, we investigated the cellular toxicity and cell proliferation of nanoparticles. Nanoparticles were found to be non-toxic at 20 and 50 μg mL^{-1} in MCF7 after 24 h of exposure, while induced about 15% mortality at 100 μg mL, probably due to the high particulate concentration in suspension. No differences were observed between untreated and nanoparticle-treated cells in terms of proliferation, further confirming the low toxicity of thes^{-1}e particles (Figure 51). These experiments suggested a good profile of safety in cultures for TMFN. (**ARTICLE 9**)

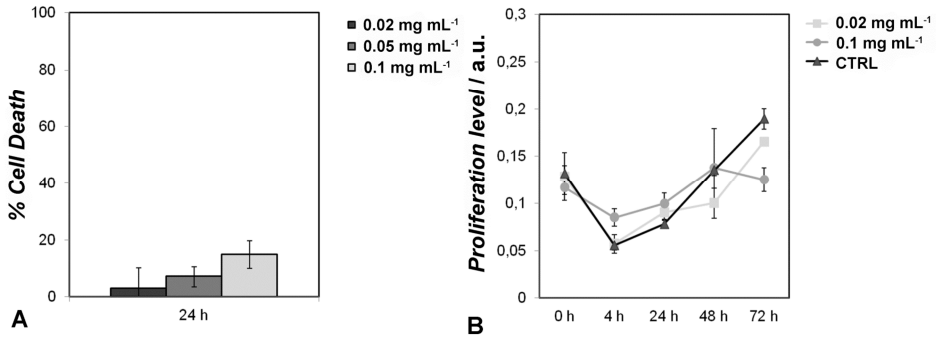

Figure 51. A) Cell death assay with TMFN. MCF7 cells. Cell death was assessed to measure the exposure of Annexin V and the incorporation of 7-aminoactinomycin D, evaluated by flow cytometry. The percentage of cell death in untreated population was substracted. B) Cell proliferation assay with TMFN. MCF7 cells were treated with TMFN Cell proliferation was tested by measuring the conversion of MTT into formazan. CTRL represents untreated control.

2. Protein oriented ligation on nanoparticles exploiting genetically encoded fusion with O_6-Alkylguanine-DNA transferase

The second approach attempted in this explorative insight was a new method based on the genetic encoding of mutants of human O_6-alkylguanine-DNA alkyltransferase, also referred to as SNAP-tag, for the reliable biofunctionalization of nanoparticles. The genetic encoding of the targeting protein produced in N-terminal-linked fusion with SNAP, reacted quickly, effectively and in a site-directed manner with guanine derivatized multifunctional nanoparticles (MFN2). This resulted in the formation of a new covalent bond between the protein and the nanoconjugate (SSMFN) with release of a guanine molecule (Scheme 8).

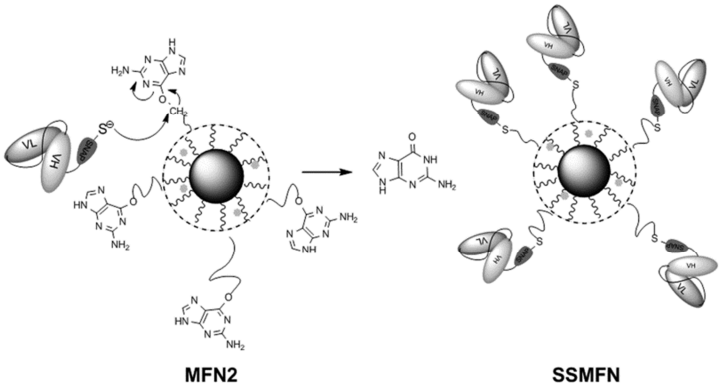

Scheme 8. Mechanism of SNAP-mediated immobilization of scFv on MFN2.

As a proof of concept of the potential of this method, we designed a bimodular genetic fusion (SNAP-scFv) comprising a bioactive scFv mutant selective for HER-2 receptor in breast cancer cells as a targeting module, and SNAP as MFN2 capture module (Scheme 9).

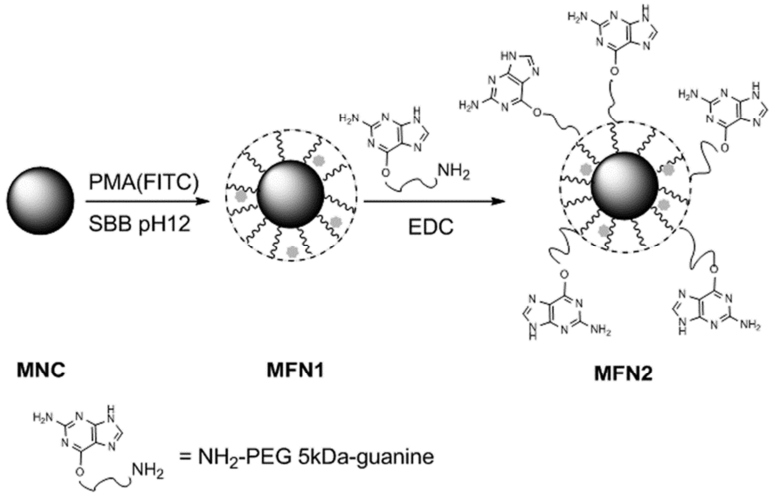

Scheme 9. Synthesis of MFN2.

We have demonstrated the utility of this method for protein nanoconjugation and cellular imaging by evaluating the effects of the treatment of HER-2-positive breast cancer cells with SSMFN. HER-2-positive MCF7 cells were used as model to assess the targeting efficiency of SSMFN. Flow cytometry performed on HER2-positive MCF7 treated with SSMFN evidenced a concentration-dependent signal right-shift associated with labeled cells. In contrast, HER-2-negative MDA cells remained unlabeled after SSMFN treatment at the highest concentration (Figure 52).

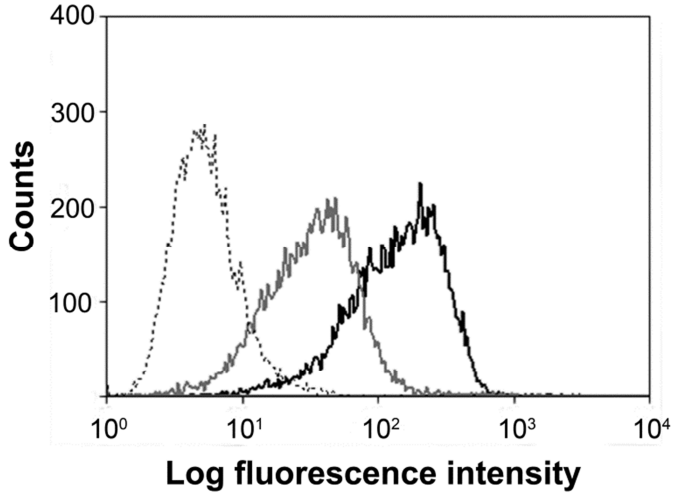

Figure 52. MCF7 cells were incubated 1 h at 37 °C with 20 μg mL^{-1} (gray line) and 100 μg mL^{-1} (black line) of SSMFN. As a negative control, MDA cells were treated with 100 μg mL^{-1} of SSMFN (dashed line).

Next, confocal laser scanning microscopy confirmed the specificity of binding between SSMFN and HER-2 receptors. SSMFN and SNAP-scFv colocalized at the cell membrane of HER2-positive cells only, which confirmed that SSMFN adhesion to cell membrane was actually mediated by specific interaction with HER-2 (Figure 53).

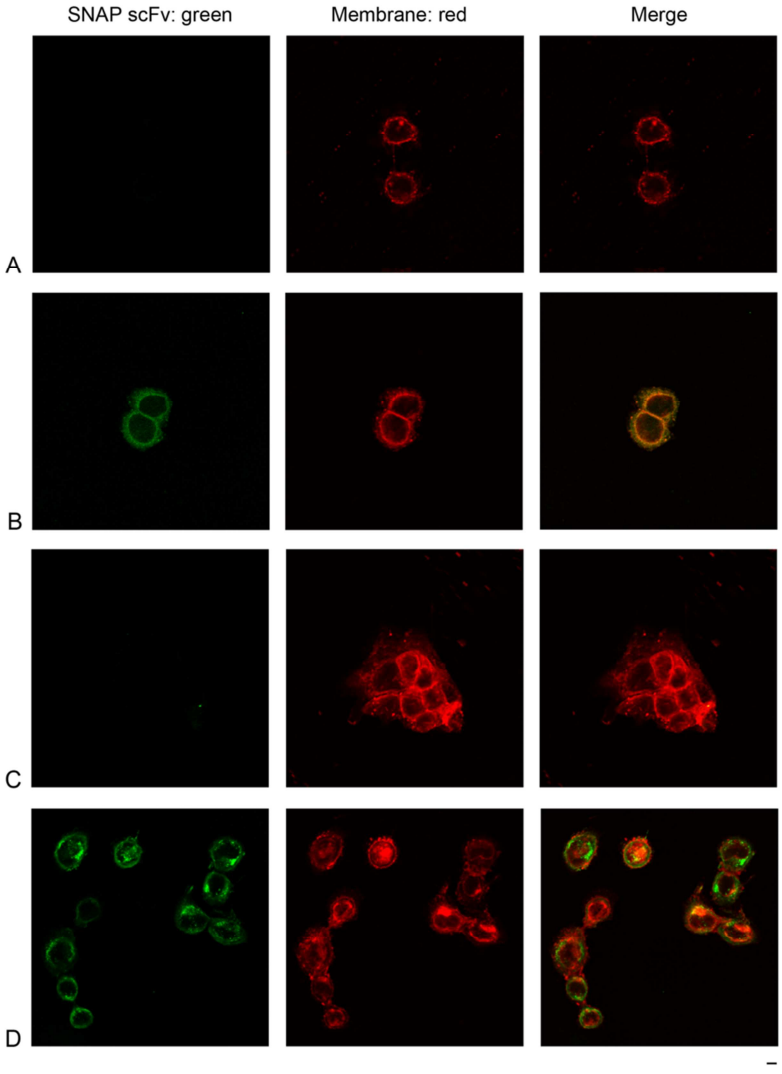

Figure 53. HER-2^{+} cells (MCF7, D) and HER-2^{-} cells (MDA, C) were incubated 1 h at 37 °C with SSMFN (100 µg mL^{-1}). SNAP-ScFv incubation with MCF7 and MDA cells was used as positive (B) and negative controls (A), respectively. SNAP-scFv was revealed by a FITC-conjugated secondary antibody against whole murine IgG (green). Membranes were stained with DiD oil (red). Scale bar = 10 µm.

Finally, cellular death experiments performed on MCF7 cell after incubation with SSMFN at 20, 50 and 100 µg mL^{-1}, demonstrated that SSMFN were non-toxic in this range of concentrations, which is

significant for in vitro and in vivo applications (Figure 54A). MTT assay showed a proliferation profile similar to that of untreated cells both at 20 and 100 μg mL^{-1} (Figure 54B).

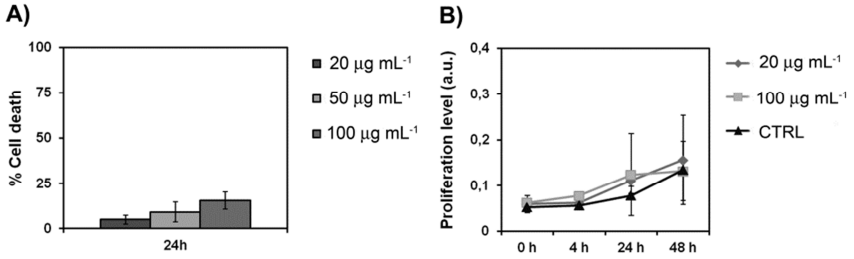

Figure 54. A) Cell death assay with SSMFN. MCF7 cells were treated with SSMFN for 24 h. Cell death was assessed by measuring the exposure of Annexin V and the incorporation of 7-aminoactinomycin D evaluated by flow cytometry. The percentage of cell death in untreated population was subtracted. The results are expressed as means ± S.D. of the mean of 3 individual experiments. B) Cell proliferation assay with SSMFN. MCF7 cells were treated with SSMFN for up to 48 h. Cell proliferation was tested by measuring the conversion of MTT into formazan. CTRL represents untreated control. The results are expressed as means ± S.D. of the mean of 5 individual experiments.

Our method proved to be rapid, efficient and potentially applicable to most proteins, especially to the increasingly popular scFv targeting ligands, without apparent loss of biological activity, which usually represents a severe obstacle in the fabrication of bioinspired hybrid materials. Another feature of attractiveness of our method is that it makes use of hydrophobic nanoparticles, which have been rendered water-soluble by coating with a suitable amphiphilic polymer. In this way, the same approach can be immediately extended to several kinds of nanomaterials, including gold, quantum dots, and many others that are prepared by solvothermal decomposition methods in organic solvents.

3. Conclusion

Cellular processes are commonly regulated by the presence of simultaneous alternative pathways at the physiological level. Such redundancies represent the main strategy exploited by the cells to perpetuate their survival, resulting in a wide range of advantageous possibilities to facilitate the persistence of normal cells. However, in the early stages of malignancies, this "multiple choice" system may cause the catastrophic fate of the host organism, as degenerated cancer cells are allowed to increase their proliferative potential in the same way. Indeed, tumor cells are able to bypass the proliferation check-point by "contriving" new mechanisms for the control of their life maintenance and for the development of their abnormal growth, thus becoming substantially immortal. Based on this rationale, several modern advanced therapeutic approaches for cancer treatment are focusing on the assumption that the inhibition of a single proliferation pathway with a suitable therapeutic agent may exhibit only limited efficacy. Actually, to enhance the probability of success of the therapy, it is imperative to selectively remove the tumor cell before it can evolve to its superior stages up to the metastases production. In the latter stages of cancer evolution, tumor cells acquire the ability to evade the proliferation inhibition by pharmacological agents. Therefore, under this scenario there is a growing need to develop novel and more sensitive diagnostic tools which should improve the early identification of rising malignancies and the accuracy of tumor tissue localization in order to improve the positive outcome of surgical interventions.

The main scope of this work was the development of organic/inorganic hybrid nanoparticles functionalized with active biomolecules for the molecular receptor recognition in cancer cells. The occurrence of a targeted ligand-receptor interaction can be sensitively detected by conjugating selective molecular probes with a metallic nanoparticle resulting in the amplification of a physical signal which would theoretically enable to localize one individual malignant cell. Thanks to the multifaceted properties of magnetic nanomaterials, we selected iron oxide nanocrystals as model nanoparticle for the investigation of new conjugation strategies and for the interaction of the resulting nanobiocomplexes with superior biological systems. As a proof of concept

of the utility of our nanobiotechnology platform we focused on the conjugation of a monoclonal antibody currently in use for clinical immunotherapy of breast cancer, the commercial trastuzumab and its engineered variants, for which the natural receptor is well-documented (the human epidermal grow factor receptor 2, HER-2).

The combination of individually FDA-approved molecular entities and non-toxic nanomaterials leads to nanovectors ideally ready for in vivo testing. If the ongoing trials on the first generation of hybrid nanoparticles based on trastuzumab conjugates will demonstrate successful, some of these systems may become a good candidate to be developed as theranostic nanoclinics, since the diagnostic technique mainly required for their use (MRI) is already a frequently used medical tool for standardized clinical protocols.

The novel bioconjugation strategies explored within this work should be generalized by validating them with alternative molecular ligands and different kinds of nanoparticles, thus extending the field of applicability of our approach. The forthcoming work will be the optimization of the in vivo administrations of theranostic agents in superior animals models, including primates, as the final goal of this project remains the clinical translation of molecular nanoclinics to be used in combination with, or even in replacement of, the current invasive diagnostic and therapeutic techniques for the treatment of human breast cancer.

Publications included in this thesis

ARTICLE 1

Pharmacological Research 62 (2010) 150–165

Contents lists available at ScienceDirect

Pharmacological Research

journal homepage: www.elsevier.com/locate/yphrs

Review

HER2 targeting as a two-sided strategy for breast cancer diagnosis and treatment: Outlook and recent implications in nanomedical approaches

Miriam Colombo[a,b], Fabio Corsi[b,1], Diego Foschi[b], Elisa Mazzantini[a], Serena Mazzucchelli[a,b], Carlo Morasso[c], Emanuela Occhipinti[a], Laura Polito[c], Davide Prosperi[a,c,*], Silvia Ronchi[c,2], Paolo Verderio[a,b]

[a] Dipartimento di Biotecnologie e Bioscienze, Università di Milano-Bicocca, Piazza della Scienza 2, 20126 Milano, Italy
[b] Dipartimento di Scienze Cliniche "Luigi Sacco", Università di Milano, Ospedale L. Sacco, Via G.B. Grassi 74, 20157 Milano, Italy
[c] Istituto di Scienze e Tecnologie Molecolari, CNR, Via Fantoli 16/15, 20138 Milano, Italy

ARTICLE INFO

Article history:
Received 9 December 2009
Received in revised form 19 January 2010
Accepted 19 January 2010

Keywords:
Antibodies
Growth factors
Breast cancer
Nanoparticles
Theranostic agents
Nanomedicine

ABSTRACT

At present, mammary carcinoma is the second most common type of malignant tumor in adult women after lung cancer, as more than one million women are diagnosed with breast cancer every year. Despite advances in diagnosis and treatment, which have resulted in a decrease in mortality in recent decades, breast cancer remains a major public health problem. One of the most significant unresolved clinical and scientific problems is the occurrence of resistance to clinical treatments and their toxicity (and how to predict, prevent and overcome them). However, the heterogeneity of human breast cancer in terms of genetic features, molecular profiles and clinical behavior represents a constraint obstructing the discovery of a solution to the disease. It is currently considered that the chances of success of therapy may increase if the tumor cells are selectively removed before they can evolve to their mature stages up to metastases production. Therefore, novel and more sensitive diagnostic tools are being developed, with the aim of improving the early and noninvasive detection of rising malignancies and the accuracy of tumor tissue localization. Meanwhile, there is an emerging use of targeted therapies in oncology, depending on the expression of specific proteins or genes present in tumor cells. Among the molecular targets considered for the treatment of breast cancer cells so far, we chose to focus on examples involving overexpression and/or gene amplification of "Human Epidermal growth factor Receptor 2" (HER2) protein. In current studies, various types of nanoparticles conjugated with the anti-HER2 monoclonal antibody, the so-called "trastuzumab", are investigated extensively due to promising results in biological and preclinical applications aimed at improving the treatment of breast cancer. In this paper, we present a critical review of the preparation and use of different kinds of trastuzumab-functionalized nanoparticles, with an emphasis on the therapeutic and diagnostic (theranostic) potential of this generation of hybrid nanoparticles, exploiting the multifaceted mechanisms of action of trastuzumab against malignant cells.

Contents

* Corresponding author at: Dipartimento di Biotecnologie e Bioscienze, Università di Milano-Bicocca, Piazza della Scienza 2, 20126 Milano, Italy. Tel.: +39 0264483302; fax: +39 0264483565.
E-mail addresses: fabio.corsi@unimi.it (F. Corsi), davide.prosperi@unimib.it (D. Prosperi), silvia.ronchi@istm.cnr.it (S. Ronchi).
[1] Tel.: +39 0239043449; fax: +39 0250319846.
[2] Tel.: +39 0250320969.

1043-6618/$ – see front matter © 2010 Elsevier Ltd. All rights reserved.
doi:10.1016/j.phrs.2010.01.013

1. Introduction

Cellular processes are commonly regulated by the presence of simultaneous alternative pathways at the physiological level. Such redundancies represent the main strategy exploited by the cells to perpetuate their survival, resulting in a wide range of advantageous possibilities to facilitate the persistence of normal cells. However, in the early stages of malignancies, this "multiple choice" system may cause the catastrophic fate of the host organism, as degenerated cancer cells are allowed to increase their proliferative potential in the same way. Indeed, tumor cells are able to bypass the proliferation check-point by "contriving" new mechanisms for the control of their life maintenance and for the development of their abnormal growth, thus becoming substantially immortal. Based on this rationale, several modern advanced therapeutic approaches for cancer treatment are focusing on the assumption that the inhibition of a single proliferation pathway with a suitable therapeutic agent may exhibit only limited efficacy. Actually, to enhance the probability of success of the therapy, it is imperative to selectively remove the tumor cell before it can evolve to its superior stages up to the metastases production. In the latter stages of cancer evolution, tumor cells acquire the ability to evade the proliferation inhibition by pharmacological agents. Therefore, under this scenario there is a growing need to develop novel and more sensitive diagnostic tools which should improve the early identification of rising malignancies and the accuracy of tumor tissue localization in order to improve the positive outcome of surgical interventions.

Highly metastasizing mammary carcinoma has been identified as the second most common type of malignant tumor in adult women after lung cancer [1], as 1.2 million women are diagnosed with breast cancer every year. Current clinical approaches to the detection of malignancy localization at the lymph nodal level are not entirely satisfactory, particularly in terms of patient care. The "Sentinel Lymph Node" method is universally accepted to be the most superior approach for the detection of lymphatic axillary chain nodal invasion. However, this approach is rather invasive, as it is based on a surgical biopsy of the first lymph node of the axillary chain spotted by a lymph-scintigraphy with ^{99m}Tc [2].

In recent years, a variety of nanoparticles (NPs) functionalized with cancer-specific targeting ligands have been investigated to image tumors and detect peripheral metastases [3]. In particular, they could be used in early identification of tumors, allowing for a timely intervention with chemopreventive therapies. Several nanotechnological approaches have been used to improve the delivery of chemotherapeutic agents to cancer cells with the goal of minimizing toxic effects on healthy tissues while maintaining antitumor efficacy. Doxorubicin has been formulated with a liposome delivery system into NP size, which maintains the efficacy of the drug and decreases cardiac toxic effects [4]. One of these delivery systems, pegylated liposomal doxorubicin, is approved for treatment of refractory ovarian cancer and Kaposi's sarcoma in the United States. NP albumin-bound paclitaxel also exhibits greater efficacy than conventional castor-oil-based paclitaxel with an improved safety profile [5], and is approved in the US for the treatment of metastatic breast cancer.

Although the number of different types of NPs is increasing rapidly, most of them can be classified into two major groups: (1) particles containing organic molecules as a major building material and (2) those that use inorganic elements, usually metals, as a core. Liposomes, dendrimers, carbon nanotubes, emulsions, and other polymers are a large and well-established group of organic particles. The use of these organic NPs has already produced promising results. The structure, function, and biomedical applications of these organic NPs have been reviewed recently [6–9].

Most inorganic NPs share the same basic structure, consisting of a central core that defines the physical properties (detectable source of signal), including fluorescence, optical, magnetic, and electronic features of the particle, with a protective organic coating on the surface which is usually responsible for the biological recognition and improvement of the particle solubility, for protecting the core from degradation in a physiologically aggressive environment and for evading the clearance action of the host immune system (Fig. 1). The present overview is essentially focused on this latter class of composite NPs.

With the increasing use of targeted therapies in oncology, there is the requirement for the methods of molecular profiling to be optimized. The success of many targeted treatments depends on the expression of specific proteins or genes present in tumor cells. In breast cancer cells, the level of hormone-receptor expression correlates directly with the benefit of endocrine treatments, and the presence of "Human Epidermal growth factor Receptor 2" (HER2) protein overexpression and/or gene amplification is a prerequisite to benefit from target specific monoclonal antibodies [10].

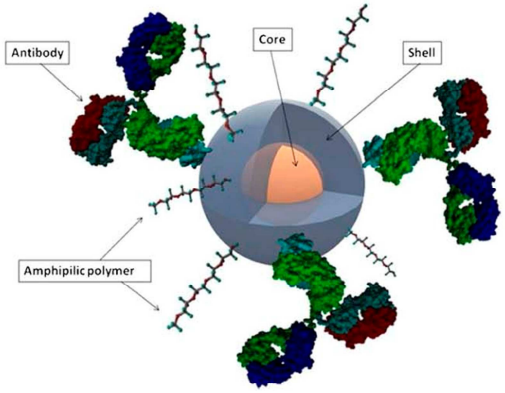

Fig. 1. Schematic representation of an ideal hybrid functional nanoparticle designed for HER2 receptor targeting. The optical/magnetic signal is produced by the metal core, which is protected by an organic/inorganic polymer shell derivatized with solubilizing stealthy molecules (e.g., PEG), and targeting ligands (e.g., trastuzumab).

Some breast cancers produce protein biomarkers (e.g., estrogen receptor, progesterone receptor, and HER2), on which therapeutic decisions are made. The use of NPs is expected to allow for the simultaneous detection and quantification of several proteins in small tumor samples, which will ultimately enable the tailoring of specific anticancer treatment to an individual patient's specific tumor protein profile, potentially leading to a personalized medicine [11].

To design a diagnostic approach to breast carcinoma using nanoagents in humans, it is necessary to fulfill several criteria for their utilization. These include high resolution and the accuracy and sensitivity of detection, which may be provided by using NPs coated with specific monoclonal antibodies against protein biomarkers overexpressed by breast cancer cells, such as HER2 receptor. In addition, they must ideally have no toxicity, and be able to interact in a physiological way with biological tissues. In particular, they should have a good safety profile and not aggregate when delivered to biological tissues. Finally, since membrane receptors are endocytosed as part of their normal response to ligand binding, functionalized NPs have to follow physiological pathways when internalized. So far, only preliminary evidence has been reported in regard to these latter factors, which are critical for clinical use [12–14]. The ultimate challenge is represented by the development of efficient strategies for the reliable conjugation of targeting biomolecules on the NP surface. In fact, a major issue is the reliable conservation of the biological activity of immobilized macromolecules.

Among the various molecular targets explored for the treatment of human carcinoma, we chose to focus on examples involving NPs conjugated with the anti-HER2 monoclonal antibody, the so-called "trastuzumab", which is commonly employed in current clinical practice. In this review, we present the recent literature reporting on the state of the art techniques for the preparation of various typologies of trastuzumab-functionalized NPs, and their application in biological and preclinical studies aimed at improving the diagnosis and treatment of breast cancer. This overview is preceded by a critical insight of the current knowledge in regard to the biological role of HER2 membrane receptor, the mechanism of action of trastuzumab, its involvement in combination therapy and proposed mechanisms of resistance developed by the malignant cell in response to prolonged treatment with the antibody.

2. The Human Epidermal growth factor Receptor 2: action and signaling inhibition

2.1. HER2 receptor mechanism of action

HER2 is a transmembrane tyrosine kinase receptor, which belongs to the ERBB family and is overexpressed in 25–30% of human breast cancers [15]. HER2 includes an extracellular domain at which ligand binding occurs, an α-helical transmembrane segment and an intracellular protein tyrosine kinase domain [16]. An essential requirement for its function and signalling activity is receptor dimerization (pairing) [16,17]. After ligand binding to the extracellular domain, a conformational rearrangement occurs, exposing the dimerization domain that forms the core of the dimer interface with another receptor [18]. Receptor dimerization is responsible for the transactivation of the tyrosine kinase portion of the dimer moiety as each receptor activates its partner by phosphorylation.

In contrast, HER2 involves an active tyrosine kinase domain and its native form exists in the extended (open) 'active' conformation state, so it is constitutively available for dimerization [19–21]. HER2 can form homodimers or heterodimers with EGFR, HER3 and HER4 and is required for key intracellular pathways that govern fundamental cellular processes, including proliferation and cell survival [19,22]. Although HER2 dimerization partners are activated by different signaling molecules, the specificity of HER2 signaling resides in its capacity to preferentially bind some effector proteins [16,19,22]. In tumor cells, HER2 is overexpressed or constitutively activates and stimulates many intracellular signaling proteins and physiological pathways, such as the mitogen-activated protein kinase (MAPK), Phosphoinositide 3 kinase/Ak transforming factor (PI3K/Akt), mammalian target of rapamycin (mTOR), Src kinase, and STAT transcription factors (signal transducers and activators of transcription) [19,23,24]. However, pathology arises here whereas the usual negative regulatory loops that function in normal cells are impaired [25]. Two key signaling pathways activated by the ERBB family dimers are the MAPK pathway, which stimulates proliferation, and the PI3K/Akt pathway, which promotes tumor cell survival. The activation of the MAPK pathway leads to the transcription of genes that drive cellular proliferation, migration, differentiation and angiogenesis [16,17]. Signaling through the PI3K/Akt pathway leads to the activation, through phosphorylation, of many other proteins that initiate processes to enable cell survival, suppression of apoptosis and cell cycle control (mTOR, STAT and FOXO transcription factor) [22,26–29]. The involvement of PI3K pathway in cancerogenesis is emphasized by the observation that many breast tumors exhibit low levels of phosphatase and tensin homolog (PTEN) [30], the lipid phosphatase that dephosphorylates and reduces PIP3 (phosphatidylinositol 3-phosphate), thereby reversing the action of PI3K.

2.2. HER2 inhibition by trastuzumab

Extracellular domain of HER2 has been the target of several monoclonal antibodies created in order to inhibit the proliferation of human cancer cells. The most popular trastuzumab is a humanized monoclonal antibody consisting of two antigen-specific sites that bind to the juxtamembrane portion of the extracellular domain of the HER2 receptor preventing the activation of its intracellular tyrosine kinase [31]. There are several possible mechanisms through which trastuzumab may decrease HER2 signaling (Fig. 2). Some recent works showed that trastuzumab mediates the activation of antibody-dependent cellular cytotoxicity (ADCC). The presence of ADCC is mainly due to the activation of natural killer (NK) cells, expressing the Fc gamma receptor, which can be bound by the Fc domain of trastuzumab [33,34]. However, Molina et al. demonstrated that, in HER2 overexpressing breast cancer cell lines, trastuzumab may follow an alternative mechanism of action involving blockage of the proteolytic cleavage of HER2 extracellular domain, and p95 serum-release by inhibiting metalloproteinase activity [35,36]. A diminished signaling mechanism may result from trastuzumab-mediated internalization and degradation of the HER2 receptor, but whether trastuzumab actually down-regulates HER2 or not is currently the subject of debate [37–39]. Moreover, it is still unclear if trastuzumab is capable of acting directly on HER2 intracellular partners [30,40]. Finally, trastuzumab treatment provokes cell cycle arrest during the G1 phase, with a concomitant reduction of proliferation. This event is accompanied by the reduced expression of proteins involved in the sequestration of the cyclin-dependent kinase (cdk) inhibitor $p27_{kip1}$, including cyclin D1. This results in the release of $p27_{kip1}$, allowing it to bind and inhibit cyclin E/cdk2 complexes [41].

2.3. Mechanism of resistance to trastuzumab

A large proportion of HER2-positive cancers demonstrate the predisposition to develop resistance to HER2-targeted therapeutics [42]. An improved understanding of the mechanisms involved in the resistance of tumor cells to trastuzumab molecules will provide the framework for developing new therapeutic strategies.

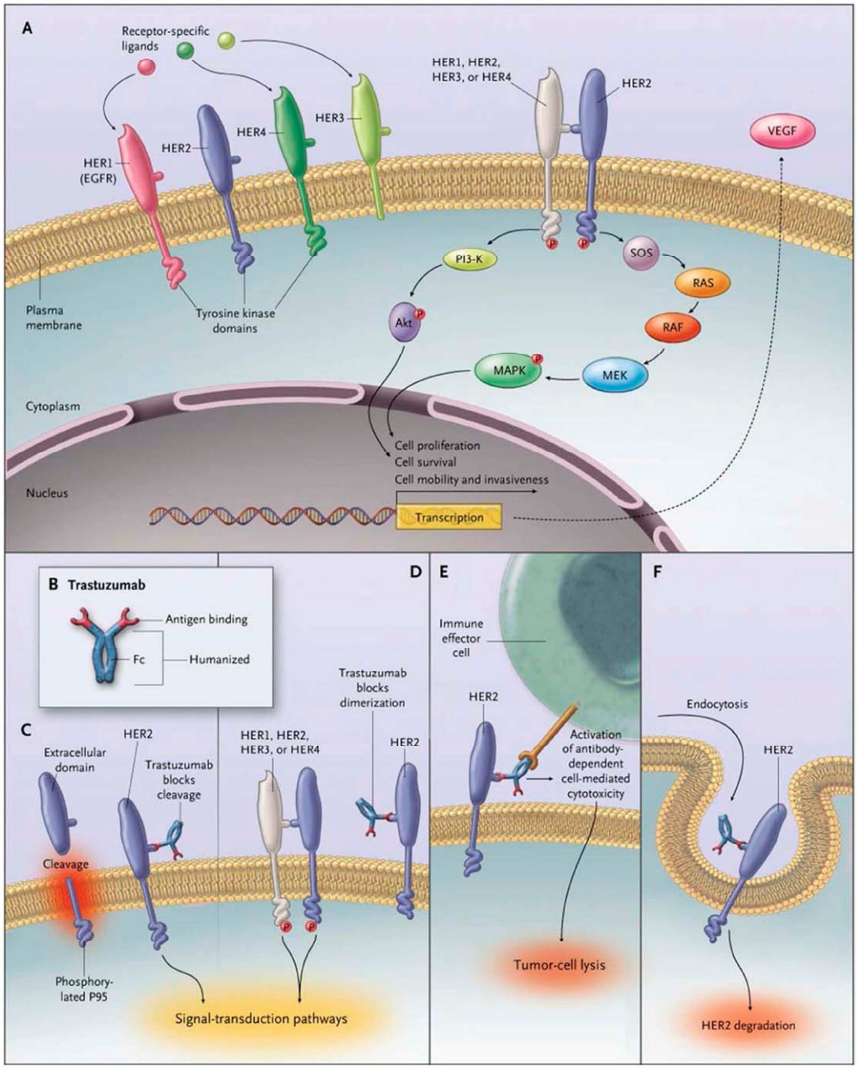

Fig. 2. Signal transduction by the ERBB family and potential mechanisms of action of trastuzumab. The four members of the ERBB family: HER1, HER2, HER3, and HER4 (Panel A). There are ligands specific for HER1, HER3, and HER4 receptors. All ERBB family receptors have an intracellular tyrosine kinase domain exclusive of HER3. Homodimerization or heterodimerization induces phosphorylation of the tyrosine kinase domain activating both cell proliferation and survival signaling. HER2 is the preferred dimerization partner for the other HER family members. Phosphorilation of the tyrosine residues on the intracellular domain of HER2 activate the lipid kinase phosphoinositide 3-kinase (PI3K), which phosphorylates a phosphatidylinositol that in turn binds and phosphorylates the enzyme Ak transforming factor (Akt), driving cell survival. In parallel, the mammalian homologue of the son of sevenless (SOS), a guanine nucleotide exchange factor, activates the rat sarcoma (RAS) enzyme that, in turn, activates receptor activation factor (RAF) and then mitogen extracellular signal kinase (MEK). MEK phosphorylates, among others, the mitogen-activated protein kinase (MAPK), driving cellular proliferation. One of many other downstream effects is the production of vascular endothelial growth factor (VEGF) supporting angiogenesis. The most well-documented potential mechanisms of action of trastuzumab (Panels B–F). In panel C cleavage of the extracellular domain of HER2 by matrix metalloproteinase-2 (MMP-2) is shown. It leaves a membrane-bound phosphorylated p95, which can activate signal-transduction pathways. Shedding reduction of the extracellular domain through binding of trastuzumab to a juxtamembrane domain of HER2 (Panel C). Trastuzumab may mediate reduction of HER2 signaling by physically inhibiting either homodimerization, as shown, or heterodimerization (Panel D). Recruitment of Fc-competent immune effector cells and the other components of antibody-dependent cell-mediated cytotoxicity by trastuzumab, leading to tumor-cell death (Panel E). Additional mechanisms such as receptor down-regulation through endocytosis have been postulated (Panel F). Reproduced with permission from Ref. [32].

Several hypotheses about trastuzumab resistance have been put forward.

For example, up-regulation of HER2 levels has been associated with resistance to HER2 antagonists. Moreover, a number of mutated forms of HER2 have been identified and thought to modulate the activities of the receptor ensemble. In particular, a HER2 mutant containing a G776 (YVMA) insertion in exon 20 exhibits higher activity than the wild-type protein in activating downstream signaling events by forming the EGFR/HER2 heterodimer, which thereby enhances survival, invasiveness, and tumorigenicity [43]. Moreover, in the presence of an excess of EGFR ligands, of HER2 or both, the resulting heterodimers drive cells towards proliferation and inhibition of apoptosis and possibly interfere with trastuzumab [44]. Among these ligands, transforming growth factor-α (TGF-α) potentially plays an important role in resistance to trastuzumab.

In their cell lines model, Nahta et al. observed IGF1R/HER2 heterodimers. In the presence of these heterodimers, trastuzumab was completely unable to arrest cell proliferation [45]. These results highlight IGF1R as a possible mediator of trastuzumab resistance and a possible therapeutic target in patients with trastuzumab-resistant disease. Nagata et al. also suggested an important role of decreased expression of the PTEN protein [30]. The authors demonstrated that, in sensitive cells, trastuzumab causes a disruption of the binding of Src kinase to HER2, allowing PTEN to inhibit Akt, which results in the growth arrest. When PTEN levels are low, however, Akt remains active and trastuzumab efficacy is diminished. Nagy et al. observed that the expression of MUC4, a membrane-associated mucin which contributes to the masking of membrane proteins, was higher in the resistant clone (JIMT1) than in trastuzumab-sensitive lines [46]. Knockdown of MUC4 expression by RNA interference increased the binding of trastuzumab. The HER2/EGFR heterodimer may undergo antibody-induced internalization, ubiquitination, and proteolysis [47–50]. The internalization of HER2/EGFR represents a mechanism by which the HER2-specific antibodies disable the transforming activity of the receptor. Before concluding this summary presentation of the proposed mechanisms of trastuzumab-mediated resistance, a recent study highlighting the contribution of the transmembrane receptor Notch-1 has to be taken into account [51]. Notch receptors operate both as recipients of extracellular signals at the cell surface and as transcription factors, playing a critical role in lineage specification and thus acting to promote breast cancer. [52,53]. It is noteworthy that cells treated with trastuzumab, or a dual EGFR/HER2 TKI, exhibit increased Notch activities. Therefore, the inhibition of the Notch signaling pathway is expected to increase the inhibitory effect of HER2-targeted therapeutics [51].

Finally, recent data suggest that cancer stem cell (CSC) population can play a role in resistance to trastuzumab treatment [54]. CSCs, first demonstrated in acute myelogenous leukemia in 1994 by Dick and colleagues, are defined as a small population of cancer cells that are capable of giving rise to a new tumor [55–57]. CSCs exhibit characteristics of both stem cells and cancer cells, as they have the properties of self-renewal, asymmetric cell division, resistance to apoptosis, independent growth, tumorigenicity and metastatic potential. The CSC population is also defined by the expression of a specific set of markers, depending on the cancer of origin. In breast cancer, all cells have the $CD44^+/CD24^-$ phenotype and carry the genetic risk factors (BRCA1 and/or HER2) [58]. The interaction between CD44 and hyaluronic acid has been implicated in resistance to trastuzumab by masking the interaction of the antibody with the HER2 receptor on the cell surface [59]. The presence of a drug-resistant population that can regenerate a tumor after treatment could have serious consequences for therapy.

3. Recent advances in the use of trastuzumab in clinical therapy

Over the last few years adjuvant therapy of HER2 positive node-negative or node-positive breast cancer has evolved dramatically, as it predominantly consisted of trastuzumab (Herceptin®; Genentech) as single agent after multi-modality anthracycline-based therapy, or as a part of therapy including doxorubicin (Adriamycin®; Pfizer), cyclophosphamide (Cytoxan®; Bristol-Myers Squibb) and paclitaxel (Taxol®; Bristol-Myers Squibb) [15]. It is now widely accepted that treatment with trastuzumab will decrease the risk of disease recurrence by approximately 50%, when administered concurrently or sequentially with chemotherapy. However, the use of trastuzumab in metastatic breast cancer (MBC) patients is limited by cardiotoxicity, specifically in patients with prior anthracycline exposure or other risk factors for cardiomyopathy.

Taxanes are now considered among the most active agents in MBC when combined with trastuzumab [60]. Preclinical studies indicate synergistic interactions of trastuzumab with docetaxel, and additive interactions with paclitaxel. Results from clinical trials demonstrate that the response rates with docetaxel in combination with trastuzumab are higher than those with paclitaxel, although no clear cross-trial differences between other efficacy endpoints have emerged. However, taxanes–trastuzumab combinations have been shown to induce superior disease control. Correlative studies of taxanes, as well as recent formulations of paclitaxel bound to albumin NPs (Abraxane®; Abraxis Bioscience), in combination with trastuzumab, will inform clinical practice regarding the optimal agent, schedule, and the use of these highly effective regimens [60]. Results from at least two phase III trials indicated a higher response rate and a longer progression-free survival time when carboplatin was co-administered with paclitaxel–trastuzumab therapy.

To improve the efficacy of trastuzumab by-passing the mechanisms of resistance, novel effective combinations of targeted therapies with chemotherapy have recently been developed. Specific interest in the development of optimal targeted therapy is directed towards several studies with lapatinib, pertuzumab, rapamycin, modified anti-HER2 antibodies and neratinib.

Lapatinib is a protein kinase inhibitor, targeting both epidermal growth factor receptor (EGFR) and HER2. It binds the ATP-binding pocket of the EGFR/HER2 protein kinase domain, preventing self-phosphorylation and subsequent activation of the signaling mechanism [61]. The results from a phase III trial demonstrated that treatment with lapatinib (Tykerb®; Glaxo SmithKline) in combination with trastuzumab helps to extend the progression-free survival of women with HER2-positive MBC [62]. This randomized study was conducted on 296 heavily pre-treated HER2-positive MBC patients, who had demonstrated disease progression after trastuzumab treatment. The analysis on randomized patients who had received either lapatinib alone, or in combination with trastuzumab, demonstrated a significant improvement in median progression-free survival and a reduced risk of disease progression in the combination group [62].

Another innovative targeted agent, which belongs to the class of HER2-dimerization inhibitors (HDIs), is pertuzumab, a humanized monoclonal antibody. Pertuzumab is designed to bind the HER2 receptor and prevent the 'pairing' or dimerization of HER2 with other HER family receptors (HER1, HER2, HER3 and HER4) [63]. A recent study suggests that pertuzumab recognizes an extracellular portion of HER2 which is different from the binding site of trastuzumab, thus acting in different ways [64]. For this reason, pertuzumab may potentially keep different cancer types from growing. Preclinical studies demonstrate that the combination of trastuzumab and pertuzumab synergistically inhibits the survival of BT474 breast cancer cell lines and suggest that the complemen-

tary mechanisms of action of the two compounds may lead to increased efficacy [65]. Combination drug treatment was able to reduce the levels of total and phosphorylated erbB2 protein and block the receptor signaling through Akt, but not to affect MAPK. New data from a phase II trial showed that half of the patients with advanced HER2-positive MBC, whose disease had progressed during a trastuzumab-containing regimen, benefited from a combination of trastuzumab and pertuzumab [66].

The combination of pertuzumab with standard therapy (trastuzumab and chemotherapy) is being investigated in the phase III CLEOPATRA (Clinical Evaluation of Pertuzumab and Trastuzumab) study, which is currently recruiting patients in 18 countries worldwide. If this study gives positive results, this combination therapy will set a new potential standard of care in HER2-positive metastatic breast cancer.

Another antagonist of a mammalian mTOR target protein is rapamycin. mTOR is a serine–threonine kinase member of the cellular PI3K pathway that is implicated in transcriptional and translational control. When nutrients and growth factors activate mTOR, 40S ribosomal protein S6 kinase and the eukaryotic initiation factor 4E-binding protein-1 are phosphorylated and activated. These proteins control the progression of the cell cycle playing a key role in ribosomal biogenesis and cap-dependent translation. mTOR has a critical role in cell survival as the downstream mediator in the PI3K-Akt signaling pathway. In breast cancer membrane receptors, including the HER family, the IGF receptor and the estrogen receptor are activated by PI3K-Akt pathway [67]. Recent data suggests that Akt promotes breast cancer cell survival and induces resistance to chemotherapy, trastuzumab and tamoxifen. This evidence suggests that rapamycin may increase the therapeutic efficacy of trastuzumab-resistant breast cancer [68].

The modulation of the chemical structure of the antibody could be one of the most powerful approaches to improve efficacy in cancer antibody therapy. There is evidence suggesting that defucosylation of antibody oligosaccharides attached to Asn297 of the heavy chain significantly enhances antibody-dependent cellular cytotoxicity (ADCC) compared to the conventional antibody [69,70]. The commercial fucosylated trastuzumab and its defucosylated version were tested using PBMC (peripheral blood mononuclear cells) drawn from the volunteers as effectors cells and two breast cancer cell lines with different HER2 expression levels as target cells. ADCC was significantly enhanced with the fucose-negative antibody compared to the fucose-positive antibody. This preliminary study suggests that the use of fucose-negative antibodies may improve efficacy for treatment of HER2-positive breast cancer [71].

Another method of increasing the potency of antibody-directed therapy is the combination of specificity of the antigen-binding site with a wide variety of effectors, including toxins. Using this approach, the toxin DM-1 has been linked to HER2-targeted antibodies in ongoing preclinical studies. Preliminary results suggest that the antibody-combining site fused directly to the toxin exhibits strong selectivity for HER2 binding [72,73]. Based on these observations, recombinant toxins should be safely delivered to experimental animals at effective doses and may penetrate tumors more effectively than trastuzumab alone. However, the potential for immune response to the protein may represent a limitation for the use of toxin targeting antibodies therapy [74].

Neratinib (HKI-272) is a dual inhibitor of the tyrosine kinase receptors, erbB1 (EGFR) and erbB2 (HER2) [75]. In a phase II study, neratinib exhibited a potent activity against trastuzumab-resistant and trastuzumab-naive HER2-positive breast cancer. In particular, antitumor activity was observed in patients with breast cancer previously treated with trastuzumab, anthracyclines, and taxanes. The results demonstrated a significant improvement in median progression-free survival and a reduced risk of disease progression [76]. For this reason, a large worldwide randomized phase III study on the combination of trastuzumab with neratinib plus paclitaxel in chemonaive advanced HER2-positive breast cancer patients will start very soon in order to determine the efficacy of neratinib compared with standard treatment.

All of the therapies reviewed mainly inhibit the bulk growing tumor cells [56,77,78] but have no or little effect on cancer stem cells due to their quiescence and to their high expression of ABC transporters, which are capable of extruding commonly used drugs [79–81]. One approach to target CSCs is to inhibit signaling pathways that result to be especially important for this cell population. The importance of NF-κB and PTEN/mTOR/STAT3 pathways in breast cancer stem-like cells has been recently demonstrated [82,83]. Hence, such pathways could be inhibited to preferentially target breast cancer stem-like cells. Very recently, 8-quinolinol was evaluated and showed significant tumor growth inhibition and marked synergistic effects in combination with paclitaxel in tumor xenograft mouse models [84]. This compound was known to inhibit the NF-κB activation in RAW 264.7 cells [85], possibly inhibiting cell proliferation through the NF-κB pathway. The toxicity of 8-quinolinol is modest according to acute toxicity studies, however its use needs to be further validated in future clinical studies.

4. Nanoparticles under investigation for breast cancer

In recent years, nanobiotechnology has imposed itself as a powerful platform of nanotechnology that raises new opportunities in the diagnosis and treatment of different human cancers. Nanotechnology has been utilized in medicine for drug delivery and for the development of treatments in a variety of diseases. Within the context of this review, we sought to explore examples regarding various types of NPs, including quantum dots (QDs), magnetic NPs (MNPs) and gold NPs (GNPs), which have been conjugated with trastuzumab for the purpose of targeting HER2 receptors overexpressed in human breast carcinoma.

QDs exhibit extraordinary photostable fluorescent signals and resistance to photobleaching. These NPs consist of a typical core/shell structure composed of heavy metals [86–88]; in many cases, QDs include a cadmium selenide or cadmium sulfide core, coated with a zinc sulfide shell. It is possible to modulate their size or change the nature of their metal core in order to vary their emission area in the range 450–850 nm. They are generally synthesized in high-boiling non-polar organic solvents. Thus, to be solubilized in aqueous buffers, their hydrophobic surface ligands must be replaced with suitable amphipathic ligands.

Superparamagnetic iron oxide NPs useful for molecular imaging and thermal therapy are typically composed of magnetite (Fe_3O_4) or maghemite (γ-Fe_2O_3) nanocrystals; they have a spinel crystal structure with oxygen ions forming a close-packed cubic lattice and iron ions located at interstices. MNPs have potential applications in the biomedical field, including use as contrast agents for magnetic resonance imaging (MRI), for their ability to decrease T_2 relaxation time of water protons, drug delivery systems (DDS), magnetic bioseparations and magnetic force-based heating mediators for hyperthermia [89–93]. In recent years, several methods focusing on the synthesis of MNPs have been developed either in aqueous or organic phases [94,95]. Many surfactants or polymers are usually employed in the synthesis to avoid aggregation and, *in vivo*, to reduce phagocytosis by macrophages and to increase circulation time in blood vessels. Among the most largely used MNP coating materials, PEG (poly-ethylene glycol) is highly water soluble and biologically inert, which renders MNPs immunologically "stealth". However, the as-prepared MNPs are often of limited usefulness in targeted diagnosis and therapy. Hence, significant efforts

have focused on the possibility to functionalize their surface with ligands in order to create multifunctional NPs.

GNPs and gold nanorods (GNRs) are under exploration in biomedicine since gold has been approved for optical detection and thermal therapy of tumors. These NPs are rapidly synthesized and their surface can be easily functionalized with targeting molecules and ligands by thiol chemistry [96,97]. Many surfactants have been described in literature, including citric acid and PEG, which are able to maintain the post-synthetic colloidal stability in aqueous physiological solutions.

We have also included in this overview a class of composite inorganic NPs, in which the metal core (QD, MNP and/or GNP) is encapsulated in a silica shell of various sizes [98,99]. In magnetite-silica NPs [14,100,101], the external silica layer can decrease cytotoxic effects of the particles resulting from the direct exposure to heavy metals and prevents photobleaching if a fluorescent organic dye is encapsulated in the shell. Another advantage provided by silica resides in its facile functionalization with targeting biomolecules.

Eventually, various types of organic particles like liposomes and dendrimers should be mentioned, as these are already being used in cancer research and clinical treatment. Their functionalization could be performed by substantially exploiting a chemistry analogous to that used for inorganic NPs. For instance, liposomes are commonly used as drug delivery systems due to their ability to target cancer and to their capacity to fuse with the cell membrane, allowing for the cargo particle content to be released inside the target cell. Instead, dendrimers are branched molecules characterized by several functionalities on their molecular shell, thus generating a highly effective multivalent functional 3D surface.

4.1. Conventional strategies for the conjugation of trastuzumab to nanoparticles

The surface of NPs may be coated with different functionalities, depending on the coating material and the functional groups present on the targeting ligand. Most commonly, amines or carboxylic acids are present on the NP surface. For this reason, the most largely employed method to attach trastuzumab to NPs is the amide coupling involving carboxyl activation *via* the highly water soluble Sulfo-NHS ester. This method was adopted by Eghtedari et al., in which trastuzumab was covalently linked to the carboxyl groups of the so-called "nanothinks", which coated GNRs through Au–S soft-soft interaction [102]. Another example is reported by Wuang et al. [103], who applied this method to Fe_3O_4 nanospheres coated with a biocompatible polymer. An interesting two-step reaction is proposed by Chen et al. [104]: in the first step, succinimidyl propionyl PEG disulfide reacted with the primary amine of the antibody; while in the second step the PEG–antibody complex was bonded to a gold nanocage by breaking its internal disulfide bond and forming a Au–S linkage.

Trastuzumab modified with heterobifunctional linkers, such as *N*-succinimidyl-3-(2-pyridyldithio)propionate (SPDP), succinimidyl-4-(*N*-maleimidomethyl)cyclohexane-1-carboxylate (SMCC), and succinimidyl iodoacetate, could also be appended on the surface of sulfhydryl or amine-coated NPs in a simple way. These types of heterobifunctional cross-linkers are all commercially available and one of the primary advantages of using SPDP is that it can be exploited to directly determine the number of reactive amines on the particle, as pyridine-2-thione is released upon reaction with dithiothreitol, which can be detected spectrophotometrically and thus quantitated. Shukla et al. reported an example of this method for the conjugation of trastuzumab to organic dendrimers [105]. In several studies, Cheon's group reported how modified trastuzumab-SMCC could be loaded on free thiol groups present on the surface of dimercaptosuccinic acid (DMSA)-coated magnetic nanocrystals [106–109]. Hapca et al. used the same strategy with poly-lactic acid NPs: first, thiol groups were introduced on the surface of NPs by reaction with cysteamine, followed by reduction of disulfide with TCEP (tris(2-carboxyethyl)-phosphine hydrochloride); and then in a second step, trastuzumab conjugated with Sulfo-MBS (*m*-maleimidobenzoyl-*N*-hydroxy-sulfosuccinimide ester) as heterobifunctional cross-linker, was introduced by covalent coupling to thiolated NPs [110]. Alternatively, trastuzumab could be artificially thiolated with suitable agents, such as 2-iminothiolane, which was conjugated to free-amine groups of the antibody [111,112].

On the basis of a classical approach, trastuzumab was biotinylated and reacted with streptavidin-modified MNPs. These derivatized MNPs were able to generate strong T_2 MR contrast in HER2 expressing cells [113].

Yezhelyev et al. have recently developed an original method in which QDs were directly conjugated to the primary antibody by covalent bonds between thiol groups of "fragment" reduced antibody and amine-coated QDs, activated by Sulfo-SMCC linkers (Fig. 3) [114]. One of the main advantages of this technique is that a partial control on the orientation of QD-Ab conjugates versus the recognizing sites can be achieved. A further example using this method was reported by Yoon et al., who demonstrated that antibody reduction with 2-mercaptoethylamine may lead to cleavage of the disulfide bonds that hold the heavy chains together [115]. The authors stated that the disulfide bonds between heavy and light chains remained unaffected after treatment. The sulfhydryl groups produced by this reduction step were then coupled with smart magnetic silica coated core–shell NPs without inhibiting the activity of the antigen binding site.

Farokhzad and colleagues have conjugated HER2 affibody $Z_{HER:342}$ to NPs to increase the affinity minimizing the size of the nanoagent [116]. Affibody is a small protein (~15 kDa) with a high affinity for the receptor that mimics the active portion of the F_{ab} region of the corresponding antibody. Barat et al. proposed a strategy for the conjugation of small bivalent engineered anti-HER2 fragments, called cys-diabodies, on fluorescent QDs for cancer marker detection [117]. In this study, amino PEG (800 kDa) QDs were activated with a maleimido heterobifunctional cross-linker. Subsequently, maleimide-modified particles were covalently conjugated to sulfhydryl groups of reduced cys-diabodies, yielding target selective immuno-QDs.

5. Impact of nanoparticles on the imaging of breast cancer: present status and perspectives

In the diagnosis of breast cancer, modern imaging techniques have a relevant impact in both experimental and clinical contexts due to the high resolution, fast scan times, noninvasive nature and high-quality data. In recent years, several medical diagnostic techniques for the rapid detection of tumors have been explored, including fluorescence imaging [118,119], positron emission tomography (PET) and MRI [106,120]. Their extensive use in clinical investigations resulted in a remarkable improvement in the efficacy of therapeutic approaches. The detection of malignancies in their early stages is still a challenge, due to the difficulty in achieving concomitant high-enough sensitivity and resolution with the available diagnostic tools.

The combined use of conventional methods provides a robust multimodal framework for tumor detection, overcoming the limitations of each individual method. MRI has the advantage of providing exceptional anatomic information and depth of imaging, but its effectiveness is limited by limited spatial resolution and it requires a sensitivity enhancement, which may be provided

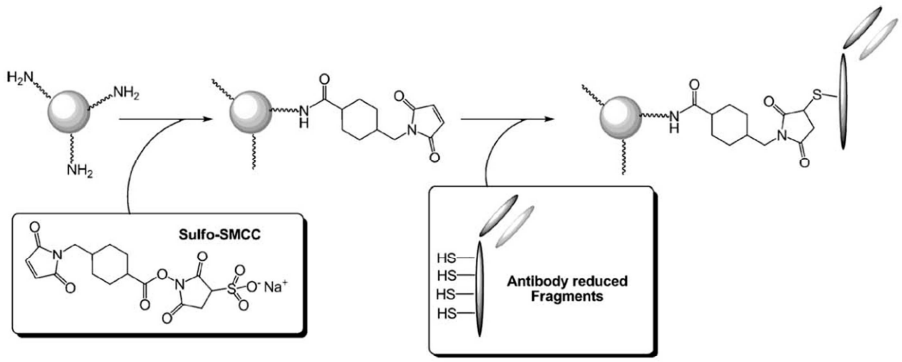

Fig. 3. Schematic conjugation of trastuzumab to QDs. Trastuzumab reduced fragments are coupled to the surface of amine nanoparticles. The mechanism describes the initial reaction of amino groups with SMCC; subsequently, sulfhydryl groups of antibody fragments react with QD linkers.

by paramagnetic contrast agents. Optical imaging yields excellent spatial resolution and is also inexpensive, trustworthy and portable, but it does not provide the penetration depth, field of view, or anatomic detail. PET scanning is a highly sensitive and noninvasive technique. However, it involves exposure to ionizing radiation; in addition, since PET isotopes are short-lived, the required radiopharmaceuticals have to be manipulated near to the scan facility.

Therefore, a primary goal in cancer diagnosis is the development of effective molecular contrast agents capable of unambiguously disclosing the presence of early-stage malignancies, tracking cell migration, and monitoring surgical and pharmacological response. Recently, NPs have been studied on a broad basis because of their specific cancer targeting and promising imaging outcomes.

Inorganic NPs functionalized with cancer-specific targeting ligands can be used to image tumors and detect peripheral metastases [106,107]. In MRI imaging of mammary carcinoma, most inorganic NPs share the same basic structure: a metal core made of superparamagnetic material (usually iron, cobalt and nickel oxides or a mixture of these components) used to improve the MRI sensitivity as contrast agents [121], with a protective organic coating on the surface, modified with different silica or gold polymers which are usually responsible for the biological recognition, for the improvement of the particle solubility and for evading the clearance by the host immune system (Fig. 4). This outside layer protects the core from degradation in a physiologically aggressive environment and can form electrostatic and/or covalent bonds with targeting biomolecules. The colloidal stability can be provided by steric repulsion of PEG, dextran or other biocompatible polymers adsorbed on the NP surface. The terminal functional groups of these polymers can be further adopted for bioconjugation [105]. Multifunctional nanoprobe structure is designed in order to fulfill the relevant requirements necessary for a detectable source of signal, including fluorescence, optical, magnetic, and electronic properties. Tuning the material properties in terms of size, shape and composition of inorganic nanocrystals is necessary to enhance MR efficiency [108]. The coupling of Au with Fe_3O_4 exhibits a synergistic magnetic effect resulting in a remarkably MR contrast with a strong relaxation rate increase [122].

The use of mesoporous core coated with thermosensitive polymers has been investigated as a suitable reservoir for the controlled pharmaceutical delivery system and for its potential to entrap hydrophilic guest molecules, including organic dyes, upon varying the temperature [123,124]. The co-delivery of chemotherapeutic drugs and targeting antibodies in the same system conferred significantly higher cellular uptake and enabled the simultaneous diagnosis and treatment, thus allowing for the monitoring of the response to the therapy using MRI [125,126].

MRI data should be confirmed and validated by alternative imaging techniques, for example, fluorescent imaging using near-IR dye-labeled fragment peptides conjugated to the NPs [127–129]. Furthermore, the surface-enhanced Raman scattering (SERS) technique, exploiting the inelastic light scattering of gold nanorods or hollow gold nanospheres, enlarges the spectrum of new applications available. Trastuzumab-conjugated gold nanosystems provide spectroscopic information and highly sensitive targeting and imaging of biomarkers expressed on the membrane of breast cancer cells [130,131]. Recently, several proteins/peptides have been investigated as alternative biomarkers for the selective targeting and detection of breast cancer; for example, the recombi-

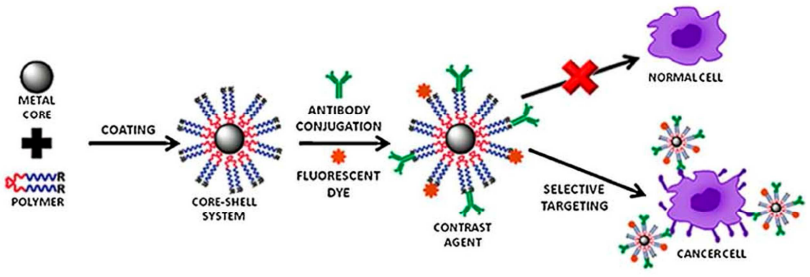

Fig. 4. Schematic development of composite contrast agent nanoprobes with inorganic core.

nant peptide containing the urokinase-type plasminogen activator (uPA) shows high affinity for the uPA receptor. This molecule is expressed by the proportion of the cancer cell relative to the tumor aggressiveness [128]. Peptides, such as EPPT and LHRH (luteinizing hormone releasing hormone), specifically recognize uMUC-1 and LH receptors respectively. These peptides collectively represent a class of tumor molecular biomarkers overexpressed by most types of breast cancer cells and their level of expression denotes a predictive parameter of the efficacy of chemotherapeutic response [131–134].

Alternative approaches, which do not include magnetic NPs, are essentially based on QDs formulation. QDs have several advantages for cancer imaging, including photostability and elevated resistance to photobleaching. Hence, the new generations of QDs show great promise for the study of intracellular processes at the single-molecule level, high-resolution cellular imaging, long-term *in vivo* observation of cell trafficking, tumor targeting, and cellular fate of labeled pharmaceuticals. However, their excessive toxicity due to the semiconductor component, limits the clinical application. The development of suitable surface coating for QDs is expected to provide a shield capable of decreasing their cytotoxicity. Alternatively, it has been proposed that it should be possible to focus their injurious effect on cancer cells through selective delivery [135].

Eventually, organic particles including polymer assemblies, liposomes and dendrimers act as multifunctional carriers and have already produced encouraging results because of their double therapeutic effect, both as drug delivery vehicles and as diagnostic tool [129,136,137].

In this vast scenario, a significant breakthrough is represented by the direct application of nanomaterial experimentation inside cancer tissues in animal models. The major concerns about *in vivo* use of NPs have been cellular toxicity, tendency to a rapid clearance after delivery in the circulatory system and intracellular labeling efficiency [106].

Lee and colleagues reported that the increase in MR sensitivity due to trastuzumab-conjugated magnetic NPs enabled the detection of a tumor mass as small as 50 mg, which is even smaller than that of recent studies from radiotracer imaging [107]. A further important issue of this study concerned biodistribution: iron concentration in blood increased after the injection of functionalized NPs into tumor-bearing nude mice and then slowly declined during the following 24 h. The iron level in some organ tissues, such as liver and spleen, showed a steady increase, while in different tissues, such as heart and lung, peaked and then gradually declined. In contrast, brain tissue was not affected [107].

Finally, new imaging probes were successfully synthesized and applied *in vivo* for both multimodal imaging and multicolor representation, providing semiquantitative information with excellent spatial resolution. This new method may find application in the sentinel node imaging of breast cancer [136,137].

To conclude, the current advances have demonstrated that the development of a new generation of composite nanosystems has the potential to bring us a step closer to the reliable and accurate detection of breast tumors at their early stages of growth, thus enabling us to monitor their invasion and metastasis and to assess their responses to therapy.

6. Targeted therapy approach

6.1. Delivery of chemotherapeutic drugs

Some classical paradigms of conventional medicine, concerning drug delivery systems, can be challenged by nanomedical platforms. Well-established drug delivery systems, for example, work on the basis of chemical gradients of drugs, that are non-specifically delivered throughout the body: this results in a number of undesired side effects to healthy cells. Only recently, targeted therapies, such as immunotherapies of cancers with monoclonal antibodies, have been able to reduce the undesired immune reactions enough to demonstrate the tremendous potential of these new "targeted therapies". The use of antibody-conjugated nanoplatforms holds the promise of a much greater localization of therapies to the diseased tissue or organ, while the introduction of significantly lower doses of drug into the body greatly reduces the possibility of side effects [138]. NPs applied as drug delivery systems are submicron-sized particles (3–200 nm), and are devices or systems that can be made using a variety of materials including polymers (polymeric NPs, micelles, or dendrimers), lipids (liposomes), viruses (viral NPs), carbon-based nanostructures (nanotubes) and even inorganic/organic, core/shell hybrid NPs [139]. In the last few years, some outstanding examples of multifunctional nanostructures for the targeted chemotherapy of breast cancer have appeared in the literature. In this paragraph, we will review the most significant studies which deal with trastuzumab conjugated NPs as drug-delivery agents for the potential therapy of HER2-positive breast cancer. The survey is focused on nanocomposites having at least one inorganic component: when the inorganic moiety of a nano-sized drug delivery system consists of a cluster of magnetic nanocrystals (Fe_3O_4 or $MnFe_2O_4$, for instance), the whole nanocomposite can become a so-called "theranostic" (both therapeutic and diagnostic) agent.

Yang et al. developed trastuzumab-conjugated magneto-polymeric nanohybrids incorporating the drug doxorubicin, a microbial-derived anthracycline acting as inhibitor of topoisomerase II and widely used in the treatment of breast carcinoma [140,141]. They synthesized monodispersed magnetic nanocrystals (by thermal decomposition of organometallic precursors) and embedded these inorganic clusters, together with doxorubicin, in an amphiphilic polymeric matrix. After the conjugation with trastuzumab, and with a human IgG as control, the targeting efficacy of trastuzumab-conjugated nanocomposites (HER-MMPNs) was investigated in fibroblast NIH3T6.7 cells, which highly express the HER2/neu cancer marker. MRI, confocal microscopy and flow cytometry demonstrated that HER-MMPNs successfully bind to NIH3T6.7 cells and are subsequently internalized by a receptor-mediated endocytosis process. Moreover, to assess the therapeutic potential for this combination of trastuzumab and doxorubicin, the degree of drug release and the inhibition of cell growth were investigated. The experimental data showed that HER-MMPNs were remarkably more cytotoxic than the conventional combination of doxorubicin and trastuzumab on NIH3T6.7 cells. To further confirm this therapeutic efficacy, the tumor growth rate of an animal model xenografted with NIH3T6.7 cells and treated with HER-MMPNs was also evaluated, demonstrating remarkable tumor growth inhibition. These results suggested that injected HER-MMPNs were target-specifically delivered to overexpressed HER2/neu receptors of NIH3T6.7 cells in the mouse model. Release of doxorubicin from the HER-MMPNs demonstrated exceptional therapeutic efficacy.

Paclitaxel was used by Sun et al. as a model anticancer drug to demonstrate the usefulness of a multifunctional nanoplatform for the targeted chemotherapy on SKBR3 breast cancer cells [142]. The authors developed a novel system based on paclitaxel-loaded poly(D,L-lactide-*co*-glycolide)/montmorillonite NPs (PLGA/MMT NPs), which were prepared by a modified solvent extraction/evaporation method and coated with trastuzumab exploiting the electrostatic attraction between the NPs and the antibody. Montmorillonite, a potent detoxifier, is a medical clay able to adsorb hydrogen ions and dietary, bacterial and metabolic toxins associated with gastrointestinal disturbance, a typical symptom of the side effects caused by anticancer drugs. The PLGA/MMT NPs thus represent a new concept in developing drug delivery systems, more specifically formulating the drug carrier from a component mate-

rial, which can have therapeutic effects to mediate the side effects of the encapsulated drug. The trastuzumab-decorated PLGA/MMT NPs can thus achieve diverse functions: to formulate anticancer drugs without the use of a harmful adjuvant; to reduce the side effects caused by the formulated anticancer drugs; to have synergistic therapeutic effects; and to achieve targeted chemotherapy for HER2-positive breast cancer. The authors demonstrated that the trastuzumab decoration significantly increased the cellular uptake by SKBR3 cells: based on IC50 values the therapeutic effects of the paclitaxel-loaded PLGA/MMT-HER NP formulation could be 13 times higher than Taxol®. The trastuzumab-decorated Pac-PLGA/MMT NPs have potential to be further confirmed by *in vivo* experiments, to be applied for targeted chemotherapy for HER2-positive cancer.

A different approach to anticancer drug delivery was recently adopted by Cheng et al. [143]. The authors focused their research on the delivery of cisplatin, a powerful therapeutic agent which acts against numerous solid tumors. Cisplatin acts by interacting with DNA to form intrastrand cross-link adducts and by interfering with cell transcription mechanisms. However, therapeutic applications of cisplatin have been restricted by its tendency to target both tumor and healthy cells, its chemical instability, its poor water solubility and its low lipophilicity. To overcome these drawbacks, the authors proposed a new approach to cisplatin storage and release using porous hollow NPs (PHNPs) of Fe_3O_4. PHNPs exhibited pores with a size of 2–4 nm, which facilitated the cisplatin diffusion into the cavity of the hollow structure. Cisplatin escape from the cavity through the same pores was a diffusion-controlled slow process with a $t_{1/2}$ of 16 h. The porous shell was stable in neutral or basic physiological conditions but, at low pH (<6) conditions, the pores were subject to acidic etching, resulting in wider pore gaps and faster release of cisplatin with a $t_{1/2}$ <4 h. PHNPs were conjugated with trastuzumab by means of a heterobifunctional PEG spacer, through dopamine-mediated grafting on the Fe_3O_4 surface, and a carboxyl moiety for the antibody covalent binding. Once coupled with trastuzumab to the surface, the bioconjugated cisplatin-loaded hollow NPs exhibited high targeting efficiency and a remarkable cytotoxicity against SKBR3 cells.

Xu et al. [144] reported on the preparation of mixed metal NPs (Au–Fe_3O_4 "dumbbell-like" NPs) able to act as target-specific nanocarriers to deliver platin into HER2-positive breast cancer cells with strong therapeutic effects. In this case, the drug to be delivered was not exactly cisplatin, but a different platin complex, bearing a thiol function for the attachment on the gold surface of the nanocomposite (Fig. 5).

The core structure of these NPs contained magnetic Fe_3O_4 NPs and optically active Au NPs. Compared with the conventional single-component iron oxide NPs, the dumbbell-like Au–Fe_3O_4 NPs showed two distinct advantages: (1) the presence of Fe_3O_4 and Au surfaces facilitates the stepwise attachment of an antibody and a platin complex, and (2) the structure can serve as both a magnetic and optical probe for tracking the platin complex in cells and biological systems. Also in this case, trastuzumab was chosen as targeting agent and it was linked to the magnetite moiety through a carboxyl-PEG.

6.2. Thermal therapies

The notion of "hyperthermia" (overheating) in the treatment of a large variety of diseases and dysfunctions is as old as medicine itself. Indeed, heat was referred to as a potential treatment for breast cancer more than 5000 years ago. Today, hyperthermia is a promising cancer therapy in its own right, alongside the well-established methods of surgery, chemotherapy and radiotherapy. Two kinds of heating treatments are currently distinguished: hyperthermia, performed between 41 and 46 °C to stimulate the immune response

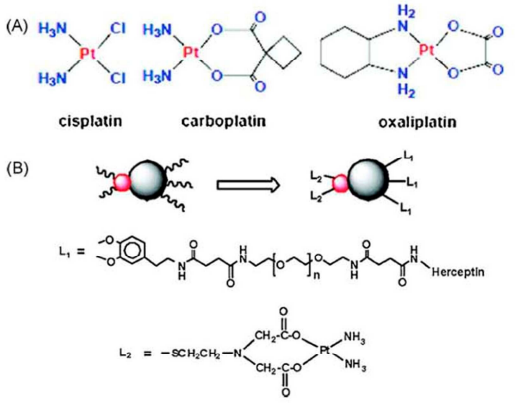

Fig. 5. (A) Platinum complexes used for therapies; (B) dumbbell-like Au–Fe_3O_4 NPs conjugated with trastuzumab (Herceptin) and a platin complex. Reproduced with permission from Ref. [144].

for non-specific immunotherapy of cancers, and thermoablation (46–56 °C) which leads to tumor destruction by direct cell necrosis, coagulation or carbonization. A fundamental drawback of this technique resides in the fact that it is impossible to heat solely a selected tumor region without negative consequences on other healthy tissues, and with reduced side effects, compared to traditional treatments. Unfortunately, the temperature at which tumor cell thermoablation occurs is too close to that of normal cells and therefore temperature control would be required. In this paragraph we will focus on the progress made towards the synthesis of breast cancer targeted nanosystems able to mediate hyperthermia: these are gold- and magnetic-based nanostructures.

The strong optical absorption of gold nanostructures can be exploited for photothermal therapy. In photothermal therapy, optical irradiation is absorbed and transformed into heat, inducing thermal denaturing of proteins inside the cell and coagulation of tissue, thus causing irreversible damage to the targeted tissue. Gold nanocages are a novel class of nanostructures, which can be prepared *via* a remarkably simple process based on the galvanic replacement reaction between Ag nanocubes and $HAuCl_4$. The Au nanocages have a tunable surface plasmon resonance peak that extends into the near-infrared region, where the optical attenuation caused by blood and soft tissue is essentially negligible. They are also biocompatible and present a well-established surface for easy functionalization [145]. When light interacts with Au nanocages, the incident photons are either scattered or absorbed. The absorbed photons are converted into phonons (vibrations of the lattice), causing an increase in temperature. Significantly, the rise of temperature can be enough to induce melting or surface reconstruction when the nanocages are placed in certain environments, such as air with poor thermal conductivity. In biological systems where water offers greater thermal conductivity, the Au nanocages should not melt but rather produce a local temperature rise that can provide a therapeutic effect on cancer cells that are selectively targeted by bioconjugated Au nanocages. Such photothermal therapy is less invasive than chemotherapy or surgery and holds strong promise as a new form of cancer treatment [146]. Chen et al. developed anti-HER2 conjugated gold nanocages for the targeted photothermal ablation of SKBR3 cancer cells [147]. These nanostructures have a size of about 45 nm in edge length and are precisely tailored to have a strong resonance absorption peak tunable in the NIR region. To be actively targeted to HER2-positive SKBR3 cells, the Au nanocages were conjugated with

trastuzumab. Using these novel nanobiocomposites, the authors demonstrated selective photothermal destruction of SKBR3 cells *in vitro*. These immuno gold nanocages showed a photothermal cell damage power density threshold about 20 times lower than that reported for gold nanoshells [148] and 6 times lower relative to gold nanorods [149]. In control experiments, cells without derivatization by immuno gold nanocages exhibited no observable loss of viability under the same experimental conditions. In a following study, Au et al. prepared similar anti-HER2 conjugated gold nanocages in order to perform quantitative studies on the targeting process and on the photothermal treatment *in vitro* [150]. First, the authors quantified the average number of Au nanocages attached per cell, by means of flow cytometry coupled with inductively coupled plasma mass spectroscopy (ICP-MS). This information should allow for the administration of immuno Au nanocages in proper dosages to induce a photothermal effect for tumors of known sizes. Then, the efficiency of the photothermal effect was evaluated *in vitro* with SKBR3 cells, by systematically varying parameters such as time of cellular response to laser irradiation, laser power density and time of laser exposure and quantifying the amount of cell death under each condition using flow cytometry coupled with propidium iodide staining. Finally, it should be pointed out that not only pure Au-based nanostructures have been employed as photothermal agents in breast cancer cells studies. Recently, Irudayaraj and co-workers synthesized multifunctional "nanopearl-necklaces" based on Au nanorods decorated with multiple Fe_3O_4 NPs and with trastuzumab, that can be used as theranostic platforms able to both image SKBR3 cells (by MRI and fluorescence) and kill them (by Au-mediated photothermal ablation) [122]. The authors prepared amine-functionalized Au rods with aspect ratio of ~3.6 using a seed-mediated surfactant-directed approach and stabilized them with a thiol-modified poly(ethylene glycol) to obtain monodispersed nanorods. Subsequently, the Au_{rod}–$(Fe_3O_4)_n$ nanocomposites were obtained through the conjugation of amino-Au_{rod} with carboxy-capped Fe_3O_4 NPs using EDC/NHS chemistry. Then, using the same chemical approach, trastuzumab was conjugated onto Fe_3O_4 NPs surface.

The multifunctional utility of these tumor targeting nanoprobes was successfully demonstrated by dual-mode imaging, single-NP intracellular dynamics monitoring, and photothermal ablation studies. The nanoprobes were shown to be magnetically and optically active (in the NIR region) and proved to be simultaneously useful for both magnetic/optical detection and targeted photothermal ablation of breast cancer SKBR3 cells.

As for Au nanostructures, magnetic NPs were introduced to exploit their unique properties, and in particular their capacity to generate heat under alternating magnetic fields, due to energy losses in the traversing of the magnetic hysteresis loop. In contrast to conventional hyperthermic techniques, which use a relatively low temperature (42 °C), leading to apoptosis, hyperthermia using magneto-nanosystems allowed the temperature to reach the target of 45 °C, without any substantial damage to the surrounding tissue. Moreover, the possibility to functionalize magnetic NPs provides the possibility of improving selectivity of MNPs uptake by cancer cells, applying hyperthermic therapy directly in cells instead of in whole tissue. In 2004, Ito et al. successfully developed a nanosystem based on magnetite cationic liposomes (MCLs), to induce selectively hyperthermia into cancer cells for the first time [151]. They actually constructed immunoliposomes, developing a HER2 antibody conjugated NPs as efficient tumor-targeting vehicles and investigated the achievability of using them for combined therapy. In fact the author proved that the combination of HER2 antibody and hyperthermia has an additive effect, even if further studies are still needed to elucidate the real mechanism of this combined effect. In this first contribution [152], they synthesized liposomes loaded with magnetic NPs while the antibody was immobilized after treatment with SPDP and subsequent reduction with 1-dithiothreitol (Fig. 6).

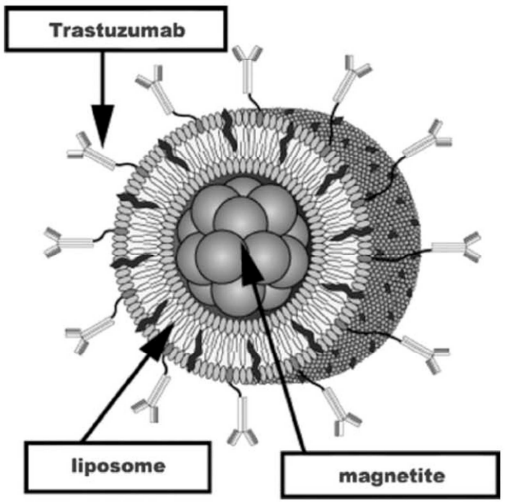

Fig. 6. Scheme of trastuzumab-functionalized liposome containing magnetite NPs. Reproduced with permission from Ref. [154].

The results obtained in *in vitro* tests on SKBR3 cells, showed that HER2 antibody retained its antiproliferative activity, even when conjugated onto nanosystems and hyperthermia resulted in a strong cytotoxic effects on the same cancer cells line, as a result of the efficient incorporation of the magneto-liposomes inside the cells. Very recently, Kikumori et al. published a remarkable work, reporting results using the same magneto-liposomes in *in vivo* models [153]. The magneto-nanosystems were tested on subcutaneous cancer nodules of BT474 (high HER2 expression) and SKOV3 (low HER2 expression) in nude mice. The results showed that the NPs only accumulated in BT474 tumors, confirming the efficiency of targeted NPs, while the hyperthermic treatments resulted in a regression of tumor, sustained for 10 weeks after two actions. Another example of targeted nanosystems used for hyperthermic treatment comes from a contribution by Hilger et al. [154]. The authors synthesized magnetic NPs, covered by a shell of dextran which was conjugated with HER2 antibody using *N*-(3-dimethylaminopropyl)-*N'*-ethyl-carbodiimid-hydrochloride. The NPs were used to treat SKBR3 cells and the authors demonstrated how the nanosystems were localized at the cell surface as well as in granules inside cytoplasm. First *in vitro* results on the possibility of using dextran-magnetic NPs in hypethermia treatment were also presented.

6.3. Gene therapy

Gene therapy, an innovative approach in the therapeutic treatment of breast cancer, involves different strategies, including: (a) transfer of tumor-suppressor genes, (b) suppression of oncogenes, (c) enhancement of immunological response, (d) transfer of suicide genes, and (e) bone-marrow protection by use of drug-resistance genes [155]. Nevertheless, the development of a clinical and routinely application of gene-therapy protocol have been hampered by the fact that oligonucleotide-containing substances undergo rapid enzymatic degradation in human plasma. Therefore, the identification of the best delivery vehicle, which is able to successfully reach the nucleus of the target cells, is still a challenge. Accordingly,

the carrier should be able to condense DNA or RNA from a large micrometer scale to a smaller nanometer scale suitable for endocytosis and to promote the escape of the gene from the endosomal compartment into the cytosol. Furthermore the vector should be designed and synthesized to be recognized by specific receptors on the target cells and then, easily, internalized. Following these concepts, NP-based DNA and RNA have been envisaged as advantageous delivery systems, using either viral or nonviral vectors for the gene transfection. Several contributions in recent years reported very interesting results on therapeutic treatment of tumors, based on nano-delivered gene therapy [156–158]. However, the delivery systems developed up to now have the disadvantage of poor pharmacokinetic characteristics, with the majority of samples typically accumulating in the first-pass organs, high inflammatory toxicity and hepatotoxicity which may limit their utility *in vivo*. In this paragraph, we will focus our attention on the contributions which used anti-HER2 antibody as targeting molecules to deliver *via* nonviral vectors therapeutic genes.

In 2006, Hayes and co-workers published their preliminary results on using a DNA plasmid coupled with cationic lipids, to form lipid-nucleic acid-NPs, called Genopsheres [159,160]. Genospheres were formed in an aqueous/organic liquid monophase, which promoted favorable interactions between DNA and cationic lipids, giving rise to NPs small in size (80–110 nm) and able to effectively protect the entrapped DNA in the presence of human plasma. The method of preparation for the NPs was interesting, using modulable pH-titrable lipids, obtaining genospheres with a positive surface charge which would decrease at neutral pH but increase upon acidification typical for endosomes. To increase the delivery of the nanosystem into the cells of interest, genospheres were immunotargeted to selectively transfect HER2 overexpressing cells, by insertion of an anti-HER2 human single-chain monoclonal antibody (scFv)-PEG conjugate. The highly internalizable anti-HER2 scFv fragment (F5) was attached to the surface of Genospheres by coincubation with the F5-lipopolymer conjugate (F5-PEG-N-[ω-methoxy-(poly(oxyethylene)-α-oxycarbonyl)] (DSPE)), which was synthesized by conjugation to the maleimide-activated PEG terminus of the PEG-DSPE lipid anchor through an engineered C-terminal cysteine [159]. The authors were able to characterize qualitatively (by fluorescence microscopy) and quantitatively (by cytofluorometry) the effect of PEGylation, charge and anti-HER2 antibody targeting on the degree of Genosphere association with HER2-overexpressing cells (SKBR3). The transfection activity of anti-HER2 immuno-Genospheres, as well as of non-targeted Genospheres in SKBR3 cells were measured *via* luciferase assay. The results obtained by the authors demonstrated that HER2-directed targeting of Genospheres increased the level of reporter gene expression in absolute terms, and decreased the dependence of transfection efficiency on the particle charge and the degree of particle surface coating. These kinds of nanosystems resulted an attractive methodology for future *in vivo* applications.

Another attractive approach to probe gene function in mammalian cells is gene silencing, using small interfering RNA (siRNA). This kind of inhibition of breast-cancer oncogenes is known to result in induction of apoptosis and in an increase of chemotherapy sensitivity in breast-cancer cells. Some of the most used nonviral methods include the use of lipid-based vectors such as liposomes, peptides, cationic polymers and NPs (NPs). Although there have been some successes in the delivery of siRNA using various methods, one of the major drawbacks resides in the difficulties in tracking their delivery and monitoring their transfection efficiency. In this field, Tan et al. developed a very interesting nanosystem to deliver HER2 siRNA to HER2-overexpressing SKBR3 cells [161]. The authors were able to encapsulate quantum dots (QDs) into chitosan NPs, whose surface was labeled with anti-HER2 antibody, targeting the HER2 receptors on SKBR3 cells. The conjugation of HER2 siRNA onto the surface of the chitosan NPs was instead achieved by simple adsorption by incubation. QDs were chosen for their unique optical and electronic properties to track and monitor the efficiency of siRNA delivery, especially if long-term tracking is required. The chitosan surface modification with anti-HER2 (achieved using EDC/NHS chemistry) antibody gave the authors the possibility to obtain a very specifically targeted system. Such a nano-construct was readily internalized into the breast cancer cells, while the gene-silencing effects were established using the luciferase and HER2 ELISA assays.

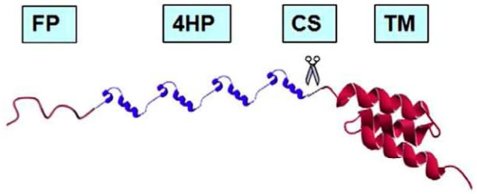

Fig. 7. Schematic illustration of a DBV. FP: fusogenic peptide; 4HP: four tandem repeating unit of histone H2A (SWISS-MODEL program prediction); CS: cathepsin D substrate; TM: HER2 targeting motif (SWISS-MODEL program prediction). Reproduced with permission from Ref. [164].

One of the most interesting key regulators for mitosis in mammalian cells are polo-like kinases (Plks), which represent highly conserved serine/threonine kinases. Plks play a crucial role in the check point of the cell cycle. Consequently, the inhibition of Plks, which can be caused by using antisense oligonucleotides (ASOs), siRNA or dominant-negative mutants, leads to a mitotic catastrophe, increased apoptosis and then tumor inhibition. Recently, novel results have been published on the use of antisense oligonucleotides to downregulate Plk1 expression [162]. In fact, it is known that ASOs are able to prevent the development of specific mammalian cancers, if well targeted to relevant signal transduction pathways. Problems related to the use of ASOs in clinical protocols are due to the fact that they have shown side effects and toxicities in their relevant doses, necessary for *in vivo* assays. For these reasons, the authors, pressed by the necessity to develop smart targeted delivery systems, designed and synthesized NPs based on human serum albumine (HSA), loaded with ASOs active against Plk1. To render such nanosystems specifically targeted to HER2-overexpressing cells, the NPs were coupled with trastuzumab. The antibody was thiolated with an excess of 2-iminothiolane and reacted with the maleimido group of the cross-linker NHS-PEG5000-Mal, while the succinimidyl group reacted with the amino groups of the particle surface of HSA [163].

The authors performed RT-PCR assay, quantitative real time PCR and Western blot analysis to determine the Plk1 mRNA and protein expression. They concluded that their efficient targeted delivery made up of HSA-ASO-trastuzumab NPs showed a significant reduction of Plk1 expression *in vitro* and apoptosis after treatment of breast cancer cells for the first time.

Recently a new technology has been developed to genetically engineer and express highly cationic biopolymers with tandem repeating units in *E. coli* expression systems. Following this technology, Wang et al. designed and synthesized a complex nonviral gene delivery system, namely Designer Biomimetic Vectors (DBVs) [164]. Such a structure was developed to specifically target cancer cells, mimic viral characteristic to break through intracellular barriers, and mediate efficient gene transfer, and was made of four precise locations (Fig. 7).

First, a fusogenic peptide (FP) named GALA, which is a synthetic pore-forming peptide, was designed to assist in escape of the cargo into cytosol. The second portion was a four tandem repeating units of N-terminal domain of histone H2A peptide (4HP), able to con-

Table 1
Performed *in vivo* trials of trastuzumab-conjugated nanoparticles.

In vivo trial	Living organism	Type of nanocomposite	Ref.
MRI	Humans	Lymphotropic superparamagnetic nanoparticles	[89]
MRI	Nude mice implanted with NIH3T6.7 cells displaying HER2/neu cancer markers	Water-soluble magnetic iron oxide-antibody conjugates	[106]
MRI	Nude mice implanted with NIH3T6.7 cell lines	MnMEIO–Herceptin conjugates	[107]
MRI	Mice bearing breast tumor allograft	Herceptin–dextran iron oxide nanoparticles	[120]
MR and fluorescence imaging	Nude mice	Core–shell magnetic nanoparticles	[85]
MR and NIR fluorescence imaging	Mice bearing mammary tumors	Amino-terminal fragment of uPA-conjugated iron oxide nanoparticles	[128]
MRI and drug delivery	Nude mice implanted with NIH3T6.7 cell lines	Magneto-polymeric nanohybrids loaded with doxorubicin	[141]
In vivo binding fluorescence	SCID mice	Dendrimer conjugated anti-HER2	[105]
NIR fluorescence imaging	Nude mice implanted with subcutaneous human breast adenocarcinoma cells	Indocyanine green-calcium phosphate nanoparticles	[137]
Radionuclide and NIR fluorescence imaging	Nude mice	^{111}In-labeled radionuclide/five-color NIR optical dualmodal imaging probes	[136]
Heating in an alternating magnetic field (hyperthermia)	Nude mice implanted with BT474 and SKOV3 cells	Immunoliposomes containing magnetite nanoparticles	[153]

dense pDNA into stable NPs in the presence of serum and broad pH range. The third sequence was a cathepsin D substrate (CS) which linked a synthetic single chain 57 amino acid affibody with high affinity towards HER2 (TM), which was introduced to significantly enhance the internalization of NPs into target cells. The positioning of a cathepsin D cleavage sited in between 4HP and TM allowed for dissociation of the targeting motif from the vector inside the endosomes where cathepsin D is abundant. The author, overcoming one of the drawbacks of DVB's approach, demonstrated that the multidomain chimeric architecture was able to retain the component's individual functionality. They showed that their complex vector was able to be specifically targeted into breast cell lines and easily internalized, resulting in significant gene expression.

7. Concerns on nanoparticle toxicity

As the nanotherapeutics field is rapidly growing, toxicity evaluation of nanoparticles becomes increasingly fundamental for NP-based antitumor treatments in medicinal clinical technology. For example, GNPs are generally considered relatively safe because gold has been demonstrated to be a biocompatible metal in many cases. In contrast, other kinds of NPs, including MNPs and QDs, which contain iron or hard metals, respectively, need to be carefully evaluated for potential toxicity, although several modified nanoscale iron oxides have been recently introduced in the clinical practice for diagnostic purposes. Due to their great potential for diagnostics, numerous studies have been performed to investigate the toxic effects of QDs in cell cultures and animals. The collected data allowed the investigators to suggest various mechanisms of toxicity of QDs. Cytotoxicity could be produced through photooxidation of cadmium telluride core (CdTe), triggering electron transfer from excited QDs to O_2 inside cells, resulting in the formation of the toxic superoxide ion ($O_2^{\bullet -}$). Moreover, released Cd^{2+} may bind sulfhydryl groups on a variety of intracellular proteins, causing decreased functionality in many subcellular organelles [165]. To confirm such hypothesis, Derfus et al. have exposed the surface of CdSe QDs to air or UV irradiation [166], facilitating oxidative release of cadmium ions: under these conditions, they observed that QDs were highly toxic. With the aim of decreasing the dangerous impact of these processes, a ZnS shell is usually introduced, thus rendering the hard metal core less susceptible to oxidative degradation and less toxic to primary cytoplasmatic organelles [165,167]. All these considerations strongly support the potential role of cadmium in QDs cytotoxicity. The toxicity of QDs is also strictly correlated with the stability of the colloidal dispersion and the surface coatings of these nanoparticles. QDs synthesized in aqueous solution are protected only by weakly bound ligands, such as small thiolate ligands (e.g., mercaptopropionic acid or mercaptoacetic acid). For this reason, they are highly prone to degradation and aggregation, associated with their cytotoxicity toward cells in culture [168,169]. Alternative to the synthesis of QDs in nonpolar solvents, followed by water-phase transfer *via* encapsulation in amphiphilic polymers, the fabrication of cross-linked silica led to significantly improved nanoparticle dispersions in terms of optical, chemical and colloidal stability, compared to their counterparts coated with small ligands [170].

Table 1 summarizes a few literature data pertinent to *in vivo* trials of different types of NPs related to preclinical investigations on HER2-overexpressing tumor cells. The above considerations make clear to the reader that careful controls will be needed before trastuzumab-conjugated NPs can be used in current medical procedures.

8. Outlook

With the aim of creating highly efficient and reliable systems able to provide both accurate diagnosis and effective therapy of breast cancer disease, novel hybrid nanostructures displaying trastuzumab or its analogues are being developed intensely. Thanks to the biochemical characteristics and the mechanisms of action of trastuzumab, this monoclonal antibody results as being an ideal targeting agent on which the attempts to develop modern and efficient technologies for specific recognition are focused. The goal of this approach is to obtain targeted multimodal NPs capable of being vectors of therapy and a source of signals for diagnosis and monitoring of endogenous response at the same time. The combination of individually FDA-approved molecular entities and non-toxic nanomaterials leads to nanovectors ideally ready for *in vivo* testing. If the ongoing trials on the first generation of hybrid nanoparticles based on trastuzumab conjugates demonstrate success, some of these systems may become a good candidate to be developed as theranostic nanoclinics, since the diagnostic technique mainly required for their use (MRI) is already a frequently used medical tool for standardized clinical protocols.

ARTICLE 1

Acknowledgments

This work was supported by "Fondazione Romeo ed Enrica Invernizzi" and the CNR-Regione Lombardia "Mind in Italy" project. We thank Stefano Negri for expert graphical assistance.

References

[1] Parker SL, Tong TA, Bolden S, Wingo PA. Cancer statistics. CA Cancer J Clin 1996;46:5–27 [CA Cancer J Clin 1996;46:3–4].
[2] Veronesi U, Paganelli G, Galimberti V, Viale G, Zurrida S, Bedoni M, et al. Sentinel-node biopsy to avoid axillary dissection in breast cancer with clinically negative lymph-nodes. Lancet 1997;349:1864–7.
[3] Batist G, Ramakrishman G, Rao RS, Chandrasekharan A, Gutheil J, Guthrie T, et al. In vivo cancer targeting and imaging with semiconductor quantum dots. J Clin Oncol 2001;19:1444–54.
[4] Gao X, Cui Y, Levenson RM, Chung LWK, Nie S. Reduced cardiotoxicity and preserved antitumor efficacy of liposome-encapsulated doxorubicin and cyclophosphamide compared with conventional doxorubicin and cyclophosphamide in a randomized, multicenter trial of metastatic breast cancer. Nat Biotechnol 2004;22:969–76.
[5] Gradishar WJ, Tjulandin S, Davidson N, Shaw H, Desai N, Bhar P, et al. Phase III trial of nanoparticle albumin-bound paclitaxel compared with polyethylated castor oil-based paclitaxel in women with breast cancer. J Clin Oncol 2005;23:7794–803.
[6] Park WJ. Liposome-based drug delivery in breast cancer treatment. Breast Cancer Res 2002;4:95–9.
[7] Lee CC, MacKay JA, Frechet JM, Szoka FC. Designing dendrimers for biological applications. Nat Biotechnol 2005;23:1517–26.
[8] Tasis D, Tagmatarchis N, Bianco A, Prato M. Chemistry of carbon nanotubes. Chem Rev 2006;106:1105–36.
[9] Duncan R. The dawning era of polymer therapeutics. Nat Rev Drug Discov 2003;2:347–60.
[10] Yezhelyev MV, Gao X, Xing Y, Al-Hajj A, Nie S, O'Regan RM. Emerging use of nanoparticles in diagnosis and treatment of breast cancer. Lancet Oncol 2006;7:657–67.
[11] Jain K. Personalised medicine for cancer: from drug development into clinical practice. Expert Opin Pharmacother 2005;6:1463–76.
[12] (a) Ferrari M. Nanogeometry: beyond drug delivery. Nat Nanotech 2008;3:131–2;
(b) Jiang W, KimBetty YS, Rutka JT, Chan WCW. Nanoparticle-mediated cellular response is size-dependent. Nat Nanotech 2008;3:145–50;
(c) Tasciotti E, Liu X, Bhavane R, Plant K, Leonard AD, Price BK, et al. Mesoporous silicon particles as a multistage delivery system for imaging and therapeutic applications. Nat Nanotech 2008;3:151–7.
[13] Gratton SEA, Ropp PA, Pohlhaus PD, Luft JC, Madden VJ, Napier ME, et al. The effect of particle design on cellular internalization pathways. Proc Natl Acad Sci USA 2008;105:11613–8.
[14] Corsi F, De Palma C, Colombo M, Allevi R, Nebuloni M, Ronchi S, et al. Towards ideal magnetofluorescent nanoparticles for bimodal detection of breast-cancer cells. Small 2009;5:2555–64.
[15] Slamon DJ, Godolphin W, Jones LA, Holt JA, Wong SG, Keith DE, et al. Studies of the HER-2/neu protooncogene in human breast and ovarian cancer. Science 1989;244:707–12.
[16] Olayioye MA, Neve RM, Lane HA, Hynes NE. The ErbB signaling network: receptor heterodimerization in development and cancer. EMBO J 2000;19:3159–67.
[17] Ferguson KM, Berger MB, Mendrola JM, Cho HS, Leahy DJ, Lemmon MA. EGF activates its receptor by removing interactions that autoinhibit ectodomain dimerization. Mol Cell 2003;11:507–17.
[18] Ogiso H, Ishitani R, Nureki O, Fukai S, Yamanaka M, Kim JH, et al. Crystal structure of the complex of human epidermal growth factor and receptor extracellular domains. Cell 2002;110:775–87.
[19] Hynes NE, Lane HA. ERBB receptors and cancer: the complexity of targeted inhibitors. Nat Rev Cancer 2005;5:341–54.
[20] Burgess AW, Cho HS, Eigenbrot C, Ferguson KM, Garrett TPJ, Leahy DJ, et al. An open-and-shut case? Recent insights into the activation of EGF/ErbB receptors. Mol Cell 2003;12:541–52.
[21] Garrett TP, McKern NM, Lou M, Elleman TC, Adams TE, Lovrecz GO, et al. The crystal structure of truncated ErbB2 ectodomain reveals an active conformation, poised to interact with other ErbB receptors. Mol Cell 2003;11:495–505.
[22] Citri A, Yarden Y. EGF-ERBB signalling: towards the system level. Nat Rev Mol Cell Biol 2006;7:505–16.
[23] Sharma SV, Settleman J. ErbBs in lung cancer. Exp Cell Res 2009;315:557–71.
[24] Wieduwilt MJ, Moasser MM. The epidermal growth factor receptor family: biology driving targeted therapeutics. Cell Mol Life Sci 2008;65:1566–84.
[25] Amit I, Wides R, Yarden Y. Evolvable signalling networks of receptor tyrosine kinase: relevance of robustness to malignancy and to cancer therapy. Mol Syst Biol 2007;3:151.
[26] Cantley LC. The phosphoinositide 3-kinase pathway. Science 2002;296:1655–7.
[27] Engelman JA, Luo J, Cantley LC. The evolution of phosphatidylinositol 3-kinases as regulators of growth and metabolism. Nat Rev Genet 2006;7:606–19.
[28] Vivanco I, Sawyers CL. The phosphatidylinositol 3-kinase–AKT pathway in human cancer. Nat Rev Cancer 2002;2:489–501.
[29] Yuan TL, Cantley LC. PI3K pathway alterations in cancer: variations on a theme. Oncogene 2008;27:5497–510.
[30] Nagata Y, Lan KH, Zhou X, Esteva LJ, Sahin AA, Klos KS, et al. PTEN activation contributes to tumor inhibition by trastuzumab, and loss of PTEN predicts trastuzumab resistance in patients. Cancer Cell 2004;6:117–27.
[31] Faltus T, Yuan J, Zimmer B, Kramer A, Loibl S, Kaufmann M, et al. Silencing of the HER2/neu gene by siRNA inhibits proliferation and induces apoptosis in HER2/neu-overexpressing breast cancer cells. Neoplasia 2004;6:786–95.
[32] Clifford A, Hudis MD. Trastuzumab—mechanism of action and use in clinical practice. N Engl J Med 2007;357:39–51.
[33] Cooley S, Burns LJ, Repka T, Miller JS. Natural killer cell cytotoxicity of breast cancer targets is enhanced by two distinct mechanisms of antibody-dependent cellular cytotoxicity against LFA-3 and HER2/neu. Exp Hematol 1999;27:1533–41.
[34] Lewis GD, Figari I, Fendly B, Wong WL, Carter P, Gorman C, et al. Differential responses of human tumor cell lines to anti-p185HER2 monoclonal antibodies. Cancer Immunol Immunother 1993;37:255–63.
[35] Christianson TA, Doherty JK, Lin YJ, Ramsey EE, Holmes R, Keenan EJ, et al. NH_2-terminally truncated HER-2/neu protein: relationship with shedding of the extracellular domain and with prognostic factors in breast cancer. Cancer Res 1998;58:5123–9.
[36] Molina MA, Codony-Servat J, Albanell J, Rojo F, Arribas J, Baselga J. Trastuzumab (herceptin), a humanized anti-Her2 receptor monoclonal antibody, inhibits basal and activated Her2 ectodomain cleavage in breast cancer cells. Cancer Res 2001;61:4744–9.
[37] Sarup JC, Johnson RM, King KL, Fendly BM, Lipari MT, Napier MA, et al. Characterization of an anti-p185HER2 monoclonal antibody that stimulates receptor function and inhibits tumor cell growth. Growth Regul 1991;1:72–82.
[38] Valabrega G, Montemurro F, Sarotto I, Petrelli A, Rubini P, Tacchetti C, et al. TGFα expression impairs trastuzumab-induced HER2 downregulation. Oncogene 2005;24:3002–10.
[39] Austin CD, De Maziere AM, Pisacane PI, van Dijk SM, Eigenbrot C, Sliwkowski MX, et al. Endocytosis and sorting of ErbB2 and the site of action of cancer therapeutics trastuzumab and geldanamycin. Mol Biol Cell 2004;15:5268–82.
[40] Delord JP, Allal C, Canal M, Mery E, Rochaix P, Hennebelle I, et al. Selective inhibition of HER2 inhibits AKT signal transduction and prolongs disease-free survival in a micrometastasis model of ovarian carcinoma. Ann Oncol 2005;16:1889–97.
[41] Lane HA, Motoyama AB, Beuvink I, Hynes NE. Modulation of p27/Cdk2 complex formation through 4D5-mediated inhibition of HER2 receptor signaling. Ann Oncol 2001;12:S21–2.
[42] Zhang H, Drebin J, Murali R, Greene MI. ErbB receptors: from oncogenes to targeted cancer therapies. J Clin Invest 2006;117:2051–8.
[43] Wang SE, Narasanna A, Perez-Torres M, Xiang B, Wu FY, Yang S, et al. HER2 kinase domain mutation results in constitutive phosphorylation and activation of HER2 and EGFR and resistance to EGFR tyrosine kinase inhibitors. Cancer Cell 2006;10:25–38.
[44] Diermeier S, Horvath G, Knuechel-Clarke R, Hofstaedter F, Szollosi J, Brockhoff G. Epidermal growth factor receptor coexpression modulates susceptibility to Herceptin in HER2/neu overexpressing breast cancer cells via specific erbB-receptor interaction and activation. Exp Cell Res 2005;304:604–19.
[45] Nahta R, Yuan LX, Zhang B, Kobayashi R, Esteva FJ. Insulin-like growth factor-I receptor/human epidermal growth factor receptor 2 heterodimerization contributes to trastuzumab resistance of breast cancer cells. Cancer Res 2005;65:11118–28.
[46] Nagy P, Friedlander E, Tanner M, Kapanen AI, Carraway KL, Isola J, et al. Decreased accessibility and lack of activation of ErbB2 in JIMT-1, a herceptin-resistant, MUC4-expressing breast cancer cell line. Cancer Res 2005;65:473–82.
[47] Gilboa L, Ben-Levy R, Yarden Y. Roles for a cytoplasmic tyrosine and tyrosine kinase activity in the interactions of Neu receptors with coated pits. J Biol Chem 1995;270:7061–7.
[48] Maier LA, Xu FJ, Hester S, Boyer CM, McKenzie S, Bruskin AM, et al. Requirements for the internalization of a murine monoclonal antibody directed against the HER-2/neu gene product c-erbB-2. Cancer Res 1991;51:5361–9.
[49] Qian X, O'Rourke DM, Drebin J, Zhao H, Wang Q, Greene MI. Identification of p185neu sequences required for monoclonal antibody- or ligand-mediated receptor signal attenuation. DNA Cell Biol 1997;16:1395–405.
[50] Srinivas U, Tagliabue E, Campiglio M, Menard S, Colnaghi MI. Antibody-induced activation of p185HER2 in the human lung adenocarcinoma cell line Calu-3 requires bivalency. Cancer Immunol Immunother 1993;36:397–402.
[51] Osipo C, Patel P, Rizzo P, Clementz AG, Hao L, Golde TE, et al. ErbB-2 inhibition activates Notch-1 and sensitizes breast cancer cells to a gamma-secretase inhibitor. Oncogene 2008;27:5019–32.
[52] Dievart A, Beaulieu N, Jolicoeur P. Involvement of Notch1 in the development of mouse mammary tumors. Oncogene 1999;18:5973–81.
[53] Politi K, Feirt N, Kitajewski J. Notch in mammary gland development and breast cancer. Semin Cancer Biol 2004;14:341–7.
[54] Bedard PL, Cardoso F, Piccart-Gebhart MJ. Stemming resistance to HER-2 targeted therapy. J Mammary Gland Biol Neoplasia 2009;14:55–66.
[55] Bonnet D, Dick JE. Human acute myeloid leukemia is organized as a hierarchy that originates from a primitive hematopoietic cell. Nat Med 1997;3:730–7.

[56] Behbod F, Rosen JM. Will cancer stem cells provide new therapeutic targets? Carcinogenesis 2004;26:703–11.
[57] Lapidot T, Sirard C, Vormoor J, Murdoch B, Hoang T, Caceres-Cortes J, et al. A cell initiating human acute myeloid leukaemia after transplantation into SCID mice. Nature 1994;367:645–8.
[58] Xiao Y, Ye Y, Yearsley K, Jones S, Barsky SH. The lymphovascular embolus of inflammatory breast cancer expresses a stem cell-like phenotype. Am J Pathol 2008;173:561–74.
[59] Palyi-Krekk Z, Barok M, Isola J, Tammi M, Szollosi J, Nagy P. Hyaluronan-induced masking of ErbB2 and CD44-enhanced trastuzumab internalisation in trastuzumab resistant breast cancer. Eur J Cancer 2007;43:2423–33.
[60] Bullock K, Blackwell K. Clinical efficacy of taxane-trastuzumab combination regimens for HER-2-positive metastatic breast cancer. Oncologist 2008;13:515–25.
[61] Spector NL, Xia W, Burris III H. Study of the biologic effects of lapatinib, a reversible inhibitor of ErbB1 and ErbB2 tyrosine kinases, on tumor growth and survival pathways in patients with advanced malignancies. J Clin Oncol 2005;23:2502–12.
[62] O'Shaugnessy JK, Blackwell L, Burstein H, Storniolo AM, Sledge G, Baselga J, et al. A randomized study of lapatinib alone or in combination with trastuzumab in heavily pretreated HER2+ metastatic breast cancer progressing on trastuzumab therapy. J Clin Oncol 2008;26(Suppl.):1015.
[63] Agus DB, Akita RW, Fox WD, Lewis GD, Higgins B, Pisacane PI, et al. Targeting ligand-activated ErbB2 signaling inhibits breast and prostate tumor growth. Cancer Cell 2002;2:127–37.
[64] Cho HS, Mason K, Ramyar KX, Stanley AM, Gabelli SB, Denney Jr DW, et al. Structure of the extracellular region of HER2 alone and in complex with the Herceptin Fab. Nature 2003;421:756–60.
[65] Nahta R, Hung MC, Esteva FJ. The HER-2-targeting antibodies trastuzumab and pertuzumab synergistically inhibit the survival of breast cancer cells. Cancer Res 2004;64:2343–6.
[66] Gelmon KA, Fumoleau P, Verma S, Wardley AM, Conte PF, Miles D, et al. Results of a phase II trial of trastuzumab (H) and pertuzumab (P) in patients (pts) with HER2-positive metastatic breast cancer (MBC) who had progressed during trastuzumab therapy. J Clin Oncol 2008;26(Suppl.): 1026.
[67] Dancey J, Sausville EA. Issues and progress with protein kinase inhibitors for cancer treatment. Nat Rev Drug Discov 2003;2:296–313.
[68] Neshat MS, Mellinghtoff IK, Tran C, Stiles B, Thomas G, Petersen R, et al. Enhanced sensitivity of PTEN-deficient tumors to inhibition of FRAP/mTOR. Proc Natl Acad Sci USA 2001;98:10314–9.
[69] Shinkawa T, Nakamura K, Yamane N, Shoji-Hosaka E, Kanda Y, Sakurada M, et al. The absence of fucose but not the presence of galactose or bisecting N-acetylglucosamine of human IgG1 complex-type oligosaccharides shows the critical role of enhancing antibody-dependent cellular cytotoxicity. J Biol Chem 2003;278:3466–73.
[70] Niwa R, Hatanaka S, Shoji-Hosaka E, Sakurada M, Kobayashi Y, Uehara A, et al. Enhancement of the antibody-dependent cellular cytotoxicity of low-fucose IgG1 Is independent of FcγRIIIa functional polymorphism. Clin Cancer Res 2004;10:6248–55.
[71] Suzuki E, Niwa R, Saji S, Muta M, Hirose M, Iida S, et al. A nonfucosylated anti-HER2 antibody augments antibody-dependent cellular cytotoxicity in breast cancer patients. Clin Cancer Res 2007;13:1875–82.
[72] Batra JK, Kasprzyk PG, Bird RE, Pastan I, King CR. Recombinant anti-erbB2 immunotoxins containing Pseudomonas exotoxin. Proc Natl Acad Sci USA 1992;89:5867–71.
[73] Rosenblum MG, Horn SA, Cheung LH. A novel recombinant fusion toxin targeting HER-2/NEU-over-expressing cells and containing human tumor necrosis factor. Int J Cancer 2000;88:267–73.
[74] Nahta R, Esteva FJ. Herceptin: mechanisms of action and resistance. Cancer Lett 2006;232:123–38.
[75] Wong KK, Fracasso PM, Bukowski RM, Lynch TJ, Munster PN, Shapiro GI, et al. A phase I study with neratinib (HKI-272), an irreversible pan ErbB receptor tyrosine kinase inhibitor, in patients with solid tumors. Clin Cancer Res 2009;15:2552–8.
[76] Burstenin HJ, Sun Y, Tan AR, Dirix L, Vermette JJ, Powell C, et al. Neratinib (HKI-272), an irreversible pan erbB receptor tyrosine kinase inhibitor: phase 2 results in patients with advanced HER2+ breast cancer. Cancer Res 2009;69(Suppl.):725.
[77] Reya T, Morrison SJ, Clarke MF, Weissman IL. Stem cells, cancer, and cancer stem cells. Nature 2001;414:105–11.
[78] Dean M, Fojo T, Bates S. Tumour stem cells and drug resistance. Nat Rev Cancer 2005;5:275–84.
[79] Jones RJ, Matsui WH, Smith BD. Cancer stem cells: are we missing the target? J Natl Cancer Inst 2004;96:583–5.
[80] Donnenberg VS, Donnenberg AD. Multiple drug resistance in cancer revisited: the cancer stem cell hypothesis. J Clin Pharmacol 2005;45:872–7.
[81] Guzman ML, Jordan CT. Considerations for targeting malignant stem cells in leukemia. Cancer Control 2004;11:97–104.
[82] Zhou J, Zhang H, Gu P, Bai J, Margolick JB, Zhang Y. NF-kappaB pathway inhibitors preferentially inhibit breast cancer stem-like cells. Breast Cancer Res Treat 2008;111:419–27.
[83] Zhou J, Wulfkuhle J, Zhang H, Gu P, Yang Y, Deng J, et al. Activation of the PTEN/mTOR/STAT3 pathway in breast cancer stem-like cells is required for viability and maintenance. Proc Natl Acad Sci USA 2007;104: 16158–63.
[84] Zhou J, Zhang H, Gu P, Margolick J, Yin D, Zhang Y. Cancer stem/progenitor cell active compound 8-quinolinol in combination with paclitaxel achieves an improved cure of breast cancer in the mouse model. Breast Cancer Res Treat 2009;115:269–77.
[85] Kim YH, Woo KJ, Lim JH, Kim S, Lee TJ, Jung EM, et al. 8-Hydroxyquinoline inhibits iNOS expression and nitric oxide production by down-regulating LPSinduced activity of NF-kappaB and C/EBPbeta in Raw 264.7 cells. Biochem Biophys Res Commun 2005;329:591–7.
[86] Michalet X, Pinaud FF, Bentolila LA, Tsay JM, Doose S, Li JJ, et al. Quantum dots for live cells, in vivo imaging and diagnostic. Science 2005;307:538–44.
[87] Smith AM, Duan H, Mohs AM, Nie S. Bioconjugated quantum dots for in *Vivo* molecular and cellular imaging. Adv Drug Del Rev 2008;60:1226–40.
[88] Rhyner MN, Smith AM, Gao X, Mao H, Yang L, Nie S. Quantum dots and multifunctional nanoparticles: new contrast agents for tumor imaging. Nanomedicine 2006;1:209–17.
[89] Harisinghani MG, Barentsz J, Hahn PF, Deserno WM, Tabatabaei S, Van de Kaa CH, et al. Noninvasive detection of clinically occult lymph-node metastases in prostate cancer. N Engl J Med 2003;348:2491–9.
[90] Evgenov NV, Medarova Z, Dai G, Bonner-Weir S, Moore A. In vivo imaging of islet transplantation. Nat Med 2006;12:144–8.
[91] Barnett BP, Arepally A, Karmarkar PV, Qian D, Gilson WD, Walczak P, et al. Magnetic resonance-guided, real-time targeted delivery and imaging of magnetocapsules immunoprotecting pancreatic islet cells. Nat Med 2007;13:986–91.
[92] El-Boubbou K, Gruden C, Huang X. Magnetic Glyco-nanoparticles: a unique tool for rapid pathogen detection, decontamination, and strain differentiation. J Am Chem Soc 2007;129:13392–3.
[93] Fortin JP, Wilhelm C, Servais J, Menager C, Bacri JC, Gazeau F. Size-sorted anionic iron oxide nanomagnets as colloidal mediators for magnetic hyperthermia. J Am Chem Soc 2007;129:2628–35.
[94] Lu AH, Salabas EL, Schlut F. Magnetic nanoparticles: synthesis, protection, functionalization, and application. Angew Chem Int Ed 2007;46:1222–44.
[95] Laurent S, Forge D, Port M, Roch A, Robic C, Vander Elst L, et al. Magnetic iron oxide nanoparticles: synthesis, stabilization, vectorization, physicochemical characterizations, and biological applications. Chem Rev 2008;108:2064–110.
[96] Grzelczac M, Perez-Juste J, Mulvaney P, Liz-Marzàn LM. Shape control in gold nanoparticle synthesis. Chem Soc Rev 2008;37:1783–91.
[97] Ghosh P. Han G, De M. Kim CK. Rotello VM. Gold nanoparticles in delivery application. Adv Drug Del Rev 2008;60:1307–15.
[98] Ghosh P, Han G, De M, Kim CK, Rotello VM. Fluorescent core–shell silica nanoparticles: towards "Lab on a particle" architectures for nanobiotechnology. Chem Soc Rev 2006;35:1028–32.
[99] Kang SM, Lee KB, Kim DJ, Choi IS. Biomimetic approach to the formation of gold nanoparticles/silica core/shell structures and subsequent conjugation. Nanotechnology 2006;17:4719–25.
[100] Yong SY, Zhang Hj, Yu JB, Wang C, Sun LN, Shi WD. Bifunctional magnetic-optical nanocomposities: grafting lanthanide complex onto core–shell magnetic silica nanoarchitecture. Langmuir 2007;23:7836–40.
[101] Yang D, Hu J, Fu S. Controlled synthesis of magnetite-silica nanocomposities via seeded sol–gel approach. J Phys Chem C 2009;113:7646–51.
[102] Eghtedari M, Liopo AV, Copland JA, Oraevsky AA, Motamedi M. Engineering of hetero-functional gold nanorods for the vivo molecular targeting of breast cancer. Nanoletters 2009;9:287–91.
[103] Wuang SC, Neoh KG, Kang EN, Pack DW, Leckband DE. HER-2-mediated endocytosis of magnetic nanospheres and the implications in cell targeting and particle magnetization. Biomaterials 2008;29:2270–9.
[104] Chen J, Saeky F, Wiley BJ, Cang H, Cobb MJ, Li ZY, et al. Gold nanocages: bioconjugation and their potential use as optical imaging contrast agents. Nano Lett 2005;5:473–7.
[105] Shukla R, Thomas TP, Peters JL, Desai AM, Kukowska-Latallo J, Patri AK, et al. HER2 specific tumor targeting with dendrimer conjugated anti-HER2 mAb. Bioconjugate Chem 2006;17:1109–15.
[106] Huh YM, Jun YW, Song HT, Kim S, Choi JS, Lee JH, et al. In vivo magnetic resonance detection of cancer by using multifunctional magnetic nanocrystals. J Am Chem Soc 2005;127:2387–91.
[107] Lee JH, Huh YM, Jun JW, Seo JW, Jang JT, Song HT, et al. Artificially engineered magnetic nanoparticles for ultra-sensitive molecular imaging. Nat Med 2007;13:95–9.
[108] Jun YW, Huh YM, Choi JS, Lee JH, Song HT, Kim S, et al. Nanoscale size effect of magnetic nanocrystals and their utilization for cancer diagnosis via magnetic resonance imaging. J Am Chem Soc 2005;127:5732–3.
[109] Song HT, Choi JS, Huh YM, Kim S, Jun YW, Suh JS, et al. Surface modulation of magnetic nanocrystals in the development of highly efficient magnetic resonance probes for intracellular labeling. J Am Chem Soc 2005;127: 9992–3.
[110] Hapca AC, Nobs LB, Buchegger F, Gurny R, Delie F. Differential tumor cell targeting of anti-HER2 (Herceptin®) and anti-CD20 (Mabthera®) coupled nanoparticles. Int J Pharm 2007;331:190–6.
[111] Steinhauser I, Spänkuch B, Strebhardt K, Langer K. Trastuzumab-modified nanoparticles: optimization of preparation and uptake in cancer cells. Biomaterials 2006;27:4975–83.
[112] Anhorn MG, Wagner S, Kreuter J, Langer K, Von Briesen H. Specific targeting of HER2 overexpressing breast cancer cells with doxorubicin-loaded trastuzumab-modified human serum albumin nanoparticles. Bioconjugate Chem 2008;19:2321–31.

ARTICLE 1

small NANO MICRO

Nanodiagnostics

Towards Ideal Magnetofluorescent Nanoparticles for Bimodal Detection of Breast-Cancer Cells

Fabio Corsi, Clara De Palma, Miriam Colombo, Raffaele Allevi, Manuela Nebuloni, Silvia Ronchi, Giuseppina Rizzi, Antonella Tosoni, Emilio Trabucchi, Emilio Clementi, and Davide Prosperi**

An increasing number of novel molecular markers based on nanomaterials for tumor diagnostics have been developed in recent years. Many efforts have focused on the achievement of site-targeted bioconjugated nanoparticles. In contrast, the mechanisms of toxicity, endocytosis, and degradation pathways are still poorly understood, despite their primary importance for clinical translation. In this study, three different model nanoscale magnetofluorescent particle systems (MFNs) are designed and fabricated. These nanoparticles are evaluated in terms of size, morphology, zeta potential, fluorescence efficiency, capability of enhancing T_2 relaxivity of water protons, and stability. Accordingly, two are developed and the mechanism of internalization, the intracellular fate, and the toxicity in MCF-7 adenocarcinoma cells are studied. Besides the well-documented size effect, the anionic charge seems to be a crucial factor for particle internalization, as MFN penetration through the cell membrane could be modulated by surface charge. Ultrastructural analysis of transmission electron micrographs combined with evidence from confocal microscopy reveals that MFNs are internalized by clathrin-mediated endocytosis and macropinocytosis. Moreover, MFNs are found in EEA1-positive endosomes and in lysosomes, indicating that they follow a physiological pathway of endocytosis. Magnetorelaxometric analysis demonstrates that MFNs enable the detection of 5×10^5 cells mL^{-1} after treatment with particle dosages as low as 30 μg mL^{-1}. Hence, MFNs appear to be a valuable and safe bimodal contrast agent that can be developed for the noninvasive diagnosis of breast cancer.

Keywords:
- cells
- magnetic materials
- nanoparticles
- toxicity
- tumor diagnostics

[*] Dr. D. Prosperi, M. Colombo
Dipartimento di Biotecnologie e Bioscienze
Università degli Studi di Milano-Bicocca
Piazza della Scienza 2, 20126 Milano (Italy)
E-mail: davide.prosperi@unimib.it

Prof. E. Clementi, Dr. C. De Palma
Dipartimento di Scienze Precliniche Lita Vialba
Università degli Studi di Milano, Ospedale L. Sacco
Via G.B. Grassi 35, 20157 Milano (Italy)
and IRCCS E. Medea
Via Don L. Monza 20, 23842 Bosisio Parini (Lecco) (Italy)
E-mail: emilio.clementi@unimi.it

Prof. E. Trabucchi, Prof. F. Corsi, Dr. M. Nebuloni, R. Allevi, Dr. A. Tosoni
Dipartimento di Scienze Cliniche "Luigi Sacco"
Università degli Studi di Milano, Ospedale L. Sacco
Via G.B. Grassi 74, 20157 Milano (Italy)

Dr. S. Ronchi, Dr. D. Prosperi, G. Rizzi
Istituto di Scienze e Tecnologie Molecolari, CNR
Via Golgi 19, 20133 Milano (Italy)

Supporting Information is available on the WWW under http://www.small-journal.com or from the author.

DOI: 10.1002/smll.200900881

1. Introduction

One of the modern challenges facing clinical translation of biomedical research is the possibility of obtaining highly sensitive, noninvasive, well-resolved, in vivo images of biological targets.[1] In the last years, several diagnostic techniques for the rapid detection of tumors have been explored, including fluorescence imaging, positron emission tomography (PET), and magnetic resonance imaging (MRI), and their extensive use in clinical investigations has significantly increased the efficacy of therapeutic approaches.[2–4] Despite these diagnostic improvements, the detection of malignancies in their early stages is still a challenge due to difficulty in achieving concomitant high sensitivity and resolution with the available diagnostic tools.[5] Therefore, a primary end-point in cancer diagnosis is the development of effective molecular contrast agents capable of unambiguously disclosing the presence of early-stage malignancies, tracking cell migration, and monitoring surgical and pharmacological response.

Worldwide, mammary carcinoma represents the second most common type of malignant tumor (after lung cancer) in adult women and the fifth most common cause of death among cancer types.[6,7] However, an improvement in the detection and monitoring of lymphatic involvement and recurrence may arise with respect to current clinical protocols. At present, the sentinel-lymph-node technique is considered the gold-standard approach for the detection of lymphatic axillary chain nodal invasion. This approach, however, is rather invasive, as it is based on a surgical biopsy of the first lymph node of the axillary chain spotted by a lymph-scintigraphy with ^{99m}Tc.[8,9]

An attractive possibility to detect mammary carcinomas in the early stages of their development in a noninvasive way consists of developing tracing agents that can be delivered and detected via magnetic nanoparticles (MNPs). Thanks to their unique magnetic properties, MNPs now find large application in many fields of biomedical research, including their use as MRI contrast agents,[10,11] heating mediators for cancer thermotherapy,[12,13] magnetic-force-based drug and gene delivery,[14,15] and selective separation and detection of biomolecules.[16] In the past, major concerns about MNPs have been in vitro and in vivo cellular toxicity, tendency to a rapid clearance after delivery in the circulatory system, and low intracellular labeling efficiency.[17] In particular, these particles need to fulfill several criteria in order to be used as nanodiagnostic materials in humans, including high resolution, accuracy, and sensitivity of detection, which may be provided by using MNPs coated with protein-targeting biomarkers overexpressed by breast cancer cells such as HER2 receptor.[18] In addition, they must be nontoxic and able to interact in a physiological way with biological tissues without aggregating when delivered to them. Finally, since membrane receptors are endocytosed as part of their normal response to ligand binding, MNPs have to follow physiological pathways when internalized. So far, only scant evidence has been reported about these latter factors, which are critical for clinical use.[19–21] On the basis of recent reports on particle internalization in human mesenchymal stem cells[22] we have designed and tested various bifunctional magnetofluorescent nanoparticle systems (MFNs) with different characteristics and identified a specific MFN type that answers the criteria outlined above with regards to sensitivity, in vitro safety, and physiological behavior. The multifunctional contrast agent based on MFN we report here appears therefore to fulfill the relevant characteristics needed for its further development for both in vitro and in vivo imaging of early mammary carcinoma.

2. Results and Discussion

The development of iron-based MNPs conjugated with stably fluorescent organic dyes is limited by the strong tendency of iron oxide to partly, sometimes completely, quench the fluorescence.[23] Moreover, the direct contact of the fluorophore with biological media often results in problems of rapid photobleaching.[24] It has been shown that the encapsulation of both MNPs and organic dyes within a silica matrix could improve the dual-mode detection by greatly reducing these undesired side effects.[25,26] Thus, our rationale in designing the MFNs for biological evaluation took into consideration two concomitant factors: we needed the maximum iron content per particle to optimize the signal-to-particle ratio for future clinical applications (dosage efficiency) together with the optimal conservation of the fluorescence intensity to enhance the sensitivity for in vitro experiments.

Firstly, we prepared the MNPs by conventional approaches both as a water dispersion of bare magnetite crystals (**MNP1**, 7 ± 3 nm) and as surfactant-coated, highly monodisperse 5-nm magnetite particles (**MNP2**) obtained by solvothermal decomposition (Figure S1 in the Supporting Information).[27]

MFNs were designed in a multilayer fashion, as schematically represented in Scheme 1. The magnetic core consisted of a MNP cluster, which has the effect of enhancing the relative transverse relaxivity of each MFN with respect to the more common single-crystal model, which contains only one MNP per nanoparticle. This MNP cluster was embedded in a silica shell of tunable thickness and coated by a fluorescent layer obtained by alkaline condensation of a mixture of fluorescein isothiocyanate (FITC), which was prior reacted with (3-aminopropyl)triethoxysilane (APTES) and tetraethyl orthosilicate (TEOS). When necessary, an excess of APTES was used in the mixture to provide surface amino groups ready for further conjugation. In order to obtain quite uniform MFNs, two main strategies were followed: i) a sol–gel process using an aqueous dispersion of as-synthesized uncoated Fe_3O_4 nanoparticles led to **MFN1** (Figure 1A) and ii) **MFN2** were obtained by reaction confinement within the submicrometer domain of a water-in-oil microemulsion system (Figure 1B) using hydrophobic monocrystalline Fe_3O_4 particles as the starting material.

MFN1 are shown in Figure 1A as slightly rod-like particles of about 150 nm in the larger dimension. The experimental conditions explored here led to a quite different result from previous observation.[23] A great number of iron oxides have been encapsulated in each **MFN1** as a consequence of the presence of MNP aggregates in the nanoparticle mother dispersion. An outer shell with remarkably lower electron density is clearly distinguishable, attributable to the fluorescent layer. Probably due to a nearly neutral surface charge (the measured zeta potential was $-1 < \zeta < +1$ mV), **MFN1** showed a tendency

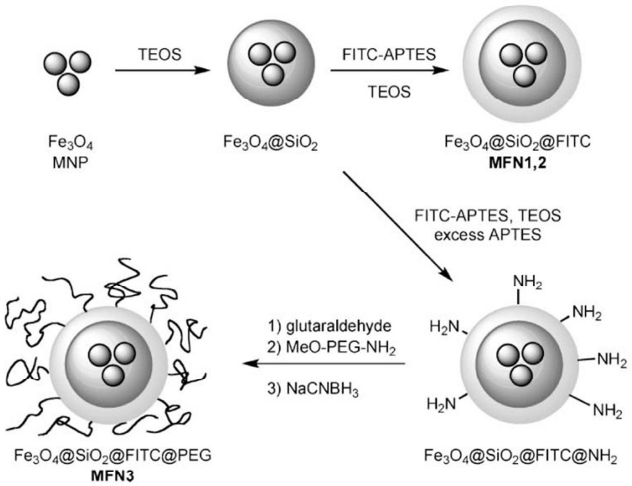

Scheme 1. Illustrative strategy for the preparation of **MFN1–3**.

to form large aggregates when dissolved in salty solution, as determined by dynamic light scattering (DLS) measurements, in which a mean hydrodynamic diameter ranging from 1.5 to 2.5 μm was detected in 0.1 M KCl.

The microemulsion system used to generate the **MFN2** provided 60-nm MFNs with a more regular spherical morphology containing a limited number of magnetic nanocrystals. **MFN2** were smaller in size than **MFN1**, and were readily dispersed in water and phosphate buffer saline (PBS). Shell thickness, fluorescence intensity, and average number of magnetite grains per MFN could be adjusted essentially by varying five parameters: initial concentrations of MNPs, TEOS, and APTES–FITC, reaction time, and stirring rate. Different from similar protocols,[22] we optimized the reaction conditions in order to obtain multiple iron oxides within each silica envelope (Figure 1B). Another important feature of our experimental setup is that it allowed us to obtain highly uniform and reproducible particles, with only 2% nanoparticles exceeding the average **MFN2** size by more than 10%. The APTES–FITC amount was also adjusted to achieve a suitable fluorescence signal for biological studies (the optimal conditions are reported in the Experimental Section). The hydrodynamic diameter was 120 nm as measured by DLS, which is consistent with a monomeric nanoparticle distribution in solution, as also demonstrated by transmission electron microscopy (TEM) (Figure 1B). This could be explained in terms of their high negative surface charge, as determined by zeta potential measurement. Indeed, we found an average ζ of −40 mV. This ζ value is significantly lower than the negative threshold of −30 mV, conventionally indicated as the ζ value below which a surface may be considered as permanently negatively charged, leading to a stable colloidal suspension.[28] Such a negative potential is partially attributable to the presence of surface fluorescein molecules, which are recovered in dianion form at neutral pH.[29]

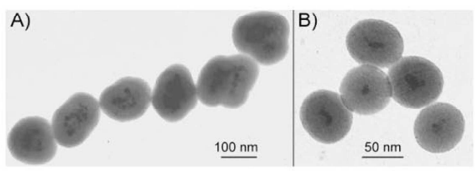

Figure 1. TEM images of A) **MFN1** and B) **MFN2** in ethanol. In both cases, an outer, less contrasted shell is visible, attributable to the presence of the incorporated organic fluorophore.

The magnetic and optical properties of **MFN1** and **MFN2** were compared in view of biomedical application. We performed a set of relaxometric experiments to determine the respective T_2 enhancing capabilities. Conventionally, the transverse relaxivity r_2 is defined as the slope obtained by plotting $1/T_2$ versus iron concentration. Nevertheless, we preferred to refer r_2 to the particle dosage for practical purposes (in Figure 2A, $1/T_2$ is plotted versus μg MFNs). We found r_2 values of 87 mg^{-1} mL s^{-1} and 184 mg^{-1} mL s^{-1} for **MFN1** and **MFN2**, respectively. Both **MFN1** and **MFN2** are very well-fitted by a line within the analyzed range of concentration (0–30 μg mL^{-1}), thus exhibiting the typical property of superparamagnetic iron oxide in shortening T_2 relaxation time. Quite surprisingly, although the number of magnetite grains is lower, **MFN2** display remarkably higher magnetic susceptibility than **MFN1**. Moreover, **MFN1** and **MFN2** were checked at concentrations up to 1 mg mL^{-1}: while **MFN2** confirmed this trend very well, revealing an exquisite magnetic stability, **MFN1** showed a progressive decrease in the T_2 shortening efficiency above 30 μg mL^{-1} up to a plateau (Figure S2 in the Supporting Information). Figure 2B illustrates the relative fluorescence intensities for **MFN1** and **MFN2** referred to a single particle. **MFN2** were about four times brighter than **MFN1**. In principle, there are two possible interpretations for this unexpected phenomenon. This behavior might be attributable to the stronger quenching effect of the higher concentration of iron oxide in **MFN1**. Alternatively, it could be due to a dye–dye quenching caused by a different arrangement and concentration of FITC molecules in these kinds of particles, as a much higher amount of APTES–FITC was used in the synthesis of **MFN1**. It was not possible to discriminate between these two quenching mechanisms at this stage, and will therefore merit a more thorough investigation in the future. Combining the magnetic, fluorescence, colloidal stability, and size/morphological characteristics, we selected **MFN2** as the best candidate for biological evaluation.

We used MCF7 carcinoma cells for in vitro study of the quality of the synthesized nanoparticles. MCF7 cells are a well-characterized, estrogen-receptor-positive human cell line and therefore are a useful in vitro model of breast cancer. Moreover,

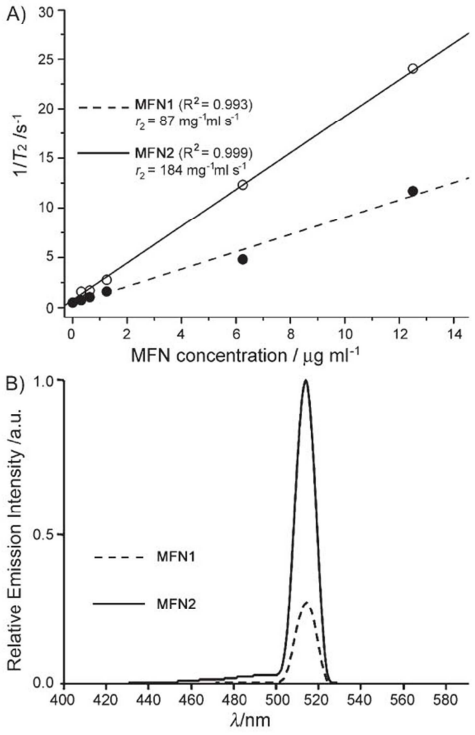

Figure 2. Magnetic and optical properties of as-synthesized MFNs. A) Relaxometric analysis of **MFN1** (full dots) and **MFN2** (empty dots). The inverse of experimental T_2 values obtained at different MFN concentrations are plotted versus μg ml^{-1} MFNs. Both **MFN1** and **MFN2** are fitted by a line and the T_2 relaxivities are given by the respective line slopes. B) Relative fluorescence emission of **MFN1** (dashed line) and **MFN2** (continuous line) in Dulbecco's PBS without calcium and magnesium.

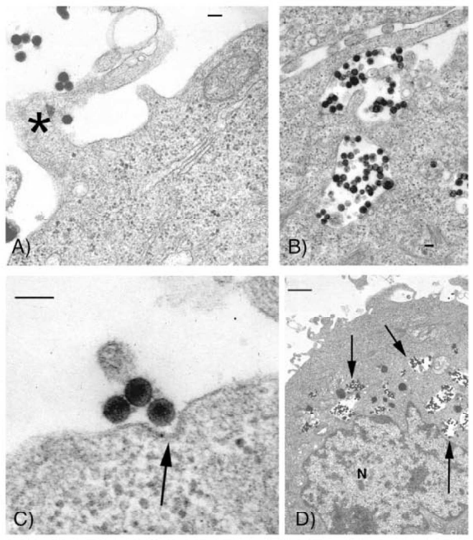

Figure 3. Ultrastructural images of MCF7–**MFN2** time course. Ultrastructural analysis demonstrated the uniformity in shape and size (about 60 nm) of **MFN2** particles during their internalization. A) Nanoparticles adhere to the cytoplasmic membrane at 30 min incubation and initial macropinocytosis is demonstrated by extension of plasma membrane (star symbol, *)-surrounding nanoparticles. B,C) After 1 h, nanoparticle uptake takes place by processes consistent with macropinocytosis (B) and clathrin-coated, vesicle-mediated internalization (C, arrow). D) At 5 h, a large amount of vacuoles (arrows) containing non-clustered nanoparticles are present in the cytoplasm of MCF7 cells (N = nucleus). Scale bars A–C: 100 nm, D: 1 μm.

in vivo, the MCF-7 cells are capable of forming tumors in nude mice treated at a tumorigenic dose of 5×10^6 cells.[30]

Since anionic nanoparticles are known to spontaneously penetrate the cell membrane,[31] we expected that **MFN2** could be efficiently internalized into cells. Cells were incubated with **MFN2** and their localization with respect to the cells was investigated by TEM over a 5 h time window. The results shown in Figure 3 demonstrate that **MFN2** initially adhered to the plasma membrane to be subsequently internalized by a process of vesicle-mediated endocytosis to reach internal vacuoles. Briefly, after 30 min incubation, initial adhesion and extension of plasma membrane around nanoparticles was observed (Figure 3A). Intracellular nanoparticle uptake took place after 1 h (23% labeled cells from 100 randomly counted cells by TEM) by means of processes consistent with macropinocytosis and clathrin-coated vesicle-mediated endocytosis (Figure 3B and C). At 5 h, an increased number of cytoplasmic vacuoles containing non-clustered nanoparticles was observed (Figure 3D, 49% of cells labeled). At all stages of **MFN2** interaction with cells, particles predominantly maintained their uniformity in shape and the absence of aggregate formation (Figure 3).

We next characterized the endocytic pathways of **MFN2** by investigating colocalization of the particles with different markers of endocytic compartments, namely the recycling endosome marker transferrin receptor, the early endosome marker EEA1, the Golgi marker GM-130, and the lysosomal marker cathepsin D. We found that **MFN2** localized with both the recycling and early endosome markers as well as the lysosomes (Figure 4), which is consistent with the initial localization of these particles in small subplasmalemmal vesicles and subsequently in more internal vacuoles observed by TEM (Figure 3D, as indicated by arrows). Importantly, no colocalization with GM-130 was observed. Macropinosomes can acquire EEA1 and TfR markers after binding with specific protein complexes and their fusion with endosomes.[32]

The combined TEM and immunofluorescence approaches therefore demonstrate that **MFN2** are incorporated by both clathrin-mediated endocytosis and macropinocytosis. This is further confirmed by the fact that **MFN2** are only minimally internalized in absence of serum, indicating that they are endocytosed by an energy-requiring active mechanism of

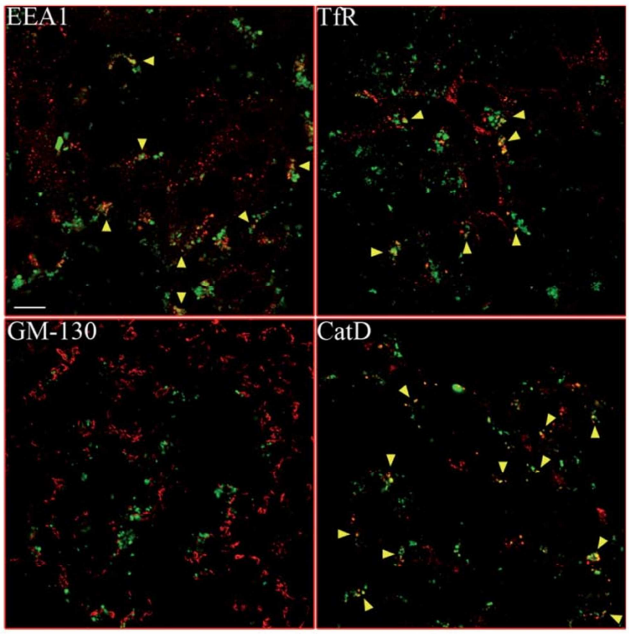

Figure 4. Intracellular localization of **MFN2** in MCF7 cells. Incubations were for 5 h with 30 μg mL^{-1} of **MFN2**. Images are representative of four reproducible experiments and reveal the localization of **MFN2**, identified by their green fluorescence versus that of the early endosome marker EEA1, the recycling endosome marker TfR, the lysosomal protein Cat D, and the Golgi marker GM-30, labeled using secondary, TRITC-conjugated Abs (red). Scale bar: 10 μm.

internalization. **MFN2** are eventually directed into the lysosomal pathways, as colocalization with cathepsin D clearly indicates. In conclusion, **MFN2** were internalized through a physiological pathway of endocytosis.

We then evaluated the toxicity of **MFN2** by analyzing their ability to induce cell death in a concentration-dependent way over a 5 h time window. Cell death was evaluated by flow cytometry measuring both annexin V exposure on the outer leaflet of the plasma membrane, a feature of apoptotic cells, and incorporation of 7-aminoactinomycin D, an index of membrane permeability and thus of necrotic death. **MFN2** were nontoxic for the cells when used up to 30 μg mL^{-1}, while at the highest concentrations used (50 μg mL^{-1}) cell death could be detected, albeit only after 5 h (Figure 5). These findings combined with the physiological behavior of these particles when internalized indicate that they possess a good in vitro safety profile.

In order to obtain similar particles with reduced interaction with cells, we elaborated **MFN2** by conjugation of the excess surface amino groups with synthetic monoamino poly(ethylene glycol) (PEG)-600 (Scheme 1). We chose such a PEG linker model with two main objectives in mind: i) avoidance of membrane fusion, which often occurs in in vitro experiments with long PEG chains and ii) absence of net charges on the molecule. The PEG covalent attachment was performed via particle–PEG glutaraldehyde crosslinking followed by imine reduction with $NaCNBH_3$ (reductive amination). This conjugation approach allowed us to introduce neutral PEG chains in contrast with classical amide formation using commercial PEG diacid. The resulting **MFN3** exhibited a strongly reduced surface zeta potential of about −8 mV. In this case, the colloidal stability was provided instead by steric repulsion of the PEG chains. Fluorescence intensity and r_2 values were on the same order of uncoated **MFN2**.

Of importance for the prospective use of **MFN3** as diagnostic markers, the internalization was significantly lower than **MFN2** (only 4% labeled cells after 1 h and 16% after 5 h by TEM analysis) and the small fraction incorporated by the cells was consistently found in EEA1-positive endosomes and in lysosomes indicating that when internalized they followed a physiological pathway of endocytosis used by cells to degrade undesired molecules (Figure 6). Accordingly, an increment in the production of lysosomes as a consequence of **MFN3** incorporation was confirmed by ultrastructural analysis obtained by TEM images (Figure 7). In perspective of a diagnostic use of **MFN3** we also tested their characteristics on the noncancerous cell line NIH-3T3. In these cells we found that **MFN3** were endocytosed only to a limited extent; endocytosis occurred through the same pathway observed for MCF7, as shown by **MFN3** localization into lysosomes (Figure S3 in the Supporting Information).

We next investigated the cellular toxicity of **MFN3** by measuring cell death over a 5 h period in a similar way to that used for **MFN2**. **MFN3** were found to be nontoxic for MCF7 even at the highest concentration (50 μg mL^{-1}) for up to 5 h (Figure 8). In a second set of experiments we analyzed long-term toxicity and, in parallel, cell proliferation both on MCF-7 and NIH 3T3 cells. As shown in Figures 9A and 10A, no signs of death were observed up to 72 h of exposure to the nanoparticles. In addition, no differences were observed between untreated and **MFN3**-treated cells in terms of proliferation (Figures 9B and 10B), further highlighting the absence of toxicity of these particles. Therefore, **MFN3** appear to have a good profile of safety in vitro, and their very low levels of internalization might be helpful in therapeutic perspective to avoid aspecific binding after their coating with tumor-specific receptor ligands.

To evaluate the potential of **MFN2** and **MFN3** as contrast agents for MRI in living cells, we performed a set of T_2 relaxation experiments on labeled MCF7 cells. Three MCF7 cell cultures were treated with 50 and 30 μg **MFN2** and 50 μg **MFN3**, respectively, for 5 h at 37 °C. The cells were washed with PBS, fixed with 2.5% buffered glutaraldehyde, and eventually resuspended in PBS (pH 7.0) at a concentration of 5×10^6 cells mL^{-1}. The samples as well as unlabeled MCF7 cells (control) were analyzed by relaxometric measurements at increasing

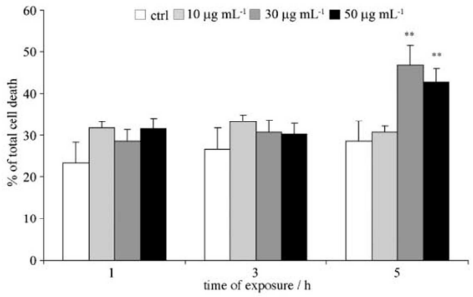

Figure 5. MCF7 cells were treated with **MFN2** at 10–30–50 μg mL^{-1} for 1–3–5 h. The exposure of Annexin V and incorporation of 7-aminoactinomycin D were evaluated by flow cytometry. Asterisks indicate statistical significance versus untreated control (ctrl: $n = 5$).

dilution levels. The results are summarized in Table 1. All the treated cells showed a significant decrease in T_2 with respect to the control at a concentration of 5×10^6 cells mL^{-1}, which confirms the internalization of iron by cultured cells. Such a T_2 effect was at least detectable down to a concentration of 5×10^5 cells mL^{-1}. As expected, cells treated with 50 μg **MFN2** exhibited higher relaxivity enhancement compared to 30 μg **MFN2**, suggesting a dose-dependent nanoparticle internalization. This effect becomes less incident with cell dilution. In contrast, cells treated with **MFN3** resulted in a remarkably lower T_2 decrease even at higher nanoparticle concentrations. Such a loss of labeling efficiency is most probably attributable to the presence of short PEG chains on the outer shell of the particles, which reduces the surface potential and renders them quite reluctant to be internalized by the cell membrane.

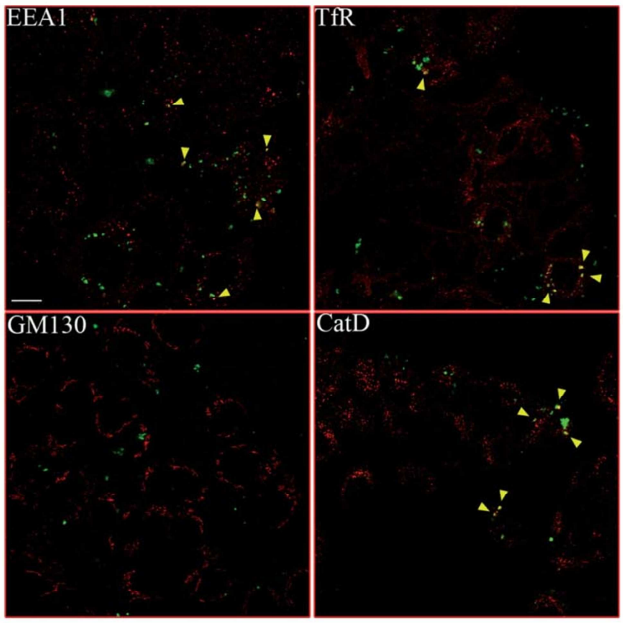

Figure 6. Intracellular localization of **MFN3** in MCF7 cells. Incubations were for 5 h with 30 μg mL^{-1} of **MFN3**. Images reveal the localization of **MFN3** identified by their green fluorescence versus that of the early endosome marker EEA1, the recycling endosome marker TfR, the lysosomal protein Cat D, and the Golgi marker GM-130 labeled using secondary, TRITC-conjugated Abs (red). Scale bar: 10 μm.

3. Conclusions

In summary, we have designed and synthesized a bifunctional MFN probe consisting of tuned multiple superparamagnetic iron oxide nanoparticles incorporated within a fluorescent silica shell for the study of the interaction with breast cancer cells in vitro. We demonstrate that unconjugated anionic MFNs are spontaneously internalized by cancerous and noncancerous cells in absence of receptor-targeting antibodies or delivery agents, and the extent of the uptake can be modulated depending on the control of the surface negative charge. MFNs are internalized by macropinocytosis and clathrin-mediated endocytosis mechanisms, follow a physiological pathway of internalization once incorporated by the cell, and display no relevant cytotoxicity in vitro. These results highlight the importance of elucidating the mechanism of cell uptake and degradation of this new class of molecular diagnostics for cancer investigation and treatment. Future work will focus on the application of the present discoveries to animal models to evaluate the effectiveness of our MFNs as contrast agents for in vivo experiments. The next step will be the implementation of our MFNs with monoclonal antibodies in order to target them directly to specific antigens. We believe that the resulting nanoparticle probes will allow us not only to identify a number of early stage tumors, but also to differentiate between cancer and inflammation, and eventually to create a new generation of personalized target therapies.

4. Experimental Section

General methods and instrument details: Solvents and other chemicals were purchased from Sigma-Aldrich (St. Louis, MO), Fluka (St. Gallen, Switzerland), and Riedel-de Haën (Seelze, Germany), and used as received without further purification. Water was deionized and ultrafiltered by a MilliQ apparatus from Millipore Corporation (Billerica, MA). Reactions involving the use of fluorescein derivatives were performed in the dark. DLS measurements were performed at 90°

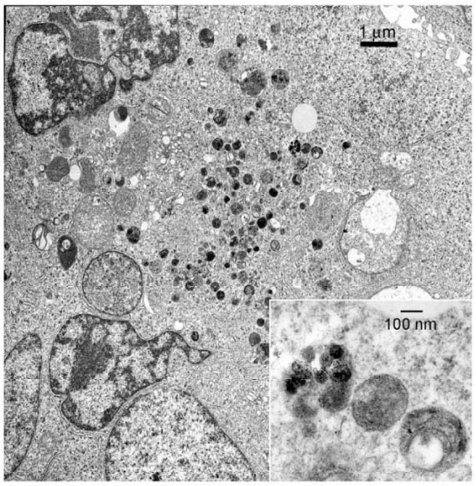

Figure 7. TEM image of a MCF7 cell section after treatment with **MFN3**. The numerous dark spots represent the lysosomes. Inset: magnification of lysosomes incorporating **MFN3** particles.

with a 90 Plus Particle Size Analyzer from Brookhaven Instruments Corporation (Holtsville, NY) working at 15 mW of a solid-state laser ($\lambda = 661$ nm). Zeta-potential measurements were performed on the same instrument equipped with AQ-809 electrodes and analyses were processed by ZetaPlus software. Viscosity and refractive index of pure water were used to characterize the solvent. Nanoparticles were dispersed either in water or in 1.0 mM KCl and sonicated in a S15H Elmasonic apparatus (Elma, Singen, Germany) before analysis. The final sample concentration used for measurements was typically of 0.01 mg mL^{-1}. For TEM analysis, MNPs were dispersed in ethanol (50 μg mL^{-1}) and a drop of the resulting solution was placed on a Formvar/carbon-coated copper grid and air dried. TEM images were obtained by a Zeiss EM-109

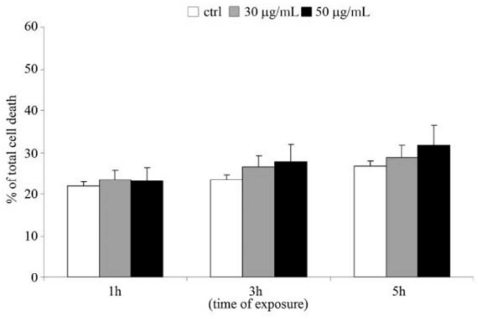

Figure 8. MCF7 cells were treated with **MFN3** at 30–50 μg mL^{-1} for 1–3–5 h, after which cell death was assessed to measure the exposure of Annexin V and the incorporation of 7-aminoactinomycin, evaluated by flow cytometry. No significant cell death was observed.

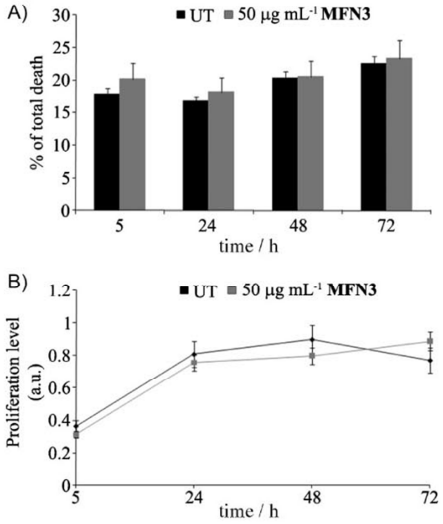

Figure 9. MCF7 cells were treated with **MFN3** at 50 μg mL^{-1} for up to 72 h. Cell death (A) and proliferation (B) were assessed at the indicated time points. Cell death was assessed as described in Figure 8, whereas proliferation was tested by measuring the conversion of MTT into formazan. **MFN3** were nontoxic and did not affect proliferation. UT = untreated control ($n = 3$).

microscope (Oberkhochen, Germany) operating at 80 kV. T_2 relaxation times were acquired at a temperature of 313 K using a Bruker Minispec mq20 system (Ettlingen, Germany) working with ^{1}H at a 20 MHz magnetic field with the following parameters: CPMG (Carr-Purcell-Meiboom-Gill) pulse sequence, 1000 echoes with a 20 ms echo time and 2 s repetition time. Samples were introduced using 10-mm NMR spectroscopy tubes pre-warmed and sonicated. In order to obtain relaxivity plots of **MFN1** and **MFN2**, magnetofluorescent nanoparticles were dispersed in water at different concentrations and the $1/T_2$ values of the corresponding solutions were plotted versus nanoparticle concentration values expressed as μg mL^{-1} or mg mL^{-1}. Relaxivity measurements on MFN-treated and untreated MCF-7 cultured cells were performed using the same 10-mm NMR tubes at different cell dilutions in the range 5×10^5–5×10^6 cells with a single acquisition for each sample.

MNP synthesis: Water-soluble MNPs (**MNP1**) were synthesized by a coprecipitation method at room temperature according to our previous work.[27] **MNP1** were stored as a dispersion in water (10 mg mL^{-1}) and used without further purification during the sol–gel reaction sequence. Oleic acid-stabilized magnetite nanoparticles were synthesized according to Reference [27] and stored as an oleic acid-stabilized dispersion in *n*-hexane (2 mg mL^{-1}). Just before use, a suitable amount of this dispersion was passed through a 0.2-μm poly(tetrafluoroethylene) (PTFE) syringe filter and the nanoparticles were precipitated with ethanol, recovered by centrifugation, and vacuum dried (**MNP2**).

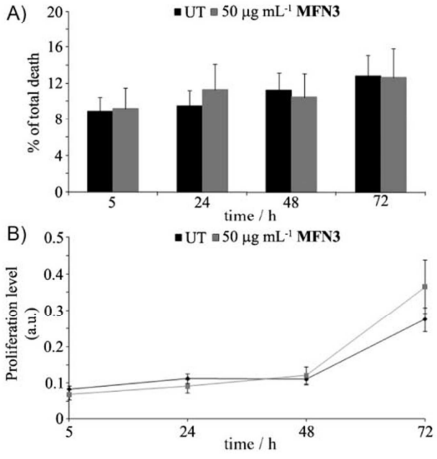

Figure 10. NIH 3T3 cells were treated with **MFN3** at 50 μg mL^{-1} for up to 72 h. Cell death (A) and proliferation (B) were assessed at the indicated time points. Cell death was assessed as described in Figure 8, whereas proliferation was tested by measuring the conversion of MTT into formazan. **MFN3** were nontoxic and did not affect proliferation. UT = untreated control ($n = 3$).

Synthesis of APTES–FITC conjugate: Method A (excess amino groups): To a solution prepared from FITC (8 mg, 20.5 μmol) and dry ethanol (1 mL), APTES (25 μL, 106.8 μmol) was added. The mixture was stirred for 4 h until thin-layer chromatography (TLC) revealed the disappearance of the starting material under a UV lamp at $\lambda = 366$ nm.

Method B (stoichiometric amines): FITC (8 mg, 20.5 μmol) was dissolved in dry ethanol (1 mL), then APTES (4.9 μL, 20.7 μmol) was added. The mixture was stirred overnight until TLC revealed the disappearance of the starting material.

Method C (excess amino groups): FITC (81 mg, 208 μmol) was dissolved in dry ethanol (10 mL), then an ethanolic APTES solution (6.6 mL, 2.56 mmol APTES) was added. The mixture was stirred for 4 h until TLC revealed the disappearance of the starting material.

Synthesis of MFN1: The synthetic procedure was adapted from Yu et al. with few modifications.[33] Briefly, an aqueous dispersion of **MNP1** (20 mL, 10 mg mL^{-1}) was diluted in a mixture of ethanol (76 mL), water (76 mL), and aqueous NH_3 (6.6 mL, 25 wt%) with magnetic stirring. An ethanol solution of TEOS (800 μL in 60 mL) was added and the mixture was stirred for 4 h. The precipitate was collected by centrifugation, washed three times with water, and precipitated again with acetone. The resulting nanoparticles were dispersed in H_2O (20 mL). This aqueous dispersion was added to a mixture of ethanol (120 mL), H_2O (76 mL), and aqueous NH_3 (5 mL, 25 wt%) under stirring. Then, APTES–FITC ethanol solution (16.5 mL, prepared by Method C) was added and the mixture was stirred overnight under argon. Fe_3O_4@SiO_2@APTES–FITC nanoparticles were recovered after centrifugation and washed twice with water and twice with ethanol before vacuum drying. In the last step, TEOS (1 mL) was dissolved in dry ethanol (10 mL) under nitrogen. The resulting solution (5 mL) was added to a mixture of H_2O (38 mL), aqueous NH_3 (3.3 mL, 25 wt%), and a dispersion of Fe_3O_4@SiO_2@APTES–FITC in ethanol (76 mL). The hydrolysis–condensation reaction was carried out under vigorous stirring for 4 h; Fe_3O_4@SiO_2@APTES–FITC@SiO_2 nanoparticles were recovered after centrifugation and washed twice with water and twice with ethanol before vacuum drying.

Synthesis of MFN2: In a typical procedure, **MNP2** (3 mg) were dispersed in cyclohexane (46 mL) at room temperature. Then, Triton X-100 (12 g), 1-hexanol (9.6 mL), deionized water (2.04 mL), and TEOS (240 μL) were added under nitrogen with continuous and regular magnetic stirring at 190 ± 5 rpm. After one night stirring to stabilize the microemulsion system, hydrolysis–condensation of TEOS was triggered by adding aqueous NH_3 (600 μL, ≈28–30 wt%). After 24 h, TEOS (180 μL) and ethanolic APTES–FITC solution (50 μL, prepared as described above either with method A or B) were added and the mixture was stirred for further 24 h, after which ethanol was added to destabilize the microemulsion system. **MFN2** were isolated by centrifugation and washed once with ethanol and once with water until they were finally redispersed in water and isolated by means of a permanent magnet. The aqueous supernatant was discarded and isolated **MFN2** were further washed with ethanol and vacuum dried.

Synthesis of MFN3: Commercial poly(ethylene glycol) monomethyl ether (MPEG) with an average molecular weight of 600 Da was converted to its amino-derivative. Briefly, MPEG (1.0 g) was vacuum dried overnight and dissolved under nitrogen in dry tetrahydrofuran (THF) (15 mL). Tetrachlorophtalimide (TCP, 3 equiv.) and resin-bound triphenylphosphine (3.3 equiv.) were added under stirring, then a solution of di-*tert*-butyl azadicarboxylate (DBAD) in dry THF (3.3 equiv. in 5 mL) was added dropwise. After 72 h, the mixture was filtered to remove the resin and concentrated with a rotary evaporator. The residue was diluted with CH_2Cl_2 and the resulting white precipitate was filtered off over a celite pad and abundantly washed with CH_2Cl_2. The

Table 1. Relaxivity measurements on labeled MCF7 cells.[a]

Concentration [cells mL^{-1}]	T_2 [ms][b]			
	MCF7 unlabeled	MFN2 [30 μg mL^{-1}]	MFN2 [50 μg mL^{-1}]	MFN3 [50 μg mL^{-1}]
5.0×10^6	2153 ± 16	851 ± 12	616 ± 10	1091 ± 15
1.0×10^6	2408 ± 21	1832 ± 15	1793 ± 14	2248 ± 22
5.0×10^5	2622 ± 23	1983 ± 14	1969 ± 16	2338 ± 22
2.5×10^5	2646 ± 29	2630 ± 27	2603 ± 24	2656 ± 32

[a] Data are the mean ± standard deviation of three different relaxivity measurements. [b] T_2 values correspond to progressive dilutions of an initial cell concentration after incubation with different concentrations and kinds of nanoparticles.

collected filtrate was concentrated to 10 mL CH_2Cl_2, then diethyl ether (30 mL) was added. The mixture was cooled down to 4 °C and kept at this temperature for 4 h to facilitate the precipitation of the PEG derivative. The white precipitate was recovered and vacuum dried. The deprotection of TCP–MPEG to yield the free amino derivative was effected on 400 mg of starting material, which was reacted with hydrazine hydrate (6 equiv.) in refluxing ethanol (40 mL) for 5 h. The deprotection was monitored by TLC (CH_2Cl_2/methanol 9:1) and visualized by ninhydrin. Finally, the solvent was evaporated and the residue was diluted with CH_2Cl_2 and washed three times with aqueous NaOH (5%). The organic layer was dried over Na_2SO_4, filtered, and evaporated yielding the amino–PEG derivative. Amino–**MFN2** (1 mg) was dispersed in 1 mL borate buffer (pH 7.2). A 5% glutaraldehyde solution (270 μL) in the same buffer was added under stirring. After 2 h, the particles were recovered by centrifugation and repeatedly washed with borate buffer to eliminate unreacted glutaraldehyde. This material was finally resuspended in the same medium (1 mL) and reacted overnight with an amino–PEG aqueous solution (20 mg in 3.5 mL). PEG-functionalized nanoparticles were recovered after centrifugation and washed once with borate buffer and once with acetate buffer (pH 5.0). A $NaBH_3CN$ solution (370 μL, 1 mg mL^{-1}) in acetate buffer was added to a nanoparticle suspension in the same medium (1 mL) and incubated for 3 h. After centrifuging, the particles were washed twice with CH_2Cl_2, once with ethanol, and vacuum dried.

Cell culture: MCF7 cells were grown in 50% Dulbecco's Modified Eagle's Medium (DMEM), 50% F12 (EuroClone Celbio, Milan, Italy) supplemented with 10% (v/v) fetal bovine serum (Hyclone Celbio, Milan, Italy), L-glutamine (2 mM), penicillin (50 UI mL^{-1}), and streptomycin (50 mg mL^{-1}) at 37 °C under a humidified 95%:5% (v/v) mixture of air and CO_2. NIH 3T3 cells were grown in DMEM, supplemented with 10% (v/v) fetal bovine serum, (Hyclone Celbio, Milan, Italy), L-glutamine (2 mM), penicillin (50 UI mL^{-1}), and streptomycin (50 mg mL^{-1}) at 37 °C under a humidified 95%:5% (v/v) mixture of air and CO_2. Cells were plated in six-well dishes at 90% of confluence and incubated for 1–3–5 h with **MFN2** and **MFN3** at the concentrations of 10 μg mL^{-1}, 30 μg mL^{-1}, and 50 μg mL^{-1} in completed culture medium.

Ultrastructural analysis (TEM): After the incubation time, cell pellets were washed in PBS (5 min, twice), fixed in 2.5% buffered glutaraldehyde, post-fixed in 1% osmium tetroxide, and embedded in epoxy resin (PolyBed 812 Polysciences Inc. USA). Ultrathin sections were stained with uranyl acetate and lead citrate and examined by means of TEM. TEM analysis was used to evaluate the intracellular presence of nanoparticles and study the different mechanisms of entry by comparison with literature data.[20,34]

Immunofluorescence: MCF7 cells grown on coverslips precoated with polylysine were washed free of the medium with PBS and fixed with and permeabilized in PBS 0.1% Triton at room temperature for 5 min. Samples were incubated with the primary antibodies in PBS 0.2% gelatin against the following antigens: early endosome antigen 1 (EEA1; BD Trasduction laboratories, Pharmingen San Jose, CA, USA), transferrin receptor (TfR; US Biological Swampscott, MA, USA), Cathepsin D (Cat D; Calbiochem International, CA, USA), and GM-130 (BD Transduction laboratories, Pharmingen, USA) in PBS 0.2% gelatin for 90 min at 22 °C, washed, and incubated for 90 min at 22 °C with the appropriate TRITC-conjugated secondary antibody. Subcellular antigen distribution was analyzed under a Leica SP2 AOBs microscope confocal system. Images were acquired with 63× magnification oil immersion lenses at 1024 × 1024 pixel resolution.

Cell death analysis: For cell-death experiments, the cells were treated as described above. After the incubation time, the cells were detached and stained with TRITC–annexin V 1:20 and 7-aminoactinomycin D 1:5 (BD Bioscience, San Jose, CA, USA) according to the kit's manufacturer's instructions and analyzed by flow cytometry in a FACStar Plus (Becton Dickinson, Sunnyvale, CA, USA) as described.[35] Therefore, we considered cell death as the populations positive for Annexin V and for 7AAD staining alone and together.

Cell proliferation assay: Cells were treated as described above. At the indicated time points cells were washed and 0.5 mL of 3-(4,5-dimethyl-2-thiazolyl)-2,5-diphenyl-2H-tetrazolium bromide (MTT) stock solution (2.4 mM in RPMI 1640 without phenol red, filtered) was added and the plates were incubated for a further 3 h at 37 °C.[36] At the end of the incubation the untransformed MTT was carefully removed and the dye crystals solubilized in 1 mL of 2-propanol. Absorbencies were read immediately in a UVKON 941 spectrophotometer using a test wavelength of 570 nm and a reference wavelength of 690 nm.

Statistical analysis: The results are expressed as means ± standard error of the mean (S.E.M.); *n* represents the number of individual experiments. Statistical analysis was carried out using the Student's *t*-test for unpaired variables (two-tailed). The asterisks in the figure panels refer to statistical probabilities (P) of <0.001, measured for the cells treated in the various experimental conditions versus control as described in details in the figure legends.

Acknowledgements

This work was supported by "Fondazione Romeo ed Enrica Invernizzi" and the CNR-Regione Lombardia "Mind in Italy" project.

[1] K. Riehemann, S. W. Schneider, T. A. Luger, B. Godin, M. Ferrari, H. Fuchs, *Angew. Chem. Int. Ed.* **2009**, *48*, 872–897.
[2] a) R. Weissleder, M. J. Pittet, *Nature* **2008**, *452*, 580–589; b) J.-L. Figueiredo, H. Alencar, R. Weissleder, U. Mahmood, *Int. J. Cancer* **2006**, *118*, 2672–2677.
[3] J. A. Witjes, J. Douglass, *Nat. Clin. Pract. Urol.* **2007**, *4*, 542–549;
[4] E. Sega, P. Low, *Cancer Metastasis Rev.* **2008**, *27*, 655–664.
[5] C. Catana, D. Procissi, Y. Wu, M. S. Judenhofer, J. Qi, B. J. Pichler, R. E. Jacobs, S. R. Cherry, *Proc. Natl. Acad. Sci. U. S. A.* **2008**, *105*, 3705–3710.
[6] *World Cancer Report* (Eds: B. W. Stewart, P. Kleihues), IARC Press, Lyon, France **2003**, pp. 11–19. Accessibility at the World Health Organization, International Agency for Research on Cancer, verified December 12, 2008.
[7] a) S. L. Parker, T. A. Tong, S. Bolden, P. A. Wingo, *CA-Cancer J. Clin.* **1996**, *46*, 5–27; b) Comment, *CA-Cancer J. Clin.* **1996**, *46*, 3–4.

[8] a) U. Veronesi, G. Paganelli, V. Galimberti, G. Viale, S. Zurrida, M. Bedoni, A. Costa, C. de Cicco, J. G. Geraghty, A. Luini, V. Sacchini, P. Veronesi, *Lancet* **1997**, *349*, 1864–1867; b) G. Viale, S. Bosari, G. Mazzarol, V. Galimberti, A. Luini, P. Veronesi, G. Paganelli, M. Bedoni, E. Orvieto, *Cancer* **1999**, *85*, 2433–2438; c) U. Veronesi, G. Paganelli, G. Viale, V. Galimberti, A. Luini, S. Zurrida, C. Robertson, V. Sacchini, P. Veronesi, E. Orvieto, C. De Cicco, M. Intra, G. Tosi, D. Scarpa, *J. Natl. Cancer Inst.* **1999**, *91*, 68–73.
[9] a) A. Shoher, A. Diwan, B. S. Teh, H. H. Lu, R. Fisher, A. Lucci, Jr., *Curr. Surg.* **2006**, *63*, 207–212; b) K. M. McMasters, T. M. Tuttle, D. J. Carlson, C. M. Brown, R. D. Noyes, R. L. Glaser, D. J. Vennekotter, P. S. Turk, P. S. Tate, A. Sardi, P. B. Cerrito, M. J. Edwards, *J. Clin. Oncol.* **2000**, *18*, 2560–2566.
[10] M. G. Harisinghani, J. Barentsz, P. F. Hahn, W. M. Deserno, S. Tabatabaei, C. H. van de Kaa, J. de la Rosette, R. Weissleder, *N. Engl. J. Med.* **2003**, *348*, 2491–2499.
[11] M. Lewin, N. Carlesso, C.-H. Tung, X.-W. Tang, D. Cory, D. T. Scadden, R. Weissleder, *Nat. Biotechnol.* **2000**, *18*, 410–414.
[12] J. P. Fortin, C. Wilhelm, J. Servais, C. Menager, J. C. Bacri, F. Gazeau, *J. Am. Chem. Soc.* **2007**, *129*, 2628–2635.
[13] C. G. Hadjipanayis, M. J. Bonder, S. Balakrishnan, X. Wang, H. Mao, G. C. Hadjipanayis, *Small* **2008**, *4*, 1925–1929.
[14] A. Gupta, A. Curtis, *J. Mater. Sci.: Mater. Med.* **2004**, *15*, 493–496.
[15] M. Chorny, B. Polyak, I. S. Alferiev, K. Walsh, G. Friedman, R. J. Levy, *FASEB J.* **2007**, *21*, 2510–2519.
[16] H. Gu, K. Xu, C. Xu, B. Xu, *Chem. Commun.* **2006**, 941–949.
[17] S. Mornet, S. Vasseur, F. Grasset, E. Duguet, *J. Mater. Chem.* **2004**, *14*, 2161–2175.
[18] J. Horton, *Cancer Control.* **2001**, *8*, 103–110.
[19] a) M. Ferrari, *Nat. Nanotechnol.* **2008**, *3*, 131–132; b) W. Jiang, Y. S. KimBetty, J. T. Rutka, W. C. W. Chan, *Nat. Nanotechnol.* **2008**, *3*, 145–150; c) E. Tasciotti, X. Liu, R. Bhavane, K. Plant, A. D. Leonard, B. K. Price, M. M.-C. Cheng, P. Decuzzi, J. M. Tour, F. Robertson, M. Ferrari, *Nat. Nanotechnol.* **2008**, *3*, 151–157.
[20] S. E. A. Gratton, P. A. Ropp, P. D. Pohlhaus, J. C. Luft, V. J. Madden, M. E. Napier, J. M. DeSimone, *Proc. Natl. Acad. Sci. U. S. A.* **2008**, *105*, 11613–11618.
[21] S. C. Wuang, K. G. Neoh, E.-T. Kang, D. W. Pack, D. E. Leckband, *Biomaterials* **2008**, *29*, 2270–2279.
[22] C. W. Lu, Y. Hung, J. K. Hsiao, M. Yao, T. H. Chung, Y. S. Lin, S. H. Wu, S. C. Hsu, H. M. Liu, C. Y. Mou, C. S. Yang, D. M. Huang, Y. C. Chen, *Nano Lett.* **2007**, *7*, 149–154.
[23] D. Ma, J. Guan, F. Normadin, S. Denommee, G. Enright, T. Veres, B. Simard, *Chem. Mater.* **2006**, *18*, 1920–1927.
[24] H. Ow, D. R. Larson, M. Srivastava, B. A. Baird, W. Webb, U. Wiesner, *Nano Lett.* **2005**, *5*, 113–117.
[25] S. Corr, Y. Rakovich, Y. Gun'ko, *Nanoscale Res. Lett.* **2008**, *3*, 87–104.
[26] Y. Piao, A. Burns, J. Kim, U. Wiesner, T. Hyeon, *Adv. Funct. Mater.* **2008**, *18*, 3745–3758.
[27] L. Polito, M. Colombo, D. Monti, S. Melato, E. Caneva, D. Prosperi, *J. Am. Chem. Soc.* **2008**, *130*, 12712–12724.
[28] T. M. Riddick, *Control of Colloid Stability through Zeta Potential*, Zeta-Meter Inc., New York **1968**.
[29] R. Sjöback, J. Nygren, M. Kubista, *Biopolymers* **1998**, *46*, 445–453.
[30] R. Mukhopadhyay, R. L. Theriault, J. E. Price, *Clin. Exp. Metastasis* **1999**, *17*, 325–332.
[31] C. Wilhelm, C. Billotey, J. Roger, J. N. Pons, J.-C. Bacri, F. Gazeau, *Biomaterials* **2003**, *24*, 1001–1011.
[32] S. Falcone, E. Cocucci, P. Podini, T. Kirchhausen, E. Clementi, J. Meldolesi, *J. Cell Sci.* **2006**, *119*, 4758–4769.
[33] S. Y. Yu, H. J. Zhang, J. B. Yu, C. Wang, L. N. Sun, W. D. Shi, *Langmuir* **2007**, *23*, 7836–7840.
[34] a) J. Dausend, A. Musyanovych, M. Dass, P. Walther, H. Schrezenmeier, K. Landfester, V. Mailänder, *Macromol. Biosci.* **2008**, *8*, 1135–1143; b) M. A. Dobrovolskaia, S. E. McNeil, *Nat. Nanotechnol.* **2007**, *2*, 469–478.
[35] a) D. P. Steensma, M. Timm, T. E. Witzig, *Methods Mol. Med.* **2003**, *85*, 323–332; b) C. Sciorati, B. G. Galvez, S. Brunelli, E. Tagliafico, S. Ferrari, G. Cossu, E. Clementi, *J. Cell Sci.* **2006**, *119*, 5114–5123.
[36] C. Sciorati, G. Nisticò, J. Meldolesi, E. Clementi, *Br. J. Pharmacol.* **1997**, *122*, 687–697.

Received: May 25, 2009
Published online: July 24, 2009

Submitted to small NANO MICRO

Supporting Information

Towards Ideal Magnetofluorescent Nanoparticles for Bimodal Detection of Breast Cancer Cells

Fabio Corsi,[1] Clara De Palma,[2,3] Miriam Colombo,[4] Raffaele Allevi,[1] Manuela Nebuloni,[1] Silvia Ronchi,[5] Giuseppina Rizzi,[5] Antonella Tosoni,[1] Emilio Trabucchi,[1] Emilio Clementi,[2,3,*] and Davide Prosperi[4,5,*]

[1] *Dipartimento di Scienze Cliniche "Luigi Sacco", Università degli Studi di Milano, Ospedale L. Sacco, Via G.B. Grassi 74, 20157 Milano (Italy).*

[2] *Dipartimento di Scienze Precliniche Lita Vialba, Università degli Studi di Milano, Ospedale L. Sacco, Via G.B. Grassi 35, 20157 Milano (Italy). Tel: (+39)0250319683, Fax: (+39)0250319682. *E-mail: emilio.clementi@unimi.it*

[3] *IRCCS E. Medea, Via Don L. Monza 20, 23842 Bosisio Parini (Lecco) (Italy).*

[4] *Dipartimento di Biotecnologie e Bioscienze, Università degli Studi di Milano-Bicocca, Piazza della Scienza 2, 20126 Milano (Italy). Tel: (+39)0264483401, Fax: (+39)0264483565. *E-mail: davide.prosperi@unimib.it*

[5] *Istituto di Scienze e Tecnologie Molecolari, CNR, Via Golgi 19, 20133 Milano (Italy).*

Submitted to small NANO MICRO

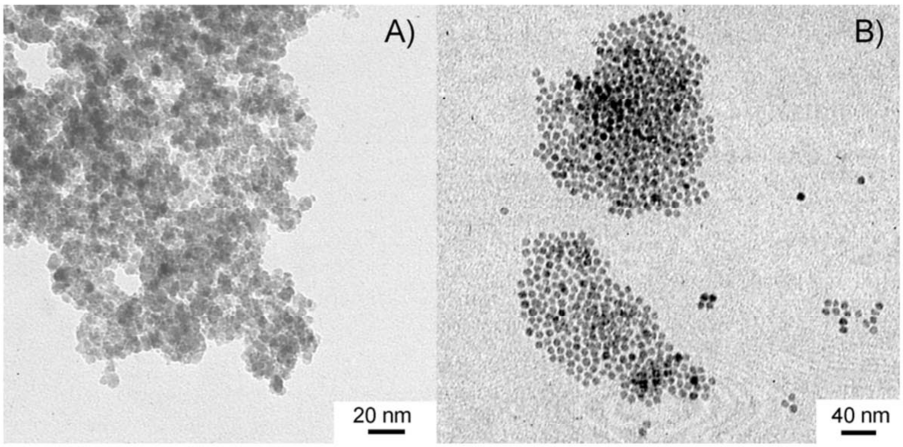

Figure S1. TEM images of A) an aqueous dispersion of bare Fe_3O_4 nanoparticles, obtained by coprecipitation of $FeCl_2 \cdot 4H_2O$ and $FeCl_3 \cdot 6H_2O$ (**MNP1**), and B) an illustrative hexane dispersion of surfactant-coated Fe_3O_4 nanoparticles obtained by solvothermal decomposition in high-boiling organic solvents (**MNP2**).

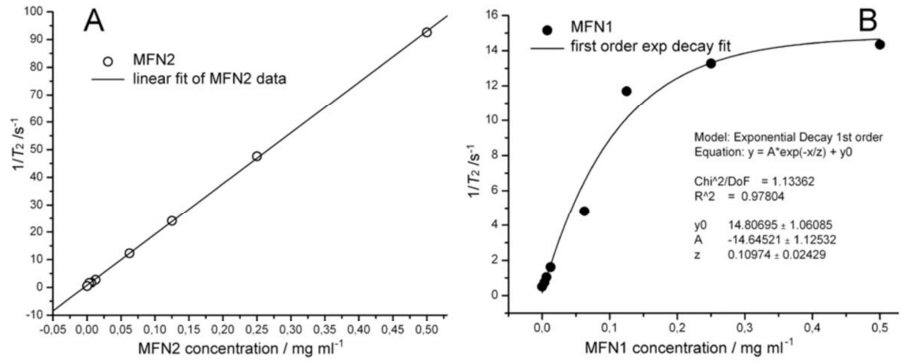

Figure S2. Relaxometric analyses of **MFN2** (empty dots, A) and **MFN1** (full dots, B) within the range 0-0.5 mg mL^{-1}. While **MFN2** maintain the linear behaviour within the entire concentration range, the **MFN1** trend is better fitted by an exponential decay above 0.3 mg mL^{-1}, thus showing a reduced magnetic stability in concentrated dispersion.

Submitted to small NANO MICRO

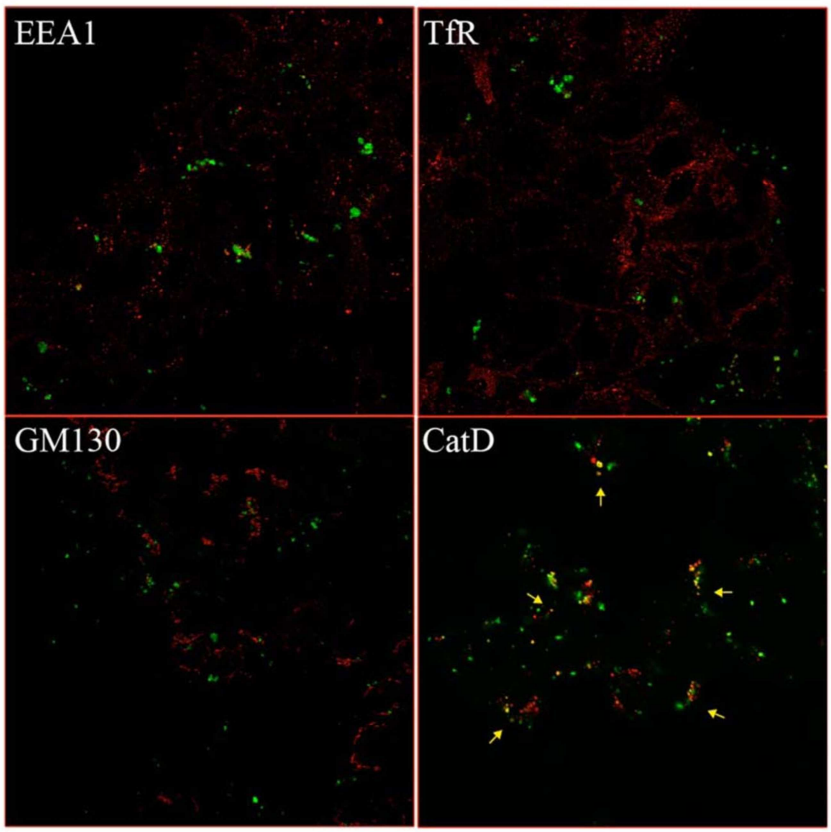

Figure S3. Intracellular localization of **MFN3** in NIH 373 cells. Incubations were for 5 h with 50 μg mL^{-1} of **MFN3**. Images are representative of four reproducible experiments and reveal the localization of **MFN3**, identified by their green fluorescence versus that of the early endosome marker EEA1, the recycling endosome marker TfR, the lysosomal protein Cat D and the Golgi marker GM-30, labeled using secondary, TRITC-conjugated Abs (red). Scale bar: 10 μm.

ARTICLE 2

ARTICLE 3

Analytical Biochemistry 392 (2009) 96–102

Contents lists available at ScienceDirect

Analytical Biochemistry

journal homepage: www.elsevier.com/locate/yabio

Femtomolar detection of autoantibodies by magnetic relaxation nanosensors

Miriam Colombo [a], Silvia Ronchi [b], Diego Monti [b], Fabio Corsi [c], Emilio Trabucchi [c], Davide Prosperi [a,b,*]

[a] Dipartimento di Biotecnologie e Bioscienze, Università di Milano-Bicocca, 20126 Milano, Italy
[b] Istituto di Scienze e Tecnologie Molecolari, CNR, 20138 Milano, Italy
[c] Dipartimento di Scienze Cliniche "Luigi Sacco," Università di Milano, 20157 Milano, Italy

ARTICLE INFO

Article history:
Received 27 April 2009
Available online 27 May 2009

Keywords:
Nanosensor
Biorecognition
Autoantibodies
T_2 relaxivity
Magnetic nanoparticles

ABSTRACT

The development of nanosystems applied to rapid and sensitive measurement of biomarkers in fluid samples is a current major goal in diagnostic biomedicine. In this article, we report the accurate and reliable detection of anti-HSA (human serum albumin) antibodies by protein-functionalized magnetic nanospherical probes due to the reversible alteration of their microaggregation state induced by protein antibody-specific interaction, sensed as changes in the T_2 relaxation time of surrounding water molecules. Once the optimal parameters were adjusted, the method proved to be very sensitive, providing concentration- and time-dependent responses. Furthermore, we demonstrate that the developed immunoassay is able to quantitatively determine the biomarker concentration from T_2 linear correlation, thereby supplying a rapid, yet accurate, assay with sensitivity in the femtomolar range. The high susceptibility and stability of these magnetic nanoparticles, as well as their accessible synthetic preparation, make these nanosensors a promising new tool for versatile and effective medical diagnostics.

The rapid and accurate detection of specific biomarkers in fluid samples for the purpose of monitoring treatment and diagnosing pathologies is an open challenge in the field of biomedicine. During recent years, a number of diagnostic tools have been developed to measure the abundance of pathogen that enable the early detection of diseases [1–4]. Human serum albumin (HSA)[1] is the most abundant serum protein in the human circulatory system. It is well documented that a few largely widespread diseases consist of anomalous concentrations of anti-HSA antibodies (Abs) as a consequence of pathological changes of the systemic condition that cause the extracellular proteins to become antigenic. The alterations in the conformation and the biological properties of HSA are usually triggered by protein oxidation [5] due mainly to the undesired presence of reactive oxygen species. Indeed, protein oxidation phenomena are generally associated with cellular functional disruption along with many other protein conformational changes. There are several studies that provide evidence that such protein oxidation is often associated with cellular disorder observed during aging and age-related neurodegenerative diseases, including Alzheimer and Parkinson diseases [6]. Although the circulating autoantibodies exhibit reactivity against both native and modified proteins, modified HSA appears to be highly immunogenic compared with native HSA [7]. A number of studies point to type 1 diabetes mellitus [8], familial dysautonomia [9], and liver failure [10] as the main pathologies in which a remarkable occurrence of anti-HSA Abs is observed, with the concentration of anti-HSA Abs in diabetic patients being 5–20 times greater than in healthy subjects. Within this context, the application of a method for rapid, sensitive, and selective detection of anti-HSA Abs in solution could be beneficial in providing a diagnostic agent for preclinical investigations and clinical use.

The conjugation of various biomolecules to different kinds of nanoparticles has led to the creation of hybrid bioorganic–inorganic nanocomposites that indicate biorecognition capabilities as well as unique photonic, magnetic, or electronic properties, the fine modulation of which can be usefully exploited in biosensing [11–13]. These biocomposite nanomaterials provide a powerful tool for the investigation of the biointeractions, which are fundamental for cell functionality as well as for modern diagnostic techniques and new therapeutic outlooks. In this context, magnetic nanoparticles (MNPs) based on iron oxides look particularly promising due to their peculiar properties that have recently led to many technological and biomedical applications, including targeted drug delivery and their use as contrast agents in magnetic resonance imaging (MRI) and biosensing [14–19].

In the current study, we report on a novel application of hybrid core–shell MNPs for the rapid and sensitive detection of anti-HSA

* Corresponding author. Address: Dipartimento di Biotecnologie e Bioscienze, Università di Milano-Bicocca, Piazza della Scienza 2, 20126 Milano, Italy. Fax: +39 0264483565.
E-mail address: davide.prosperi@unimib.it (D. Prosperi).

[1] *Abbreviations used:* HSA, human serum albumin; Ab, antibody; MNP, magnetic nanoparticle; MRI, magnetic resonance imaging; SPION, superparamagnetic iron oxide nanoparticle; TEM, transmission electron microscopy; NMR, nuclear magnetic resonance; PTFE, polytriflouroethylene; TEOS, tetraethyl orthosilicate; APTES, aminopropyl triethoxysilane; SMNP, silica-encapsulated magnetic nanoparticle; BB, borate buffer; MNS, magnetic nanosensor; TLC, thin-layer chromatography.

0003-2697/$ - see front matter © 2009 Elsevier Inc. All rights reserved.
doi:10.1016/j.ab.2009.05.034

Abs that have the potential to offer a robust diagnostic device by measuring subtle changes in the spin–spin relaxation times (T_2) induced on the adjacent water protons by the presence of Ab-mediated nanoparticle clusters. During recent years, considerable efforts have been made by the research groups of Weissleder and Josephson to develop iron oxide-based molecular nanoswitches exploiting the effect of reducing the T_2 of the water protons as a consequence of the formation of aggregates of controlled size mediated by the occurrence of tridimensional-specific interactions. In particular, superparamagnetic iron oxide nanoparticles (SPIONs) have been demonstrated to be potent enhancers of the spin–spin relaxation processes. The effect of SPIONs on T_2 is caused by the large difference in susceptibility between the nanoparticles and the surrounding medium, resulting in microscopic magnetic field gradients. The diffusion of protons through these field gradients leads to a loss of phase coherence of the proton magnetic moments and, thus, decreases the transverse relaxation times of adjacent protons. Interestingly, this pronounced T_2 effect is significantly affected by the aggregation state of the SPION dispersion. When clustering is induced by the specific binding of a multivalent biomolecule, such agglomeration can be detected by relaxometric analysis of the nanoparticle dispersion and the biomolecules can be detected. Using this approach, DNA, proteins, glucose, and viruses were investigated [20–24]. In a recent preliminary communication, we synthesized HSA-conjugated iron oxide nanoparticles and evaluated them as sensors of the presence of the corresponding Ab [25]. Our aim in that work was to evaluate the residual activity of the conjugated protein. However, the poor stability of such nanoparticle dispersion meant that we were able to obtain qualitative information only on the presence/absence of the biomolecular counterpart in solution. In the current study, we have optimized the stability of the HSA-functionalized nanoparticle system by incorporating clusters of multiple magnetite nanocrystallites in a spherical silica matrix, enabling us to obtain a quantitative determination of anti-HSA Abs.

Materials and methods

General methods and instrument details

Solvents and chemicals, HSA, and anti-HSA polyclonal Abs were purchased from Sigma–Aldrich (St. Louis, MO, USA), Fluka (St. Gallen, Switzerland), and Riedel–de Haën (Seelze, Germany) and were used as received without further purification. Anti-rabbit immunoglobulin G (IgG) secondary Ab was obtained from GE Healthcare (Hampshire, UK). Water was deionized and ultrafiltered by a Milli-Q apparatus from Millipore (Billerica, MA, USA). Dynamic light scattering measurements were performed at 90° with a 90Plus Particle Size Analyzer from Brookhaven Instruments (Holtsville, NY, USA) working at 15 mW of a solid-state laser (λ = 661 nm). For transmission electron microscopy (TEM) analysis, nanoparticles were dispersed in ethanol (50 μg ml^{-1}) and a drop of the resulting solution was placed on a Formvar/carbon-coated copper grid and air-dried. TEM images were obtained by a Zeiss EM-109 microscope (Oberkhochen, Germany) operating at 80 kV. T_2 relaxation times were acquired at a temperature of 313 K using a Bruker Minispec mq20 system (Ettlingen, Germany) working with ^{1}H at 20 MHz magnetic field with the following parameters: CMPG pulse sequence, 1000 echoes, with a 20-ms echo time and a 2-s repetition time. Samples were introduced using 10-mm nuclear magnetic resonance (NMR) tubes prewarmed and sonicated in a S15H Elmasonic apparatus (Elma, Singen, Germany).

Preparation of silica-encapsulated magnetic nanoparticles

Oleylamine-coated MNPs were synthesized according to a previously reported protocol [26,27] and were stored as an oleic acid-stabilized dispersion in *n*-hexane (2 mg ml^{-1}). Just before use, a suitable amount of this dispersion was syringe-filtered through 0.2 μm porous polytriflouroethylene (PTFE) septa, and the nanoparticles were precipitated with ethanol, recovered by centrifugation, and vacuum-dried. MNPs were used as starting nucleation materials for the preparation of composite nanoparticles. In a typical procedure, Fe_3O_4 nanoparticles (3 mg) were dispersed in cyclohexane (46 ml) at room temperature. Triton X-100 (12 g), 1-hexanol (9.6 ml), deionized water (2.04 ml), and tetraethyl orthosilicate (TEOS, 240 μl) were added under nitrogen with continuous and regular magnetic stirring at 190 ± 5 rpm. After 1 night of stirring to stabilize the microemulsion system, hydrolysis–condensation of TEOS was triggered by adding aqueous ammonia (600 μl, 28–30 wt%). After 24 h, TEOS (180 μl) and 50 μl of an ethanolic solution of aminopropyl triethoxysilane (APTES), obtained by dissolving 25 ml of APTES in 1μl of EtOH, were added and the mixture was stirred for a further 24 h, after which ethanol was added to destabilize the microemulsion system. Silica-encapsulated magnetic nanoparticles (SMNPs) were recovered by centrifugation and washed once with ethanol and twice with water. The nanoparticles were finally redispersed in water and isolated by means of a permanent magnet. The aqueous supernatant was discarded, and the isolated SMNPs were washed further with ethanol and vacuum-dried.

Synthesis of HSA-biofunctionalized magnetic nanosensors

SMNPs (2 mg) were dispersed in borate buffer (BB, pH 7.4, 400 μl) and magnetically stirred. To this suspension, a solution of glutaraldehyde (5% in borate buffer, 1.3 ml) was added and the mixture was stirred for 2 h, after which the particulate was centrifuged. The precipitate was washed three times with BB and finally resuspended in BB (4 ml). A solution of HSA in BB (2 mg ml^{-1}, 2.5 ml) was added to the nanoparticle suspension, and the mixture was stirred for 3 h, after which a solution of lysine in BB (2 mg ml^{-1}, 3.5 ml) was added. The mixture was reacted for 24 h, centrifuged to yield a nanoparticle precipitate (magnetic nanosensor [MNS]) that was washed four times with BB (until thin-layer chromatography [TLC] of the supernatant visualized by ninhydrin confirmed the absence of free amino groups), and finally separated from the solution by means of a permanent magnet.

Measurement of proton transverse relaxation times

Proton relaxation time (T_2) measurements were performed at 313 K in a 0.47-T Bruker Minispec mq20 relaxometer. Nanoparticle samples were incubated at 313 K for 10 min for thermal equilibration before the addition of anti-HSA Ab solutions. MNS starting samples were prepared by diluting 66 μl of MNS solution (1 mg ml^{-1} in BB) with 2964 μl of BB to give a final MNS concentration of 21.8 μg ml^{-1}. To these samples, a 13-μl volume of nine differently concentrated anti-HSA Ab solutions was added, giving final Ab concentrations ranging from 10 fM to 1 μM. Reported concentrations are the final analyte concentrations obtained after mixing. Relaxivity was determined as the slope of a $1/T_2$ plot as a function of the nanoparticle concentration expressed in μg ml^{-1}.

Results and discussion

Synthesis and characterization of HSA-functionalized magnetic nanosensors

We developed SMNPs that were designed in a core–shell fashion, resulting in uniform nanoparticles of approximately 70 nm in diameter with a nearly spherical morphology (Fig. 1). The

corresponding hydrodynamic diameter was 110 nm, as determined by dynamic light scattering, and the magnetic core consisted of a cluster of multiple MNPs embedded in a 20-nm-thick silica shell. This composite structure has the effect of enhancing the relative transverse relaxivity compared with a model consisting of a single iron oxide nanocrystal per particle. The silica coating was obtained by reaction confinement within the submicrometer domain of a water-in-oil microemulsion system using surfactant-coated monocrystalline Fe_3O_4 nanoparticles as starting material and a mixture of TEOS and APTES as coating agents so as to provide surface available amino groups.

We were interested in evaluating the magnetic properties of the as-synthesized SMNPs for relaxometric tasks. To reach this aim, we performed a set of relaxation experiments to determine the respective T_2-enhancing capabilities of the composite nanoparticles. Conventionally, the transverse relaxivity r_2 is defined as the slope obtained by plotting $1/T_2$ versus iron concentration. Nevertheless, in this case we preferred to refer r_2 to the SMNP concentration for practical purposes. To assess the minimal useful SMNP concentration for biosensing analysis, we first evaluated the range of concentrations within which the signal was suitably stable. Fig. 2 illustrates the r_2 trend of SMNPs in the range of 0–250 μg ml^{-1}. The linear fit is very confident between 20 and 250 μg ml^{-1} (R^2 = 0.999), providing an r_2 value of 0.188 mg^{-1} ml s^{-1}. In contrast, such a linear slope was not confirmed below the 20–μg ml^{-1} threshold (inset in Fig. 2). In accordance with our expectations, as the T_2 value increases by decreasing iron concentration, we observed a proportional T_2 decrease by increasing the SMNP amount in solution. As noted previously, the ideal Fe concentration for clustering measurements by magnetorelaxometry is the same as the one providing a T_2 value of at least 160 ms [28]. For this reason, we chose the concentration of 21.8 μg ml^{-1} (T_2 = 328 ms) as the best compromise between signal intensity and particle stability.

Bioconjugated MNSs were obtained by surface functionalization of SMNPs with HSA using glutaraldehyde as a homobifunctional crosslinking agent (see Fig. 3). Unreacted amino groups on the nanoparticles were saturated with an excess of lysine to avoid successive glutaraldehyde-mediated interparticle crosslinking that would have resulted in the irreversible formation of large particle agglomerates.

Sensing anti-HSA Abs by T_2 relaxometry

When the magnetic nanosensors were used to probe the presence of specific Abs in diluted solution, significant T_2 relaxation time changes were observed in response to the Ab-mediated formation of nanoparticle aggregates. These T_2 alterations were time and dose dependent.

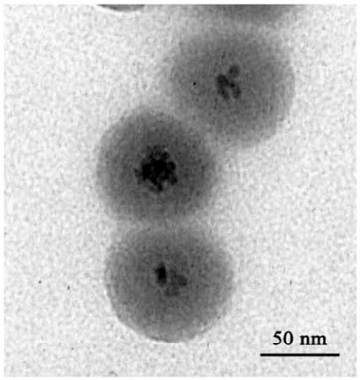

Fig. 1. Transmission electron micrographs of SMNPs in ethanol. Contrasted silica shell and Fe_3O_4 nanoparticles core are visible.

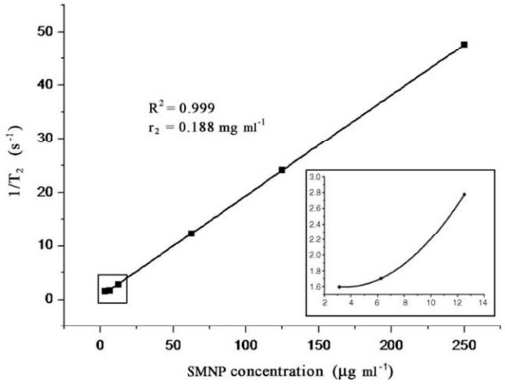

Fig. 2. T_2 relaxometry analysis of as-synthesized SMNPs. The inverse of experimental T_2 values obtained at different SMNP concentrations is plotted versus particle concentration (μg ml^{-1}). The experimental data are fitted by a line in the range of 20–250 μg ml^{-1}. The T_2 relaxivity is indicated by the line slope. Inset: magnification of the selected region, point fitting in the range of 3–13 μg ml^{-1}.

First, we performed a set of measurements to evaluate the temporal change of water T_2 relaxation time induced by MNSs (21.8 μg ml^{-1}) in the presence of 100 pM target complementary polyclonal Ab. Fig. 4A depicts the time course of T_2 relaxation correlating to the evolution of MNS nanoassemblies. The presence of agglomeration was detected sensitively by the kinetic properties of HSA-functionalized nanoparticles. When MNSs bound the intended molecular target (i.e., the specific anti-HSA Abs), they formed soluble nanoscale clusters, leading to a relevant decrease in the bulk spin–spin relaxation time of surrounding water molecules by more than 40 ms (t_m). The subsequent formation of larger aggregates of particles reversed this effect, causing a detectable increment of spin–spin relaxation time up to a T_2 value approximating the baseline (t_M). Indeed, owing to magnetite high density (5.2 g ml^{-1}), large MNS clusters induced a loss of the colloidal status of the particulate, thereby sequestrating active contrast agent as sensed by water protons, which significantly influenced the overall relaxation rates. We then investigated the Ab displacement by adding an excess of free HSA, which reacted with the Abs involved in the MNS agglomerates. The redispersed smaller MNS clusters released by aggregates again induced a decrease in T_2 down to a t_1 limit corresponding to t_m. Afterward, a further increment in T_2 related to the formation of MNS monomers was observed until an equilibrium between the Abs and the HSA excess in solution was established (t_2) up to a T_2 value approaching the baseline t_0. Fig. 4B represents the nanoparticle aggregation states corresponding to each consecutive stage outlined in Fig. 4A on a schematic basis.

As negative control, two supplementary experiments were carried out using (i) deionized water and (ii) a 10-pM solution of IgG secondary Ab, which were added to the initial MSN sample. In both cases, no T_2 alteration occurred, confirming that the previously observed effect was indeed mediated by specific recognition, whereas it was not recovered in the absence of the complementary Ab.

In a second set of experiments, we acquired eight different T_2 sequences, each within a 3-min period at 1-min intervals, corresponding to eight different anti-HSA Ab concentrations in the range of 1 μM to 100 fM (Fig. 5). Eight batches containing a

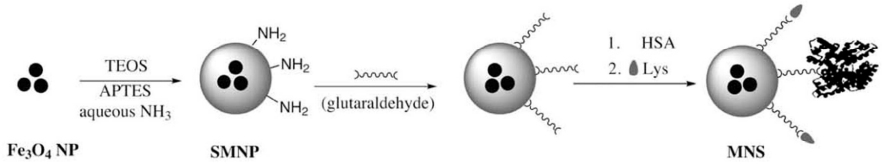

Fig. 3. Illustrative strategy for the synthesis of MNS. NP, nanoparticle.

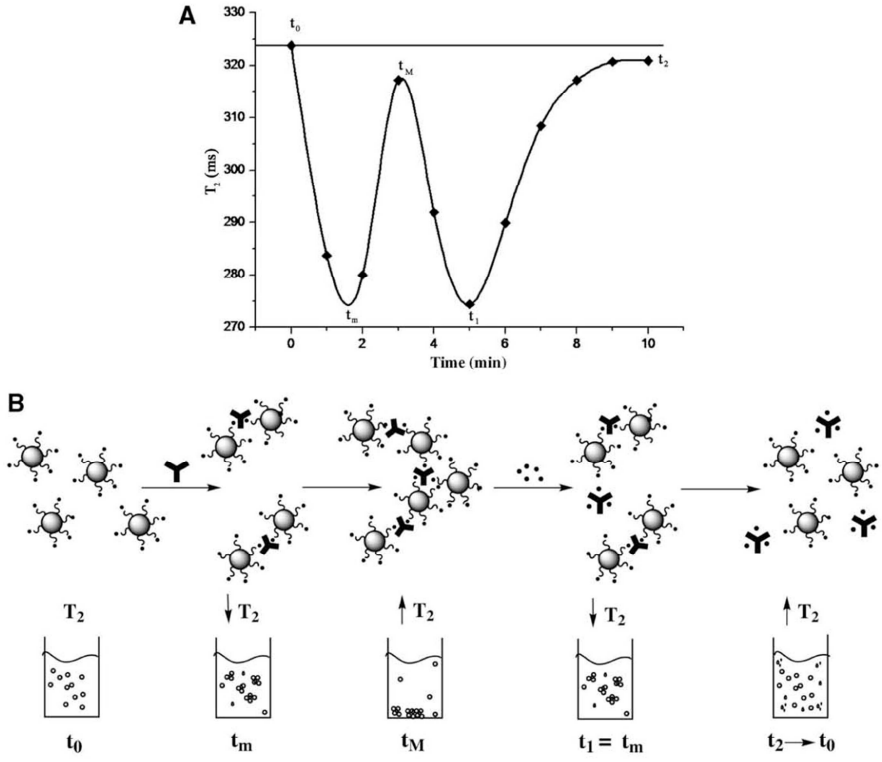

Fig. 4. (A) Time course of changes in water T_2 using 21.8 μg ml^{-1} MNS in the presence of 100 pM anti-HSA Abs. At t_M, 200 μl of HSA (1 mg ml^{-1}) was added. (B) Schematic of the particle aggregation sequence in response to the addition/subtraction of anti-HSA Abs. t_0, t_m, t_M, t_1, and t_2 values refer to the corresponding T_2 states outlined in panel A.

mixture of the MNS dispersion and anti-HSA Abs at concentrations of 1 μM, 100 nM, 10 nM, 1 nM, 100 pM, 10 pM, 1 pM, and 100 fM, respectively, were obtained by Ab additions of diluted aliquots from a mother solution of 2.75 mg ml^{-1} Abs in BB. All of the experiments were repeated in triplicate, with a standard deviation (SD) that varied in the range of 5–12 ms for each acquisition. Depending on the individual Ab concentration, different behaviors in the plotted T_2 versus time were evidenced. Fig. 5A displays a continuously increasing slope from an initial T_2 value of 328 ± 3 ms at $t = 0$ (T_2 before the addition of Abs). Note that T_2 at t_0 was normalized to this initial value also in the following sequences (maximal experimental SD of ±9 ms). In this first case, the significant amount of Ab solution triggered the immediate immunoprecipitation of MNSs, resulting in the rapid formation of large nanoparticle aggregates. Fig. 5B–G show a pseudo-parabolic lineshape, with an initial decrement analogous to that observed in the first part of the curve reported in Fig. 4A. It is notable that the position of the minimum in each curve shows a tendency to shift toward higher time values in dependence of Ab dilution. As expected, the kinetics of formation of "highest contrast" clusters, corresponding to the minimum in the curve, is slowed down by decreasing the probability of interaction of MNSs with Ab molecules in solution. Beyond the minimum, the slope of the curve exhibits a gradually increasing gradient that is associated with the slow formation of bulky immunoprecipitated aggregates. At femtomolar Ab concentrations (Fig. 5H), an anomalous lineshape was noticed, with a remarkable change in the slope after 2 min approximating an asymptotic plateau. This was probably due to the fact that the Ab molecules were so diluted that they were quickly withdrawn from the solution, resulting in aggregates of controlled average size, and the T_2 value soon reached a plateau. Eventually, we evaluated the minimal concentration at which the T_2 effect was detectable, and we found that

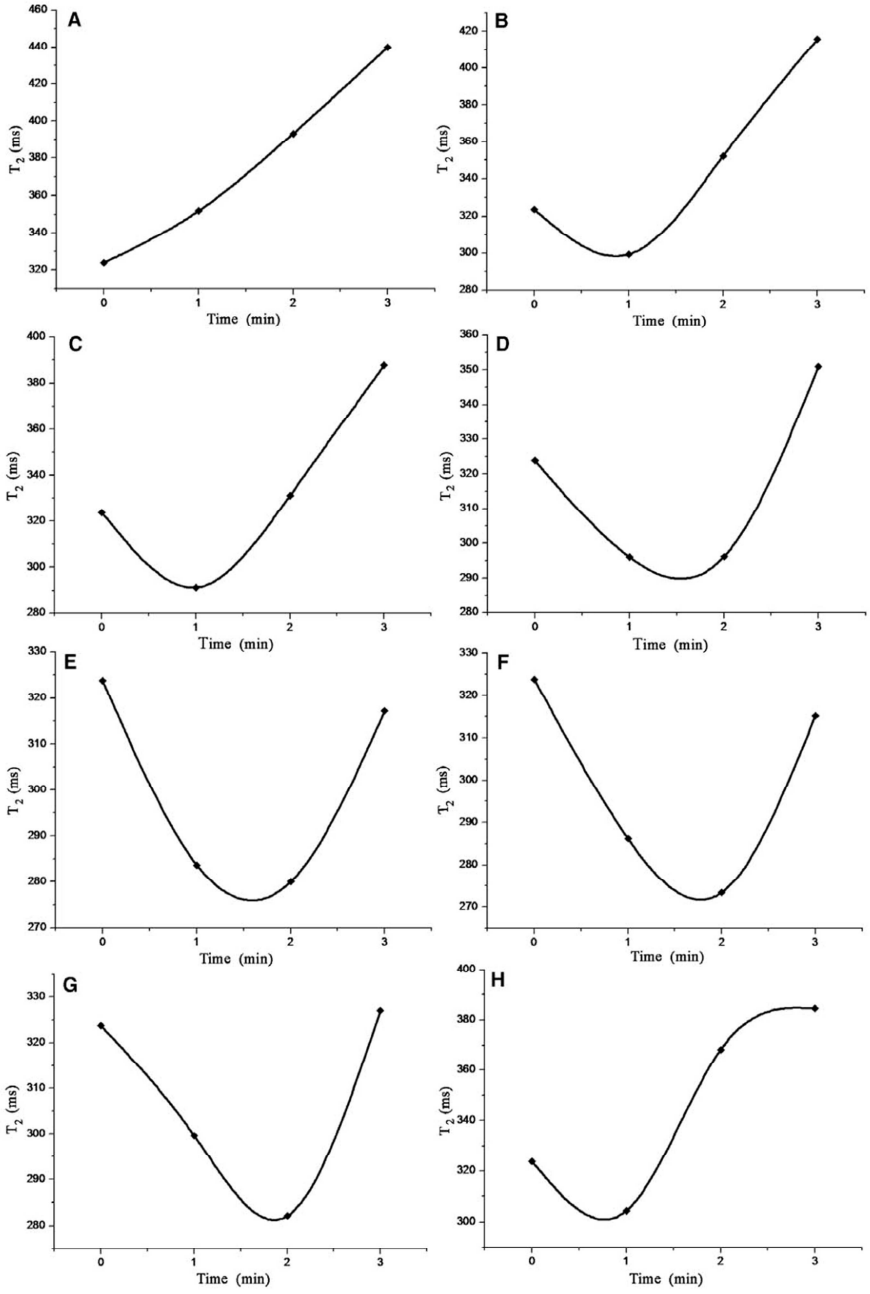

Fig. 5. Time-depending changes in T_2 resulting from the aggregation states induced by different anti-HSA Ab concentrations: (A) 1 μM; (B) 100 nM; (C) 10 nM; (D) 1 nM; (E) 100 pM; (F) 10 pM; (G) 1 pM; (H) 100 fM. All experiments were performed in triplicate with SDs varying from 5 to 12 ms.

above a concentration of 10 fM no further T_2 variation was observed.

The above-mentioned results demonstrate that an important feature of our nanodevice concerns the sensitivity of this method.

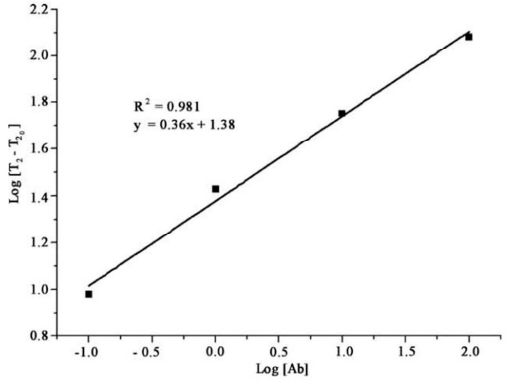

Fig. 6. Logarithmic plot of relaxometric analysis of MNS incubated with different concentrations of anti-HSA Abs. Units for $T_2 - T_{2_0}$ and [Ab] are s and $\mu g\,ml^{-1}$, respectively.

The reported nanoassembly of MNPs enables a rapid, reliable, sensitive, and selective detection of a ligand in solution, allowing the direct detection of concentrations as low as a few tenths of femtomolar of reagent without the need for amplification.

A further major advance of our MNS-based method is that the T_2 relaxometry experiment can be used to determine concentrations of a specific target quantitatively when its concentration is not known a priori. As illustrated in Fig. 6, we first obtained a standard calibration curve by plotting $\log(T_2 - T_{2_0})$ versus log[Ab], where the Ab concentration is expressed in $\mu g\,ml^{-1}$ and T_{2_0} is a fitting parameter useful for normalization. The standard function reported in Fig. 6 allowed us to quantify the Ab concentration in a series of Ab-containing samples with a confidence of ±2% simply by a comparison between the experimentally detected spin–spin relaxation time T_2 of the sample added to the MNS dispersion and the calibration curve. The tested range of function linearity (100 pM–1 μM) refers to the anti-HSA Ab concentration that can be relevant for medical diagnosis. Indeed, it is well documented that at least fivefold HSA autoantibodies occur in pathological patients, for example, diabetic subjects compared with nondiabetic subjects [7]. However, at much higher concentrations of Ab in solution, the plotted function loses its linearity (data not shown).

Conclusion

We have reported on the development of a novel biosensor for the recognition and real-time monitoring of proteins capable of detecting the presence, and measuring the concentration, of diluted anti-HSA Abs in solution. The sensor is based on the use of core–shell silica-coated iron oxide nanoparticles with elevated magnetic susceptibilities due to the encapsulation of multiple iron-containing crystals inside each composite nanoparticle. These nanoparticles, called MNSs, exhibit a number of advantages compared with previous monocrystalline models, including (i) optimal control of their size and shape, (ii) good signal stability in a wide range of concentrations even at remarkable dilutions, and (iii) ease of surface biofunctionalization thanks to the well-developed silica surface chemistry that enables us to anchor nearly every biomolecular target. In light of this evidence, the method presented here has the potential to be adapted to other types of biomolecular interactions and can be run in a high-throughput format using MRI and NMR, as was recently demonstrated in a microfluidics setup for multiplex analysis [1]. In addition, because the assay makes use of NMR techniques for signal detection, the measurements can be performed in complex biological media, such as blood, plasma, sputum, and urine, that often seriously compromise other diagnostic techniques having sensitivity on the same order (e.g., those based on the amplification of an optical signal). These qualities make the developed MNS system ideal both for the rapid screening of large numbers of blood samples and for the accurate quantitative detection of different targets in positive sera without extensive purification of the sample or signal amplification.

Acknowledgments

This work was supported by "Fondazione Romeo ed Enrica Invernizzi" and the CNR–Regione Lombardia "Mind in Italy" project. We thank R. Allevi for help in acquisition of TEM images.

References

[1] H. Lee, E. Sun, D. Ham, R. Weissleder, Chip–NMR biosensor for detection and molecular analysis of cells, Nat. Med. 14 (2008) 869–874.
[2] J.T. Mason, L. Xu, Z.-M. Sheng, T.J. O'Leary, A liposome–PCR assay for the ultrasensitive detection of biological toxins, Nat. Biotechnol. 24 (2006) 555–557.
[3] K.L. Abbott, K. Aoki, J.-M. Lim, M. Porterfield, R. Johnson, R.M. O'Regan, L. Wells, M. Tiemeyer, M. Pierce, Targeted glycoproteomic identification of biomarkers for human breast carcinoma, J. Proteome Res. 7 (2008) 1470–1480.
[4] C.-C. You, O.R. Miranda, B. Gider, P.S. Ghosh, I.-B. Kim, B. Erdogan, S.A. Krovi, U.H.F. Bunz, V.M. Rotello, Detection and identification of proteins using nanoparticle–fluorescent polymer "chemical nose" sensors, Nat. Nanotechnol. 2 (2007) 318–323.
[5] H.F. Poon, K.A. Vaishnav, T.V. Getchell, M.L. Getchell, D.A. Butterfield, Quantitative proteomics analysis of differential protein expression and oxidative modification of specific proteins in the brains of old mice, Neurobiol. Aging 27 (2006) 1010–1019.
[6] B.J. Tabner, S. Turnbull, O. El-Agnaf, D. Allsop, Production of reaction oxygen species from aggregating proteins implicated in Alzheimer's disease, Parkinson's disease, and other neurodegenerative disease, Curr. Top. Med. Chem. 1 (2001) 507–517.
[7] Z. Rasheed, R. Ali, Reactive oxygen species damaged human serum albumin in patients with type 1 diabetes mellitus: biochemical and immunological studies, Life Sci. 79 (2006) 2320–2328.
[8] E. Suzuki, K. Yasuda, N. Takeda, S. Sakata, S. Era, K. Kuwata, M. Sogami, K. Miura, Increased oxidized form of human serum albumin in patients with diabetes mellitus, Diabetes Res. Clin. Pract. 18 (1992) 153–158.
[9] J. Chapman, C. Maayan, D.M. Michaelson, Antibodies to human serum albumin in familial dysautonomia, Int. Arch. Allergy Appl. Immunol. 100 (1993) 42–46.
[10] N. Tamura, T. Suou, C. Hirayama, Anti-albumin antibodies in sera patients with liver disease, J. Gastroenterol. 17 (1982) 469–475.
[11] J.-M. Nam, C.S. Thaxton, C.A. Mirkin, Nanoparticle-based bio-bar codes for the ultrasensitive detection of proteins, Science 301 (2003) 1884–1886.
[12] H. Yao, Y. Zhang, F. Xiao, Z. Xia, J. Rao, Quantum dot/bioluminescence resonance energy transfer based highly sensitive detection of proteases, Angew. Chem. Int. Ed. 46 (2007) 4346–4349.
[13] M.S. Martina, J.P. Fortin, C. Menager, O. Clement, G. Barratt, C. Grabielle-Madelmont, F. Gazeau, V. Cabuil, S. Lesieur, Generation of superparamagnetic liposomes revealed as highly efficient MRI contrast agents for in vivo imaging, J. Am. Chem. Soc. 127 (2005) 10676–10685.
[14] I.J.M. de Vries, W.J. Lesterhuis, J.O. Barentsz, P. Verdijk, J.H. van Krieken, O.C. Boerman, W.J.G. Oyen, J.J. Bonenkamp, J.B. Boezeman, G.J. Adema, J.W.M. Bulte, T.W.J. Scheenen, C.J.A. Punt, A. Heerschap, C.G. Figdor, Magnetic resonance tracking of dendritic cells in melanoma patients for monitoring of cellular therapy, Nat. Biotechnol. 23 (2005) 1407–1413.
[15] N.V. Evgenov, Z. Medarova, G. Dai, S. Bonner-Weir, A. Moore, In vivo imaging of islet transplantation, Nat. Med. 12 (2006) 144–148.
[16] J.M. Perez, L. Josephson, R. Weissleder, Use of magnetic nanoparticles as nanosensors to probe for molecular interactions, ChemBioChem 5 (2004) 261–264.
[17] S.I. Stoeva, J.-S. Lee, C.S. Thaxton, C.A. Mirkin, Multiplexed DNA detection with biobarcoded nanoparticle probes, Angew. Chem. Int. Ed. 45 (2006) 3303–3306.
[18] A.K. Gupta, M. Gupta, Synthesis and surface engineering of iron oxide nanoparticles for biomedical applications, Biomaterials 26 (2005) 3995–4021.
[19] J. Dobson, Gene therapy progress and prospects: magnetic nanoparticle-based gene delivery, Gene Ther. 13 (2006) 283–287.
[20] I. Koh, R. Hong, R. Weissleder, L. Josephson, Sensitive NMR sensors detect antibodies to influenza, Angew. Chem. Int. Ed. 47 (2008) 4119–4121.
[21] S. Taktak, D. Sosnovik, M.J. Cima, R. Weissleder, L. Josephson, Multiparameter magnetic relaxation switch assays, Anal. Chem. 79 (2007) 8863–8869.
[22] J.M. Perez, L. Josephson, T. O'Loughlin, D. Hogemann, R. Weissleder, Magnetic relaxation switches capable of sensing molecular interactions, Nat. Biotechnol. 20 (2002) 816–820.

ARTICLE 3

[23] L. Josephson, J.M. Perez, R. Weissleder, Magnetic nanosensors for the detection of oligonucleotide sequences, Angew. Chem. Int. Ed. 40 (2001) 3204–3206.
[24] C. Sun, J.S.H. Lee, M. Zhang, Magnetic nanoparticles in MR imaging and drug delivery, Adv. Drug Deliv. Rev. 60 (2008) 1252–1265.
[25] L. Polito, D. Monti, E. Caneva, E. Delnevo, G. Russo, D. Prosperi, One-step bioengineering of magnetic nanoparticles via a surface diazo transfer/azide–alkyne click reaction sequence, Chem. Commun. (2008) 621–623.
[26] L. Polito, M. Colombo, D. Monti, S. Melato, E. Caneva, D. Prosperi, Resolving the structure of ligands bound to the surface of superparamagnetic iron oxide nanoparticles by high-resolution magic-angle spinning NMR spectroscopy, J. Am. Chem. Soc. 130 (2008) 12712–12724.
[27] J. Xie, C. Xu, N. Kohler, Y. Hou, S. Sun, Controlled PEGylation of monodisperse Fe_3O_4 nanoparticles for reduced non-specific uptake by macrophage cells, Adv. Mater. 19 (2007) 3163–3166.
[28] E.Y. Sun, R. Weissleder, L. Josephson, Continuous analyte sensing with magnetic nanoswitches, Small 2 (2006) 1144–1147.

ARTICLE 3

Single-Domain Protein A-Engineered Magnetic Nanoparticles: Toward a Universal Strategy to Site-Specific Labeling of Antibodies for Targeted Detection of Tumor Cells

Serena Mazzucchelli,[†,‡,¶] Miriam Colombo,[†,‡,¶] Clara De Palma,[†] Agnese Salvadè,[†,‡] Paolo Verderio,[†,‡] Maria D. Coghi,[‡] Emilio Clementi,[†,§] Paolo Tortora,[‡] Fabio Corsi,[†] and Davide Prosperi[‡,⊥,*]

[†]Dipartimento di Scienze Cliniche "Luigi Sacco", Università di Milano, Ospedale L. Sacco, via G.B. Grassi 74, 20157 Milano, Italy, [‡]Dipartimento di Biotecnologie e Bioscienze, Università di Milano-Bicocca, piazza della Scienza 2, 20126 Milano, Italy, [§]Istituto Scientifico Eugenio Medea, 23842 Bosisio Parini, Italy, and [⊥]Istituto di Scienze e Tecnologie Molecolari, CNR, via Fantoli 16/15, 20138 Milano, Italy. [¶]These authors contributed equally to the research.

ABSTRACT Highly monodisperse magnetite nanocrystals (MNC) were synthesized in organic media and transferred to the water phase by ultrasound-assisted ligand exchange with an iminodiacetic phosphonate. The resulting biocompatible magnetic nanoparticles were characterized by transmission electron microscopy, dynamic light scattering, and magnetorelaxometry, indicating that this method allowed us to obtain stable particle dispersions with narrow size distribution and unusually high magnetic resonance T_2 contrast power. These nanoparticles were conjugated to a newly designed recombinant monodomain protein A variant, which exhibited a convincingly strong affinity for human and rabbit IgG molecules. Owing to the nature of antibody-protein A binding, tight antibody immobilization occurred through the Fc fragment thus taking full advantage of the targeting potential of bound IgGs. If necessary, monoclonal antibodies could be removed under controlled conditions regenerating the original IgG-conjugatable MNC. As a proof of concept of the utility of our paramagnetic labeling system of human IgGs for biomedical applications, anti-HER-2 monoclonal antibody trastuzumab was immobilized on hybrid MNC (TMNC). TMNC were assessed by immunoprecipitation assay and confocal microscopy effected on HER-2-overexpressing MCF-7 breast cancer cells, demonstrating excellent recognition capability and selectivity for the target membrane receptor.

KEYWORDS: magnetic nanoparticles · targeted MRI contrast agents · phase transfer · biolabeling · protein A · breast cancer

Noninvasive medical imaging methods currently represent a major issue in the prevention and treatment of malignant diseases.[1] Among them, magnetic resonance imaging (MRI) is rapidly becoming the gold-standard technique for an in-depth tissue investigation with high-spatial resolution.[2,3] However, in several circumstances, MRI suffers from low sensitivity, which is critical when accurate detection and monitoring of localized malignancies developing in the early stages of the disease are required. For this reason, great efforts have been made to develop efficient contrast enhancing agents aimed at improving the signal difference between the area of interest (*e.g.*, the blood pool) and the background. In clinical application, the systemic injection of appropriate doses of contrast agents, mostly based on gadolinium complexes (*e.g.*, Gd-DTPA),[4,5] results in a nonspecific enhancement of the MRI signal. When a sharp tissue distribution is desired, targeted contrast agents are designed in such a way that they localize to specific cell type through active binding mechanisms, which exploit the conjugation of the signal enhancer with suitable markers. Among them, most used are folate, small peptides, and antibodies, which stimulate specific recognition with the respective tumor cell receptor.[6−8] Unfortunately, in most cases, antibody-conjugated Gd-DTPA proved to be largely unsuccessful due to the relatively low sensitivity of MRI and the low density of cell target receptors, thus requiring administration of excessive gadolinium doses. This drawback can be partially overcome by using magnetic nanoparticles based on iron oxide (MNPs), which have been demonstrated to induce large increments in transverse relaxation rate upon binding with a 10^6 signal amplification over Gd-DTPA.[9] While Gd-based agents enhance the signal in T_1-weighted images, MNPs provide strong signal enhancement in T_2-weighted images, owing to a different contrasting mechanism.[10,11] For this reason, MNPs have attracted much attention in biomedical diagnostics in view of their usefulness as contrast agents for magnetic

*Address correspondence to davide.prosperi@unimib.it.

Received for review June 10, 2010 and accepted August 31, 2010.

Published online September 8, 2010. 10.1021/nn101307r

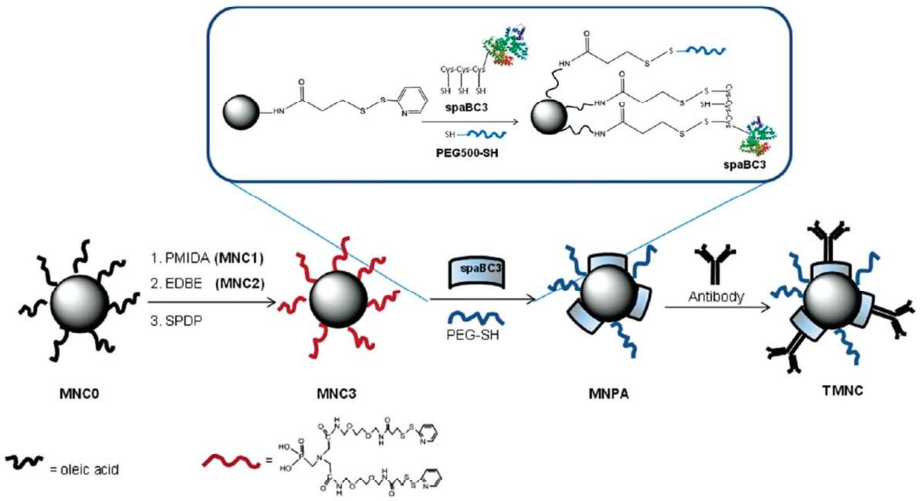

Scheme 1. Synthesis of Pegylated Trastuzumab-Functionalized MNC (TMNC)

resonance imaging (MRI)[12−14] and biosensing.[15] Moreover, the hydroxyl-rich surface of iron oxides promotes the direct conjugation of organic and biological molecules by surface chemical technology.[16] The design and construction of a successful target-oriented biohybrid paramagnetic nanoprobe is a primary goal toward the development of highly efficient contrast enhancer for MRI, standing at the interface between nanotechnology and molecular biology. The ultimate challenge is represented by the development of reliable strategies for the conjugation of targeting biomolecules, especially monoclonal antibodies (IgGs), to MNPs. These include passive/electrostatic physical adsorption of IgGs, tight immobilization exploiting the strong interaction of biological counterparts, such as biotin-streptavidin, which requires prior IgG biotinylation,[17] or the formation of covalent chemical connections, which is often considered the most practical choice.[18,19] Although these approaches may offer different solutions and have been successfully employed in several circumstances, they all share the same basic limitation, that is a non-site-specific binding to IgG molecule, which affects the targeting efficiency of the antibody. As a matter of fact, the actual conservation of the targeting bioactivity of immobilized IgGs is not obvious and remains a crucial issue, which must be addressed in designing a successful targeted nanoprobe.

An interesting option might be envisaged in the use of a natural peptide linker endowed with high affinity for IgGs, such as protein A. Protein A is a cell-wall associated protein exposed on the surface of the gram-positive bacterium *Staphilococcus aureus*.[20] The primary structure consists of a 42 kDa single polypeptide chain, folded into five highly homologous domains, named E, D, A, B, and C, each consisting of 56−61 residues.[21] The interest for this molecule in biotechnology resides mainly in three useful properties: (1) the protein structure is stable over a broad range of pH (2−12) and in the presence of various detergents; (2) it can bind reversibly a large variety of IgGs *via* their Fc fragment through its consensus sequence (Asn-Gln-Phe-Asn-Lys-Glu),[21] (3) IgG-protein A complex can be dissociated under controlled conditions (pH 3.5−4.5) without apparent loss of activity.[22] The affinity of protein A for immunoglobulins is not conserved among the different classes and isotypes. In particular, it exhibits high affinity to human, rabbit, and guinea pig IgGs. Recently, natural protein A has been used immobilized on magnetic polyadsorbent for IgG separation and/or purification procedures.[23] As protein A recognizes the Fc portion of IgGs, it is expected to mediate an orderly Fc site-specific antibody immobilization on MNPs resulting in a target-directed Fab presentation.[24]

In this paper, we present a multidisciplinary approach to the design and synthesis of a universal magnetic nanohybrid consisting of a high-quality iron oxide nanocrystal core conjugated to a suitably bioengineered small variant of protein A for the smart immobilization of IgGs. The resultant targeted nanoparticle is shown to exhibit high affinity and selectivity for the appropriate tumor markers. As a case study for our investigations, we focused on the monoclonal antibody trastuzumab, which is commonly employed in clinical therapy of breast cancer, as a model for the development of our tumor-targeting magnetic nanoprobe. Trastuzumab (tz) is a humanized monoclonal antibody consisting of two antigen-specific sites that bind to the juxtamembrane portion of the extracellular domain of

the "Human Epidermal growth factor Receptor 2" (HER-2), which is found overexpressed in several metastasizing breast cancer cells.[25]

RESULTS AND DISCUSSION

Our aim was to synthesize a model magnetic nanoparticle hybrid system containing a specific IgG binding functionality with the lowest molecular weight to reduce the nanoparticle overall size. We reasoned that a recombinant derivative of protein A consisting of one single IgG-binding domain, namely the B domain, would meet such criteria. This strategy displays several advantages: (1) as for entire protein A, all the antibodies are presented in the same orientation on the nanoparticle, with the active Fab portions directed in an optimal configuration for antigen binding; (2) the use of a single B domain of protein A results in a very small biomolecular support for the antibody, which is expected to partially reduce the immunogenicity of the whole hybrid nanoparticle, while conserving remarkable binding affinity for IgGs; (3) the bioengineering approach to the protein A variant allows for the artificial introduction of selectively reactive functionalities in the peptide sequence, such as cysteine thiols, for site-specific conjugation onto the nanoparticle surface. The promising combination of all these potential advantages prompted us to explore the possibility of improving the current methods for the synthesis of IgG-functionalized nanohybrids. We chose an organic-phase approach for the synthesis of the magnetite core nanostructure, providing highly uniform and crystalline magnetic nanoparticles endowed with strong intrinsic relaxivity and narrow size distribution. This approach, while effective, had a main limitation, which was the poor solubility of the resulting surfactant-coated nanoparticles. Hence, an efficient ligand exchange was required to transfer them into an aqueous environment avoiding particle aggregation. Scheme 1 depicts the general strategy followed to synthesize tz-functionalized magnetic nanocrystals (TMNC), which were then assessed according to their capability to recognize the HER-2 receptor antigen both in a whole cell extract and in living cultured breast cancer cells.

Development of Water-Stable Profunctional Iron Oxide Nanocrystals. High-quality, 8 nm hydrophobic iron oxide nanocrystals (MNC0, Figure 1, inset) were synthesized by solvothermal decomposition from iron−oleate complex in a solution of octadecene in the presence of oleic acid as capping agent.[26] The synthesized uniform nanocrystals were finely dispersed in chloroform and treated under continuous sonication with an excess of *N*-phosphonomethyl iminodiacetic acid phosphonate (PMIDA) dissolved in aqueous ammonia solution to promote the ligand exchange on the MNC0 surface, leading to the highly water dispersible, readily functionalizable MNC1. The phase transfer reaction occurred quickly thanks to the higher affinity of PMIDA phosphonate group toward iron oxide compared to oleic carboxylate (Figure 1a, inset). After the phase transfer, MNC1 maintained the original average crystal size (8

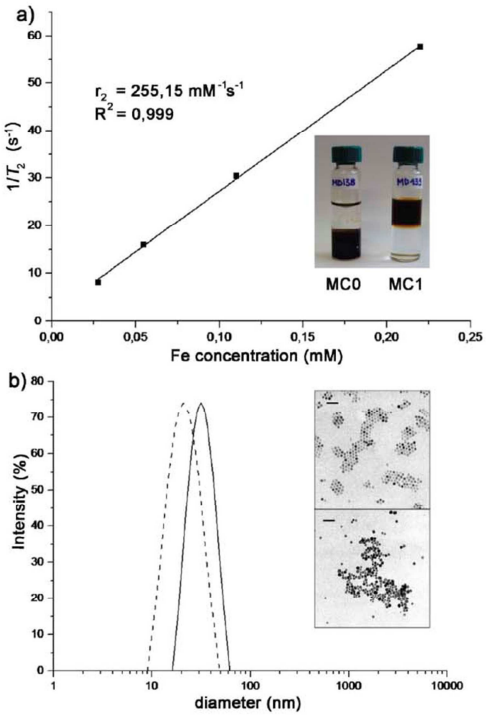

Figure 1. (a) T_2 relaxometry analysis of as-synthesized MNC1. The inverse of experimental T_2 values obtained at different MNC1 concentrations is plotted *vs* iron concentration. The experimental data are fitted by a line. The line slope indicates the T_2 relaxivity. Inset: MNC phase transfer from organic solvent (chloroform) to aqueous solution. (b) Hydrodynamic size distribution histograms of oleic-coated Fe_3O_4 nanoparticles (dashed line) and after ligand exchange with PMIDA (MNC1, continuous line). Diameters were measured by DLS in chloroform and water, respectively. Inset: TEM images of as-synthesized MNC0 in hexane (top) and of MNC1 in PBS (bottom). Scale bars = 50 nm.

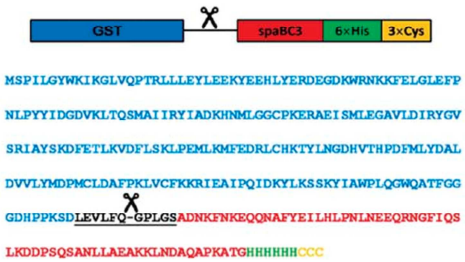

Figure 2. Schematic representation of spaBC3 engineered sequence. Glutathione *S*-transferase (GST, blue), spaBC3 (red), histidine tag (green), and cysteine tripod (orange). PreScission protease cleavage site between amino acids Gln_{226} and Gly_{227} is evidenced.

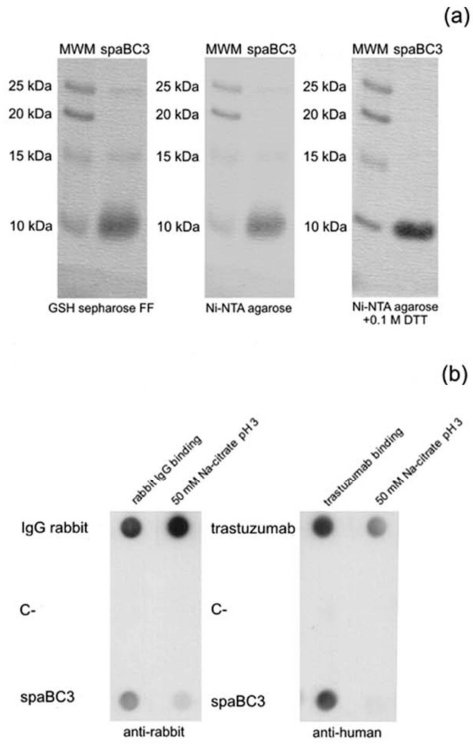

Figure 3. (a) SDS-PAGE of spaBC3 purified fractions. Molecular weight markers (MWM, 5 μL) Precision Plus Unstained were used. Purified protein (4 μg) was loaded after elution with PreScission protease (left). After purification with Ni-NTA agarose to remove GST contaminants, the same amount of spaBC3 was loaded on SDS-PAGE with or without 0.1 M DTT in running buffer (right and middle, respectively). (b) SpaBC3 binding assay. SpaBC3 (250 ng) was filtered through PVDF membrane and incubated with rabbit IgG or tz. IgG removal was obtained by Na-citrate incubation. GST protein (C-, 250 ng), as negative control, and rabbit IgG or tz (250 ng), as positives, were used. The presence of rabbit IgG or tz was revealed by antirabbit or antihuman secondary antibodies conjugated to HRP, respectively.

nm, by TEM), the final nanoparticle shape was uniformly spherical, while a slight increase in the hydrodynamic diameter from 21 ± 2 nm (MNC0 in chloroform) to 32 ± 3 nm (MNC1 in water) was determined by dynamic light scattering (DLS) (Figure 1b), probably due to the change of solvent and solvation aptitude of the new ligands. The resulting MNC1 surface, rich of accessible carboxyl groups, stabilized well the colloidal particles in buffered solution by electrostatic repulsions, concomitantly providing a useful support for further functionalization. In addition, we performed relaxometric measurements to determine the T_2 enhancing capability of synthesized nanocrystals. The water-soluble MNC1 exhibited a remarkably high transverse relaxivity (r_2 = 255 mM^{-1} s^{-1} at 20 mHz, $\mathbf{B}_0$ = 0.47 T), deduced by the slope of the line obtained by plotting $1/T_2$ *vs* iron concentration. This value, as compared with the relaxivity of commercially available T_2 contrast agents based on polymer-coated iron oxides, such as Endorem (Guerbet, 160 mM^{-1} s^{-1}), Ferumoxytol (Adv. Magnetics, 83 mM^{-1} s^{-1}), and Resovist (Schering, 151 mM^{-1} s^{-1}), suggests that high contrast power can be achieved with MNC1, on the same order of the best T_2 contrast agents reported so far.[27]

Carboxylate functionalities were converted into amine ends by reaction with the bifunctional diamino-linker 2,2-(ethylenedioxy)bis(ethylamine) (EDBE) *via* *N*-hydroxysuccinimidyl ester (NHS) activation. EDBE-modified nanoparticles (MNC2) exhibited a hydrodynamic diameter of 57 ± 3 nm, as determined by DLS. The average number of amino groups on MNC2 was quantified by an adapted version of the Dunnill's protocol,[28] resulting in 150 amines per particle. Our two-step procedure involving hot organic synthesis of monocrystalline iron oxide followed by ligand exchange and phase transfer allowed us to obtain stable water-soluble nanoparticles with unique contrast power and narrow size distribution, typical of the thermal synthesis in high-boiling organic solvent, yet devoid of the drawbacks associated to the biological fluid incompatibility. The high relaxivity value of our soluble MNC makes this nanoprobe a promising contrast agent applicable in magnetic resonance imaging (MRI) for the potential noninvasive diagnosis of malignances.

MNC2 were stable for months with nondetectable precipitation in several buffered media, including Dulbecco's PBS, pH 7.4; borate buffer, pH 8.5; acetate buffer, pH 5.0; and tris HCl, pH 6−8. The amino functionalities on the particle surface allowed the MNC2 conjugation with *N*-succinimidyl-3-[2-pyridyldithio]-propionate (SPDP) *via* NHS ester resulting in the thiol-reactive pro-functional MNC3 (Scheme 1). MNC3 were the ideal building block for bioconjugation with thiol-engineered protein A variant, as PDP functionality is unaffected by nucleophiles but very reactive toward sulfhydryl ends of organic and biological thiol-containing molecules under mild conditions by formation of stable disulfide bridges.

Design, Expression, and Purification of an Engineered Cys_3-Ended Variant of a Single-Domain Fragment of Protein A from *Staphylococcus aureus*. The B domain sequence, previously reported by Abrahmsen *et al.*,[21] was modified inserting *Bam*HI and *Sma*I restriction sites at the 5′ and 3′ positions, respectively. The modified gene was cloned to express the B domain in fusion with glutathione *S*-transferase (GST). However, proteins purified by GST affinity chromatography may contain small amounts of GST and GST-affine contaminants in eluted fractions. For this reason, a supplementary 6× His affinity tag was introduced at the C-terminal to completely remove the residual GST-deriving impurities through an additional affinity purification step.[29] To achieve a site-specific con-

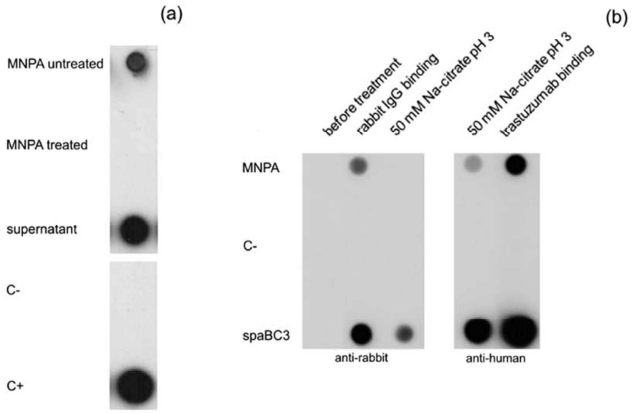

Figure 4. (a) Assessment of SpaBC3-MNC conjugation. MNPA was treated with 0.1 M DTT, resulting in spaBC3 release. The reduced MNPA was loaded on a PVDF membrane, together with untreated MNPA and the supernatant from the reduction mixture as controls. The presence of spaBC3 was detected by antihuman HRP-antibody only in untreated MNPA and in supernatant samples, confirming that SpaBC3 was anchored onto MNC essentially *via* disulfide bridges. C− and C+ are GST protein (250 ng) and spaBC3 (250 ng), respectively. (b) SpaBC3 on MNPA retains its IgG binding activity. MNPA (500 ng) was filtered through PVDF membrane and incubated with rabbit IgG or tz. IgG removal was obtained by Na-citrate incubation. GST protein (C−, 250 ng) and spaBC3 (C+, 250 ng) were used as negative and positive controls, respectively. MNPA capture of rabbit IgG or tz was revealed by antirabbit or antihuman secondary HRP-antibodies, respectively.

jugation of the protein A variant to MNC, the presence of one selectively reactive group in the protein primary structure was required. As the recombinant B domain was devoid of cysteine residues, we envisaged that the incorporation of a cysteine tail would result in the introduction of a highly reactive thiol group, concomitantly avoiding potentially competitive interferences from other functional moieties in the peptide sequence. In light of our preliminary results showing an unexpected weakness of the protein−nanoparticle linkage with one single Cys tagged behind the His_6 terminal (data not shown), we substituted the single Cys residue with a Cys_3 tripod leading to an improved binding effectiveness of the thiol end (Figure 2).

The engineered domain B of protein A from *Staphilococcus aureus* containing a C-terminal His_6Cys_3 tail (spaBC3) was cloned in fusion with GST tag in pGEX-6P-1 vector and expressed in BL21(DE3) *E. coli* strain. SpaBC3 was subsequently purified using a GST affinity column and eluted with cleavage with PreScission protease, obtaining a 7.48 kDa protein with a good degree of purity showing the presence of two residual contaminants at 15 and 25 kDa, respectively, which were removed by further purification through a Ni-NTA agarose column. SDS-PAGE performed under conventional reducing conditions showed a remarkably diffuse band at *ca.* 10 kDa in correspondence of spaBC3, suggesting that during acrylamide gel migration the formation of disulfide bridges between spaBC3 molecules leading to aggregates might occur. By addition of 0.1 M dithiothreitol (DTT) in the running buffer, a more defined thin spaBC3 band was obtained. These experiments are summarized in Figure 3a. While a DTT concentration of about 25 mM is usually estimated to be sufficient to break intermolecular monodentate disulfide bridges,[30] here the presence of a cysteine tripod forced us to use more strongly reducing conditions to maintain spaBC3 in its monomer form until its conjugation with nanoparticles.

SpaBC3 Retains IgG Binding Activity. Recombinant spaBC3 produced in *E. coli* and filtered on a polyvinylidene fluoride (PVDF) membrane was assessed in regard to its ability to bind IgG molecules. In Figure 3b, a dot blot example of spaBC3 complex incubated with rabbit IgG is presented. The presence of bound IgG was revealed by a strong signal of antirabbit secondary antibody conjugated with horseradish peroxidase (HRP). To evaluate the possibility to recycle spaBC3 for multiple usages, we tested the IgG removal by incubating the spaBC3-IgG complex in 50 mM Na-citrate buffer, pH 3 at room temperature (RT), observing a remarkable reduction of the signal from 30 min of treatment. The same spaBC3 sample was then incubated with a solution containing tz, confirming the ability of spaBC3 to capture different IgGs even after Na-citrate treatment. These results suggested to us that spaBC3 might be exploited for the pro-functionalization of nanoparticles leading to a universal nanocarrier for the efficient, recyclable, and target-directed conjugation of a large variety of IgGs.

Conjugation of spaBC3 to MNC through Sulfhydryl Groups. SpaBC3 was incubated in 0.1 M DTT to reduce the cysteine residues, and then the excess of DTT was removed by gel filtration. The purified monomer protein obtained by this procedure was immediately incubated with MNC3 and left overnight. Under these conditions, the thiol groups of cysteine residues displayed high re-

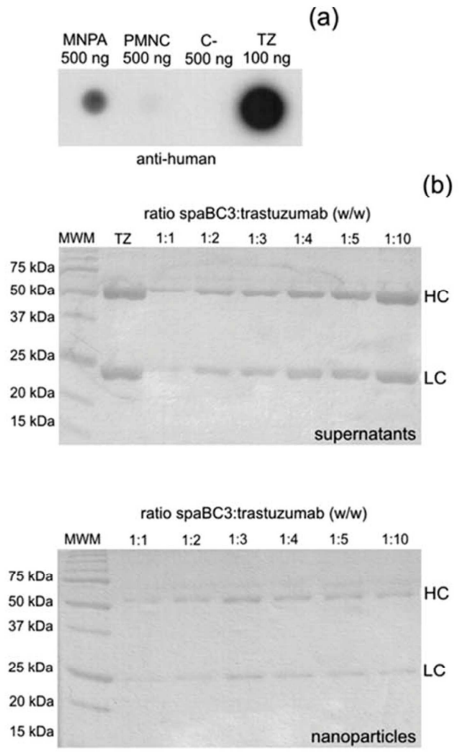

Figure 5. (a) Trastuzumab conjugation to MNPA. MNPA and PMNC incubated in parallel with an equal amount of tz for 1 h at 25 °C were filtered through a PVDF membrane. Tz and GST were used as positive and negative controls, respectively. Membrane dot blot was probed with antihuman HRP-antibodies and the immobilization of tz was revealed by an ECL detection system. (b) Coomassie-stained gels demonstrating the binding capability of MNPA. A fixed amount of MNPA was mixed with increasing amounts of tz and precipitated after 1 h incubation. Supernatants and resuspended pellets were analyzed by SDS-PAGE using tz as control. HC, IgG heavy chain; LC, IgG light chain; MWM, molecular weight marker Precision Plus Unstained.

activity and reacted rapidly with PDP functionalities on MNC3, which could be monitored by UV detection at 343 nm of the released pyridine-2-thione.[31] Notably, given the reactivity of the Cys_3 tripod, we noticed that it is of primary importance that reduced spaBC3 is incubated with MNC3 immediately after DTT treatment to obtain a satisfactory extent of conjugation. Next, we determined the amount of spaBC3 immobilized on MNC by Bradford assay of the supernatant and found that 1 mg of MNC3 was able to bind 167 μg of protein. The residual PDP functionalities on spaBC3-MNC were reacted with an excess of PEG_{500}-SH to saturate the reactive groups on the nanoparticles thus minimizing the possibility of accidental interaction with nonspecific proteins.

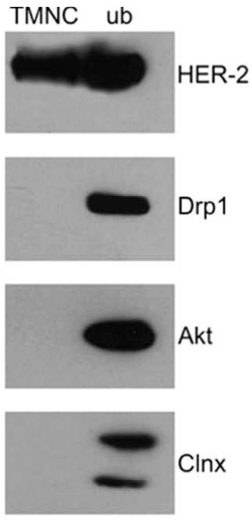

Figure 6. HER-2 receptor is selectively recognized by TMNC. Immunoprecipitation was performed using 200 μg of TMNC. Nanoparticles were incubated overnight at 4 °C with 1 mg protein in a whole extract of MCF-7 cells. Bound and unbound proteins were then eluted in SDS-PAGE application buffer, electrophoresed, and immunoblotted using either anti-HER-2, anti-Drp1, anti-Akt, and anti-Clnx antibodies.

To prove that spaBC3 was actually anchored to the MNC surface through disulfide bridges, the spaBC3-MNC conjugate (MNPA) was treated with 0.1 M DTT, which was expected to break the disulfide bridges leading to spaBC3 release. On the contrary, in case spaBC3 was captured by MNC through nonspecific physical adsorption, the protein should at least partially remain anchored to the MNC surface after DTT treatment, as the reducing environment would not affect its surface adhesion. Hence, the reduced MNPA was loaded on a PVDF membrane, together with untreated MNPA and the supernatant from the disulfide bridges reduction mixture as controls (Figure 4a). The signal of spaBC3 was indeed recovered only in untreated MNPA and in supernatant samples. This result clearly demonstrates that spaBC3 was bound to MNC exploiting the tripod tail selectively *via* disulfide bridge formation without aspecific adsorption.

Eventually, we evaluated the capability of MNPA to retain the ability to capture an IgG molecule and be reutilized to bind different monoclonal antibodies after Na-citrate treatment. MNPA, free spaBC3, and a protein used as negative control, namely GST, were individually filtered through a PVDF membrane. Each sample was incubated with rabbit IgG, then treated with Na-citrate buffer, and finally incubated with tz. Figure 4b clearly shows that both the IgG binding experiments performed with MNPA and their recycle after Na-citrate treatment were successful. We concluded that MNPA

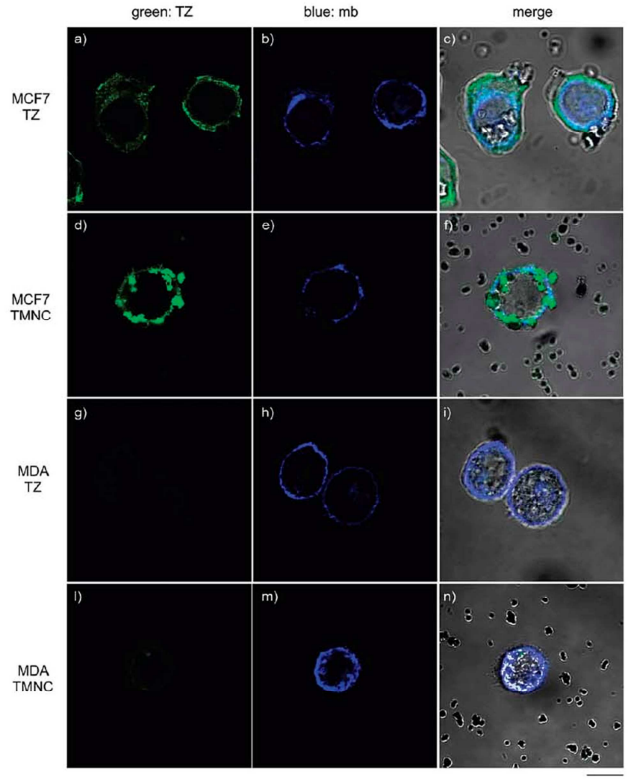

Figure 7. Confocal laser images of MCF-7 and MDA cells cultured with TMNC or free tz. MCF-7 and MDA were incubated for 15 min with TMNC (150 μg mL^{-1}; panels d−f and l−n, respectively) and tz (15 μg mL^{-1}; panels a−c and g−i, respectively). Cell membranes (mb) were stained with DiD oil (blue). TMNC and tz were labeled with antihuman FITC secondary antibodies. Scale bar =10 μm.

is a good candidate to be developed as a universal magnetic nanoparticle model system useful for the reliable and straightforward conjugation of human(ized) antibodies.

Trastuzumab Immobilization on MNPA. MNPA and fully pegylated MNC devoid of spaBC3 (PMNC, control) were incubated in parallel with an equal amount of tz. Trastuzumab conjugation was assessed in each sample by filtering the respective solutions through a PVDF membrane, which was subsequently probed with antihuman antibodies conjugated to HRP. Trastuzumab and GST were used as positive and negative controls, respectively. Dot blot assay was positive only with MNPA, which confirmed the occurred immobilization of tz through spaBC3 specific interaction (Figure 5a). Next, we optimized the antibody/MNPA ratio to maximize the number of tz molecules bound to MNPA while maintaining the minimal excess in the supernatant. This is important because our results showed that it was not possible to saturate the whole spaBC3 supported on MNC. MNPA was incubated with increasing amounts of tz. Coomassie stain of both supernatant and nanoparticles used in the conjugation reaction evidenced that the best results were obtained incubating MNPA in a spaBC3/tz ratio of 1:3. The comparison between upper and lower gels in Figure 5b evidence that, above the 1:3 ratio, the amount of loaded antibody did not increase, while a remarkable progressive increment of IgG concentration in the supernatant was observed. Under the above conditions, we determined that the tz-functionalized MNC (TMNC) displayed an average of 1.8 IgG molecules per MNC, corresponding to *ca.* 0.1 mg tz per mg MNC.

TMNC Display Binding Capability to HER-2 Receptor. MCF-7 whole cell extracts were incubated overnight at 4 °C on a rotating wheel with TMNC. TMNC and the supernatant (unbound, ub) were analyzed by Western blotting with anti-HER-2 antibody in order to reveal HER-2 binding to TMNC (Figure 6). Our data confirmed that TMNC were able to immunoprecipitate HER-2 membrane receptor in a whole cell extract. This immunoprecipitation was highly specific, as antibodies recognizing dynamin-

related protein (Drp1) and Akt, two soluble cytosolic proteins, or calnexin (Clnx), an integral protein of the endoplasmic reticulum, which were tested as negative controls, displayed a detectable signal only in the ub sample. These results indicate that Clnx was absent in the TMNC sample, whereas it was detected in the unbound, suggesting that the interaction between TMNC and HER-2 is specific and related to antibody conjugation. This clearly highlights the remarkable target-selectivity of TMNC toward the HER-2 breast cancer cell marker.

To validate the immunoprecipitation data, the specificity of binding between TMNC and HER-2 was observed by confocal laser scanning microscopy. Indeed, as HER-2 is a trans-membrane receptor, TMNC were expected to accumulate in correspondence of the external surface of HER-2-overexpressing cells. This should allow us to discriminate between receptor-mediated particle capture by cell membrane and residual unspecific uptake promoted by alternative pathways.[32] HER-2 positive MCF-7 cells[33] (Figure 7a−c) and, as a negative control, HER-2 negative MDA cells (Figure 7g−i) were treated with tz in order to assess HER-2 expression and cellular surface distribution. TMNC were incubated in parallel with both MCF-7 and MDA cells at a concentration of 150 μg mL^{-1} culture medium. Trastuzumab and TMNC were labeled with antihuman FITC-labeled secondary antibodies (green), whereas cell membranes were stained with DiD oil (mb, blue). As expected, after 15 min incubation, TMNC were observed in HER-2 positive MCF-7 cell surfaces (Figure 7d−f), but not in MDA negative control cells (Figure 7l−n), demonstrating that they localized selectively in correspondence of transmembrane receptors owing to the presence of the specific targeting agent.

CONCLUSIONS

High-quality biocompatible magnetite nanocrystals (MNC) were obtained by phase transfer of oleate-coated iron oxides *via* successful ligand exchange with an iminodiacetic acid phosphonate exploiting the strong affinity of phosphonate for iron oxide. Such water-soluble nanocrystals exhibited a transverse relaxation rate of 255 mM^{-1} s^{-1}, which is significantly higher than commercially available T_2 contrast agents based on polymer-coated iron oxides. A recombinant low-molecular-weight fragment of protein A modified to present a terminal cysteine tripod was synthesized, characterized, and conjugated to MNPs through an appropriate bifunctional linker affording a molecular nanohybrid suitable for site-specific immobilization of antibodies. The antibody capture capacity of our hybrid nanoparticles was successfully tested with trastuzumab and rabbit IgGs. In particular, trastuzumab-conjugated MNC were effective in selectively recognizing HER-2 receptor expressed in MCF-7 breast cancer cells. The model nanoparticle system (MNPA) presented here enables efficient and reversible labeling of a large variety of human monoclonal antibodies with highly conserved biological activity toward their natural receptors. The combination of all these properties renders our newly developed MNPA a promising versatile nanoscale probe for application in targeted diagnosis of tumor cells and tissues.

EXPERIMENTAL SECTION

Synthesis of MNC3. All reagents and solvents were analytical grade (Sigma-Aldrich, St. Louis, MO). MNC0 were synthesized according to Park *et al.*[26] TEM images of the nanoparticles were obtained by a Zeiss EM-109 microscope (Oberkhochen, Germany) operating at 80 kV. Hydrodynamic diameters were obtained by DLS measurements performed at 90° with a 90Plus Particle Size Analyzer working at 15 mW of a 661 nm solid state laser (Brookheaven Inst., Holtsville, NY). Surface ligand exchange was performed as follows. Dried MNC0 (40 mg) were dispersed in chloroform (4 mL). A 0.1 M PMIDA solution was prepared dissolving PMIDA (345 mg) in diluted ammonium hydroxide (28%, 4.5 mL in 11.5 mL water) and added to the above MNC0 dispersion. The mixture was sonicated and sporadically stirred for 30 min without capping the reaction flask, so to encourage the evaporation of the organic solvent. The PMIDA-coated particles (MNC1) were then recovered by magnetic decantation, washed once with 10 mL of the above 0.1 M PMIDA solution, and separated again by permanent magnet. Particles were washed several times with water until pH was neutral and precipitated by the addition of a mixture of acetone/ethanol. Next, a concentrated solution of MNC1 was dialyzed in deionized water and finally diluted to a concentration of 1 mg mL^{-1}. Relaxation measurements were performed at a temperature of 313 K on a Bruker Minispec mq20 system (Ettlingen, Germany) working with ^1H at 20 MHz magnetic field with the following parameters: CMPG pulse sequence, 1000 echoes with a 20 ms echo time and 2 s repetition time. NHS (15.4 mg) and EDC (11.2 mg) were added to 7 mL of the above MNC1 solution, followed by 0.5 M NaOH until pH 8 (*ca.* 2.6 mL). EDBE (196 μL) was then added and the reaction was left under stirring overnight. Excess EDBE was removed by dialysis obtaining MNC2, and the amount of amine groups was quantified by Dunnill's protocol.[28] MNC2 (10 mg) were suspended in a mixture of dry DMF (1.6 mL) and DMSO (0.4 mL) under Ar and sonicated 15 min to obtain a proper dispersion. SPDP[34] (3 mg) dissolved in dry DMSO (0.5 mL) and diisopropylethylamine (1 μL) were consecutively added under stirring. The reaction was quenched after 15 h adding acetic acid (1 μL). Particles (MNC3) were recovered by centrifugation and washed with water until neutral pH and finally exsiccated under vacuum, ready for the next conjugation steps.

DNA Synthesis and Cloning in pGEX-6P-1 Vector. A modified DNA sequence encoding for domain B of *Staphilococcus aureus* protein A was synthesized (Eurofins MWG Operon, Ebersberg) to obtain a fragment variant containing a 6 × His C-terminal tail and *Bam*HI and *Sma*I restriction sites, respectively, at 5′ and 3′ positions (SpaB). SpaB DNA sequence was cloned in a pGEX-6P-1 vector (GE Healthcare, Life Sciences, Little Chalfont, UK) between *Bam*HI and *Sma*I restriction sites according to the Molecular Cloning Handbook,[35] to obtain spaB as a GST-fusion protein containing a PreScission protease recognition site. Plasmidic DNA was then mutated using Quick Site-change mutagenesis kit (Stratagene, La Jolla, CA) in order to introduce a cysteine tripod at C-terminal. The following mutagenesis primers were used: 5′-Cys-5′-CCGGTCACCACCATTGCTGCTGTTAACCCGGGTCGAC-3′ and 3′-Cys-5′-GTCGACCCGGGTTAACAGCAGCAA-TGGTGGTGACCGG-3′. Plasmidic DNA obtained by this procedure (pGEX/spaBC3) was sequenced and used to transform *E.*

coli expression strain BL21(DE3)-RIL (*E. coli* B F^- *ompT hsdS* (rB^- mB^-) *dcm*$^+$ *gal*λ(DE3) (Stratagene).

SpaBC3 Expression and Purification. *E. coli* strain BL21(DE3)-RIL expressing spaBC3 as GST-fusion protein were grown at 37 °C in LB-ampicillin medium and induced with 0.5 mM IPTG at A_{600} 0.8 for 3 h. Cells of mass 1.5 g were obtained from 500 mL of culture. To prepare crude extract, cells were resuspended in lysis buffer (5 mL g^{-1} wet weight; 25 mM potassium phosphate, pH 7.2, 150 mM NaCl, 0.5 mM phenylmethanesulfonyl fluoride, 5 mM DTT, 100 mM $MgCl_2$) plus 1 mg mL^{-1} lysozyme and incubated for 1 h at 4 °C. The cell suspension was then frozen at −80 °C for 30 min and thawed, DNaseI (0.2 mg g^{-1} cells, wet weight) and 1% Triton X-100 were added, and the sample was further incubated for 30 min at RT. Finally, it was centrifuged for 30 min at 39000*g*. Supernatant was loaded onto Glutathione Sepharose 4B affinity column (0.5 mL bed volume, GE Healthcare). Then, it was washed with 20 volumes of washing buffer (25 mM potassium phosphate, pH 7.2, 150 mM NaCl) and equilibrated with 10 volumes of cold cleavage buffer (50 mM Tris-HCl, pH 7.0, 150 mM NaCl, 1 mM EDTA, 1 mM DTT). To elute spaBC3, the resin was incubated at 4 °C overnight under shaking with Prescission protease (400 U mL^{-1} resin) (GE Healthcare). Protein eluted with PreScission protease cleavage was then loaded onto Ni-NTA affinity column (0.5 mL bed volume) and washed with 50 mM sodium phosphate, pH 8.0, 0.3 M NaCl, 20 mM imidazole. SpaBC3 was eluted with 50 mM sodium phosphate, pH 8.0, 0.3 M NaCl, 0.5 M imidazole. Protein was assayed using the reagent Coomassie brilliant blue G-250 (Pierce Biotechnology, Rockford, IL), using bovine serum albumin (BSA) as standard protein.

SDS-PAGE and spaBC3 Binding Assay Using Dot Blot. SDS-PAGE[36] was carried out in a Mighty Small apparatus (Hoefer Scientific Instruments, San Francisco, CA) with a 15% running gel and a 4% stacking gel, 2 h at 25 mA. An aliquot of 0.1 M DTT was added to running buffer. Proteins were revealed by gel code staining (Pierce Biotechnology). Dot blot was performed by filtering proteins and/or nanoparticles onto PVDF membranes, utilizing a Minifold I dot blot apparatus (GE Healthcare), and incubating in blocking solution (5% skim milk in PBS) for 1 h at RT. To evaluate spaBC3 activity, membranes were then probed for 1 h at 25 °C using rabbit IgG (1 mg mL^{-1}) at a 1:800 dilution, or tz (1 mg mL^{-1}) at a 1:6000 diluition in PBS buffer, respectively. Membranes were rinsed three times in 0.05% Tween in PBS for 10 min each and subsequently incubated for 1 h at RT with a secondary antibody (1:5000 horseradish peroxidase−goat antirabbit antibodies in 0.05% Tween in PBS or 1:20000 horseradish peroxidase−rabbit antihuman antibodies, respectively). IgG bound to spaBC3 was removed by incubating 30 min with 50 mM sodium citrate, pH 3.0, at RT. IgG removal was validated by incubating the membrane with an appropriate secondary antibody. Immunoreactive spots were revealed using ECL Western blotting reagent (GE Healthcare).

SpaBC3-MNC Conjugation *via* Disulfide Bridges. Aliquots from a stock 2.5 M DTT solution were added to 2.8 mg of purified spaBC3 to a final concentration of 100 mM and incubated under gentle agitation for 40 min at RT. The excess of DTT was then removed by gel filtration using a prepacked PD10 column (GE Healthcare) and pre-equilibrated with 0.1 M sodium phosphate, pH 7.5, 0.1 M NaCl. Protein obtained by gel filtration (MNPA, 2.0 mg) was quantified by Bradford assay and immediately incubated at RT overnight with MNC3 (15 mg). The amount of spaBC3 bound to MNC was quantified performing a Bradford assay of supernatant. MNPA suspension (5 μL) was treated overnight with 1 M DTT. Nanoparticle content and supernatant were analyzed by dot blot.

Trastuzumab Conjugation to MNPA. The best MNPA/tz ratio to be used in the conjugation reaction was determined: MNPA containing 1 μg spaBC3 was incubated with increasing amounts of tz. After 1 h incubation, supernatants and MNPA, heated at 100 °C for 10 min in a 5× sample buffer, were loaded on SDS-PAGE performed as mentioned above. Proteins were revealed by gel code staining (Pierce Biotechnology). MNPA suspension (0.5 mL, 1 mg mL^{-1} containing 50 μg spaBC3) and PMNC (0.5 mL, 1 mg mL^{-1}) were incubated 1 h at RT with tz (150 μg). The extent of tz on the surface of MNPA and of PMNC was revealed by dot blot analysis. The amount of tz conjugated to MNPA and to PMNC was determined by difference from Bradford assay of the supernatants.

Cell Cultures. MCF-7 cells were grown in 50% Dulbecco's Modified Eagle's Medium (DMEM) and 50% F12 (EuroClone Celbio, Milan, Italy), supplemented with 10% fetal bovine serum (Hyclone Celbio, Milan, Italy), L-glutamine (2 mM), penicillin (50 UI mL^{-1}), and streptomycin (50 mg mL^{-1}, culture medium) at 37 °C in a humidified atmosphere containing 5% CO_2 and subcultured prior to confluence using trypsin/EDTA.

Immunoprecipitation Assay. MCF-7 cells were lysed with lysis buffer containing 20 mM Tris HCl, 150 mM NaCl, 10 mM EGTA, 10% glycerol, and 1% Triton X-100, pH 7.4 for 30 min at 4 °C and then centrifuged at 8500 rpm for 10 min to remove membranes and cell debris from the protein fraction. Bradford assay was used to determine protein content of whole cell extract. The preclearing step was performed with PMNC (200 μL, 1 mg mL^{-1}) for 1 h on wheel at 4 °C. The immunoprecipitation was carried out with 1 mg of precleared lysate and TMNC (200 μL, 1 mg mL^{-1}, corresponding to 3.75 μg of bound antibody) for 16 h at 4 °C on wheel. Samples were washed three times in lysis buffer and boiled in sodium dodecyl sulfate sample buffer containing 5% 2-mercaptoethanol to cleave the linkages to the beads. Samples were run on 8% polyacrylamide gel. Proteins were blotted onto PVDF membranes and incubated in blocking solution (5% skim milk in TBS, 0.05% Tween) for 1 h at RT. For HER-2 detection, membranes were then probed for 1 h at RT using anti-HER-2 polyclonal antibodies (1:500 Millipore, Billerica, MA), in blocking solution. Specificity of the interaction between the HER-2 and TMNC was verified with immunoblot of immunoprecipitated samples with unrelated proteins such as anti-Clnx pAb (1:500 Genetex), anti-Drp1 mAb (1:1000 BD transduction) both at RT for 1 h and anti-Akt pAb (1:1000 Cell Signaling, Danvers, MA) overnight in TBS + 0.05% tween +5% BSA. Specific HRP-conjugated secondary-antibodies were used always 1 h at RT (antimouse 1:10000, Bio-Rad, and antirabbit 1:2000, Cell Signaling). Immunoreactive bands were revealed using ECL Western blotting reagent (GE Healthcare).

Confocal Laser Scanning Microscopy. Cells were cultured on collagene (Sigma) precoated coverglass slides until 90% of confluence and incubated for 15 min with TMNC at a concentration of 150 μg mL^{-1} (corresponding to 15 μg of tz) or 15 μg tz in culture medium. Tz and TMNC were revealed by labeling with secondary antibodies antihuman Alexa fluor 488 (Invitrogen, Carlsbad, CA). Cultures were washed with PBS, fixed for 10 min with 4% paraformaldehyde (Sigma) and then treated for 10 min with 0.1 M glycine (Sigma) in PBS. A blocking step was performed for 1 h at RT with a solution containing 5% BSA (Sigma) and 0.1% Saponin (Sigma) in PBS, followed by 2 h incubation at RT with secondary antibody (1:300) and 30 min incubation at 37 °C with 33 μg of DiD oil (Invitrogen) in PBS for 30 min at 37 °C. Microscopy analysis was performed with a Leica SP2 AOBs microscope confocal system. Images were acquired with 63× magnification oil immersion lenses at 1024 × 1024 pixel resolution.

Acknowledgment. This paper is dedicated to Prof. Emilio Trabucchi on the occasion of his 70th birthday. We thank R. Allevi for TEM images, L. Fiandra for help in cell analyses, and E. Trabucchi for helpful discussion. This work was supported by "Fondazione Romeo ed Enrica Invernizzi" and "Centro di Microscopia Elettronica per lo sviluppo delle Nanotecnologie applicate alla medicina" (CMENA, University of Milan).

REFERENCES AND NOTES

1. Frangioni, J. V. New Technologies for Human Cancer Imaging. *J. Clin. Oncol.* **2008**, *26*, 4012–4021.
2. Weissleder, R.; Mahmood, U. Molecular Imaging. *Radiology* **2001**, *219*, 316–333.
3. Kim, E. E. *Molecular and Cellular MR Imaging.*; Modo, M. M. J., Bulte, J. W. M., Eds.; CRC Press: Boca Raton, FL, 2007; pp 1−421.
4. Caravan, P.; Ellison, J. J.; McMurry, T. J.; Lauffer, R. B. Gadolinium(III) Chelates as MRI Contrast Agents: Structure, Dynamics, and Applications. *Chem. Rev.* **1999**, *99*, 2293.

5. Terreno, E.; Delli Castelli, D.; Viale, A.; Aime, S. Challenges for Molecular Magnetic Resonance Imaging. *Chem. Rev.* **2010**, *110*, 3019–3042.
6. Konda, S. D.; Aref, M.; Brechbiel, M.; Wiener, E. C. Development of a Tumor-Targeting MR Contrast Agent using the High-Affinity Folate Receptor-Work in Progress. *Invest. Radiol.* **2000**, *35*, 50–57.
7. Ke, T.; Jeong, E.-K.; Wang, X.; Feng, Y.; Parker, D. L.; Lu, Z.-R. RGD Targeted Poly(L-glutamic acid)-cystamine-(Gd-DO3A) Conjugate for Detecting Angiogenesis Biomarker Anb3 Integrin with MR T_1 Mapping. *Int. J. Nanomed.* **2007**, *2*, 191–199.
8. Curtet, C.; Tellier, C.; Bohy, J.; Conti, M. L.; Saccavini, J. C.; Thedrez, P.; Douillard, J. Y.; Chatal, J. F.; Koprowski, H. Selective Modification of NMR Relaxation Time in Human Colorectal Carcinoma by Using Gadolinium-diethylenetriaminepentaacetic Acid Conjugated with Monoclonal Antibody 19-9. *Proc. Natl. Acad. Sci. U.S.A.* **1986**, *83*, 4277–4281.
9. Morawski, A. M.; Winter, P. M.; Crowder, K. C.; Caruthers, S. D.; Fuhrhop, R. W.; Scott, M. J.; Robertson, J. D.; Abendschein, D. R.; Lanza, G. M.; Wickline, S. A. Targeted Nanoparticles for Quantitative Imaging of Sparse Molecular Epitopes with MRI. *Magn. Reson. Med.* **2004**, *51*, 480–486.
10. Mendonca Dias, M. H.; Lauterbur, P. C. Ferromagnetic Particles as Contrast Agents for Magnetic Resonance Imaging of Liver and Spleen. *Magn. Reson. Med.* **1986**, *3*, 328–330.
11. Semelka, R. C.; Helmberger, T. K. Contrast Agents for MR Imaging of the Liver. *Radiology* **2001**, *218*, 27–38.
12. Harisinghani, M. G.; Barentsz, J.; Hahn, P. F.; Deserno, W. M.; Tabatabaei, S.; van de Kaa, C. H.; de la Rosette, J.; Weissleder, R. Noninvasive Detection of Clinically Occult Lymph-Node Metastases in Prostate Cancer. *N. Engl. J. Med.* **2003**, *348*, 2491–2499.
13. de Vries, I. J. M.; Lesterhuis, W. J.; Barentsz, J. O.; Verdijk, P.; van Krieken, J. H.; Boerman, O. C.; Oyen, W. J. G.; Bonenkamp, J. J.; Boezeman, J. B.; Adema, G. J.; *et al.* Magnetic Resonance Tracking of Dendritic Cells in Melanoma Patients for Monitoring of Cellular Therapy. *Nat. Biotechnol.* **2005**, *23*, 1407–1413.
14. Evgenov, N. V.; Medarova, Z.; Dai, G.; Bonner-Weir, S.; Moore, A. *In Vivo* Imaging of Islet Transplantation. *Nat. Med.* **2006**, *12*, 144–148.
15. Perez, J. M.; Josephson, L.; O'Loughlin, T.; Hogemann, D.; Weissleder, R. Magnetic Relaxation Switches Capable of Sensing Molecular Interactions. *Nat. Biotechnol.* **2002**, *20*, 816–820.
16. Shultz, M. D.; Reveles, J. U.; Khanna, S. N.; Carpenter, E. E. Reactive Nature of Dopamine as a Surface Functionalization Agent in Iron Oxide Nanoparticles. *J. Am. Chem. Soc.* **2007**, *129*, 2482–2487.
17. Narain, R.; Gonzales, M.; Hoffman, A. S.; Stayton, P. S.; Krishnan, K. M. Synthesis of Monodisperse Biotinylated p(NIPAAm)-Coated Iron Oxide Magnetic Nanoparticles and Their Bioconjugation to Streptavidin. *Langmuir* **2007**, *23*, 6299–6304.
18. Polito, L.; Monti, D.; Caneva, E.; Delnevo, E.; Russo, G.; Prosperi, D. One-Step Bioengineering of Magnetic Nanoparticles *via* a Surface Diazo Transfer/Azide−Alkyne Click Reaction Sequence. *Chem. Commun.* **2008**, *5*, 621–623.
19. Polito, L.; Colombo, M.; Monti, D.; Melato, S.; Caneva, E.; Prosperi, D. Resolving the Structure of Ligands Bound to the Surface of Superparamagnetic Iron Oxide Nanoparticles by High-Resolution Magic-Angle Spinning NMR Spectroscopy. *J. Am. Chem. Soc.* **2008**, *130*, 12712–12724.
20. Hober, S.; Nord, K.; Linhult, M. Protein A Chromatography for Antibody Purification. *J. Chromatogr., B* **2007**, *848*, 40–47.
21. Abrahmsen, L.; Moks, T.; Nilsson, B.; Hellmann, U.; Uhlèn, M. Analysis of Signal for Secretion of *Staphylococcal* Protein A Gene. *EMBO J.* **1985**, *13B*, 3901–3906.
22. Chalon, M. P.; Milne, R. W.; Vaerman, J. P. Interactions between Mouse Immunoglobulins and *Staphylococcal* Protein A. *Scand. J. Immunol.* **1979**, *9*, 359–364.
23. Holschuh, A.; Schwammle, J. Preparative Purification of Antibodies with Protein A—An Alternative to Conventional Chromatography. *J. Magn. Magn. Mater.* **2003**, *293*, 345–348.
24. Hoffman, W. L.; O'Shannessy, D. J. Site-Specific Immobilization of Antibodies by their Oligosaccharide Moieties to New Hydrazide Derivatized Solid Supports. *J. Immunol. Methods* **1998**, *112*, 113–120.
25. Colombo, M.; Corsi, F.; Foschi, D.; Mazzantini, E.; Mazzucchelli, S.; Morasso, C.; Occhipinti, E.; Polito, L.; Prosperi, D.; Ronchi, S.; *et al.* HER2 Targeting as a Two-Sided Strategy for Breast Cancer Diagnosis and Treatment: Outlook and Recent Implications in Nanomedical Approaches. *Pharmacol. Res.* **2010**, *62*, 150–165.
26. Park, J.; An, K.; Hwang, Y.; Park, J.-G.; Noh, H.-J.; Kim, J.-Y.; Park, J.-H.; Hwang, N.-M.; Hyeon, T. Ultra-large-Scale Syntheses of Monodisperse Nanocrystals. *Nat. Mater.* **2004**, *3*, 891–895.
27. See, for example: Ma, H.-l.; Qi, Xi.-r.; Maitani, Y.; Nagai, T. Preparation and Characterization of Superparamagnetic Iron Oxide Nanoparticles Stabilized by Alginate. *Int. J. Pharm.* **2007**, *333*, 177–186.
28. Halling, P. J.; Dunnill, P. Hydrolysis of Lactose in Milk by Lactase Immobilized to a Non-porous magnetic Support. *Appl. Microbiol. Biotechnol.* **1979**, *8*, 27–36.
29. De Marco, V.; Stier, G.; Blandin, S.; De Marco, A. The Solubility and Stability of Recombinant Proteins are Increased by their Fusion to NusA. *Biochem. Biophys. Res. Commun.* **2004**, *322*, 766–771.
30. Carlsson, J.; Drevin, H.; Axèn, R. Protein Thiolation and Reversible Protein−Protein Conjugation. *Biochem. J.* **1978**, *173*, 727–730.
31. Stuchbury, T.; Shipton, M.; Norris, R.; Malthouse, P. J.; Brocklehurst, K. A; Herbert, J. A. L.; Suschitzky, H. Reported Group Delivery System with Both Absolute and Selective Specificity for Thiol Groups and an Improved Fluorescent Probe Containing the 7-Nitrobenzo-2-oxa-1,3-diazole Moiety. *Biochem. J.* **1975**, *151*, 417–432.
32. Corsi, F.; De Palma, C.; Colombo, M.; Nebuloni, M.; Ronchi, S.; Rizzi, G.; Allevi, R.; Tosoni, A.; Trabucchi, E.; Clementi, E.; Prosperi, D. Towards Ideal Magnetofluorescent Nanoparticles for Bimodal Detection of Breast Cancer Cells. *Small* **2009**, *5*, 2555–2564.
33. Yuste, L.; Montero, J. C.; Espari's-Ogando, A.; Pandiella, A. Activation of ErbB2 by Overexpression or by Transmembrane Neuregulin Results in Differential Signaling and Sensitivity to Herceptin. *Cancer Res.* **2005**, *65*, 6801–6810.
34. Navath, R. S.; Kurtoglu, Y. E.; Wang, B.; Kannah, S.; Romero, R.; Kannan, R. M. Dendrimer−Drug Conjugates for Tailored Intracellular Drug Release Based on Glutathione Levels. *Bioconjugate Chem.* **2008**, *19*, 2446–2455.
35. Sambrook, J.; Fritsch, E. F.; Maniatis, T. In *Molecular Cloning: A Laboratory Manual*, 2nd ed.; Nolan, C., Ed.; Cold Spring Harbor Laboratory Press: Cold Spring Harbor, NY, 1989; Vol. 1.
36. Laemmli, U. K. Cleavage of Structural Proteins During the Assembly of the Head of Bacteriophage T4. *Nature* **1970**, *227*, 680–685.

COMMUNICATION www.rsc.org/nanoscale | Nanoscale

Investigating the structural biofunctionality of antibodies conjugated to magnetic nanoparticles†

Emanuela Occhipinti,‡[a] Paolo Verderio,‡[b] Antonino Natalello,[a] Elisabetta Galbiati,[a] Miriam Colombo,[ab] Serena Mazzucchelli,[b] Agnese Salvadè,[b] Paolo Tortora,[a] Silvia Maria Doglia[a] and Davide Prosperi*[ab]

Received 23rd June 2010, Accepted 3rd September 2010
DOI: 10.1039/c0nr00436g

We present the synthesis of trastuzumab-functionalized pegylated iron oxide nanoparticles and provide an FTIR-based approach to gain a direct evidence of the actual conservation of the native structure of conjugated antibody. Their target-selectivity to specific cancer cell receptors has been also assessed.

The successful development of targeted nanoprobes for noninvasive medical imaging represents a new frontier in the prevention and treatment of malignant diseases.[1] Among the available choices to obtain an effective targeting action, the conjugation of nanoparticles with monoclonal antibodies (mAbs) is a well-established strategy to deliver the nanoprobe to specific cell types.[2] This approach combines the unique physical properties of nanoparticles, with the specific and selective recognition capability of mAbs to cells and tissues. Moreover, the potential improvement in the cellular uptake and the enhanced intracellular stability could be two of the major advantages of using mAb-conjugated nanoparticles.

Trastuzumab (TZ) is a recombinant, humanized IgG mAb that selectively binds with high affinity to the extracellular domain of the human epidermal growth factor receptor 2 (HER2), which is expressed in several primary tumors, including breast, ovarian, gastric and salivary cancers, and in metastatic sites.[3] For this reason, TZ has been developed for clinical immunotherapy and the conjugation of TZ with chemotherapeutics may offer an excellent strategy for targeted delivery of drugs to malignant cells.[4] The therapeutic action of TZ mainly consists in blocking the dimerization of the two components of HER2 complex resulting in an interruption of the signal transduction. Colloidal systems, such as those based on inorganic nanomaterials, provide higher drug carrier capacities than individual mAbs, concomitantly acting as signal emitters for medical diagnosis. Therefore, in view of the outstanding potential of mAb-based hybrid nanovehicles, the conjugation of mAbs to nanoparticles is now a widespread practice to gain selective delivery and localization of nanoparticle probes to the desired target site.

However, despite the huge interest for mAb nanoconjugates, only poor evidence is presently available on the actual conservation of the protein biofunctionality at the molecular structural level, once mAb has been covalently conjugated to the nanoparticle. Such difficulty mainly resides in the lack of reliable methods capable of providing exhaustive information on structural/conformational features sustaining the protein functionalities of bioconjugate systems. This is indeed a crucial point, which urgently needs to be addressed. Weiss *et al.* exploited circular dichroism to investigate proteins immobilized on gold nanoparticles.[5] Unfortunately, this technique is expected to fail with magnetic nanoparticles due to the strong absorption of iron oxide in the UV range. The purpose of the present study is to provide a direct evidence on the extent of preservation of the structural bioactivity of IgGs immobilized onto the surface of iron oxide nanoparticles deduced by accurate analysis of the essential folding features obtained by Fourier-transform infrared (FTIR) spectroscopy. As a model for this study, PEG-stabilized, TZ-modified magnetite nanoparticles (TMNP) were developed (Scheme 1). Thanks to the unique magnetic properties of nanoscale iron oxides, this class of nanoparticles could be useful as targeted contrast agents for magnetic resonance imaging of cancer cells.[6–8]

Bare monodisperse magnetite nanoparticles (MNP1) were obtained by aqueous alkaline coprecipitation of Fe^{2+} and Fe^{3+} ions in 1 : 2 molar ratio, as described in a previous work.[9] A bifunctional linker α-ω-dicarboxyl-terminated polyethylene glycol (PEG, M_w 600 Da) was grafted on the Fe_3O_4 surface by ultrasound-assisted reaction and the unreacted excess of PEG was removed by dialysis. The synthesized carboxyPEG-functionalized nanoparticles (MNP2) were highly soluble in water, thus the MNP2 suspension was diluted to a final concentration of 1 mg mL^{-1}, which was stable for several months at room temperature. According to previous reports, PEG-coated nanoparticles are more biodegradable, non-antigenic, non-irritative for tissues and less toxic than unmodified nanoparticles.[10–12] At the same time, the PEG chains are responsible for the so-called "stealth effect", preventing nonspecific adsorption of opsonin proteins.[13]

TEM image showed that the core size of MNP2 was unchanged after PEG grafting (10 ± 3 nm, Fig. S2, ESI†). The hydrodynamic diameter of MNP2 was determined to be 82.4 ± 1.0 nm by dynamic light scattering (DLS, Fig. S3a, ESI†). A good contrast power for MNP2 in PBS was deduced by the relaxivity value r_2, which was calculated to be 131.9 mM^{-1} s^{-1} (Fig. S4, ESI†). The pH-dependent stability of MNP2 in water was also investigated by UV-vis absorption spectra (Fig. S5 and Table S1, ESI†). MNP2 were dispersed in deionized water and evaluated in the pH range from 1 to 11, in which they did not display any aggregation up to pH 7–8. A critical formation of large clusters of nanoparticles was instead observed above pH 9 right after 90 min incubation, which resulted in collapsing of the colloidal suspension (Fig. S6, ESI†). Zeta potential (ζ) of MNP2 in water in a range of pH between 3 and 9 was also

[a]*Dipartimento di Biotecnologie e Bioscienze, Università di Milano-Bicocca, P.za della Scienza 2, 20126 Milano, Italy. E-mail: davide.prosperi@unimib.it; Fax: +39 026448 3565; Tel: +39 026448 3302*
[b]*Centro di Microscopia Elettronica per le Nanotecnologie applicate alla medicina, Università di Milano, Via G.B. Grassi 74, 20157 Milano, Italy*

† Electronic supplementary information (ESI) available: Experimental details, TEM images, DLS and relaxivity plots, additional FT-IR spectra and analyses. See DOI: 10.1039/c0nr00436g

‡ These authors contributed equally to the research.

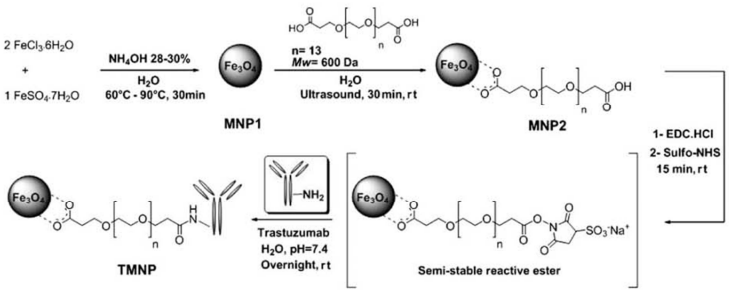

Scheme 1 Schematic representation of the synthesis of pegylated trastuzumab-modified iron oxide nanoparticles (TMNP).

investigated (Fig. S3b, ESI†). At pH 3, MNP2 were strongly positively charged with $\zeta = +42.0 \pm 3.2$ mV, probably due to a tendency of PEG to capture acidic protons. In contrast, at pH 9, MNP2 exhibited a strongly negative surface charge of $\zeta = -43.3 \pm 1.3$ mV, confirming the presence of completely deprotonated carboxylate groups on the external surface of nanoparticles. Similar results were obtained in PBS: as expected, in this case, MNP2 were less negatively charged, with $\zeta = -19.5 \pm 0.5$ mV.

MNP2 were ready for conjugation with amine-containing biomolecules by amide coupling owing to the high surface density of carboxyl functionalities. To examine their potential in mAb conjugation, purified TZ was covalently bound to MNP2 at pH 7.4 in the presence of coupling agents, such as sulfo-NHS and EDC, exploiting the lysine amine groups present on the peptide sequence of the antibody. The resulting TMNP were washed with PBS to remove unbound antibodies, which would lead to false-positives in biological experiments, resuspended in PBS at a final concentration of 0.8 mg mL^{-1} and stored at 4 °C. The average number of TZ loaded on TMNP was estimated to be about 2 mAb per nanoparticle by a Bradford protein assay. The hydrodynamic size of these mAb-conjugates was 224.9 ± 2.7 nm (Fig. S8, ESI†), which was remarkably higher than that of MNP2, while only a slight decrease in relaxivity was observed (Table 1). In addition, ζ values showed a marked decrease in the negative charge to $\zeta = -7.8 \pm 1.1$ mV (Table S2, ESI†), which demonstrated that several carboxylate groups from the surface PEG chains were involved in the linkage with TZ, and the residual negative charges were partially compensated by the positive charges on the IgG molecule, consistent with the basic isoelectric point of TZ ($IP_{TZ} = 8.45$). The physical/chemical characteristics of MNP2 and TMNP are summarized in Table 1.

Table 1 Comparison between physico-chemical characteristic of MNP2 and TMNP

Parameter	Unit	MNP2	TMNP
Particle size (from DLS)	nm	82.2 ± 1.0	224.9 ± 2.7
Polydispersity		0.239 ± 0.01	0.194 ± 0.02
ζ-Potential	mV	−19.5 ± 0.5	−7.8 ± 1.1
T_2 relaxivity (r_2)	mM^{-1} s^{-1}	131.9	103.0
Ab binding efficiency (Ab/NP)	μg mg^{-1}	—	217
		—	2

An important prerequisite to keep in mind when designing an appropriate conjugation strategy is maintaining intact, as much as possible, the biological activity and full receptor binding capability of immobilized mAbs. We had a first immediate evidence of the immunoreactivity of mAbs in TMNP performing a dot blot analysis (Fig. S9, ESI†). Our results confirmed that TMNP were able to cross-react with anti-human antibody with the same sensitivity of free TZ.

In order to explore the structural properties of the conjugated antibody, we applied FTIR spectroscopy to obtain information on protein secondary structure.[14,15] This method has been seldom exploited to investigate protein molecules physically adsorbed onto nanoscale gold surfaces. Shang *et al.* observed remarkable conformational changes in the protein secondary structure occurring upon

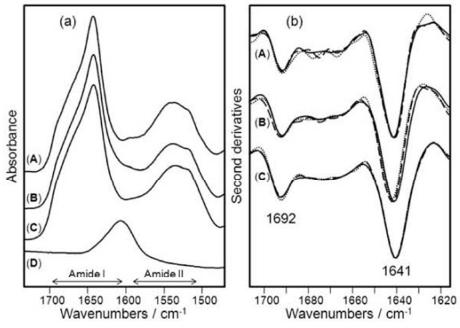

Fig. 1 Structural characterization of TZ, TMNP, and MNP2 by FTIR spectroscopy. (a) FTIR absorption spectra in the amide I and amide II regions of (A) free TZ at 1.0 mg mL^{-1}, (B) a mixture of free TZ at 1.0 mg mL^{-1} and free MNP2 at 4.7 mg mL^{-1}, (C) TMNP at 4.7 mg mL^{-1} (1.0 mg mL^{-1} TZ), and (D) MNP2 at 7.0 mg mL^{-1}. In this spectral region, MNP2 (D) displayed only a broad absorption around 1606 cm^{-1}, while TMNP (C) showed the protein amide I and amide II bands confirming the success of the bioconjugation. The spectra were collected immediately after sample preparation. (b) Second derivatives of the spectra reported in (a). Spectra were collected at time 0 (continuous lines), after 24 h (dashed lines), and after 96 h (dotted lines) of incubation at 37 °C. The spectra are dominated by two components at 1692 cm^{-1} and 1641 cm^{-1} assigned to the native β-sheet structure of TZ that were found to be stable upon incubation at 37 °C both in the free and in the bioconjugated protein.

adsorption.[16] However, to the best of our knowledge, the present study represents the first example aimed at assessing the conformational effects caused by covalent conjugation of antibodies to nanoparticles. Herein, the secondary structure and stability of the conjugated mAb were investigated by FTIR spectroscopy, which has previously been used to determine the folding features of antibodies.[17] In Fig. 1a, the absorption spectra of free TZ (A), of a mixture of MNP2 and free TZ (B), of TMNP (C), and of MNP2 (D) are reported in the 1500–1700 cm^{-1} spectral region, where the amide I and amide II bands occur. These bands are due, respectively, to the absorption of the C=O stretching and N–H bending vibrations of the protein backbone.[14,15] The presence of these two bands in the TMNP spectrum confirmed that the conjugation reaction occurred successfully. Indeed, unconjugated MNP2 displayed a completely different profile in this spectral region, with only a broad absorption centered at about 1606 cm^{-1}.

Information on the secondary structure of the protein can be obtained through the analysis of the amide I band, as it is the spectral region most sensitive to the structural conformation changes of the protein.[15,18] In order to resolve the amide I band components, we performed the second derivatives of the measured spectra (Fig. 1b).[14] The spectrum of freshly purified TZ is dominated by two main components, which appear as negative peaks in the second derivative, at 1692 cm^{-1} and 1641 cm^{-1} that can be both assigned to the native β-sheet structure of the protein.[15,17] The spectrum of TMNP was almost identical to that of free TZ under native condition indicating that the amidic conjugation used in this work did not affect significantly the protein secondary structure. To monitor the stability of the conjugated mAb, we collected the FTIR spectra of the samples at different times of incubation up to 96 h at 37 °C. The comparison of the FTIR second derivative spectra of native TZ at the beginning of incubation with that after 96 h indicates that the protein secondary structures were substantially unchanged. The same result was obtained for conjugated TZ after incubation at 37 °C. We tested the storage stability of TMNP, and found that conjugated TZ was stable even after two months incubation at 4 °C without any additional stabilizing agents.

Next, we examined the FTIR absorption of all the above samples after being lyophilized and resuspended in buffered heavy water (PBS/D_2O), pH 7.4, to simulate the physiological environment. In this way, it was possible to monitor in real time the stability of the conjugated antibodies by transmission FTIR at 37 °C, exploiting the low absorbance of D_2O in the amide I region.[15,17] These results confirmed once again that conjugation did not affect the native protein secondary structure, which was found to be stable over 24 h incubation at 37 °C (data not shown). Altogether, these data provided a compelling evidence on the preserved stability of mAb in TMNP system and demonstrated that under these synthetic conditions the conjugated protein did not change its physiological biofunctionality.

To quantitatively assess the secondary structure components of the conjugated antibodies, we performed a Gaussian curve fitting of the absorption spectra of free TZ and of TMNP, whose results are reported in the ESI† (Fig. S11). The relative weights of the β-sheet components (1641 and 1692 cm^{-1}) and of the random coil component (R.c. 1663 cm^{-1}) were very similar, with only minor differences. In particular, TMNP seems to display a slightly larger R.c. that could account for a partially reduced bioactivity. Next, we examined the infrared absorption spectra of TZ physically adsorbed on bare MNP1 (Fig. S10 and S11 in ESI†). As expected, the bioactivity of the antibody was strongly reduced. The spectra were very different in the amide I band, whose maximum shifted from 1641 cm^{-1} for free TZ to 1650 cm^{-1} for adsorbed TZ. Indeed, the Gaussian curve fitting of these spectra indicates a strong change in the antibody secondary structures. The β-sheet components were reduced from ~50% in free TZ to ~34% in the adsorbed TZ immediately after preparation, and to ~22% after 96 h incubation at 37 °C. R.c. increased from ~ 44% in free TZ to ~55% and ~66% in the adsorbed TZ at 0 and 96 h incubation, respectively. In this case, the loss of native secondary structure predicted by the above FTIR analysis is in agreement with the decreased bioactivity observed for the adsorbed TZ.

To check whether TMNP were able to maintain effectively the specific targeting capability of TZ for HER2-positive breast cancer cells, we investigated the TMNP binding to HER2 in HER2-overexpressed MCF7 cells.[19] Two MCF7 whole cell extracts were incubated in parallel at 4 °C with TMNP and with unconjugated MNP2 (control), respectively. Immunoprecipitants (bound) and the supernatants (unbound) were first analyzed by western blotting with anti-HER2 antibody in order to reveal TMNP binding to HER2 receptor (Fig. 2, upper). The comparison between TMNP and MNP2 confirmed that the conjugation with TZ was necessary to immunoprecipitate HER2 membrane receptor in MCF7 whole cell extract. Next, calnexin (Clnx), an integral protein of the endoplasmic reticulum,[20] was tested as negative control to assess the possible nonspecific interaction of TMNP with undesired biomolecules. To this aim, a labeled anti-Clnx mAb was used, which displayed a detectable signal only in unbound sample (Fig. 2, lower). Such immunoprecipitation assay revealed that Clnx was completely absent in the TMNP sample whereas it was detected in the unbound supernatant, suggesting that the interaction between TMNP and HER2 is specific and correlated to antibody conjugation.

The immunoprecipitation data were confirmed by relaxivity measurements, which provided evidence on iron oxide capture by MCF7 (Table S3, ESI†), and by immunofluorescence after TMNP incubation with living cells. Since HER2 is a trans-membrane receptor,[3] TMNP were expected to localize on the membrane of HER2 positive MCF7 cells. In order to assess HER2 surface distribution, MCF7 cells were first treated with TZ (Fig. 3d–f). TMNP were then incubated with MCF7. Next, TZ and TMNP were labeled with anti-human FITC-labeled secondary antibodies (green), whereas cell membranes were stained with DiD oil (mb, blue). After 20 min incubation, TMNP were observed in MCF7 cell surfaces (Fig. 3a–c), demonstrating that they localized selectively in

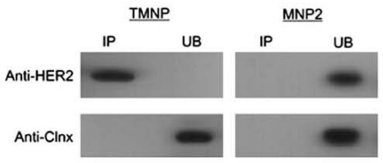

Fig. 2 Immunoprecipitation of HER2 in MCF7 cells. Immuno-precipitation was performed using anti-HER2 or anti-calnexin antibodies cross-linked to TMNP and MNP2 (as negative control). Nanoparticles were incubated overnight at 4 °C in a whole extract of MCF7 cells. Bound (IP) and unbound (UB) proteins were eluted in SDS-PAGE application buffer, electrophoresed and immunoblotted.

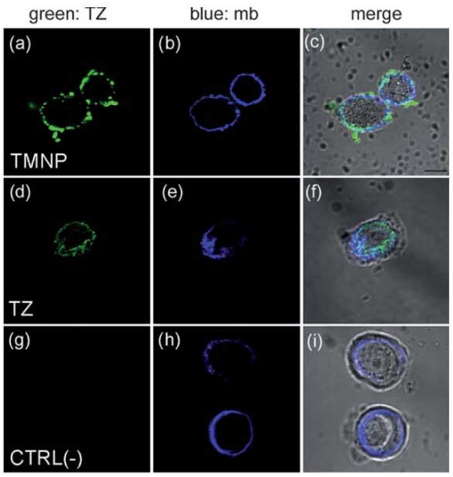

Fig. 3 Confocal laser images of MCF7 cells cultured with TMNP or free TZ. MCF7 were incubated for 20 min with TMNP (100 μg mL^{-1}; a–c) or TZ (11 μg mL^{-1}; d–f). As negative control, MCF7 were stained with secondary antibodies anti-human FITC (g–i). Cell membranes (mb) were stained with DiD oil (blue). TMNP and TZ were labeled with anti-human FITC secondary antibodies. Scale bar = 10 μm.

correspondence of trans-membrane receptors. The combined results of these experiments clearly evidenced the target-selectivity of TMNP towards HER2 breast cancer marker.

In summary, we have synthesized a trastuzumab-modified, fully pegylated iron oxide nanoparticle (TMNP) as a model for the study of the interaction between a mAb nanoconjugate and the relevant natural receptor. In particular, we have demonstrated for the first time that accurate analysis of the FTIR signals in the 1500–1700 cm^{-1} absorption range may be a valuable method enabling the determination of protein conformational changes in mAb conjugate. As a proof of concept, testing our TMNP by FTIR revealed that, different from physically adsorbed protein, mAb conjugated to the nanoparticle surface *via* a dicarboxylic PEG linker did not change its structural properties maintaining the folding characteristics basically intact. This simple and fast structural characterization tool is versatile and of wide utility, as it might be easily applied to other typologies of proteins and nanoparticles different from the ones used in this study. As the functionality of a protein is essentially related to its native folding, the approach presented here is able to provide a preliminary evidence on the actual bioactivity expected for a protein in a biohybrid nanoconjugate system. Such rapid evidence could be of large utility in designing and testing novel hybrid targeted nanovectors, preventively providing a chance to reduce those side effects, which usually lead to nonspecific uptake by normal tissues.

Acknowledgements

We thank R. Allevi for TEM images. This work was supported by "Fondazione Romeo ed Enrica Invernizzi", CMENA (University of Milano) and Regione Lombardia (NanoMeDia Project). S.M.D., P.T., and D.P. acknowledge the financial support of F.A.R. and A.N. the post-doctoral fellowship of the University of Milano-Bicocca.

Notes and references

1 J. V. Frangioni, *J. Clin. Oncol.*, 2008, **26**, 4012–4021.
2 D. Peer, J. M. Karp, S. Hong, O. C. Farokhzad, R. Margalit and R. Langer, *Nat. Nanotechnol.*, 2007, **2**, 751–760.
3 M. Colombo, F. Corsi, D. Foschi, E. Mazzantini, S. Mazzuchelli, C. Morasso, E. Occhipinti, L. Polito, D. Prosperi, S. Ronchi and P. Verderio, *Pharmacol. Res.*, 2010, **62**, 150–165.
4 G. L. Plosker and S. J. Keam, *Drugs*, 2006, **66**, 449–475.
5 A. Weiss, T. C. Preston, J. Popov, Q. Li, S. Wu, K. C. Chou, H. M. Burt, M. B. Bally and R. Signorell, *J. Phys. Chem. C*, 2009, **113**, 20252–20258.
6 M. V. Yezhelyev, X. Gao, Y. Xing, A. Al-Hajj, S. Nie and R. M. O'Regan, *Lancet Oncol.*, 2006, **7**, 657–667.
7 M. G. Harisinghani, J. Barentsz, P. F. Hahn, W. M. Deserno, S. Tabatabaei, C. H. van de Kaa, J. de la Rosette and R. Weissleder, *N. Engl. J. Med.*, 2003, **348**, 2491–2499.
8 M. Zhao, D. A. Beauregard, L. Loizou, B. Davletov and K. M. Brindle, *Nat. Med. (N. Y.)*, 2001, **11**, 1241–1244.
9 L. Polito, M. Colombo, D. Monti, S. Melato, E. Caneva and D. Prosperi, *J. Am. Chem. Soc.*, 2008, **130**, 12712–12724.
10 F. Corsi, C. De Palma, M. Colombo, R. Allevi, M. Nebuloni, S. Ronchi, G. Rizzi, A. Tosoni, E. Trabucchi, E. Clementi and D. Prosperi, *Small*, 2009, **5**, 2555–2564.
11 C. Sun, K. Du, C. Fang, N. Bhattarai, O. Veiseh, F. Kievit, Z. Stephen, D. Lee, R. G. Ellenbogen, B. Ratner and M. Zhang, *ACS Nano*, 2010, **4**, 2402–2410.
12 F. Hu, L. Wei, Z. Zhou, Y. Ran, Z. Li and M. Gao, *Adv. Mater.*, 2006, **18**, 2553–2556.
13 W. Lin, M. C. Garnett, E. Schacht, S. S. Davis and L. Illum, *Int. J. Pharm.*, 1999, **189**, 161–170.
14 H. Susi and D. M. Byler, *Methods Enzymol.*, 1986, **130**, 290–311.
15 J. L. R. Arrondo and F. M. Goni, *Prog. Biophys. Mol. Biol.*, 1999, **72**, 367–405.
16 L. Shang, Y. Wang, J. Jiang and S. Dong, *Langmuir*, 2007, **23**, 2714–2721.
17 A. Dong, P. Huang and W. S. Caughey, *Biochemistry*, 1990, **29**, 3303–3308.
18 A. Natalello, D. Ami, S. Brocca, M. Lotti and S. M. Doglia, *Biochem. J.*, 2005, **385**, 511–517.
19 L. Yuste, J. C. Montero, A. Esparís-Ogando and A. Pandiella, *Cancer Res.*, 2005, **65**, 6801–6810.
20 J. J. Carmelo and A. J. Parodi, *J. Biol. Chem.*, 2008, **283**, 10221–10225.

ARTICLE 5
Supplementary Material (ESI) for *Nanoscale*

Supporting Information

Investigating the structural biofunctionality of antibodies conjugated to magnetic nanoparticles

Emanuela Occhipinti,[a] Paolo Verderio,[b] Antonino Natalello,[a] Elisabetta Galbiati,[a] Miriam Colombo,[a,b] Serena Mazzucchelli,[b] Paolo Tortora,[a] Silvia Maria Doglia[a] and Davide Prosperi[a,*]

[a] Dipartimento di Biotecnologie e Bioscienze, Università di Milano-Bicocca, P.za della Scienza 2, 20126 Milano, Italy. [b] Dipartimento di Scienze Cliniche "Luigi Sacco", Università di Milano, Ospedale L. Sacco, Via G.B. Grassi 74, 20157 Milano, Italy.

Fax: 39 026448 3565; Tel39 026448 3302; E-mail: davide.prosperi@unimib.it

General Materials and Instrument details.

All reagents and solvents were purchased from Sigma-Aldrich (St. Louis, MO), Fluka (St. Gallen, Switzerland) and Riedel-de Haën (Seelze, Germany) and used as received without further purification. Trastuzumab was received from Roche Products Ltd. (UK) as a powder lyophilized for intravenous administration; before reactions it was purified from additives by dialysis (membrane, MW cutoff 12-14000 Da) in phosphate buffer solution, pH 7.4, 300 mM NaCl, 2.7 mM KCl, 10 mM phosphate. Water was deionized and ultrafiltered by a MilliQ apparatus (Millipore Corporation, Billerica, MA). Unless otherwise specified, all of the reactions were performed in an inert atmosphere of argon under dry conditions. Ultrasounds were generated by S15H Elmasonic Apparatus (Elma, Singen, Germany). TEM images of nanoparticles were obtained by a Zeiss EM-109 microscope (Oberkhochen, Germany) operating at 80 kV. T_2 relaxation times were performed at a temperature of 313 K using a Bruker Minispec mq20 system (Ettlingen, Gerrmany) working with ^{1}H at 20 MHz magnetic field with the following parameters: Carr-Purcell-Meiboom-Gill pulse sequence, 1000 echoes with a 20 ms echo times and 2 s repetition time. Samples were introduced using a 10 mm NMR spectroscopy tubes prewarmed and sonicated at 40 °C. Dynamic Light Scattering (DLS) measurements were performed at 90° with a 90 Plus Particle Size Analyzer from Brookhaven Instrument Corporation (Holtsville, NY) working at 15 mW of a solid-state laser (λ = 661 nm). Zeta-potential measurements were elaborated on the same instrument equipped with AQ-809 electrode and data were processed by ZetaPlus Software. UV-vis spectra were recorded by using a Uvikon 930 UV/Vis Spectrophotometer (Kontron Instruments) in a range of wavelenghts from 190 nm to 600 nm. The FTIR absorption spectra were acquired using the Varian 610-IR infrared microscope coupled to a Varian 670-IR spectrometer (Varian Australia Pty Ltd, Mulgrave

VIC, Australia) and equipped with a nitrogen-cooled, mercury–cadmium–tellurium (MCT) detector. Spectra were collected in transmission under the following conditions: 2 cm^{-1} spectral resolution, 25 kHz scan speed, 512 scan co-additions, and triangular apodization. Measured spectra were smoothed by a binomial function (11 points) and the second-derivatives were obtained by the Savitsky–Golay method (3rd grade polynomial, 5 smoothing points) using the GRAMS/32 software (Galactic Industries Corporation, Salem, NH, USA). For FTIR measurements, 2 µL of the sample solution were deposited on a BaF_2 infrared window and dried at room temperature for 30 min. For measurements in heavy water solution, samples were lyophilized and resuspended in D_2O PBS, pH 7.4. A BaF_2 transmission cell (Wilmad, Buena, NJ, U.S.A.) with path length of 100 µm was employed and the spectra were collected under the same conditions reported above.

Synthesis of MNP1 and MNP2

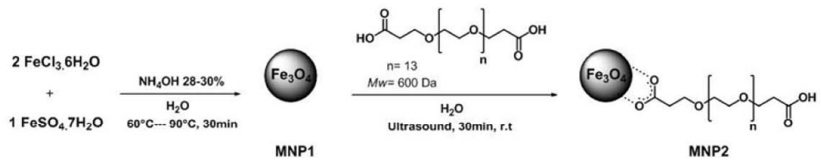

Fig. S1 Synthesis of MNP1 and of pegylated MNP2.

Synthesis of Fe_3O_4 nanoparticles (MNP1) by coprecipitation method: Monodisperse magnetic nanoparticles were obtained as previously described in our previous work with minor modification.[1] Briefly, to a solution of distilled water (173 mL) and NH_4OH 28-30% (14 mL), prewarmed at 60 °C under vigorous stirring, was added a mixture of 1 M $FeCl_3 \cdot 6H_2O$ in distilled water (20 mL) and 2 M $FeSO_4 \cdot 7H_2O$ in 2 N HCl (5 mL); the solution turned dark instantaneously and a black precipitate was formed. The reaction suspension was heated immediately at 90 °C under vigorous magnetic stirring for 30 min. At the end of the reaction, the product was collected from the suspension with a rare-hearth permanent magnet while the supernatant was discarded. The particulate was washed several times with distilled water until neutral pH of the washings. Finally obtained MNP1 were redispersed in distilled water (220 mL) at a concentration of 7.5 mg_{Fe3O4} mL^{-1}.

Supplementary Material (ESI) for *Nanoscale*

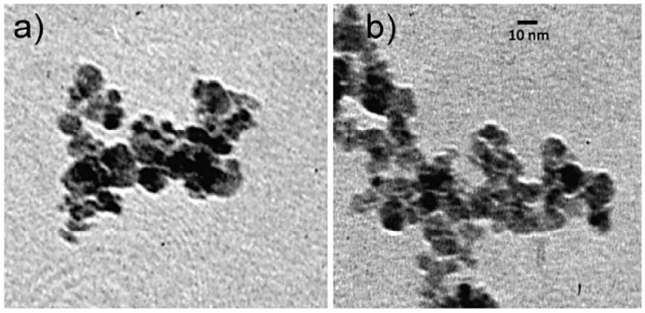

Fig. S2 TEM images of a) MNP1 synthesized by the coprecipitation method and b) MNP2 obtained by reaction of MNP1 with polyethylene glycol 600 diacid. For TEM analyses, the nanoparticles were dispersed under sonication in ethanol (50 μg mL^{-1}) and a drop of the resulting solution was placed on a Formvar/carbon-coated copper grid and air-dried.

Synthesis of PEG-coated Fe_3O_4 nanoparticles (MNP2): A water suspension of MNP1 (3 mL, 7.5 mg mL^{-1}) was sonicated 30 min at r.t.; subsequently, polyethylene glycol 600 diacid (57 μL, 0.112 mmol) was added to the suspension and the resultant mixture was sonicated for 30 min at r.t. At the end of the reaction, nanoparticle suspension was transferred in a centrifuge tube and unreacted nanoparticles were centrifuged at 10000 rpm min^{-1} for 5 min. In this way, supernatant solution, which appeared as a brown clear solution, was separated from the precipitates, which were discarded. To remove the excess of the unreacted reagent, the solution was purified by dialysis membrane (*MW CutOff* 12-14000 Da) overnight; finally MNP2 were diluted with double distilled water to a final concentration of 1 mg mL^{-1}. Under these conditions, nanoparticle suspension was stable for several months at r.t.

Measurement of proton transverse relaxation times (T_2) of MNP2: Before T_2 measurements, the tubes were pre-warmed at this temperature for 10 min in order to obtain thermal equilibration and T_2 values were acquired on the samples at this stage. Relaxivity was determined as the slope of a $1/T_2$ plot as a function of iron concentration expressed in mM.

Dynamic Light Scattering and zeta-potential measurements: Viscosity and refractive index of pure water were used to characterize the solvent. Nanoparticles were dispersed in water under sonication for several minutes before analyses; sporadically, to avoid the formation of large aggregates, the suspension was filtered on a 0.45 μm cellulose acetate filter. The final sample concentration used for measurements was typically 0.01 mg mL^{-1}.

Supplementary Material (ESI) for *Nanoscale*

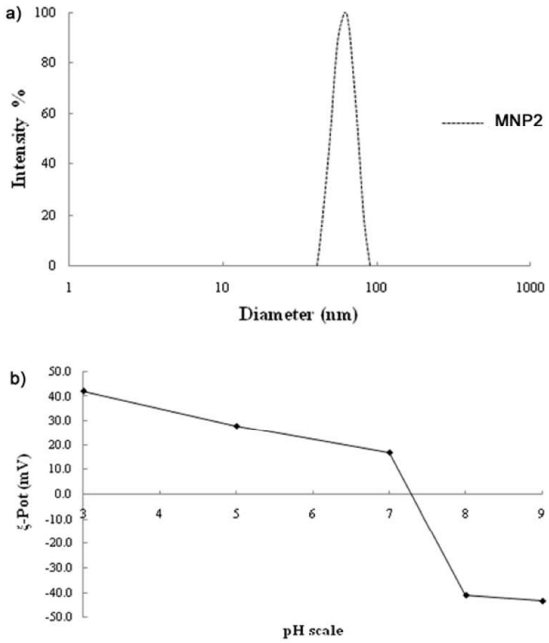

Fig. S3 a) Hydrodynamic size distribution histogram of MNP2 in pure water (the horizontal bare scale is semi-logarithmic). b) Behavior of ζ-Potential of MNP2 in pure water by varying the pH value in the 3 to 9 range. Acidic pHs were gained by dropwise adding 0.02 N HCl, alkaline pHs were obtained by adding 0.02 N NaOH.

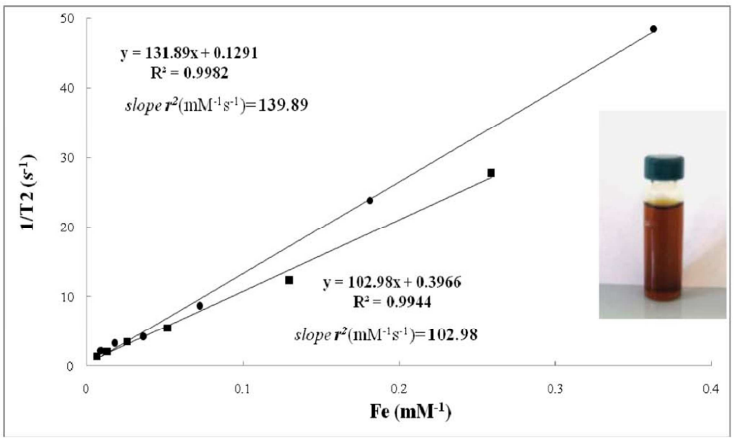

Fig. S4 T_2 relaxometry analyses of as-synthesized MNP2 (dots) and TMNP (squares) in phosphate buffer saline (PBS). The inverse of experimental T_2 values obtained at different MNP2 concentration were plotted vs. iron concentration. Experimental data were fitted by a line. Inset: photographic view of the MNP2 suspension at 1 mg mL^{-1} in pure water.

Supplementary Material (ESI) for *Nanoscale*

Dependence of MNP2 stability on pH: different vials with MNP2 suspension (200 µL) in double distilled water (1.8 mL) were prepared at different pH (C_{NPs} = 0.1 mg mL^{-1}). Initial pH value of **MNP2** was around 5. The acidic pH values were obtained adding 0.5 M HCl dropwise in a range of pH from 1 to 5. The alkalinity was raised above this value by adding 0.5 M NaOH dropwise in the range between 7 and 11. In this way, the stability of MNP2 was controlled by monitoring the decreasing of UV-vis spectra of the PEG absorption from 0 to 90 min (in the range of λ from 200 and 600 nm).

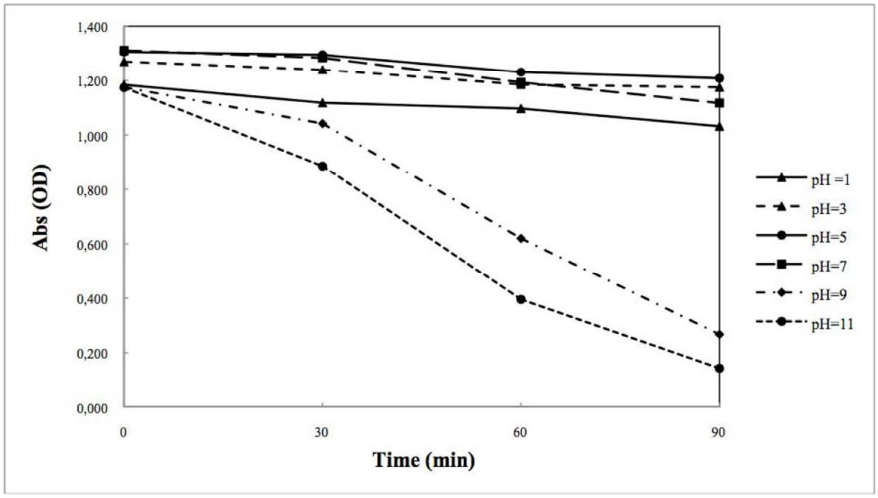

Fig. S5 Stability of Uv-Vis absorbance values at λ_{max} = 290 nm for MNP2 after 90 min incubation as a function of pH.

Table S1. Summary of the ΔAbs of MNP2 at λ_{max} = 290 nm after 90 min incubation.

	Initial Abs (λ = 290nm)	**Abs after 90 min (λ = 290nm)**	**Δ Abs**
pH=1	1.184	1.032	-0.152
pH=3	1.271	1.175	-0.096
pH=5	1.306	1.208	-0.098
pH=7	1.311	1.117	-0.194
pH=9	1.175	0.267	-0.908
pH=11	1.173	0.143	-1.030

Supplementary Material (ESI) for *Nanoscale*

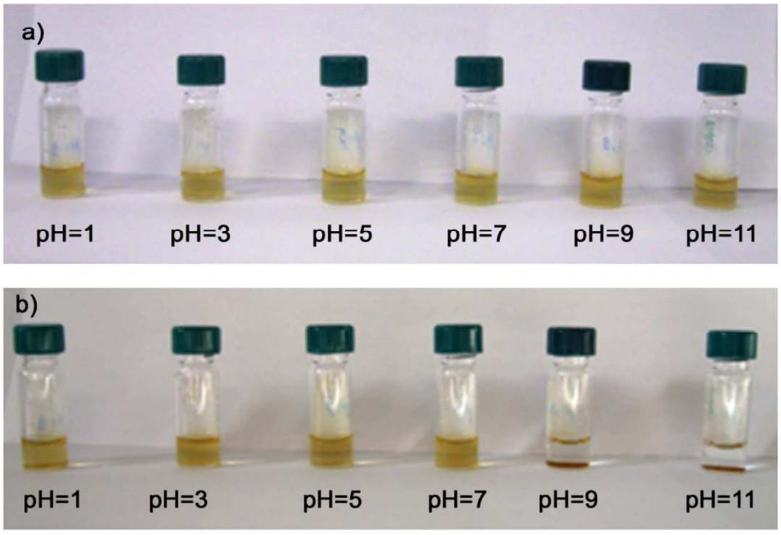

Fig. S6 MNP2 solutions (0.1 mg mL^{-1}) in deionized water at different pH values. a) Freshly prepared solutions and b) after 90 min.

Synthesis of TMNP

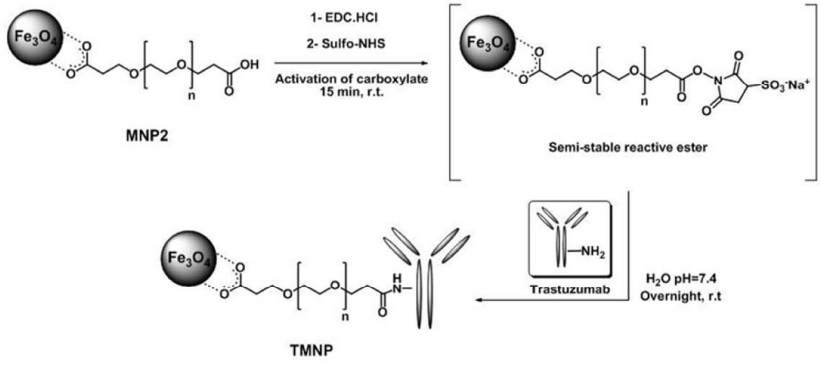

Fig. S7 Schematic synthesis of trastuzumab-modified pegylated nanoparticles (TMNP).

Amide coupling of MNP2 with TZ: The conjugation reaction was performed at room temperature as follows. EDC·HCl (1.9 mg, 10 µmol) and Sulfo-NHS (5.42 mg, 25 µmol) were dissolved in MNP2 water suspension (800 µg, 0.8 mg mL^{-1}, pH 5) under vigorously magnetic stirring. After the activation of the carboxylic acid (approximately 15 min), purified TZ (48 µL, 33.3 mg mL^{-1}) was

added to this solution. Next, the pH of the reaction system was adjusted to 7.4 using 1 M NaOH. The reaction lasted overnight at r.t under magnetic stirring. At the end of the reaction, the particulate was precipitated by centrifugation at 6000 rpm min^{-1} for 10 min and the supernatant was discarded; in order to remove the unbound antibodies, the resultant particulate was washed three times (3 × 1 mL) with phosphate buffered saline solution (PBS: 10 mM phosphate, 300 mM NaCl, 2.7 mM KCl, pH 7.4). Finally, the product was redispersed in the same PBS (1 mL) and stored at 4 °C before further experiments.

Determining TZ loading on nanoparticles surface: Fe_3O_4 nanoparticles were spherical in shape with an average radius of about 5 nm; the average volume of nanoparticles was 5.23 10^{-25} m^3 and the density of magnetite was 5 10^6 g m^{-3}; the mass of a single nanoparticle that is 2.615 10^{-18} g. Hence, 1 mg of Fe_3O_4 contains 3.824 10^{14} nanoparticles. The amount of antibodies appended on nanoparticles surface was determined by using a Bradford Protein Assay. According this method and the curve calibration standard elaborated at different concentation of the antibody, we estabilished that 217 μg of TZ were loaded on 1 mg of MNP2. In 217 μg of TZ (*MW*= 150 KDa) there are 8.71 10^{14} molecules of antibody for 1 mg of nanoparticles. In conclusion, 2 molecules of TZ per nanoparticle were statistically determined.

Protein assay onto nanoparticles: The functionalized nanoparticles were magnetically separated, washed with PBS to remove unbound antibodies and resuspended at the final concentrations of 1 mg mL^{-1}. The amount of antibody bound to magnetic nanoparticles was determined by using a Bradford Protein Assay. We used unreacted nanoparticles at the same concentrations as a blank. The concentration of antibodies needed to gain optimal signal from the surface-modified nanoparticles was determined to be 50 μg mL^{-1}.

Dynamic Light Scattering and zeta-potential measurements of TMNP: TMNP were dispersed in PBS buffer, pH 7.4, under sonication for 1 minute before analyses; the final sample concentration used for measurements was typically 0.01 mg mL^{-1}. For TMNP the average hydrodynamic radius was 224.9 nm (± 0.194). By ζ-potential analysis we found that TMNP were slightly negatively charged, $\zeta = -7.8 \pm 1.1$ mV.

Supplementary Material (ESI) for *Nanoscale*

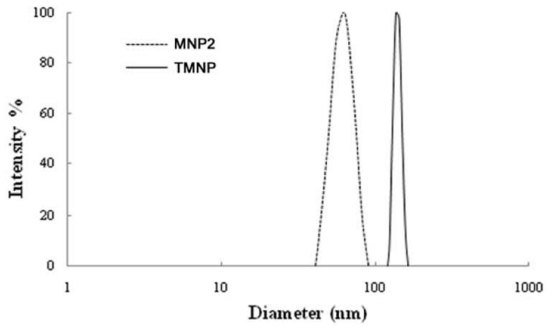

Fig. S8 Hydrodynamic size distribution histograms of MNP2 (dashed line) and TMNP (continuous line). As we expected, there was a great difference in diameter before the conjugation of the antibody (MNP2) and after the reaction (TMNP). However, the narrow peaks showed the high stability of the suspension in both cases, without formation of large clusters of nanoparticles.

Table S2. ζ-Potential behaviour of MNP2 and TMNP in physiological buffer. There was a great difference in the charge (11.7 mV) before the conjugation of the antibody and after the reaction.

	ζ-Potential (mV) (PBS buffer pH=7.4)	**Δ mV**
MNP2	-19.5 ± 0.5	11.7
TMNP	-7.8 ± 1.1	

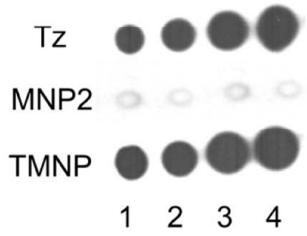

Fig. S9 Immunodot blot assays carried out in parallel with increasing amount (1, 50 ng; 2, 100 ng; 3, 200 ng; 4, 300 ng) of soluble and immobilized (TMNP) trastuzumab. Pegylated nanoparticles (MNP2) were the negative control. TMNP were incubated with anti-human antibodies conjugated with horseradish peroxidase (HRP-rabbit) at a 1:1000 dilution in PBS buffer. The immunoreaction was revealed by a strong signal using ECL western blotting as reagent.

Supplementary Material (ESI) for *Nanoscale*

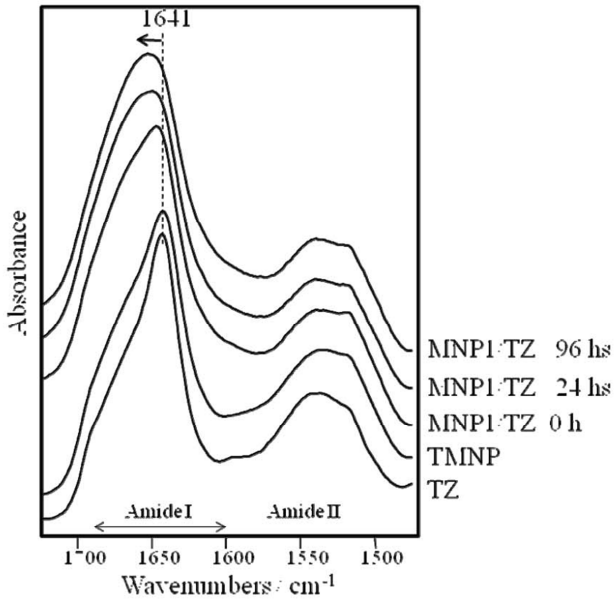

Fig. S10 FTIR absorption spectra of free TZ, of TMNP, and of TZ adsorbed to MNP1 at different times of incubation at 37 °C (0, 24, and 96 hours). The maximum of the Amide I band shifts from 1641 cm^{-1} in the free TZ to 1650 cm^{-1} in the adsorbed TZ at 96 hours of incubation, consistent with a gradual unfolding of protein secondary structure.

Supplementary Material (ESI) for *Nanoscale*

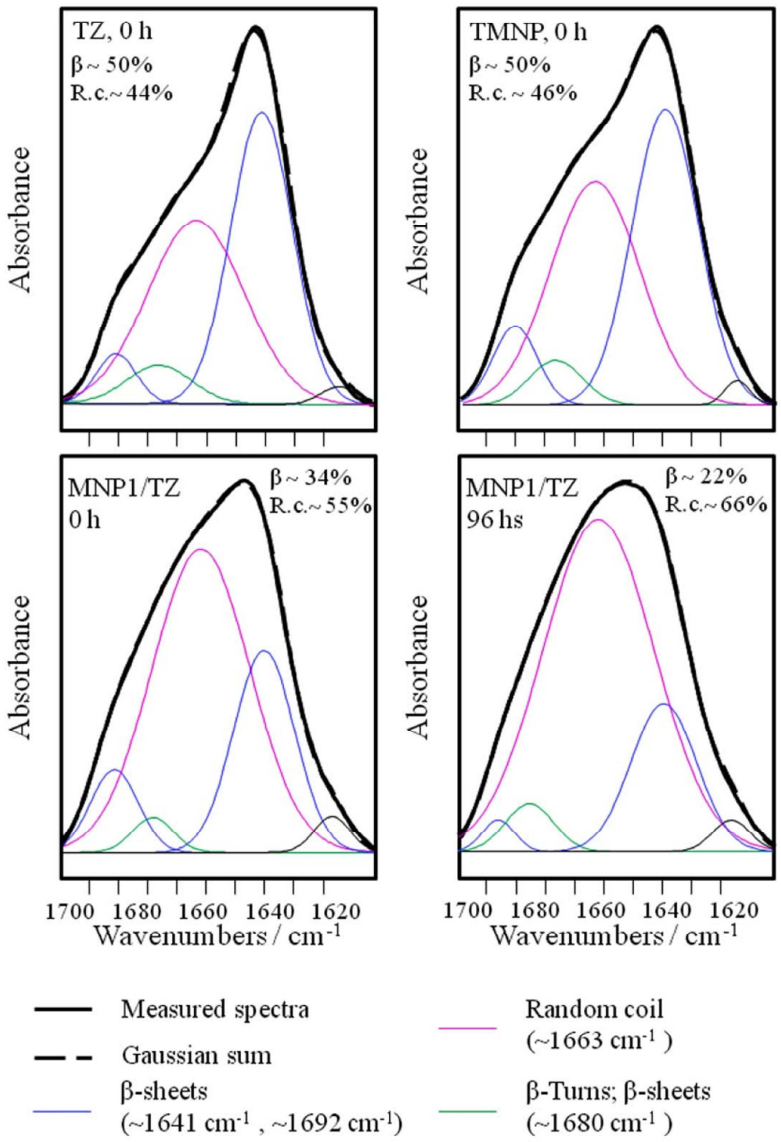

Fig. S11 Gaussian curve fitting of the absorption spectra in the Amide I region of free TZ, of TMNP, and of TZ adsorbed to MNP1 immediately after preparation and after 96 h of incubation at 37 °C. The β-sheet components are reported in blue and their percentage weights over the total Amide I band are indicated. The component peaked at ~1663 cm^{-1} (reported in pink) is mainly due to random coil structures (R.c.) with possible contribution of β-turns.[2] The curve fitting of the measured spectra into Gaussian function was performed following the method previously described.[2,3]

Table S3. Relaxivity measurements on labeled MCF7 cells.[a]

Concentration (cells/mL)	T_2 (ms) (untreated)	T_2 (ms) (TMNP)[b]
1.0×10^6	2809 ± 34	294 ± 9
5.0×10^5	3185 ± 31	712 ± 13

[a] Data are the mean ± SD of three different relaxivity measurements. [b] Cells were treated with TMNP at a concentration of 50 μg mL^{-1}. The remarkable decrease in T_2 confirms the presence of TMNP on cells, thus demonstrating that fluorescently labeled antibodies localized on cell membrane (see Fig. 3) are still bound to magnetic nanoparticles.

Dot Blot Assay: Standard Minifold I dot blot apparatus were used in this assay. TZ or purified nanoparticle suspension were spotted onto PVDF membrane. After all samples were fixed the membrane was incubated in blocking solution (5% skim milk in PBS) for 60 min at RT. To evaluate TZ activity, membranes were then probed for 60 min at 25 °C using horseradish peroxidase-rabbit anti-human antibodies at a 1:20000 dilution in PBS buffer. Immunoreactive spots were revealed using ECL Western blotting reagent.

Cell cultures: MCF-7 cells were grown in 50% Dulbecco's Modified Eagle's Medium (DMEM) and 50% F12 (EuroClone Celbio, Milan, Italy), supplemented with 10% fetal bovine serum (HycloneCelbio, Milan, Italy), L-glutamine (2 mM), penicillin (50 UI mL^{-1}), and streptomycin (50 mg mL^{-1}, culture medium) at 37 °C in a humidified atmosphere containing 5% CO_2 and subcultured prior to confluence using trypsin/EDTA.

Immunoprecipitation assay: MCF7 cells were lysed with lysis buffer containing 20 mM Tris HCl, 150 mM NaCl, 10 mM EGTA, 10% glycerol and 1% Triton X-100, pH 7.4 for 30 min at 4 °C and then centrifuged at 8500 rpm for 10 min to remove membranes and cell debris from protein fraction. Bradford assay was used to determine protein content of whole cell extract. Preclearing step was performed with 200 μL of MNP2 (1 mg mL^{-1}) for 1 h on wheel at 4 °C. The immunoprecipitation was carried out with 1 mg of pre-cleared lysate and TMNP (200 μL, 1 mg mL^{-1}, corresponding to 3.75 μg of linked-antibody) for 16 h at 4 °C on wheel. Samples were washed three times in lysis buffer and boiled in sodium dodecyl sulfate sample buffer containing 5% 2-mercaptoethanol to cleave the binding to the beads. Samples were run on 8% poliacrilammide gel. Proteins were blotted onto PVDF membranes and incubated in blocking solution (5% skim milk in TBS, 0.05% Tween) for 1 h at r.t.. For HER-2 detection, membranes were then probed for 1 h at r.t. using anti-HER2 polyclonal antibodies (1:500 Millipore, Billerica, MA) in blocking solution. Specificity of the interaction between the HER2 and TMNP was verified with immunoblot

of immune-precipitated samples with unrelated proteins such as anti-Clnx pAb (1:500 Genetex) at r.t. for 1 h in TBS + 0.05% tween + 5% BSA. Specific HRP-conjugated secondary-antibodies were used always 1 h at r.t. (anti-mouse 1:10000 BioRad Cell Signaling, Danvers, MA). Immunoreactive bands were revealed using ECL Western blotting reagent (GE Healthcare).

Confocal Laser Scanning Microscopy: MCF7 cells were cultured on collagene (Sigma) pre-coated coverglass slides until 90% of confluence and incubated for 20 min with TMNP at a concentration of 100 μg mL^{-1} (corresponding to 11 μg of Tz) or 11 μg Tz in culture medium. Tz and TMNP were revealed by labeling with secondary antibodies anti-human Alexa fluor 488 (Invitrogen, Carlsbad, CA) at a 1:500 dilution. Cultures were washed with PBS, fixed for 10 min with 4% paraformaldehyde (Sigma) and then treated for 10 min with 0.1 M glycine (Sigma) in PBS. A blocking step was performed 1 h at RT with a solution containing 5% BSA (Sigma) and 0.1% Saponin (Sigma) in PBS, followed by staining with 33 μg of DiD oil (Invitrogen) in PBS for 30 min at 37 °C. Microscopy analysis was performed with a Leica SP2 AOBs microscope confocal system. Images were acquired with 63× magnification oil immersion lenses at 1024×1024 pixel resolution.

[1] L. Polito, M. Colombo, D. Monti, S. Melato, E. Caneva and D. Prosperi, *J. Am. Chem. Soc.*, 2008, **130**, 12712-12724.

[2] J. L. R. Arrondo and F. M. Goni, *Prog. Biophys. Mol. Biol.*, 1999, **72**, 367-405.

[3] A. Natalello, D. Ami, S. Brocca, M. Lotti and S. M. Doglia, *Biochem. J.*, 2005, **385**, 511-517.

Bioconjugate Chemistry

Article

pubs.acs.org/bc

Multiple Presentation of Scfv800E6 on Silica Nanospheres Enhances Targeting Efficiency Toward HER-2 Receptor in Breast Cancer Cells

Serena Mazzucchelli,[‡,§,†] Paolo Verderio,[§,†] Silvia Sommaruga,[‡,§] Miriam Colombo,[‡,§] Agnese Salvadè,[‡] Fabio Corsi,[‡] Patrizia Galeffi,[∥] Paolo Tortora,[§] and Davide Prosperi*[,§,⊥]

[‡]Dipartimento di Scienze Cliniche "Luigi Sacco", Università di Milano, Ospedale L. Sacco, Via G.B. Grassi 74, 20157 Milano, Italy

[§]Dipartimento di Biotecnologie e Bioscienze, Università di Milano-Bicocca, Piazza della Scienza 2, 20126 Milano, Italy

[∥]UTAGRI-GEN, ENEA, R. C. Casaccia, Via Anguillarese 301, 00123 Roma, Italy

[⊥]Istituto di Scienze e Tecnologie Molecolari, CNR, via Fantoli 16/15, 20138 Milano, Italy

Supporting Information

ABSTRACT: Spherical silica nanoparticles (SNP) have been synthesized and functionalized with anti-HER-2 scFv800E6 antibody by both localized histidine-tag recognition, leading to an oriented protein ligation, and glutaraldehyde cross-linking, exploiting a statistical reactivity of lysine amine groups in the primary sequence of the molecule. The targeting efficiency of nanocomplexes in comparison with free scFv was evaluated by flow cytometry using a HER-2 antigen-positive MCF-7 breast cancer cell line, exhibiting a 4-fold increase in scFv binding efficacy, close to the affinity of intact anti-HER-2 monoclonal antibody, which suggests the effectiveness of presenting multiple scFv molecules on nanoparticles in improving antigen recognition. Unexpectedly, the conjugation method did not affect the binding efficacy of scFv, suggesting a structural role of lysines in the scFv molecule. Confocal laser scanning microscopy confirmed the binding of nanocomplexes to HER-2 and also provided evidence of their localization at the cell surface.

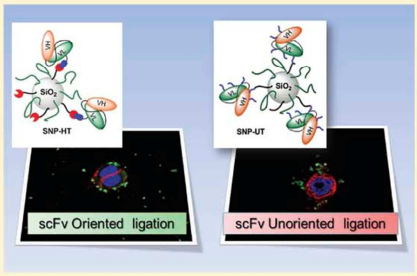

INTRODUCTION

Monoclonal antibodies (mAbs) are versatile and unique molecules that have found applications in the investigation, diagnosis, and treatment of many diseases, including cancer.[1] Although mAbs display high affinity and selectivity for the target, antibody-based therapies are often less effective toward solid tumors, because only a small amount of mAbs can indeed accumulate at the tumor tissue, due to their high immunogenicity and low penetration. Moreover, mAbs remain circulating for an extended time because their large size prevents excretion by renal clearance.[2] Recently, recombinant antibodies with modified properties have been designed in order to improve tissue penetration and biodistribution.[3] Among them, small antibody fragments consisting of the variable V_H and V_L regions connected through a synthetic loop, called single-chain fragment variable recombinant antibodies (scFv), hold great promise.[4] Target-specific scFvs are usually obtained through genetic engineering by phage display technology.[5] ScFv display has improved biodistribution compared to intact IgGs due to small size (typically in the 20−30 kDa range) and absence of a highly immunogenic stem. However, a poor retention time and a decreased affinity and specificity caused by their monovalent binding strongly limit their application in cancer immunotherapy. Hence, while immunogenicity is remarkably reduced and scFv clearance is accelerated, the binding efficacy is often reduced compared to their parent mAb resulting in a remarkably lower affinity for the receptor.

Multimerization has been recently envisaged as a strategy to enhance the functional affinity (avidity) of scFv increasing the k_a by 2−3 orders relative to the monovalent fragment.[6−8] Different multimerization strategies have been proposed to couple monovalent domains to produce multivalent antibodies, by chemical manipulation or using protein engineering approaches, including formation of diabodies, tribodies, tetrabodies, and minibodies.[9,10] Multimerized scFvs combine features from mAb and scFv that improve tumor penetration, as low immunogenicity and high affinity toward their receptor, and increase circulation time due to their large size, which prevents renal excretion.[10] So far, the conjugation of antibody fragments to nanoparticles has been seldom exploited. It has been observed that scFv having low affinity toward the epidermal growth factor receptor, when present in multiple copies on a liposome, allowed for tight receptor binding, thus filling the affinity gap between scFv and a high-affinity mutant obtained by molecular evolution.[11] However, functionalization

Received: July 4, 2011
Revised: October 14, 2011
Published: October 20, 2011

of immunoliposomes does not offer a suitable control of number and orientation of the scFv ligand displayed on their surface. Such control of scFv presentation could be better optimized by using inorganic nanoparticles.[12−14] Here, we present a strategy to enhance scFv target binding efficacy that makes use of silica nanoparticles as a multimerization scaffold. As proof of concept, we chose scFv800E6 produced in *Pichia pastoris*, that recognizes the breast cancer membrane marker HER-2.[15] Among the numerous examples of inorganic nanoparticles available so far, silica nanoparticles have been extensively studied, due to their broad application and the ease of synthesis and stable functionalization with organic ligands.[16,17] In this work, we have explored synthesis and surface functionalization of silica nanoparticles (SNP) in order to immobilize scFv800E6 by two different approaches (Scheme 1): (1) the first method exploits a localized histidine tag recognition leading to an oriented ligation of scFv; (2) the second involves a reductive amination strategy *via* glutaraldehyde cross-linking on the nanoparticle exploiting a statistical reactivity of lysine amine groups on the primary sequence of the scFv molecule.

Scheme 1. Mechanism of "Oriented" and "Unoriented" Immobilization of scFv800E6 on Functionalized Silica Nanospheres[a]

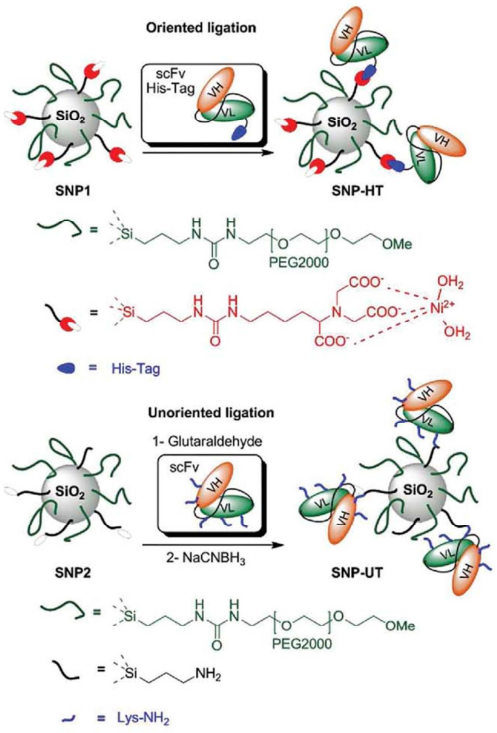

[a]Method 1: SNP1 functionalized with Ni-NTA groups tightly and specifically interact with scFv histidine tag leading to an oriented protein immobilization (SNP-HT). Method 2: the available amino groups of lysine residues of scFv bind to SNP2 via the aldehydic groups, which have been generated on the surface of nanoparticles by glutaraldehyde addition, resulting in a random ligation (SNP-UT).

EXPERIMENTAL PROCEDURES

Materials and Methods. All reagents and solvents were purchased from Sigma-Aldrich (St. Louis, MO), Fluka (St. Gallen, Switzerland), and Riedel-de Haën (Seelze, Germany) and used as received without further purification. Water was deionized and ultrafiltered by a Milli-Q apparatus (Millipore Corporation, Billerica, MA). Ultrasounds were generated by S15H Elmasonic Apparatus (Elma, Singen, Germany). TEM images of nanoparticles were obtained by a Zeiss EM-109 microscope (Oberkhochen, Germany) operating at 80 kV. Dynamic light scattering (DLS) measurements were performed at 90° with a 90 Plus Particle Size Analyzer from Brookhaven Instrument Corporation (Holtsville, NY) working at 15 mW of a solid-state laser (λ = 661 nm). Zeta-potential measurements were elaborated on the same instrument equipped with AQ-809 electrode and data were processed by *ZetaPlus* software. UV−vis spectra were recorded by using a Nanodrop 2000C spectrophotometer (Thermo Fisher Scientific, Wilmington, Germany) in a range of wavelengths from 190 to 600 nm.

Synthesis of SNP. Monodisperse silica nanospheres were obtained as described in previous work.[18] Briefly, a 25% NH_4OH solution in water (12.5 mL) and ethanol (250 mL) were mixed under magnetic stirring at 300 rpm. To the above solution was added a mixture of TEOS (6.25 mL, 28 mmol) dissolved in ethanol (7 mL) at a rate of 1 mL min^{-1} through a dropping funnel. The reaction was stirred for 20 h at room temperature (RT). At the end of the reaction, the solution became milky and the product was collected from the suspension by centrifugation at 8300 × *g* for 30 min. The white particulate was washed several times with ethanol (4 × 100 mL). Next, SNP (1.5 g) was dried under vacuum. SNP (100 mg) was redispersed in ethanol at a concentration of 4 mg mL^{-1} for further experiments.

Synthesis of Fully PEG-Coated SNP (SPEG). In a dried round-bottom flask, *O*-(2-aminoethyl)-*O*′-methylpolyethylene glycol 2000 (100 mg, 50 μmol) was dissolved in anhydrous CH_2Cl_2 (1 mL); subsequently, Et_3N (8 μL, 55 μmol) and (3-isocyanatopropyl)triethoxysilane (15 μL, 60 μmol) were added and the reaction run overnight at RT with magnetic stirring under argon atmosphere. When the reaction was completed, the solution was filtered and the clear filtrate was evaporated under reduced pressure. The resultant yellow pale oil was redissolved in a minimum amount of CH_2Cl_2 (300 μL), and cold Et_2O (10 mL) was added to precipitate the product as a white solid. The product was washed twice with Et_2O (10 mL) and finally dried under vacuum. APTS-PEG2000 (98 mg) was used immediately without further purification. The conjugation reaction was performed as follows.[18,19] A suspension of SNP in EtOH (20 mL, 1 mg mL^{-1}) was warmed at 60 °C; next, 25% NH_4OH (50 μL) and APTS-PEG2000 (20 mg, 10 μmol) were added and the resultant mixture was subjected to vigorous magnetic stirring at 60 °C overnight. The particulate was collected by centrifugation at 8300 × *g* for 15 min and washed with EtOH (2 × 10 mL) and water (10 mL). The resultant SPEG were redispersed in water (10 mL) for analyses.

Synthesis of SNP1. N^{α},N^{α}-Bis(carboxymethyl)-L-lysine (NTA) was synthesized according a previous work.[20] NTA (100 mg, 380 μmol) was suspended in anhydrous CH_2Cl_2 (8 mL) and THF (3 mL). Subsequently, Et_3N (211 μL, 1.52 mmol) and (3-isocyanatopropyl)triethoxysilane (113 μL, 456

μmol) were added and the reaction run overnight at RT with magnetic stirring under argon atmosphere. The resulting suspension was filtered, and the clear filtrate was evaporated under reduced pressure. The pale yellow oil was redissolved in a minimum amount of MeOH (500 mL) and cold Et_2O (10 mL) was added to precipitate the product as a white solid. The product was washed twice with Et_2O (10 mL) and finally dried under vacuum. APTS-NTA (132 mg) was used immediately without further purification.

For the conjugation reaction,[18,19] a suspension of SNP in EtOH/H_2O 1:1 (20 mL, 1 mg mL^{-1}) was warmed at 60 °C; 25% NH_4OH (50 μL), APTS-NTA (10 mg, 20 μmol), and APTS-PEG2000 (10 mg, 5 μmol) were added, and the mixture was left under vigorous stirring at 60 °C overnight. Next, the particulate was collected by centrifugation at 8300 × *g* for 15 min and washed with EtOH (2 × 10 mL) and water (10 mL). Nanoparticles were resuspended in water (20 mL) for further chelation with nickel ions. A green solution of 0.1 M $NiCl_2 \cdot 6H_2O$ in deionized water (2 mL) was added to the above suspension of nanoparticles; the pH was adjusted to pH 8.0 with 0.1 N NaOH, and the resultant mixture were kept under magnetic stirring for 30 min at RT. Then, particles were collected by centrifugation and the pale blue supernatant was discarded. The pale green particulate was washed thrice with water (10 mL) and, finally, SNP1 were resuspended in water (5 mL) and stored for further conjugation with His-tagged scFv800E6.

Synthesis of SNP2. The conjugation reaction[18,19] was performed as follows. A suspension of SNP in EtOH (20 mL, 1 mg mL^{-1}) was warmed at 60 °C; then, 25% NH_4OH (50 μL), APTS (5 μL, 20 μmol), and APTS-PEG2000 (10 mg, 5 μmol) were added and the resultant mixture was kept under vigorous magnetic stirring at 60 °C overnight. The particulate was collected by centrifugation at 8300 × *g* for 15 min and washed with EtOH (2 × 10 mL) and water (10 mL). The resultant SNP2 were stored in water (10 mL) for further conjugation with scFv.

Determination of Amine Groups on SNP2. Following a method described in the literature,[21] an aqueous mixture containing 1 M picrylsulfonic acid TNBS (10 μL) and 0.05 M $Na_2B_4O_7$ (1.5 mL) was added to a sample of aminated SNP2 (6 mg). The suspension was sonicated for 1 min and then heated at 70 °C for 10 min. At the end of reaction, the mixture was allowed to cool to RT; SNP2 was then separated from the supernatant by centrifugation at 11 200 × *g* and washed with water (1 mL), 50% acetone in water (1 mL), 100% acetone (1 mL), and water (2 × 1 mL). SNP2 was then suspended in NaOH 1 M (5 mL) and heated to 70 °C under vigorous stirring for 10 min. The suspension was cooled to RT and SNP2 were separated by centrifugation. An aliquot of the particle-free supernatant (1 mL) was then withdrawn and its absorbance read at 410 nm. Each particle contained silica (d = 2.2×10^6 g m^{-3}) with an average radius of 40 nm = 4.0×10^{-8} m. The average volume and mass of SiO_2 nanoparticles were 2.68×10^{-22} m^3 and 5.90×10^{-16} g, respectively. Hence, 1 mg of SiO_2 contained 1.02×10^{14} particles. By determination of residual absorbance due to picric acid released from reaction (Supporting Information Scheme S4), we established that 0.012 μmol of ligand APTS were immobilized on the particle surface corresponding to about 708 NH_2 groups/particle.

Dynamic Light Scattering and ζ-Potential Measurements. Viscosity and refractive index of deionized water were used to characterize the solvent. Nanoparticles were dispersed in water under sonication for several minutes before analyses; sporadically, to avoid the formation of large aggregates, the suspension was filtered through a 0.45 μm cellulose acetate filter. The final sample concentration used for measurements was typically 0.025 mg mL^{-1} (Figure S1). The same procedure was followed for hydrodynamic size distribution behavior of nanoparticles in deionized water by different Na^+ concentrations (1 mM to 20 mM) (Figure S2).

Strains and Plasmids. *P. pastoris* KM71H (*arg4; aox1::ARG4*) (Invitrogen) was used as host for expressing scFv800E6 gene. Plasmid pPICZαA (Invitrogen) was used for constructing plasmid vector, as previously described.[15]

Purification of scFv800E6. The clone KM71H-pPICZαA-scFv800E6-4 was grown in 10 mL YPD medium (1% yeast extract, 2% peptone, 2% dextrose) at 30 °C overnight with shaking at 250 rpm. The cultures were centrifuged at 1500 × *g* for 4 min, and then, the pellets were resuspended in 200 mL of BMMY (1% yeast extract, 2% peptone, 100 mM potassium phosphate pH 6.0, 1.34% YNB, 0.00004% biotin, 0.5% methanol) with 0.8% glycerol yielding an initial OD 600 value of 10. The culture was induced by daily addition of methanol to a final concentration of 0.5%. After 48 h of methanol treatment, the culture supernatant was filtered through 0.22 μm filters and dialyzed overnight in 50 mM sodium phosphate pH 8.0, 300 mM NaCl. The dialyzed medium was loaded at a flow rate of 0.5 mL/min onto a Ni-NTA Agarose (Qiagen) column (bed volume 0.5 mL) pre-equilibrated with 50 mM sodium phosphate pH 8.0, 300 mM NaCl, and 10 mM imidazole. The column was washed with 50 mM sodium phosphate pH 8.0, 300 mM NaCl, 20 mM imidazole, and the protein eluted with a stepwise imidazole gradient, 100 mM to 200 mM, in the same buffer. Fractions were collected and analyzed by SDS-PAGE. SDS-PAGE was performed according to Laemmli,[22] using 12% (v/v) polyacrylamide gels. The proteins were detected by Coomassie Brilliant Blue R-250 staining. Protein content was determined both by measuring absorbance at 280 nm and by using the Coomassie Plus Protein Assay Reagent (Termo Fisher Scientific) and bovine plasma immunoglobulin G as the standard protein.

Conjugation of His-tag scFv800E6 (SNP-HT). In a plastic tube, SNP1 (1 mg) were incubated with purified scFv800E6 (50 μg) in phosphate-buffered saline (PBS; EuroClone) in a final volume of 1000 μL and the mixture was stirred on an orbital shaker for 10 min at RT. SNP-HT were isolated from unreacted scFv800E6 by centrifugation at 11 200 × *g* for 5 min and the supernatant was discarded. Nanoparticles were washed three times with PBS (500 μL) and stored in PBS at 4 °C for further experiments. By measuring the absorbance at 280 nm, we determined an amount of scFv800E6 immobilized on nanoparticles of 26 μg per mg of SNP-HT.

Unoriented Conjugation of scFv800E6 (SNP-UT). Particle-glutaraldehyde cross-linking,[23] followed by imine reduction[24] with $NaCNBH_3$ were performed as follows. In a plastic tube, amino SNP2 (1 mg) was dispersed in borate buffer pH 7.6 (600 μL). A 5 mM glutaraldehyde solution in the same buffer (400 μL, 20 μmol) was added under stirring at RT. After 2 h, particles were isolated by centrifugation and washed once with borate buffer pH 7.6 (1 mL) and twice with PBS pH 7.4 (1 mL). At the end of the washing, nanoparticles were resuspended at a concentration of 1 mg mL^{-1} in the same buffer (1 mL) and the suspension cooled at 4 °C with an ice bath. scFv800E6 (50 μg in PBS) was added to the suspension

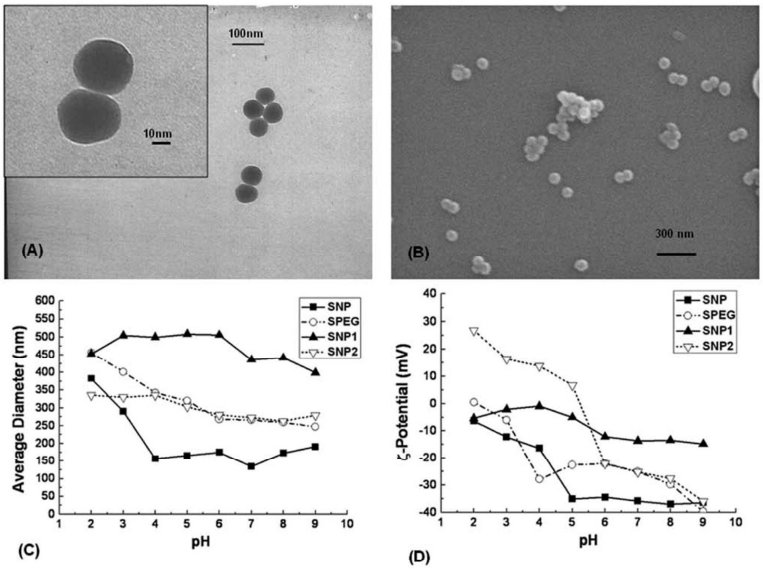

Figure 1. Characterization of modified silica nanoparticles: (A) TEM (Inset: magnification) and (B) SEM images of as-synthesized SNP. (C) DLS and (D) ζ-potential measurements of SNP, SPEG, SNP1, and SNP2 as a function of pH in aqueous solution.

and the resultant mixture was stirred on the orbital shaker for 3 h at 4 °C. ScFv-functionalized nanoparticles were recovered after centrifugation and washed twice with PBS (1 mL). Subsequently, a $NaBH_3CN$ solution (10 μL, 1 mg mL^{-1}) in PBS buffer pH 7.4 was added to the nanoparticle suspension in the same medium (1 mL) and incubated for 3 h at 4 °C. After centrifuging, SNP-UT were washed several times with PBS (3 × 1 mL) and finally were stored in the same buffer at 4 °C for further experiments. By measuring the absorbance at 280 nm, we determined an amount of scFv800E6 of 43 μg per mg of SNP-UT.

Dot Blot Assay. Dot blot was performed by filtering proteins and/or nanoparticles onto PVDF membranes, utilizing a Manifold I dot blot apparatus (GE Healthcare), and incubating in blocking solution (5% skim milk in PBS, Tween 0.05%) for 1 h at RT. The membrane was then probed for 1 h at RT in blocking solution using rabbit anti-Myc-HRP antibody (Invitrogen) at a 1:5000 dilution. Membranes were rinsed thrice in 0.05% Tween in PBS for 10 min. Immunoreactive spots were revealed using ECL Western blotting reagent (GE Healthcare).

Cell Cultures. MCF-7 and MDA cell lines were used as HER-2 positive and HER-2 negative targets, respectively. Cells were cultured in 50% Dulbecco's Modified Eagle's Medium (DMEM) and 50% F12, supplemented with 10% fetal bovine serum, L-glutamine (2 mM), penicillin (50 UI mL^{-1}), and streptomycin (50 mg mL^{-1}) at 37 °C and 5% CO_2 in a humidified atmosphere and subcultured prior to confluence using trypsin/EDTA. Cells culture medium and chemicals were purchased from EuroClone.

Flow Cytometry. Cells were cultured on a multiwell dish until subconfluence. Then, equal aliquots were incubated 15 min at 37 °C in the presence of one of the following: (i) 5 μg mL^{-1} scFv, (ii) 25.6 μg mL^{-1} TZ, (iii) SNP-HT, and (iv) SNP-UT. For each sample, 0.171 nmole of antibody, either free or immobilized on nanoparticles, was used. After incubation time, cells were washed twice with PBS and treated with typsin for 3 min. Digestion with trypsin was stopped with culture medium, cells were transferred in FACS tubes and washed twice with PBS. Then, cells were incubated for 30 min at 4 °C in blocking solution (PBS, 2% Bovine Serum Albumin) and immunodecorated with 1 μL of FITC-conjugated antibody to whole murine IgG (MP Biomedicals) for 30 min at 4 °C. The excess secondary antibody was removed by washing cells six times with PBS. Labeled cells were resuspended with 0.5 mL of PBS and analyzed on a FACS Calibur flow cytometer (Becton Dickinson). Ten thousand events were acquired for each analysis, after gating on viable cells, and isotype-control antibodies were used to set the appropriate gates.

Stability Assay of scFv Conjugation on SNP-HT. Five micrograms of scFv immobilized on SNP-HT was incubated at 37 °C with 0.1 mL of culture medium. After incubation time, SNP-HT was centrifuged 15 min at 15 000 × g at 4 °C, and supernatants (S1, S4, S24, and S48) were filtered onto a PVDF membrane utilizing a Manifold I dot blot apparatus (GE Healthcare). The membrane was incubated in blocking solution (5% skim milk in PBS, Tween 0.05%) for 1 h at RT, then probed 1 h at RT in blocking solution using rabbit anti-Myc-HRP antibody (Invitrogen) at a 1:5000 dilution. Membranes were rinsed thrice in 0.05% Tween in PBS for 10 min. Immunoreactive spots were revealed using ECL Western blotting reagent (GE Healthcare). Five micrograms of scFv immobilized on SNP-HT and 0.1 mL of culture medium were used, respectively, as positive and negative control.

Confocal Laser Scanning Microscopy. Cells were cultured on collagen (Sigma) precoated coverglass slides until subconfluence. Cells were incubated 1 h at 37 °C with 20 μg/mL of free-scFv800E6, and with equal amounts of scFv800E6

immobilized on SNP-HT and SNP-UT. Then, cells were washed with PBS, fixed for 10 min with 4% paraformaldehyde (Sigma), and treated for 10 min with 0.1 M glycine (Sigma) in PBS. A blocking step was performed for 1 h at RT with a solution containing 2% bovine serum albumin (Sigma) and 2% goat serum in PBS. ScFv was revealed by a FITC-conjugated antibody to whole murine IgG (MP Biomedicals) at a 1:300 dilution by incubating for 2 h at RT. Nuclei were stained with DAPI (4′,6-diamidino-2-phenylindole, Invitrogen) at 0.2 μg mL^{-1} in PBS with 0.1% Saponin (Sigma) for 20 min at RT. Membranes were stained with DiD oil (Invitrogen) at a 1:300 dilution by incubating 30 min at 37 °C. Microscopy analysis was performed with a Leica SP2 AOBs microscope confocal system. Images were acquired with 63× magnification oil immersion lenses at 1024 × 1024 pixel resolution.

■ RESULTS AND DISCUSSION

Uniform 60 nm spherical SNPs were synthesized by hydrolysis and condensation of tetraethyl orthosilicate (TEOS) in a 25% NH_4OH ethanolic solution.[18] In method 1, previously prepared APTS-PEG2000-OMe[25] and APTS-NTA in a 1:1 molar ratio were co-condensed on SNP in alkaline ethanol resulting in NTA-functionalized SNP1 (Schemes S1,2 in SI).[19] According to previous reports,[26] PEG chains enhanced the nanoconjugate solubility in buffered media and prevented nonspecific adsorption of proteins. ScFv800E6 protein containing a 6 × His-affinity tag was produced in *P. pastoris*, secreted in culture medium, and purified through affinity chromatography, as previously described.[15] Subsequent Ni^{2+} chelation by nitrilo-acetic acid groups of SNP1 promoted the active Ni^{2+}-NTA affinity-oriented immobilization of His-tagged scFv (SNP-HT) by incubation at room temperature. In method 2, APTS-PEG2000-OMe and APTS in a 1:1 molar ratio were co-condensed on SNP (Scheme S3 in SI).[23] Next, the covalent attachment of scFv was performed via glutaraldehyde cross-linking resulting in functional SNP2, stabilized by reduction of the diimine intermediate with $NaCNBH_3$,[27] to give SNP-UT. In Figure 1, TEM (A) and SEM (B) images show that the core size of SNP was 60 ± 5 nm indicating a homogeneous formulation of silica nanospheres. The hydrodynamic diameter of SNP in ethanol was 78.3 ± 2.2 nm, as determined by dynamic light scattering (DLS, Figure S1 in SI). The pH-dependent behavior of SNP, SNP1, SNP2, and fully PEG-coated nanosilica (SPEG) was investigated by DLS in the 2−9 pH range (Figure 1C). All the nanosilica tested did not exhibit the formation of critical aggregates between pH 4 and 9. Zeta potential (ζ) of SNP, SPEG, SNP1, and SNP2 in water in the 2−9 pH range was also investigated (Figure 1D). From pH 5 to 9, SNP were strongly negatively charged (−35.85 ± 0.64 mV), whereas at pH 4 and lower, the charge approached neutrality (−6.40 ± 1.77 mV). Similar behavior was also observed for SPEG, although they were only −25.01 ± 0.38 mV at pH 7 because of the charge-shielding effect of the PEG layer on the nanoparticle surface. In contrast, SNP1 exhibited a remarkably low surface charge at pH 7 (−13.64 ± 0.74 mV), in accordance with the presence of the Ni^{2+} chelates on the external carboxylic groups of NTA. This charge did not appreciably change in the pH range tested. SNP2 were negatively charged (−25.23 ± 1.03 mV) at pH 7−9. However, below pH 5, a gradual shift of the charge to positive values (+16.39 ± 1.35 mV at pH 3) was observed, in line with the presence of protonated amino groups of APTS in acidic conditions.

After conjugation, the amount of scFv800E6 on SNP-HT and SNP-UT was quantified by protein assay of supernatants at 280 nm using a calculated $\varepsilon_{280\ nm}$ of 55 600 M^{-1}. The immobilization of scFv on SNP-HT was also confirmed by dot-blot assay (Figure 2). SNP-HT (5 μg) and free scFv (0.5, 0.2, 0.1, and 0.05 μg) were filtered onto a polyvinylidene fluoride (PVDF) membrane and then probed with an anti-Myc-HRP antibody. Intensities of immunoreactive spots of SNP-HT and 0.1 μg of free scFv were comparable. This reasonably fits with the amount of bound scFv that we inferred from the determination of unbound protein, i.e., 0.125 μg.

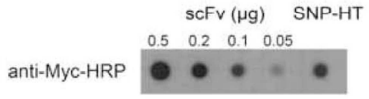

Figure 2. Dot-blot assay of SNP-HT conjugated with scFv. Different amounts of scFv800E6 (0.5, 0.2, 0.1, and 0.05 μg) and an aliquot of SNP-HT were filtered on a PVDF membrane, then probed with anti-Myc-HRP antibody and revealed with an ECL substrate.

To assess the effect of multivalent presentation of scFv on silica nanoparticles, SNP-HT and SNP-UT binding toward HER-2 receptor in breast cancer cells was evaluated by flow cytometry. Free scFv, the commercial anti-HER-2 mAb (trastuzumab, TZ), SNP-HT, and SNP-UT, containing equal amounts of conjugated scFv, were incubated 15 min with HER-2-positive MCF-7 cells.[28] Flow cytometry evidenced a right-shift of fluorescence signal accounting for an increase in scFv binding efficacy upon multimerization due to SNP conjugation (Figure 3). Values reported in Figure 3B show a 3-fold increase in mean fluorescence intensity of SNP-UT sample in comparison with free scFv at the same scFv concentration. Moreover, scFv multimerized on SNP *via* glutaraldehyde cross-linking (SNP-UT) exhibited a mean fluorescence intensity value very close to that of intact TZ, indicating that there was a significant improvement in receptor binding capability, which can be attributed to avidity effect. However, the conjugation strategy exploited for scFv multimerization on SNP surfaces (method 1 vs method 2) did not prove to be crucial in enhancing scFv binding efficiency. Indeed, SNP-HT and SNP-UT exhibited similar fluorescence intensities when assessed by flow cytometry. To account for this unexpected result, we inspected the localization of lysines in scFv sequence. Multiple sequence alignment of scFv800E6 with other scFv sequences available in the NCBI database revealed that all lysine residues are highly conserved. This clearly indicates that these residues are not directly involved in HER-2 binding. Instead, quite likely they only play a structural role. Therefore, an involvement of this residue in glutaraldehyde cross-linking is not expected to interfere significantly with HER-2 binding.

Moreover, to exclude the release of scFv from SNP-HT and assess the stability of this conjugation method, we have incubated SNP-HT for 1, 4, 24, and 48 h at 37 °C and 5% CO_2 atmosphere. Supernatants of incubation were then filtered on PVDF membrane and probed with an anti-Myc-HRP antibody. Release of scFv800E6 in cell culture medium was not observed under the conditions tested, confirming that scFv conjugation on SNP-HT was stable within 48 h of incubation at 37 °C (Figure 4).

To validate flow cytometry data, the specificity of binding between SNP-HT or SNP-UT and HER-2 was assessed by

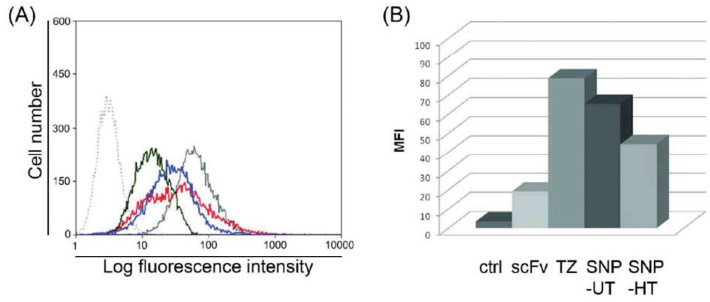

Figure 3. Multivalent presentation of scFv800E6 onto SNP-HT and SNP-UT enhances binding avidity toward HER-2 receptor. (A) MCF-7 cells were incubated with scFv (black), SNP-HT (blue), SNP-UT (red), or trastuzumab (TZ; gray continuous) and processed by flow cytometry. ScFv incubation with HER-2 cells as negative control (gray dashed line). (B) Mean fluorescence intensity (MFI).

Figure 4. Stability assay of scFv conjugation on SNP-HT. 5 μg of scFv immobilized on SNP-HT was incubated at 37 °C with 0.1 mL of culture medium. After incubation time, SNP-HT were centrifuged 15 min at 15 000 × *g* at 4 °C and supernatants (S1, S4, S24, and S48) were filtered on a PVDF membrane. Membranes were then probed with anti-Myc-HRP antibody and revealed with an ECL substrate. 5 μg of scFv immobilized on SNP-HT was used as a positive control. 0.1 mL of culture medium (M) was used as negative control.

confocal laser scanning microscopy (Figure 5). As HER-2 is a transmembrane receptor, we expected an accumulation of SNP-HT and SNP-UT at the level of the cell membrane of HER-2-positive cells only, which would confirm that nanoparticle capture occurs via specific membrane receptor-mediated internalization. HER-2 positive MCF-7 cells (Figure 5) were treated with scFv to assess HER-2 expression and cellular surface distribution. SNP-HT and SNP-UT were incubated in parallel with both MCF-7 and MDA cells (Figure 6) at a scFv concentration of 25 μg mL^{-1} of culture medium for 1 h at 37 °C. In order to discriminate between specific binding to the membrane receptor and a possible nonspecific adsorption of SNP, we revealed scFv, SNP-HT, and SNP-UT with FITC-labeled antiwhole mouse secondary antibodies (green), instead of exploiting intrinsically fluorescent silica nanospheres (Figures 5A,6A). Nuclei were stained with DAPI (Figures 5B,6B) while membranes were stained with DiD oil (Figures 5C,6C). As expected, both SNP-HT and SNP-UT (Figure 5A) were observed on HER-2-positive MCF-7 cell surface but not on HER-2-negative MDA cells (Figure 6A), which demonstrates that they are actually capable of specifically targeting their transmembrane receptor. Merged images in Figure 5D also show that SNP-UT and SNP-HT were mostly localized on cell membrane after 1 h incubation, although a small amount of nanoparticles were already internalized.

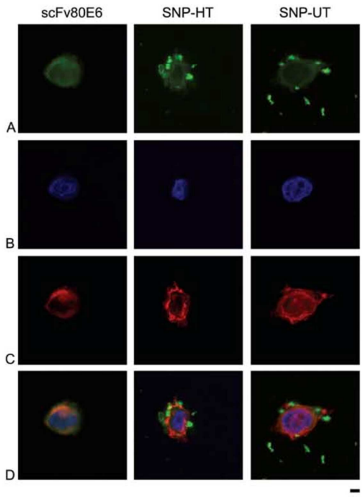

Figure 5. Assessment of HER-2 target efficacy of SNP-HT and SNP-UT on HER-2 positive cells. SNP-HT and SNP-UT were incubated with MCF-7 cells at a scFv concentration of 25 μg mL^{-1}. Free scFv was used as a positive control. ScFv, SNP-HT, and SNP-UT were revealed with FITC-labeled antiwhole mouse secondary antibodies (green, A). Nuclei were stained with DAPI (B), membranes (MB) with DiD oil (C). Merge images are shown in D. Scale bar: 10 μm.

■ CONCLUSION

In summary, we present a nanoparticle-based multimerization strategy aimed at enhancing the functional affinity of scFv toward cancer cell receptors. So far, the increase in binding efficiency of an antibody fragment has been primarily obtained by either chemically linking the individual scFv units or constructing multivalent variants by connecting antibody fragment with oligomerization domains. Our strategy lead to the facile and reliable development of nanoparticles allowing for multiple presentation of scFv molecules on a rigid nanosized spherical surface, which proved very effective and selective in binding the specific transmembrane receptor in living cells, as assessed by flow cytometry and confocal microscopy. These results suggest that the use of size- and shape-controlled inorganic nanoparticles as a multimerization scaffold is capable

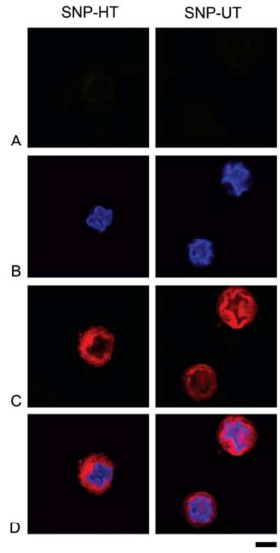

Figure 6. Assessment of HER-2 target efficacy of SNP-HT and SNP-UT on HER-2 negative cells. SNP-HT and SNP-UT were incubated with MDA cells at a scFv concentration of 25 μg mL^{-1}. ScFv on SNP-HT and SNP-UT was revealed with FITC-labeled antiwhole mouse secondary antibodies (green, A). Nuclei were stained with DAPI (B), membranes (MB) with DiD oil (C). Merge images are shown in D. Scale bar: 10 μm.

to improve scFv target binding efficacy, reaching an affinity value very close to that of native TZ, the mAb currently utilized in clinical practice.

■ ASSOCIATED CONTENT

Ⓢ Supporting Information

Experimental details for fully PEG-coated SNP (SPEG), SNP1 and SNP2, scheme of conjugation of SNP-HT and SNP-UT, determination of amine groups on SNP2, Dynamic Light Scattering and ζ-potential measurements. This material is available free of charge via the Internet at http://pubs.acs.org.

■ AUTHOR INFORMATION

Corresponding Author

*E-mail: davide.prosperi@unimib.it; Phone: (+39) 0264483302; Fax: (+39)0264483565.

Author Contributions

†These authors contributed equally to the research.

■ ACKNOWLEDGMENTS

We thank R. Allevi for TEM images, S. Citterio for helpful discussion of cell cytometry result. This work was partly supported by "Assessorato alla Sanità", Regione Lombardia, and Sacco Hospital (NanoMeDia Project), "Fondazione Romeo ed Enrica Invernizzi" and "Centro di Microscopia Elettronica per lo sviluppo delle Nanotecnologie applicate alla medicina" (CMENA, Univ. of Milan). M.C. and S.M. acknowledge "Centro di Microscopia Elettronica per lo sviluppo delle Nanotecnologie applicate alla medicina" (CMENA, University of Milan) for doctoral and postdoctoral fellowships, respectively.

■ REFERENCES

(1) Sanz, L., Cuesta, A. M., Compte, M., and Alvarez-Vallina, L. (2005) Antibody engineering: facing new challenges in cancer therapy. *Acta Pharmacol. Sin. 26*, 641−648.

(2) Holliger, P., and Hudson, P. J. (2005) Engineered antibody fragments and the rise of single domains. *Nat. Biotechnol. 9*, 1126−1136.

(3) Goel, A., Augustine, S., Baranowska-Kortylewicz, J., Colcher, D., Booth, B. J. M., Pavlinkova, G., Tempero, M., and Batra, S. K. (2001) Single-dose versus fractionated radioimmunotherapy of human colon carcinoma xenografts using 131I-labelled multivalent CC49 single chain fvs. *Clin. Cancer Res. 7*, 175−184.

(4) Sanz, L., Blanco, B., and Alvarez-Vallina, L. (2004) Antibodies and gene therapy: teaching old "magic bullets" new tricks. *Trends Immunol. 25*, 85−91.

(5) Bayly, A. M., Kortt, A. A., Hudson, P. J., and Power, B. E. (2002) Large-scale bacterial fermentation and isolation of scFv multimers using a heat-inducible bacterial expression vector. *J. Immunol. Methods 262*, 217−227.

(6) Wittel, U. A., Jain, M., Goel, A., Chauhan, S. C., Colcherand, D., and Batra, S. K. (2005) The in vivo characteristics of genetically engineered divalent and tetravalent single-chain antibody constructs. *Nucl. Med. Biol. 32*, 157−164.

(7) Gall, L. F., Kipriyanov, S. M., Moldenhauer, G., and Little, M. (1999) Di-, tri- and tetrameric single chain Fv antibody fragments against human CD19: effect of valency on cell binding. *FEBS Lett. 453*, 164−168.

(8) Ravn, P., Danielczyk, A., Jensen, K. B., Kristensen, P., Christensen, P. A., Larsen, M., Karsten, U., and Goletz, S. (2004) Multivalent scFv display of phagemid repertoires for the selection of carbohydrate-specific antibodies and its application to the Thomsen−Friedenreich antigen. *J. Mol. Biol. 343*, 985−996.

(9) Natarajan, A., Du, W., Xiong, C-Y, DeNardo, G. L., DeNardo, S. J., and Gervay-Hague, J. (2007) Construction of di-scFv through a trivalent alkyne−azide 1,3-dipolar Cycloaddition. *Chem. Commun. 695*, 685−697.

(10) Devey, S. M., and Lebedenko, E. N. (2008) Multivalency: the hallmark of antibodies used for optimization of tumor targeting by design. *BioEssays 30*, 904−918.

(11) Zhou, Y., Drummond, D. C., Zou, H., Hayes, M. E., Adams, G. P., Kirpotin, D. B., and Marks, J. D. (2007) Impact of single-chain Fv antibody fragment affinity on nanoparticle targeting of epidermal growth factor receptor-expressing tumor cells. *J. Mol. Biol. 371*, 934−947.

(12) Ackerson, C. J., Jadzinsky, P. D., Jensen, G. J., and Kornberg, R. D. (2006) Rigid, specific, and discrete gold nanoparticle/antibody conjugates. *J. Am. Chem. Soc. 128*, 2635−2640.

(13) Yang, L., Mao, H., Wang, A., Cao, Z., Peng, X., Wang, X., Duan, H., Ni, C., Yuan, Q., Adams, G., Smith, M. Q., Wood, W. C., Gao, X., and Nie, S. (2009) Single chain epidermal growth factor receptor antibody conjugated nanoparticles for in vivo tumor targeting and imaging. *Small 5*, 235−243.

(14) Huang, X., Peng, X., Wang, Y., Wang, Y., Shin, D. M., El-Sayed, M. A., and Nie, S. (2010) A reexamination of active and passive tumor targeting by using rod-shaped gold nanocrystal and covalently conjugated peptide ligands. *ACSNano 4*, 5887−5896.

(15) Sommaruga, S., Lombardi, A., Salvadè, A., Mazzucchelli, S., Corsi, F., Galeffi, P., Tortora, P., and Prosperi, D. (2011) Highly efficient production of anti-HER2 scFv antibody targeting for tumor targeting breast cancer cells. *Appl. Microbiol. Biotechnol. 91*, 613−621.

(16) Burns, A., Ow, H., and Weisner, U. (2006) Fluorescent core-shell silica nanoparticles: towards "lab on a particle" architectures for nanobiotechnology. *Chem. Soc. Rev. 35*, 1028−1042.

(17) Rossi, M. L., Shi, L., Rosenzweig, N., and Rosenzweig, Z. (2006) Fluorescent silica nanosphere for digital counting assay of the breast cancer marker HER2/neu. *Biosens. Bioelectron. 21*, 1900−1906.

(18) Wu, T., Zhang, Y., Wang, X., and Liu, S. (2008) Fabrication of hybrid silica nanoparticles densely grafted with thermoresponsive poly(N-isopropylacrylamide) brushes of controlled thickness via surface-initiated atom transfer radical polymerization. *Chem. Mater. 20*, 101−109.
(19) Kim, S. H., Jeyakumar, M., and Katznellenbogen, J. A. (2007) Dual-mode fluorophore-doped nickel nitriloacetic acid-modified silica nanoparticles combine histidine-tagged protein purification with site-specific fluorophore labeling. *J. Am. Chem. Soc. 129*, 13254−13264.
(20) Scmitt, L., Dietrich, C., and Tampè, R. (1994) Synthesis and characterization of chelator-lipids for reversible immobilization of engineered proteins at self-assembled lipid interfaces. *J. Am. Chem. Soc. 116*, 8485−8491.
(21) Halling, P. J., and Dunnill, P. (1979) Improved nonporous magnetic supports for immobilized enzymes. *Biotechnol. Bioeng. 21*, 393−416.
(22) Laemmli, U. K. (1970) Cleavage of structural proteins during the assembly of the head of bacteriophage T4. *Nature 227*, 680−85.
(23) Corsi, F., De Palma, C., Colombo, M., Allevi, R., Nebuloni, M., Ronchi, S., Rizzi, G., Tosoni, A., Trabucchi, E., Clementi, E., and Prosperi, D. (2009) Towards ideal magnetofluorescent nanoparticles for bimodal detection of breast-cancer cells. *Small 5*, 2555−2564.
(24) Han, H. J., Kannan, R. M., Wang, S., Mao, G., Kusanovic, J. P., and Romero, R. (2010) Multifunctional dendrimer template antibody presentation on biosensor surfaces for improved biomarker detection. *Adv. Funct. Mater. 20*, 409−421.
(25) Kohler, N., Fryxell, G. E., and Zhang, M. (2004) A bifunctional poly(ethylene glycol) silane immobilized on metallic oxide-based nanoparticles for conjugation with cell targeting agents. *J. Am. Chem. Soc. 126*, 7206−7211.
(26) Lin, W., Garnett, M. C., Schacht, E., Davis, S. S., and Illum, L. (1999) Preparation and in vitro characterization of HSA-mPEG nanoparticles. *Int. J. Pharm. 189*, 161−170.
(27) Hu, F., Wei, L., Zhou, Z., Ran, Y., Li, Z., and Gao, M. (2006) Preparation of biocompatibile magnetite nanocrystals for in vivo magnetic resonance detection of cancer. *Adv. Mater. 18*, 2553−2556.
(28) Mazzucchelli, S., Colombo, M., De Palma, C., Salvadè, A., Verderio, P., Coghi, M. D., Clementi, E., Tortora, P., Corsi, F., and Prosperi, D. (2010) Single-domain protein A-engineered magnetic nanoparticles: a step towards a universal strategy to site-specific labeling of antibodies for targeted detection of tumor cells. *ACS Nano 10*, 5693−5702.

ARTICLE 6

Supporting Information

Multiple Presentation of Scfv800E6 on Silica Nanospheres Enhances Targeting Efficiency Towards Breast Cancer Cells

Serena Mazzucchelli,[1] Paolo Verderio,[1] Silvia Sommaruga,[2] Miriam Colombo,[1,2] Agnese Salvadè,[2] Fabio Corsi,[2] Patrizia Galeffi,[3] Paolo Tortora,[1] Davide Prosperi[1,4,*]

[1]Dipartimento di Biotecnologie e Bioscienze, Università di Milano-Bicocca, Piazza della Scienza 2, 20126 Milano, Italy. [2]Dipartimento di Scienze Cliniche "Luigi Sacco", Università di Milano, Ospedale L. Sacco, Via G.B. Grassi 74, 20157 Milano, Italy. [3]UTAGRI-GEN, ENEA, R. C.Casaccia, Via Anguillarese 301, 00123 Roma, Italy. [4]Istituto di Scienze e Tecnologie Molecolari, CNR, via Fantoli 16/15, 20138 Milano, Italy.

E-mail: davide.prosperi@unimib.it

LIST OF CONTENTS

I. Scheme of synthesis of fully PEG-coated SNP (SPEG).

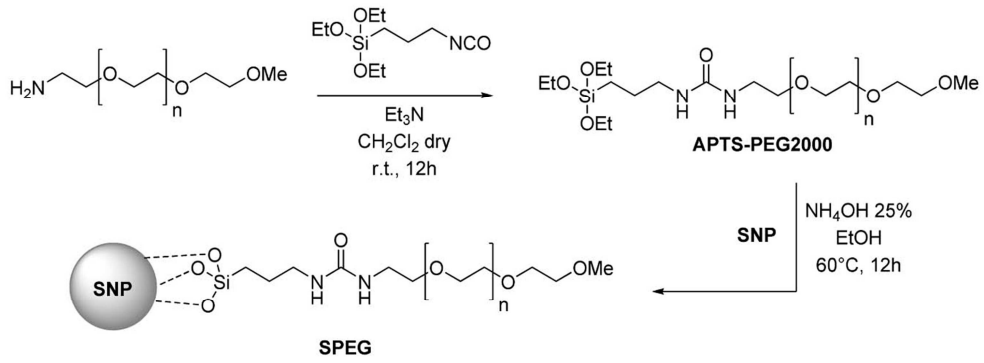

Scheme S1: Synthetic strategy to SPEG

II. Scheme of synthesis of SNP1.

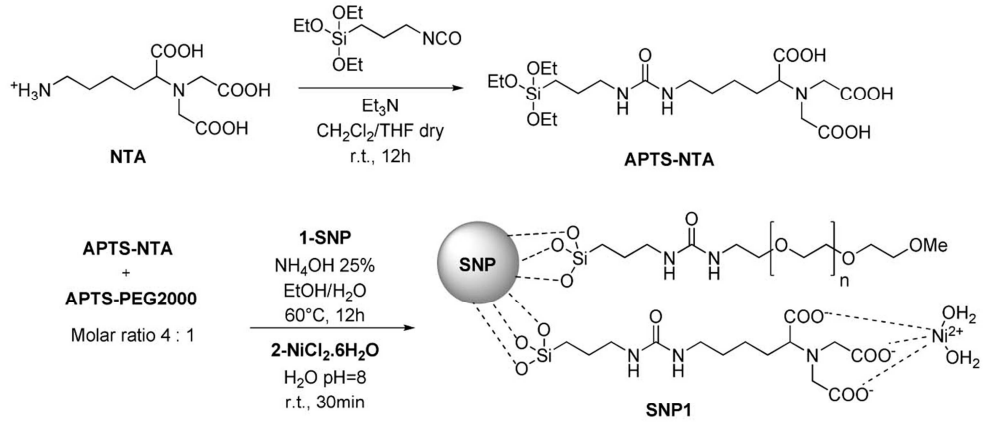

Scheme S2: Synthetic strategy to SNP1

III. Scheme of synthesis of SNP2.

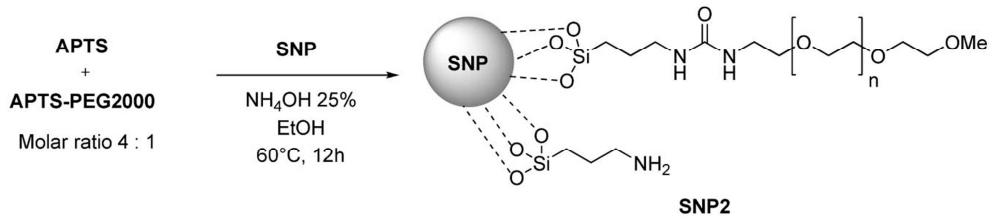

Scheme S3: Synthetic strategy to SNP2

IV. Determination of amine groups on SNP2.

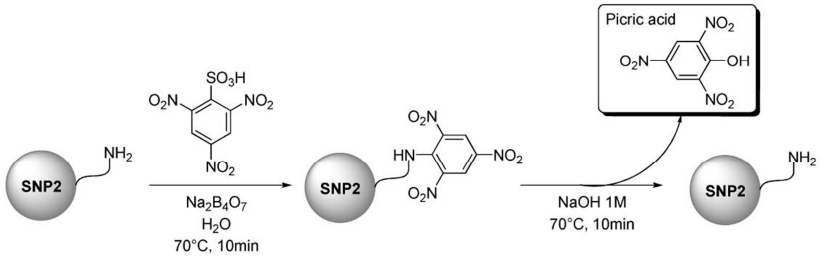

Scheme S4: Quantification of amine reactive groups: TBNS assay.

V. Scheme of conjugation of His-tag scFv800E6 (SNP-HT).

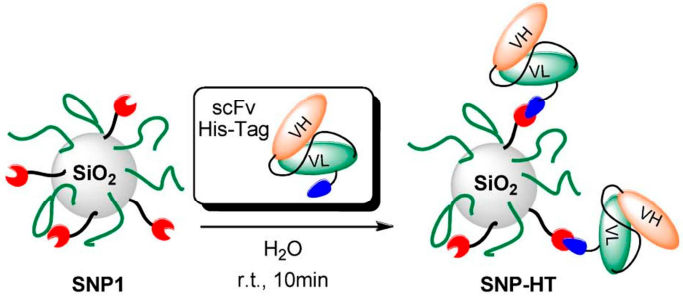

Scheme S5: Synthetic strategy to SNP-HT.

VI. Scheme of the unoriented conjugation of scFv800E6 (SNP-UT).

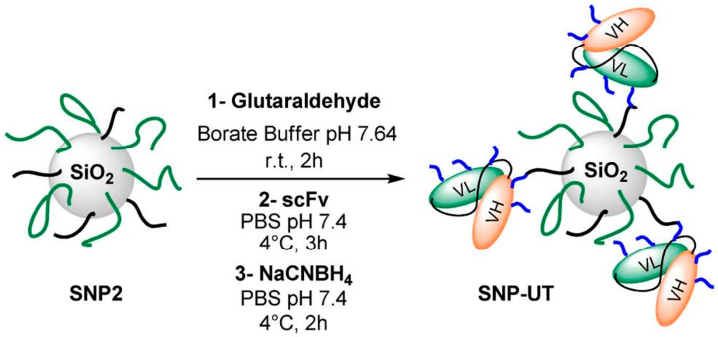

Scheme S6: Synthetic strategy to SNP-UT.

VII. Dynamic Light Scattering and ζ-Potential measurements.

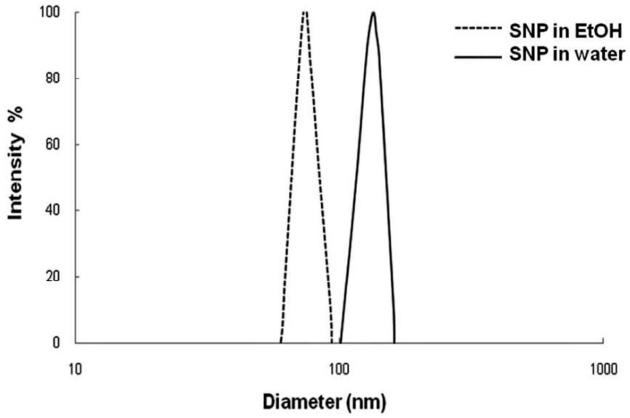

Figure S1. Hydrodynamic size distribution histogram of SNP in ethanol (73.3 nm, polydispersity 0.132; dashed line) and in deionized water (133.8 nm, polydispersity 0.232; continous line). The horizontal scale is semi-logarithmic. SNP ζ-Potential in deionized water was -35.86 mV (± 0.64).

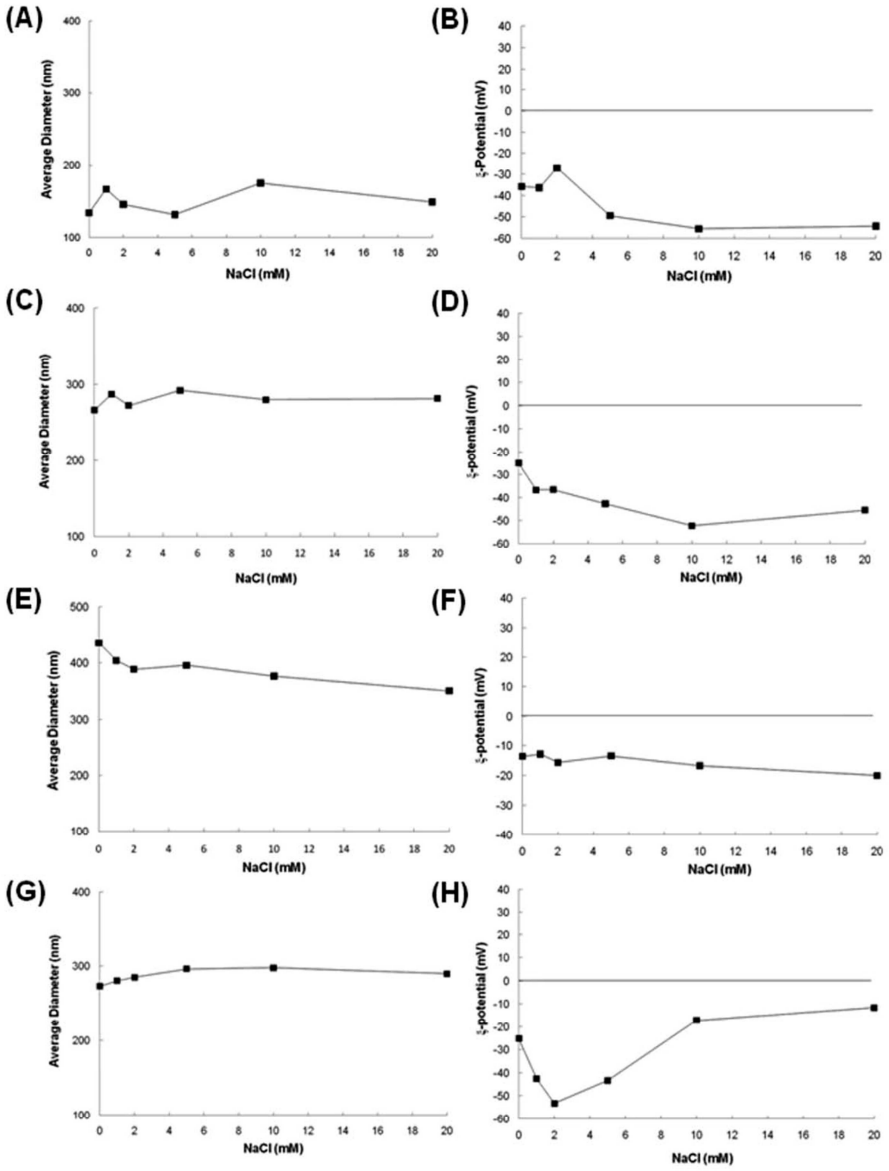

Figure S2. (A) Hydrodynamic size distribution behavior of SNP in deionized water at different Na^+ concentrations. SNP hydrodynamic radius was unaltered by the salts concentration. (B) ζ-Potential profiles of SNP in deionized water at increasing of Na^+ concentrations: as expected, Na^+ was adsorbed in the liquid hydration sphere of nanoparticles in order to increase solubility of silica in aqueous medium. The charge became strongly negative at higher concentration of salts (NaCl 10 mM , –55.50 mV ± 0.54) which implied an enhanced stability of colloidal suspension. (C)

Hydrodynamic radius of SPEG at pH 7.0 in deionized water (266.2 nm, polydispersity 0.322) was unaltered by different Na^+ concentrations (1 mM to 20 mM). (D) ζ-Potential profiles of SPEG at increasing of Na^+ concentrations (1 mM to 20 mM): as expected, Na^+ was adsorbed in the liquid hydration sphere of nanoparticles in order to increase solubility of silica in aqueous medium. The charge became strongly negative at higher concentration of salts (NaCl 10 mM, -52.19 mV ± 1.13) which implied an enhanced stability of colloidal suspension. (E) Hydrodynamic radius of SNP1 at pH 7.0 in deionized water (435.8 nm, polydispersity 0.325) decreased with increasing Na^+ concentrations; at pH 7.0 with 20 mM NaCl SNP1 hydrodynamic radius was 350.2 nm, polydispersity 0.199. (F) ζ-Potential profiles of SNP1 at increasing of Na^+ concentrations. In this case the charge was similar even at higher concentration of salts (20 mM NaCl, -20.02 mV ± 1.78). (G) Hydrodynamic radius of SNP2 at pH 7.0 in water (272.8 nm, polydispersity 0.298) was unaltered by different Na^+ concentrations; at pH 7.0 and 20 mM NaCl, SNP2 hydrodynamic radius was 289.3 nm, polydispersity 0.303. (H) ζ-Potential profiles of SNP2 at increasing of Na^+ concentrations. In this case, the charge was strongly negative at low salt concentrations (2 mM NaCl, -53.24 mV ± 0.70), but at higher concentrations (20 mM NaCl) the charge decreased to -11.62 mV ± 1.10.

REFERENCES

[1] Wu, T., Zhang, Y., Wang, X., and Liu, S. (2008) Fabrication of hybrid silica nanoparticles densely grafted with thermoresponsive poly(*N*-isopropylacrylamide) brushes of controlled thickness via surface-initiated atom transfer radical polymerization. *Chem. Mater. 20*, 101-109.

[2] Kim, S. H., Jeyakumar, M., and Katznellenbogen, J. A. (2007) Dual-mode fluorophore –doped Nickel nitriloacetic acid-modified silica nanoparticles combine Histidine-tagged protein purification with site-specific fluorophore labeling. *J. Am. Chem. Soc. 129*, 13254-13264.

[3] Scmitt, L., Dietrich, C., and Tampè, R. (1994) Synthesis and characterization of chelator-lipids for reversible immobilization of engineered proteins at self-assembled lipid interfaces. *J. Am. Chem. Soc. 116*, 8485-8491.

[4] Halling, P. J., and Dunnill, P. (1979) Improved nonporous magnetic supports for immobilized enzymes. *Biotechnol. Bioeng. 21*, 393-416.

[5] Sommaruga, S., Lombardi, A., Salvadè, A., Mazzucchelli, S., Corsi, F., Galeffi, P., Tortora, P., and Prosperi, D. (2011) Highly efficient production of anti-HER2 scFv antibody targeting for tumor targeting breast cancer cells. *Appl. Microbiol. Biotechnol.* DOI: 10.1007/s00253-011-3306-3

[6] Laemmli, U. K. (1970) Cleavage of structural proteins during the assembly of the head of bacteriophage T4. *Nature 227*, 680-85.

[7] Corsi, F., De Palma, C., Colombo, M., Allevi, R., Nebuloni, M., Ronchi, S., Rizzi, G., Tosoni, A., Trabucchi, E., Clementi, E., and Prosperi, D. (2009), Towards ideal magnetofluorescent nanoparticles for bimodal detection of breast-cancer cells. *Small*. *5*, 2555-2564.

[8] Han, H. J., Kannan, R. M.., Wang, S., Mao, G., Kusanovic, J. P., and Romero, R. (2010), Multifunctional dendrimer template antibody presentation on biosensor surfaces for improved biomarker detection. *Adv*. *Funct*. *Mat*. *20*, 409-421.

ARTICLE 6

Lipopolysaccharides

DOI: 10.1002/anie.201004655

Uniform Lipopolysaccharide (LPS)-Loaded Magnetic Nanoparticles for the Investigation of LPS–TLR4 Signaling**

Matteo Piazza, Miriam Colombo, Ivan Zanoni, Francesca Granucci, Paolo Tortora, Jerrold Weiss, Theresa Gioannini, Davide Prosperi, and Francesco Peri**

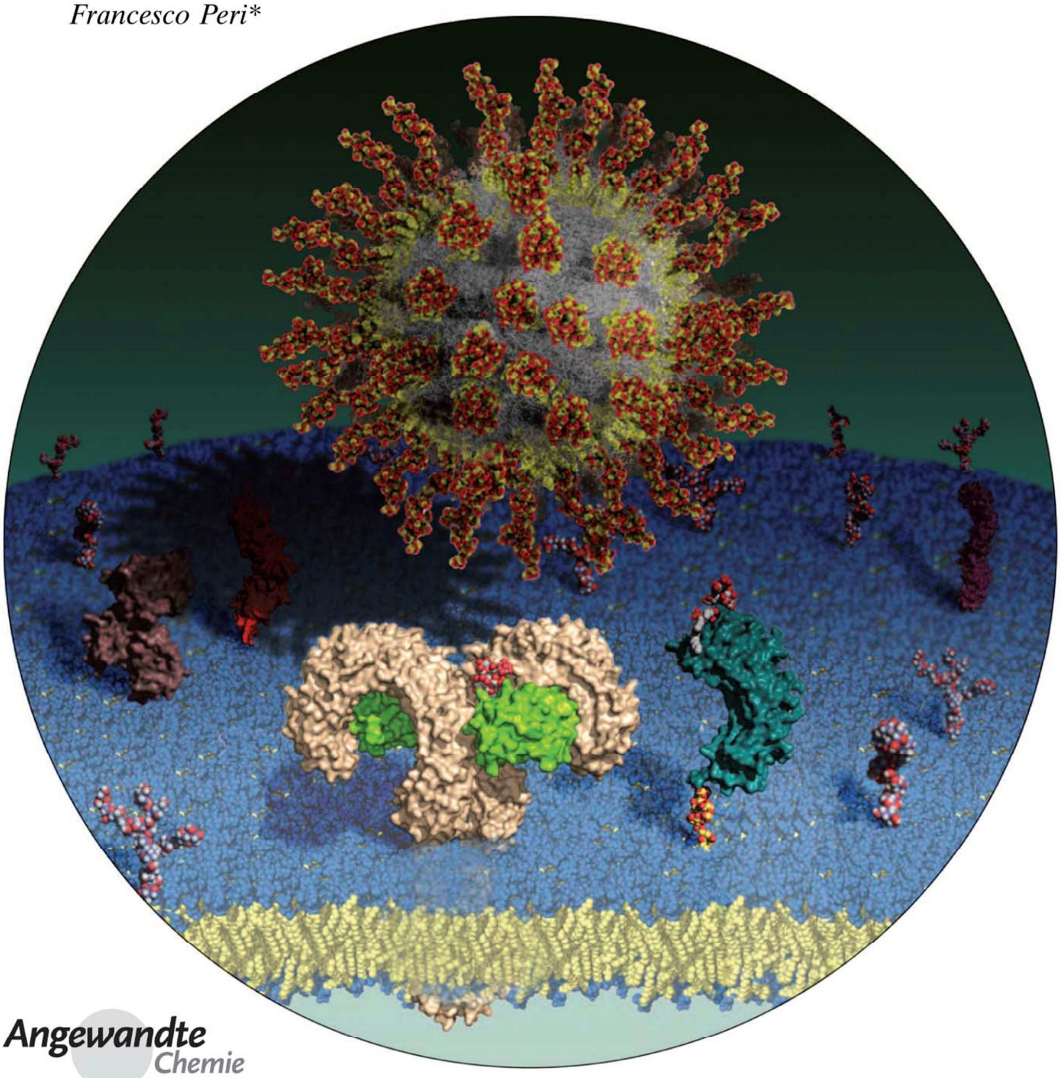

Angewandte 50 International Edition Chemie

The interaction of highly conserved microbial constituents with the innate immune system contributes greatly to the recognition and reaction against intruding pathogens by mammals. Examples of such microbial constituents include the lipopolysaccharides (LPSs) and lipooligosaccharides (LOSs), also known as endotoxin (E), of Gram-negative bacteria. These potent proinflammatory molecules include a hydrophilic oligosaccharide chain of variable length and a hydrophobic, membrane-anchoring moiety, termed lipid A.[1–3] The interaction of E with cells of the innate immune system leads to the formation and release of endogenous mediators, which initiate inflammatory and immune responses essential for optimal antibacterial defense.[4,5] Such a cascade of events is triggered by activation of the Toll-like receptor 4 (TLR4) by E. This is the last step of a sequential process of E recognition and interaction with extracellular and cell-surface host proteins, including LPS-binding protein (LBP), soluble and membrane-associated CD14 glycoprotein, secreted and TLR4-associated myeloid differentiation protein 2 (MD-2), and TLR4 itself.[6–8]

The amphiphilic character of both LPSs and LOSs results in the formation of micelles in an aqueous environment above their critical micellar concentration (CMC; Scheme 1, top).[9] CMC values between 10^{-8} and 10^{-7} M for deep rough mutant LPS Re,[10,11] and between 1.3 and 1.6 μM for *Escherichia coli* LPS,[12] were reported. In balanced salt solutions containing physiological extracellular concentrations of Mg^{2+} and Ca^{2+}, CMC values of 1 nM or lower are likely.[13,14] From these data and from the fact that LPS aggregates are usually highly stable, aggregated forms of LPS should predominate in the concentration range relevant for biological responses. In physiological fluids, LPS aggregates were also found as membrane "blebs", which are constitutively released from growing Gram-negative bacteria.[15] Transmission electron microscopy (TEM) revealed that blebs exist predominantly as vesicles with an average size of 40–80 nm.[15]

The current view of mammalian LPS sensing and signaling is that it is initiated by the LBP-catalyzed extraction and transfer of an LPS monomer from aggregates[16] to CD14[17] and subsequent transfer of the LPS monomer from CD14 to MD-2 or to the MD-2–TLR4 heterodimer.[7] While monomeric E–CD14 and E–MD-2 complexes are therefore the proximal vehicles for activation of MD-2–TLR4 and TLR4, respectively, by E, the preceding interactions of host E-binding proteins that preferentially interact with E-rich interfaces and either promote (LBP) or preclude (bactericidal/permeability-increasing (BPI) protein) transfer of E to CD14 play key roles in determining the potency of TLR4 activation by E.[18] Accordingly, variables in the aggregation state and the 3D form of E aggregates may directly influence the kinetics and potency of TLR4 activation and signaling.[9]

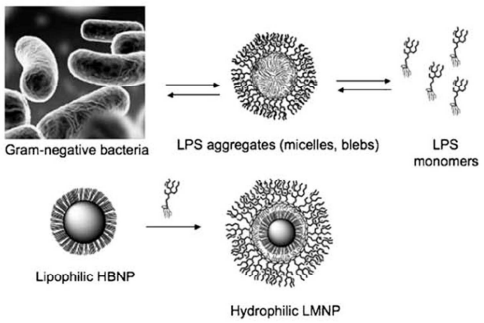

Scheme 1. LPSs or LOSs either extracted and purified or spontaneously released from Gram-negative bacteria form large aggregates (micelles, membrane blebs) in an aqueous environment. LPS-coated magnetic nanoparticles (LMNPs) mimicking LPS aggregates are obtained by coating a hydrophobic brush nanoparticle (HBNP) with bacterial LPS.

The design of metal-based nanoparticles that possess a suitable rigid size-controlled support for the reversible anchorage of a limited number of E molecules suggests a novel approach to the development of nanoscale vectors for delivery of TLR4 agonists. The potential of integrating inorganic nanoparticles with biomolecular probes has been demonstrated by the creation of targeted contrast agents for magnetic resonance imaging achieved by the conjugation of multiple ligands to iron oxide nanoparticles,[19] and by the development of multivalent magnetic relaxation nanosensors for the detection of biomolecules, such as DNA and proteins, and of metabolic activity.[20–22] An additional advantage of these particles is the capability of the magnetic core to facilitate the separation of hybrid nanoparticles after ligand conjugation.

Herein, we present the synthesis and application of novel bioactive LPS-coated magnetic nanoparticles (LMNPs). LMNPs were designed to mimic natural E micelles or membrane blebs (Scheme 1, bottom) that contain an E-rich monolayer on the surface with the fatty acyl chains of lipid A oriented inward away from the aqueous surroundings.

The strategies commonly employed for the stable anchorage of organic molecules on the surface of nanoparticles were not appropriate for our purpose, as they usually involve irreversible ligand immobilization or nonspecific physical

[*] Dr. M. Piazza,[+] M. Colombo,[+] Dr. I. Zanoni, Prof. F. Granucci, Prof. P. Tortora, Dr. D. Prosperi, Prof. F. Peri
Dipartimento di Biotecnologie e Bioscienze, Università di Milano Bicocca
Piazza della Scienza 2, 20126 Milano (Italy)
Fax: (+39) 026-448-3565
E-mail: davide.prosperi@unimib.it
francesco.peri@unimib.it
Prof. J. Weiss, T. Gioannini
Department of Internal Medicine, University of Iowa and Department of Veterans Affairs Medical Center
Iowa City, IA 52246 (USA)

[+] These authors contributed equally to this work.

[**] We thank R. Allevi from CMENA for help with TEM images. M.C. acknowledges the research fellowship of CMENA. This work was supported by NIH/NIAID (1R01AI059372), "Regulation of MD-2 function and expression" and "Fondazione Romeo e Enrica Invernizzi". TLR4 = Toll-like receptor 4. Frontispiece image realized with PyMOL and GIMP by Roberto Cighetti.

Supporting information for this article is available on the WWW under http://dx.doi.org/10.1002/anie.201004655.

adsorption onto the nanoparticle surface. The latter typically results in a very unstable hybrid system with unregulated release of the bound molecules and, quite possibly, nonuniform arrangement of the bound ligands on the nanoparticle surface.

To provide nanoparticles that would more likely make possible the stable and reversible binding of a monolayer of E monomers, we designed a hydrophobic brush nanoparticle (HBNP) system with an outer layer of exposed hydrocarbon chains at the surface (Scheme 1). Spherical HBNPs were oleylamine-coated iron oxide nanocrystals, for which a tight control on size and shape could be achieved by wet chemical synthesis.[23] HBNPs were resuspended in hexane and added to an aqueous dispersion of commercial LPS (from *E. coli* 055:B5, Sigma, purified by gel-filtration chromatography) at a 5:1 weight ratio. This biphasic mixture was mildly warmed (40 °C) and sonicated to cause the slow evaporation of the organic solvent while mixing. This process promoted the formation of hydrophilic LMNPs with the polysaccharide chains of LPS forming the outer shell. Of the various buffered media tested, dispersion of LPS in 50 mM Tris–HCl buffer with 5 mM ethylenediaminetetraacetic acid (EDTA; pH 7.5) was optimal for the formation of LMNPs.

LMNP stability was dependent on the reaction time and on the initial relative concentrations of HBNPs and LPS in the mixture. These parameters were optimized by monitoring the hydrodynamic size of isolated LMNPs and of the supernatant solutions containing excess LPS. In the absence of HBNPs, LPS micelles had a mean hydrodynamic diameter of 80–100 nm (see Figure S1 in the Supporting Information).

If the coating reaction with LPS was stopped at shorter times, larger size distributions of the recovered particles were observed, possibly reflecting varying aggregation of particles that were only partially covered by LPS. These observed nanoparticle agglomerates of varying size could be reversed (disaggregated) by continued sonication in the presence of LPS until LPS coating was completed. The coating process resulted in stable particle dispersion with a hydrodynamic diameter of (193 ± 4) nm. TEM images of LMNPs in water confirmed that the recovered hybrid nanoparticles

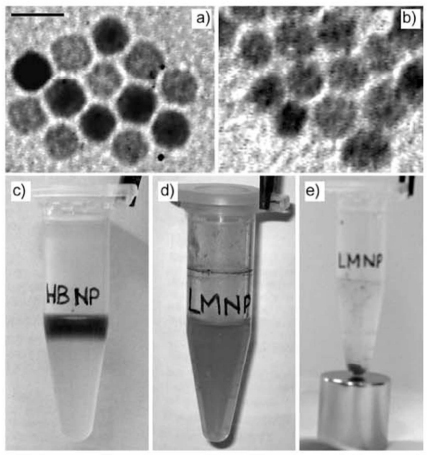

Figure 1. TEM images of a) HBNPs in hexane and b) LMNPs in distilled water. Scale bar: 10 nm. c) The upper colored phase is a HBNP dispersion in hexane, while the lower colorless phase is 16.7 μM LPS in Tris–EDTA. d) LMNP aqueous dispersion after phase mixing and evaporation of the organic solvent. e) Purification of LMNPs by magnetic decantation.

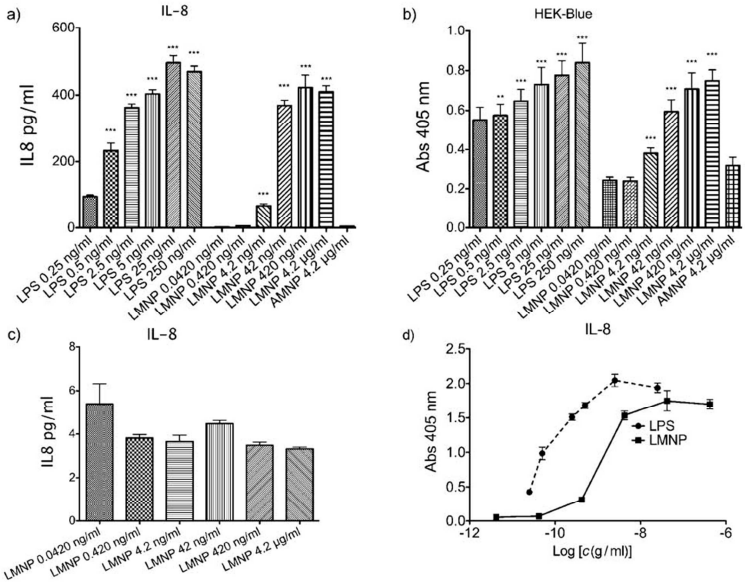

Figure 2. a) LMNP-dependent IL-8 production in HEK–TLR4 cells. b) Measurement of LMNP-induced activation of the transcription factor NF-κB level in HEK–Blue cells. c) LMNPs do not stimulate IL-8 production in parental HEK cells. d) Comparison of dose–response curves for LPS and LMNPs from data shown in (a). The results shown represent the mean ± standard error of the mean (SEM) of three independent experiments, each in triplicate. The asterisks indicate a significant statistical difference ($P < 0.01$; ANOVA, Dunnett's test) between data in the analyzed group and reference data (LPS 25 pM and LMNP 4.2 pM for both (a) and (c)).

retained their shape and were generally organized as small clusters of individual particles after solvent evaporation on the sample grid (Figure 1a,b). LMNPs prepared with the described procedure were very stable and could be purified and isolated by magnetic decantation (Figure 1c–e) without apparent loss of water stability once resuspended, even after several purification cycles. Moreover, LMNPs could be stored at 4°C for longer than 1 month and showed no sign of aggregation, as determined by dynamic light scattering, and no degradation in terms of biological activity.

Quantitative evidence of the stability of LMNPs in water and physiological aqueous environments was obtained from relaxivity measurements, as the T_2 value was almost unvaried after 2 hours (see Figure S3 in the Supporting Information). By comparison of the measured T_2 with a standard calibration curve, we could assess the iron content in LMNP dispersions, which was determined to be 1.35 mM Fe. The amount of bound E was quantified by measuring the bound radioactivity of purified LMNPs obtained with the described procedure using tritiated LOS,[13] which yielded an estimate that each individual LMNP contained an average of 130 E molecules.

The bioactivity of LPS bound to LMNPs was assessed by measuring the ability of LMNPs to stimulate TLR4-dependent cell activation. Increasing concentrations of LMNPs (from 4.2 pM to 4.2 nM of nanoparticle-bound LPS) induced a dose-dependent activation of transformed HEK293 cells expressing CD14, MD-2, and TLR4, as manifested by extracellular accumulation of interleukin-8 (IL-8) from treated "HEK–TLR4" cells (Figure 2a) and of secreted embryonic alkaline phosphatase (SEAP; an NF-kB/AP-1 reporter gene) from treated "HEK–Blue" cells (Figure 2b). In contrast, LMNPs did not activate the parental HEK293 cells that do not express CD14, MD-2, or TLR4 (Figure 2c), thus confirming that activation of HEK–TLR4 and HEK–Blue cells by LMNPs was CD14- and MD-2–TLR4-dependent.

To further define the ability of LMNPs to stimulate TLR4-dependent cellular responses, LMNP-induced activation of cells of the innate immune system was investigated using wild-type (wt), CD14$^{-/-}$, and TLR4$^{-/-}$ murine bone-marrow-derived dendritic cells (BMDCs) and bone-marrow-derived macrophages (BMDMs). Cell activation was monitored by the accumulation of extracellular tumor necrosis factor α (TNF-α) during incubation for 24 hours. As shown in Figure 3, LMNPs produced dose-dependent activation of both cell types derived from wt mice. The potency of the LMNPs was reduced about tenfold toward CD14$^{-/-}$ cells and little or no cell activation was induced by LMNPs in TLR4$^{-/-}$ cells. Thus, activation of BMDCs and BMDMs by LMNPs was TLR4-dependent and promoted by CD14, consistent with action of the bound LPS in the LMNPs. This view was further supported by demonstrating that activation of HEK–Blue cells by LMNPs could be inhibited by IAXO-101 (Figure 4), a synthetic glycolipid previously shown to interrupt E-triggered TLR4 activation by antagonizing the LPS–CD14 interaction.[24,25]

To verify that the biological activity observed for LMNPs was exclusively related to the immobilized E and not influenced by the inorganic core, we tested LPS-free, water-soluble magnetic nanoparticles (MNPs) as a negative control. To this aim, hydrophobic HBNPs were transferred to aqueous

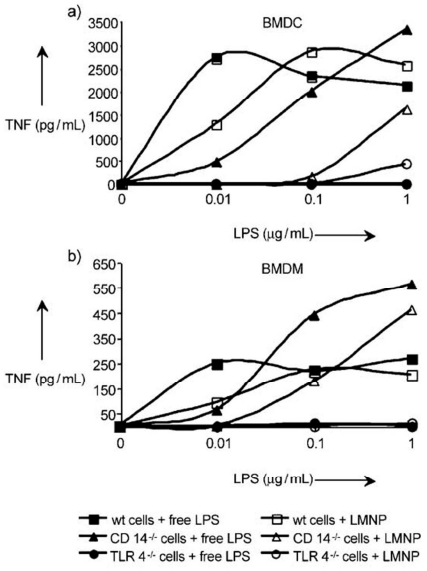

Figure 3. LMNP- and free LPS-mediated activation of BMDCs (left) and BMDMs (right). Cells of the innate immune system were activated with LMNPs and the corresponding amounts of free LPS and the release of TNF-α were measured in the supernatant 24 h later. Data are means of at least three independent experiments.

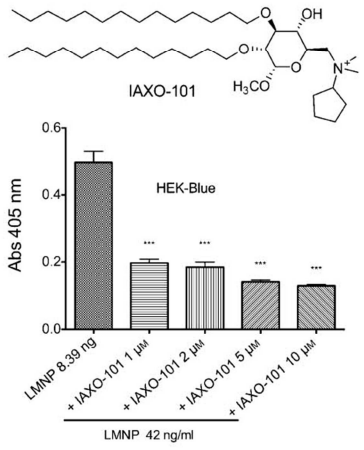

Figure 4. Co-administration of LMNPs (42 ng/mL) and increasing amounts of IAXO-101 (0–10 μM) to HEK–Blue cells. The results shown represent the mean ± SEM of three independent experiments, each in triplicate. The asterisks indicate a significant statistical difference ($P < 0.01$; ANOVA, Dunnett's test) between data in the analyzed group and reference data (LMNPs alone).

solution by ligand exchange with *N*-phosphonomethyl iminodiacetic acid phosphonate (PMIDA) to give water-soluble anionic MNPs (AMNPs),[26] which exhibited a zeta potential of $-(25\pm2)$ mV, very close to that of LMNPs ($-(18\pm3)$ mV). As expected, when treating HEK–Blue cells with AMNPs, no TLR4-dependent SEAP production was observed.

Comparison of the dose-dependent activation by LMNPs and by LPS of HEK–TLR4 and HEK–Blue cells (Figure 2) and of wt and $CD14^{-/-}$ murine BMDMs and BMDCs (Figure 3) revealed that the LMNPs were about tenfold less potent than LPS when normalized for the amount of LPS added. Even at the highest dose tested (4.2 nM), LMNPs had no detectable cytotoxic effect (see Figure S4 in the Supporting Information), which indicated that the reduced potency of LMNPs in inducing TLR4-dependent cell activation was most likely due to reduced efficiency of delivery of LPS from LMNPs (versus aggregates of LPS) to CD14 and to MD-2–TLR4 and not a general cytotoxic effect of the LMNPs.

In summary, we have developed an efficient and reproducible synthetic strategy to prepare LMNPs with defined size and shape. The hydrophobic coating of the spherical HBNPs has made possible binding of LPS molecules on the nanoparticle surface in an orientation that resembles the natural presentation of LPS in the outer membrane of Gram-negative bacteria as well as in aggregates of extracted and purified LPS. The LMNPs are stable in solution and the LPS is stably immobilized on the nanoparticles in the absence of suitable E acceptors. LMNPs trigger cell activation in an LPS- and TLR4-dependent manner that is promoted by CD14, which makes it likely that cell activation is dependent on mobilization of LPS monomers from the surface of the LMNPs to MD-2–TLR4. Work is in progress to further investigate the in vitro and in vivo effects of controlled LPS release from LMNPs and the possible application of these reagents as new, nanoparticle-based vaccine adjuvants or immunotherapeutics.

Received: July 28, 2010
Published online: November 9, 2010

Keywords: endotoxin · immunology · lipopolysaccharides · nanoparticles · receptors

[1] M. Freudenberg, T. Merlin, M. Gumenscheimer, C. Kalis, R. Landmann, C. Galanos, *Microbes Infect.* **2001**, *3*, 1213.
[2] H. Heine, E. Rietschel, A. Ulmer, *Mol. Biotechnol.* **2001**, *19*, 279.
[3] C. Alexander, E. Rietschel, *J. Endotoxin Res.* **2001**, *7*, 167.
[4] M. Freudenberg, S. Tchaptchet, S. Keck, G. Fejer, M. Huber, N. Schütze, B. Beutler, C. Galanos, *Immunobiology* **2008**, *213*, 193.
[5] B. Beutler, K. Hoebe, X. Du, R. Ulevitch, *J. Leukocyte Biol.* **2003**, *74*, 479.
[6] T. Gioannini, D. Zhang, A. Teghanemt, J. Weiss, *J. Biol. Chem.* **2002**, *277*, 47818.
[7] T. Gioannini, A. Teghanemt, D. Zhang, N. Coussens, W. Dockstader, S. Ramaswamy, J. Weiss, *Proc. Natl. Acad. Sci. USA* **2004**, *101*, 4186.
[8] R. Jerala, *Int. J. Med. Microbiol.* **2007**, *297*, 353.
[9] T. Gutsmann, A. Schromm, K. Brandenburg, *Int. J. Med. Microbiol.* **2007**, *297*, 341.
[10] K. Takayama, Z. Din, P. Mukerjee, P. Cooke, T. Kirkland, *J. Biol. Chem.* **1990**, *265*, 14023.
[11] K. Takayama, D. Mitchell, Z. Din, P. Mukerjee, C. Li, D. Coleman, *J. Biol. Chem.* **1994**, *269*, 2241.
[12] L. Yu, M. Tan, B. Ho, J. Ding, T. Wohland, *Anal. Chim. Acta* **2006**, *556*, 216.
[13] P. Giardina, T. Gioannini, B. Buscher, A. Zaleski, D. Zheng, L. Stoll, A. Teghanemt, M. Apicella, J. Weiss, *J. Biol. Chem.* **2001**, *276*, 5883.
[14] N. Iovine, J. Eastvold, P. Elsbach, J. Weiss, T. Gioannini, *J. Biol. Chem.* **2002**, *277*, 7970.
[15] D. Post, D. Zhang, J. Eastvold, A. Teghanemt, B. Gibson, J. Weiss, *J. Biol. Chem.* **2005**, *280*, 38383.
[16] A. Schromm, K. Brandenburg, E. Rietschel, H. Flad, S. Carroll, U. Seydel, *FEBS Lett.* **1996**, *399*, 267.
[17] R. Schumann, *Res. Immunol.* **1992**, *143*, 11.
[18] J. Weiss, *Biochem. Soc. Trans.* **2008**, *31*, 785.
[19] M. G. Harisinghani, J. Barentsz, P. F. Hahn, W. M. Deserno, S. Tabatabaei, C. H. van de Kaa, J. de La Rosette, R. Weissleder, *N. Engl. J. Med.* **2003**, *348*, 2491.
[20] J. M. Perez, L. Josephson, T. O'Loughlin, D. Hogemann, R. Weissleder, *Nat. Biotechnol.* **2002**, *20*, 816.
[21] G. Prencipe, S. Maiorana, P. Verderio, M. Colombo, P. Fermo, E. Caneva, D. Prosperi, E. Licandro, *Chem. Commun.* **2009**, 6017.
[22] M. Colombo, S. Ronchi, D. Monti, F. Corsi, E. Trabucchi, D. Prosperi, *Anal. Biochem.* **2009**, *392*, 96.
[23] L. Polito, M. Colombo, D. Monti, S. Melato, E. Caneva, D. Prosperi, *J. Am. Chem. Soc.* **2008**, *130*, 12712.
[24] M. Piazza, C. Rossini, S. Della Fiorentina, C. Pozzi, F. Comelli, I. Bettoni, P. Fusi, B. Costa, F. Peri, *J. Med. Chem.* **2009**, *52*, 1209.
[25] M. Piazza, L. Yu, A. Teghanemt, T. Gioannini, J. Weiss, F. Peri, *Biochemistry* **2009**, *48*, 12337.
[26] S. Mazzucchelli, M. Colombo, C. De Palma, P. Verderio, M. D. Coghi, E. Clementi, P. Tortora, F. Corsi, D. Prosperi, *ACS Nano* **2010**, *4*, 5693.

Angewandte Chemie
Eine Zeitschrift der Gesellschaft Deutscher Chemiker

Supporting Information

69451 Weinheim, Germany

Uniform Lipopolysaccharide (LPS)-Loaded Magnetic Nanoparticles for the Investigation of LPS–TLR4 Signaling**

Matteo Piazza, Miriam Colombo, Ivan Zanoni, Francesca Granucci, Paolo Tortora, Jerrold Weiss, Theresa Gioannini, Davide Prosperi, and Francesco Peri**

anie_201004655_sm_miscellaneous_information.pdf

Materials and methods. All chemicals were purchased from Sigma-Aldrich (St. Louis, MO) and used as received. Water was deionized and ultrafiltered by a MilliQ apparatus from Millipore Corporation (Billerica, MA) before use. Commercial LPS from *E. coli* 055:B5 was used as supplied (Sigma, purified by gel-filtration chromatography). TEM images were obtained by a Zeiss EM-109 microscope operating at 80 kV, available at the "Centro di Microscopia Elettronica per le Nanotecnologie applicate alla medicina" (CMENA, University of Milan). T_2 relaxation times were acquired at a temperature of 313 K using a Bruker Minispec mq20 system working with 1-H at 20 MHz magnetic field with the following parameters: CMPG sequence, 1000 echoes with a 20 ms echo time and 2 s repetition time. Samples were introduced using 10 mm NMR tubes wormed in a thermostatic bath. Dynamic light scattering (DLS) measurements were performed at 90° with a 90Plus Particle Size Analyzer from Brookhaven Instruments Corporation (Holtsville, NY), working at 15 mW of a solid state laser (λ = 661 nm). Zeta-potential measurements were performed on the same instrument, equipped with a couple of AQ-809 electrodes, and analyses were processed by a ZetaPlus software. Viscosity and refractive index of pure water were used to characterize the solvent. Nanoparticles were dispersed in water and sonicated in a S15H Elmasonic apparatus (Elma, Singen, Germany) before analysis. Final sample concentration used for measurements was typically of 0.01 mg mL^{-1}.

Synthesis of surfactant-coated Fe_3O_4 nanoparticles (HBNPs) by thermal decomposition. $Fe(acac)_3$ (4 mmol) was dissolved in a mixture of oleylamine (20 mL) and benzyl ether (20 mL). The mixture was heated at 110 °C under argon flux for 1 h, then refluxed (ca. 300 °C) for 2 h, and finally cooled to room temperature. Ethanol (100 mL) was added and the black precipitate was centrifuged. The supernatant was discarded and the product washed several times with ethanol to remove the unbound surfactant, providing spherical, surfactant-coated magnetite nanocrystals (HBNPs).

Synthesis of LMNPs by HBNP coating with endotoxin. The following steps were performed under sterile conditions. HBNPs (100 μg) dissolved in hexane (100 μL) were added to a solution of endotoxin (500 μg in 1 mL of 50 mM TRIS HCl/5 mM EDTA, pH 7.5). The biphasic mixture was sonicated for 30 min and then heated without capping at 40 °C until complete disappearance of the organic layer, obtaining a homogeneous brownish LMNP dispersion. LMNPs were purified by magnetic decantation and washed several times with freshly prepared sterile PBS (pII 7.4) buffer.

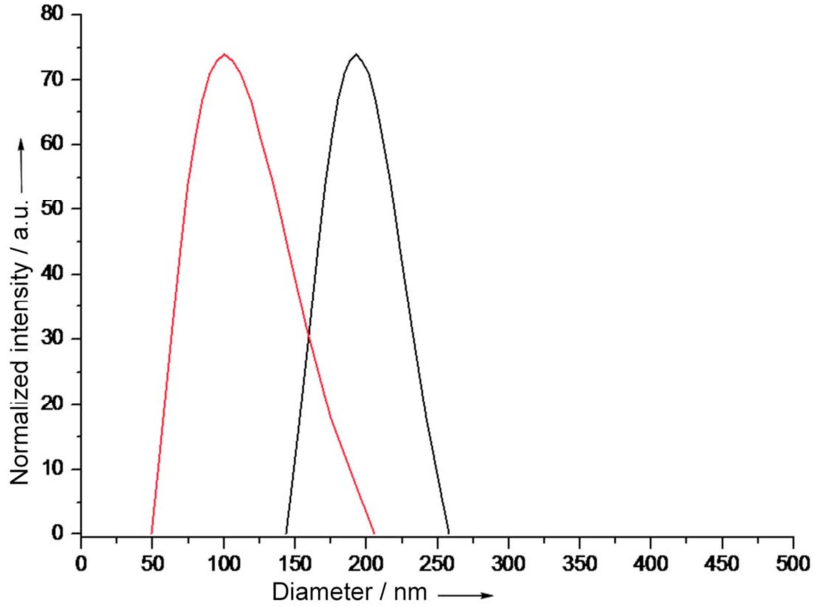

Figure S1. Hydrodynamic size distribution of LPS micelles (red line) and of purified LMNPs (black line) in PBS buffer obtained by DLS. The micelles were recovered in the supernatant solution after magnetic sequestration of LMNPs from the reaction mixture.

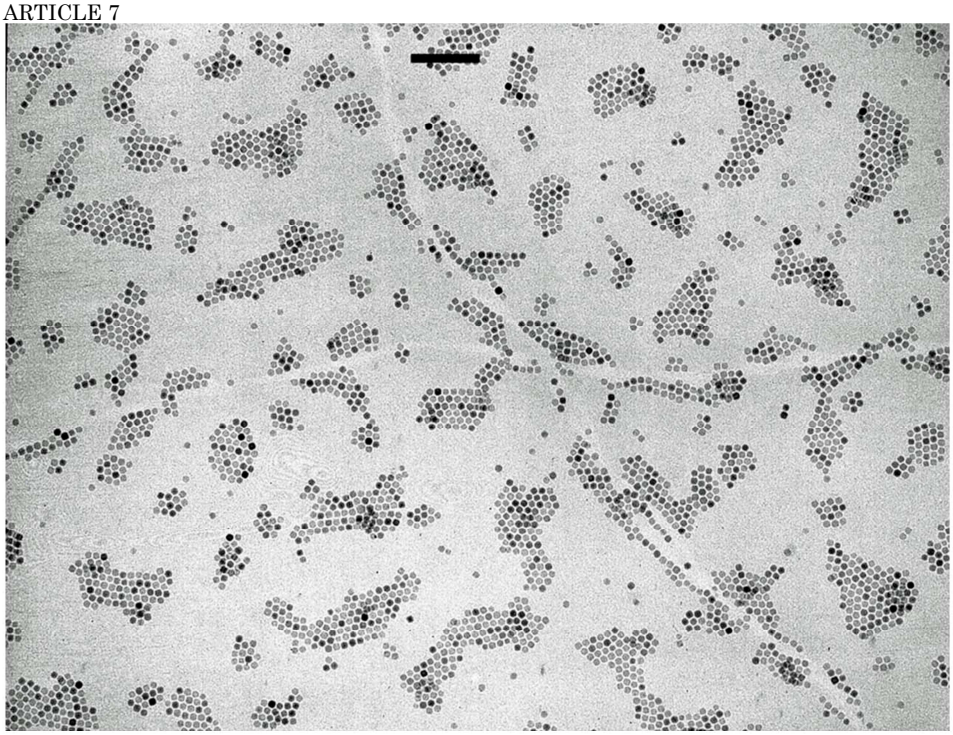

Figure S2. Wide view of TEM image of HBNPs. Bar = 100 nm.

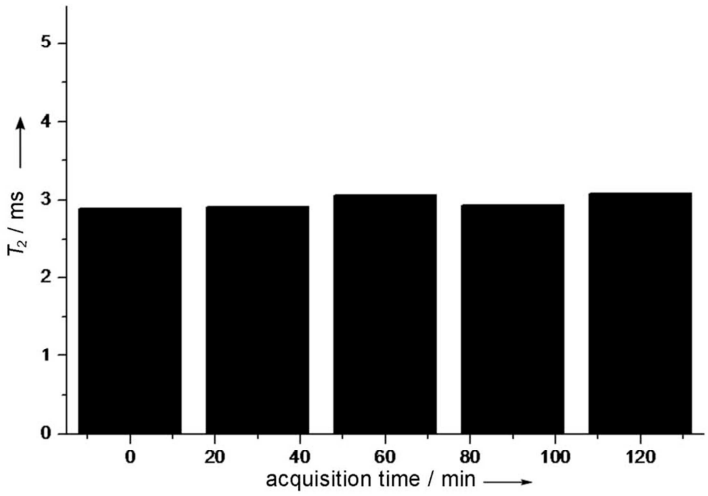

Figure S3. Time course of T_2 values of LMNPs (1.35 mM Fe) as measured by magnetorelaxometry.

HEK cell activation assay. 293/hTLR4A-MD2-CD14 cells and parental HEK, as negative control, have been purchased by Invivogen and cultured as described.[18] For cell activation assays, 293/hTLR4A-MD2-CD14 or parental HEK cells were grown to confluency in 96-well plates. Cell monolayers were washed twice with warm PBS and incubated 18 h at 37 °C, 5% CO_2, and 95% humidity in 200 µL DMEM supplemented with LMNP (from 0.0042 nM to 420 nM), and commercial LPS (from *E. coli* 055:B5, Sigma) as stimulus and hydrophilic magnetic nanoparticles (420 nM) as negative control. The final organic solvent (DMSO/ethanol) concentration per well is less then 0.5%. After the incubation, plates were centrifuged at 1000 rpm for 5 min and supernatants were collected. Activation of HEK cells was assessed by measuring the accumulation of extracellular IL-8 by ELISA according to supplier protocol (BD Clontech, Inc., Palo Alto, CA).

HEK-Blue™ assay. HEK-Blue™-4 cells (HEK-Blue™ LPS Detection Kit, InvivoGen) were cultured according to manufacturer's instructions. Briefly, cells were cultured in DMEM high glucose medium supplemented with 10% fetal bovine serum (FBS), 2 mM glutamine, 1X Normocin™ (InvivoGen), 1X HEK-Blue™ Selection (InvivoGen). HEK-Blue™-4 cells were detached by the use of a cell scraper and the cell concentration was estimated by using a counting cell. The cells were diluted in DMEM high glucose medium supplemented with DMEM high glucose medium supplemented with 10% fetal bovine serum (FBS), 2 mM glutamine, 1X Normocin™ (InvivoGen), 1X HEK-Blue™ Selection (InvivoGen) and 200 µL of cell suspension (20 000 cells) were added to each well. After 18 h incubation at 37 °C in a CO_2 incubator cells reached 80% confluency and supernatant removed, cell monolayers were washed twice with warm PBS without Ca^{2+} and Mg^{2+} and incubated 18 h at 37 °C, 5% CO_2, and 95% humidity in 200 µL DMEM supplemented with LMNP (from 0.0042 nM to 420 nM), and LPS_{agg} (from 0.025 nM to 25 nM, from Sigma-Aldrich) as stimulus and hydrophilic magnetic nanoparticles (420 nM) as negative control. The plate was incubated 18 h at 37 °C in a CO_2 incubator. LPS induce TLR4 pathway activation leading to alkaline phosphatase secretion. After the incubation, plates were centrifuged at 1000 rpm for 5 min and supernatants were collected. 5µL of each sample were added to 95 µL PBS, pH 8, 0.84 mM pNpp for a final concentration of 0.8 mM pNpp. Plates were incubated for 2 h in the dark at RT then the plate reading was assessed by using a spectrophotometer set on 505 nm.

DCs and macrophages.

Bone marrow cells from C57BL/ mice were cultured as previously described in: Granucci F, Vizzardelli C, Pavelka N, Feau S, Persico M, Virzi E, Rescigno M, Moro G, Ricciardi-Castagnoli P (2001). Inducible IL-2 production by dendritic cells revealed by global gene expression analysis. *Nat. Immunol.* **9**:882-8.

In vitro stimulation assay.

The day of the experiment, cells were seeded in 96-well plates at a concentration of 0.5×10^6 cells/mL in 200 µL of complete IMDM + GM-CSF (for BMDCs) or M-CSF (for BM-macrophages) in presence or absence of free LPS or LMNPs. After 18 h, TNF-α was measured in the colture supernatant.

TNF-α measurement. ELISA was performed with the DuoSet kits (R & D, Minneapolis, MN).

HEK-Blue™ inhibition assay. HEK-Blue™-4 cells were seeded in 96-well plate as described in the previous paragraph. After 18 h incubation media was removed, cell monolayer washed two times with pre-warmed PBS and 200 µL of DMEM supplemented with IAXO-101 (1-10 µM) were added. After 1 h incubation at 37 °C in a CO_2 incubator ± LMNPs (42 ng/mL) were added. After 18 h incubation at 37 °C and 5% CO_2 plates were centrifuged at 1000 rpm for 5 min and supernatants were collected. Quantification of alkaline phosphatase in the samples was performed as described in the previous paragraph.

MTT cell viability assay® (Sigma-Aldrich™). HEK-Blue™, 293/hTLR4A-MD2-CD14 cells were seeded at a density of 2×10^4 cells/mL in 100 µL medium (DMEM without red phenol) per well in 96-well-plate. LMNP was diluted with PBS and added to the cells to yield a final concentration of 420 nM. 24 h after incubation at 37 °C, the medium was removed, monolayer washed two times with warm PBS and 100 µL of DMEM without phenol red + 0.05 mg MTT was added per well. After 2 h incubation at 37 °C and 5% CO_2, formazan crystals were dissolved by adding 100 µL of MTT solubilization solution (anhydrous isopropanol 0.1 N HCl with 10% Triton X-100). Formazan concentration in the wells was determined measuring the absorbance at 570 nm. As positive control for cytotoxicity (C+), we set up triplicate wells containing cells treated with a compound known to be toxic to the cells.

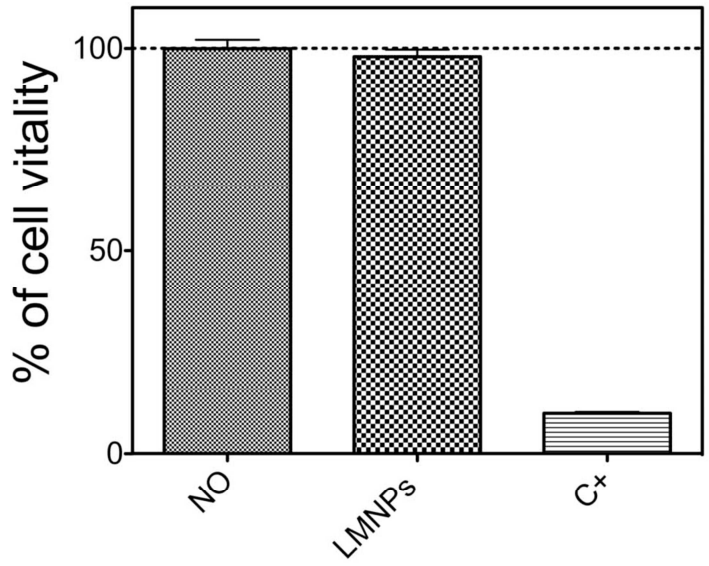

Figure S4. 293/hTLR4A-MD2-CD14 cells viability in presence of 4.2 µM of LMNP. As a positive control was used highly concentrated DMSO as a positive control (column C+).

HER2 Expression in Breast Cancer Cells Is Downregulated Upon Active Targeting by Antibody-Engineered Multifunctional Nanoparticles in Mice

Fabio Corsi,[†,∥] Luisa Fiandra,[†,∥] Clara De Palma,[†] Miriam Colombo,[†,‡] Serena Mazzucchelli,[†] Paolo Verderio,[‡] Raffaele Allevi,[†] Antonella Tosoni,[†] Manuela Nebuloni,[†] Emilio Clementi,[†,§] and Davide Prosperi[‡,⊥,*]

[†]Dipartimento di Scienze Cliniche "Luigi Sacco", Università di Milano, Ospedale L. Sacco, via G.B. Grassi 74, 20157 Milano, Italy, [‡]Dipartimento di Biotecnologie e Bioscienze, Università di Milano-Bicocca, piazza della Scienza 2, 20126 Milano, Italy, [§]Istituto Scientifico Eugenio Medea, 23842 Bosisio Parini, Italy, and [⊥]Laboratorio di Biofisica e Nanomedicina, Polo Tecnologico, Fondazione Don Gnocchi IRCCS-ONLUS, 20148 Milan, Italy. [∥]These authors contributed equally to the research.

ABSTRACT Subcellular destiny of targeted nanoparticles in cancer cells within living organisms is still an open matter of debate. By *in vivo* and *ex vivo* experiments on tumor-bearing mice treated with antibody-engineered magnetofluorescent nanocrystals, in which we combined fluorescence imaging, magnetic relaxation, and trasmission electron microscopy approaches, we provide evidence that nanoparticles are effectively delivered to the tumor by active targeting. These nanocrystals were demonstrated to enable contrast enhancement of the tumor in magnetic resonance imaging. In addition, we were able to discriminate between the fate of the organic corona and the metallic core upon cell internalization. Accurate immunohistochemical analysis confirmed that hybrid nanoparticle endocytosis is mediated by the complex formation with HER2 receptor, leading to a substantial downregulation of HER2 protein expression on the cell surface. These results provide a direct insight into the pathway of internalization and degradation of targeted hybrid nanoparticles in cancer cells *in vivo* and suggest a potential application of this immunotheranostic nanoagent in neoadjuvant therapy of cancer.

KEYWORDS: magnetic nanoparticles · breast cancer · tumor targeting · imaging · ligand–receptor recognition · theranostic agent

A primary goal in cancer diagnostics is to develop molecular contrast agents that identify the presence of a malignant tumor at early stages, track possible migration of tumor cells, and monitor tumor response to surgical or pharmacological treatments.[1−3] The diagnosis of axillary localization of breast cancer metastases is at present essentially based on highly invasive and seldom conclusive detection methods, often requiring the sentinel lymph node dissection.[4] In this context, a primary challenge is the design of new tools allowing easy, reliable, and noninvasive identification of lymph node metastases. A possible strategy resides in the development of new target-specific multifunctional tracers capable of optimizing breast cancer diagnosis *in vivo* by combining low-invasive fluorescence techniques and magnetic resonance imaging (MRI).[5] In the past decade, nanotechnology has provided new tools in this direction. In particular, the development of a new generation of multifunctional hybrid organic/inorganic nanomaterials, including iron oxide nanoparticles, held great promises for diagnosis and treatment of malignant tumors.[6,7]

A broad range of new synthetic strategies for iron oxide nanoparticles have been reported, enabling fine-tuning of size, shape, and magnetic properties.[8] Recently, novel biofunctionalization approaches have been successfully attempted to improve the nanoparticle stability in physiological media and to gain a control on tight immobilization, distribution, and suitable orientation of target ligands on the nanoparticle surface, which is essential for optimizing the targeting efficiency toward cell receptors.[9−12] Several *in vivo* studies have demonstrated the potential of targeted iron oxide nanoparticles as local enhancers of MRI contrast, and the first clinical trials conducted on patients bearing metastatic lymph nodes have provided promising perspectives.[13,14] From these studies, a crucial point has emerged and still needs to be thoroughly examined, that is, the targeting mechanisms and the fate of the different components of hybrid nanoparticles when they have reached their final destination. Although a few investigations have provided important data with cell cultures,[15] the molecular features of the interaction of hybrid nanoparticles with cells and tissues *in vivo* remain unexplored. In

* Address correspondence to davide.prosperi@unimib.it.

Received for review April 29, 2011 and accepted July 26, 2011.

Published online July 26, 2011
10.1021/nn201570n

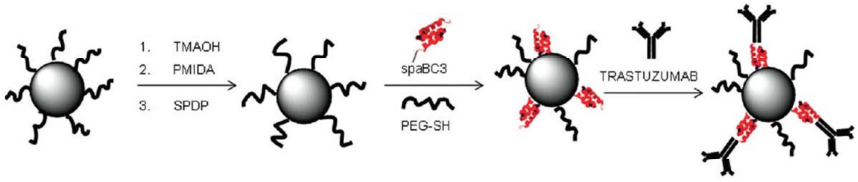

Scheme 1. Step sequence for the preparation of TMNC.

particular, it is still a matter of debate whether functionalization with homing ligands is able to guide nanoparticles to the tumor by active targeting also in living organisms, or nanoparticle delivery is rather mediated by passive transport *via* opsonization and/or macrophage incorporation.[16,17]

Recently, we have designed a versatile molecular nanohybrid suitable for site-specific immobilization of antibodies.[18] This nanocomplex was a magnetite nanocrystal conjugated with a recombinant low molecular weight monodomain of protein A, which exhibited a strong affinity for human and rabbit IgG molecules. Magnetic nanocrystals conjugated to the commercial anti-HER2 monoclonal antibody trastuzumab (TMNC) were demonstrated to be effective in selectively recognizing the "human epidermal growth factor receptor 2" (HER2) expressed in MCF-7 breast cancer cells in cultures. HER2 is a membrane tyrosine kinase receptor belonging to the family of the erbB and is overexpressed in 25−40% of human mammary carcinomas. HER2 regulates cell growth, adhesion, migration, and cell differentiation and is referred to as an "orphan" receptor because no known endogenous ligand has yet been identified.[19,20]

In the present work, we have improved the preparation of TMNC for *in vivo* application, allowing us to carry out a careful investigation of their targeting efficiency and biodistribution by combining MRI monitoring, highly sensitive epifluorescence tracking of TMNC in Balb/c nude mice bearing MCF-7 cells, and accurate tissue analyses. The results we are presenting here provided a new insight into the fate of the individual components of the hybrid nanocomposites once they reached the target cells *in vivo*. In order to track the organic moiety separately from the metal core, we preferred to label only trastuzumab (Tz) with AlexaFluor660 (AF660), rather than making the nanoparticle entirely fluorescent.

Due to the targeting efficiency of antibodies, IgG-functionalized nanoparticles have found broad interest for application in cancer diagnosis and as carriers of chemotherapeutic agents for the treatment of malignant tumors.[21−23] A further aim of this work was to investigate the potential of TMNC as a neoadjuvant agent for combination therapy of breast cancer exploiting the attitude of Tz to inhibit the signaling processes triggered by HER2 overexpression.

RESULTS AND DISCUSSION

Optimization of TMNC Synthesis for *In Vivo* Studies. The original procedure for the synthesis of TMNC involved a nanocrystal controlled nucleation and growth by solvothermal decomposition in the presence of oleic acid followed by ligand exchange with *N*-phosphonomethyl iminodiacetic acid phosphonate (PMIDA), which led to a dispersion soluble in the aqueous phase. The ligand was modified by condensation with 2,2′-(ethylenedioxy)bis(ethylamine) (EDBE) and further functionalized with *N*-succinimidyl-3-[2-pyridyldithio]propionate (SPDP). The resulting thiol-reactive PDP functionalities were exploited for the conjugation with a recombinant Cys_3-ended single-domain variant of protein A (spaBC3), capable of capturing IgG molecules by strong binding with their Fc fragment.[18] SpaBC3 allowed for the tight immobilization of Tz in the optimal orientation for binding to HER2. TMNC proved to be long-term stable in several buffered media and thus suitable for studies with cell cultures. However, when we explored the possibility of using TMNC for intravenous administration, they invariably showed a tendency to accumulate at the mouse tail, in correspondence to the site of injection. After having thoroughly checked each step of the synthetic procedure in terms of particulate stability, we found that the critical step was the ligand exchange. Hence, we improved the phase transfer by an intermediate reaction with tetramethylammonium hydroxide (TMAOH), which led to the same final antibody nanocomplex dramatically reducing the TMNC localization at the site of injection, as it was capable of diffusing quickly in the bloodstream. The complete sequence is reported in Scheme 1. Next, Tz was cross-linked to spaBC3 with glutaraldehyde to enforce the antibody grafting to the nanoparticle, which unfortunately resulted in particle aggregation. Thus, we evaluated the spontaneous release of Tz labeled with AF660 from TMNC in serum to assess the tightness of Tz−spaBC3 binding under physiological conditions, and we did not find any traces of released Tz after 1 week at 37 °C. Hence, we decided to utilize the optimized TMNC for the *in vivo* studies.

HER2-Positive Tumor Imaging with AF660-TMNC. MCF-7 breast cancer cells were grown subcutaneously in Balb/c nude mice. Once the tumor reached the size of approximately 1 cm of diameter, 5 μg/g body weight of AF660-TMNC was injected in mice by the tail vein,

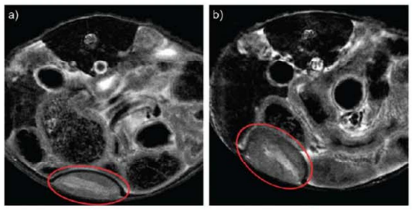

Figure 1. Monitoring of TMNC uptake *in vivo* by MRI. The axial T_2-weighted MR images have been obtained from MCF-7 tumor-bearing mice (a) before and (b) 24 h after the injection of nanocrystals. The images, obtained by a T_2-mapping sequence, were acquired at 32.2 ms echo time.

and their localization in the MCF-7 tumor was monitored 24 h after injection by MRI to assess their potential as targeted contrast agent for the detection of HER2-positive breast cancer cells *in vivo*. T_2-weighted axial images of a tumor-bearing mice acquired preinjection (Figure 1a, control) and 24 h postinjection (Figure 1b) of TMNC exhibited an increase in negative contrast in correspondence to MCF-7 xenograft (red circle) caused by nanocrystal accumulation at the tumor. A remarkable decrease in T_2^* maps was also observed in the tumor region at 24 h (Figure S2 in Supporting Information). To confirm the specificity of targeting after antibody conjugation, control MRI images were acquired with PEG-coated MNCs (Figure

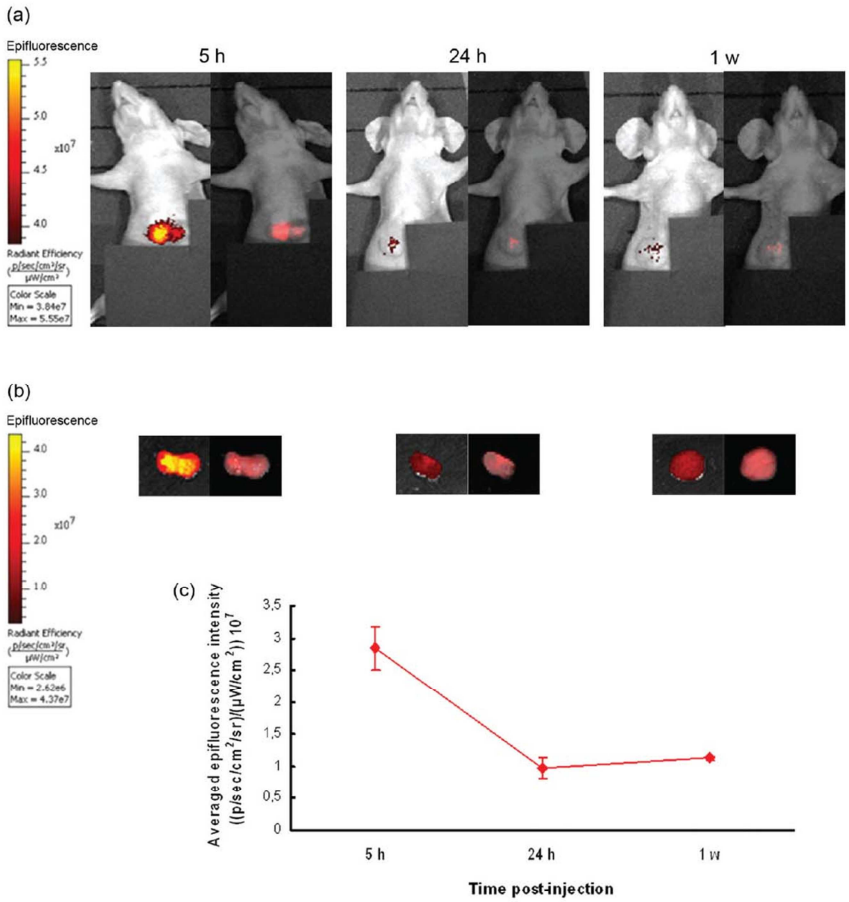

Figure 2. CCD camera images of mice bearing MCF-7 xenografts (a) and of the isolated tumors (b) at 5 h, 24 h, and 1 week postinjection of AF660-TMNC. Epifluorescence intensity images and spectrally unmixed fluorescence images are reported on left and right, respectively. (c) Averaged epifluorescence intensity of isolated tumors. Mean ± SE of three different samples for each experimental time.

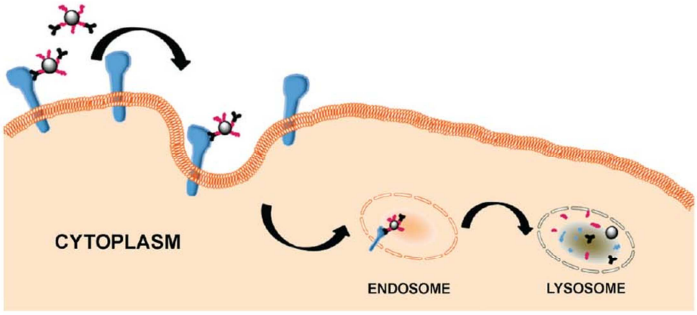

Scheme 2. Mechanism of TMNC internalization and degradation in HER2-positive MCF-7 cells. In a first step, TMNC binds to HER2 membrane receptors, inhibiting homodimer formation. Next, the TMNC−HER2 complex formation triggers the local membrane invagination, followed by the complex incorporation within internal early endosomes, which evolve in late endosomes and, eventually, in lysosomes, where the organic corona is rapidly degraded. This process results in a reduced surface expression of HER2 receptor.

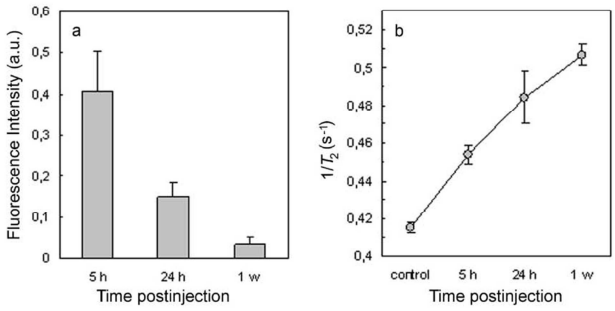

Figure 3. Fluorescence intensity (a) and inverse relaxation time (b) of MCF-7 lysates, at 5 h, 24 h, and 1 week postinjection of AF660-TMNC. Mean ± SE of three different samples.

S3). Next, epifluorescence (Epf) images of supine mice, obtained with a CCD camera (IVIS Lumina II, Calipers Life Sciences, UK) at 5 h, 24 h, and 1 week after injection, confirmed the capability of AF660-TMNC to target the HER2-positive tumors (Figure 2a). The maximal Epf emission in xenografts was observed at 5 h, while the signal intensity in the tumor unexpectedly decreased after 24 h. *Ex vivo* analysis of Epf in isolated tumors confirmed the maximal signal intensity at the shorter time of exposure (Figure 2b), as also indicated by the averaged Epf intensity, reported in Figure 2c as the mean value from three different tumors for each experimental condition. The drop in Epf was initially attributed to the surface-weighted properties of Epf imaging, which usually allows for an optimal detection sensitivity but is strongly limited by the short penetration depth of photons, which is dependent on diffusion time, as previously observed.[24] Nevertheless, we could not exclude that the fall of fluorescence observed by CCD images could, at least partially, reflect the degradation of the organic corona, subsequent to the receptor-mediated TMNC internalization. Indeed, the metabolization of the organic moiety, including the fluorochrome, associated with the saturation of membrane HER2 receptors, could cause an overall fluorescence decrease. This hypothesis is supported by previous evidence that one possible mechanism, by which Tz inhibits the tumor development, involves HER2 downregulation mediated by the rapid degradation of the Tz−HER2 complex upon endocytosis.[25] Such a postulated mechanism suggested that TMNC was likely to be directed to lysosomal degradation *via* receptor-mediated endocytosis triggered by formation of the Tz−HER2 complex (Scheme 2). In a recent study, Wuang *et al.* observed that the internalization of Tz-modified nanoparticles in HER2-positive breast cancer cells could be prevented by treatment with excess free Tz, which corroborates the assumption that the nanoconjugate endocytosis could be receptor-mediated.[26] Therefore, within our model, we predicted that fluorescence signal associated with the presence of Tz in TMNC would rapidly decrease, while in contrast, iron oxide would progressively accumulate inside the tumor tissue. Further investigations were needed to assess the reliability of our interpretation.

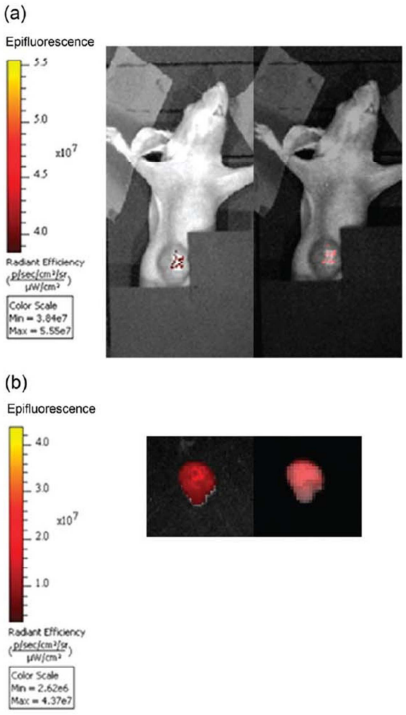

Figure 4. CCD camera images of a MDA-bearing mouse (a) and of the isolated MDA tumor (b) at 5 h postinjection of AF660-TMNC. Epifluorescence intensity images and spectrally unmixed fluorescence images are reported on left and right, respectively.

Mechanism of TMNC Incorporation in MCF-7 Cells. Spectrofluorimetric assays performed on lysates of the same tumors analyzed by the CCD camera provided support to the latter interpretation, as tissue depth was not an issue in this case. Fluorescence intensity, normalized to the overall mass of proteins in each lysate, once again was maximal at 5 h and progressively decreased over time (Figure 3a). The same samples were also analyzed by magnetic relaxation measurements to assess the relative amount of iron due to the presence of magnetic nanocrystals incorporated in the tumor tissue. Magnetic relaxometry shares the same basic principle with MRI but exhibits several advantages in semiquantitative determinations, including (1) higher sensitivity, (2) it enables a direct measurement of the magnetic power of a sample, and (3) image deconvolution is not needed, which in some cases may cause artifacts. As a matter of fact, most studies making use of MRI for semiquantitative analysis require whole-body perfusion to eliminate blood interferences.[24] However, we were interested in investigating the nanoparticle distribution under normal blood flow conditions, which

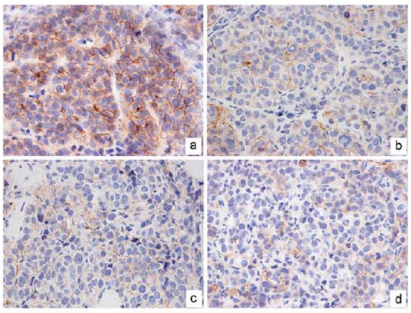

Figure 5. Immunohistochemistry of tumor section extracts before (a) and after treatment with TMNC (b–d). Samples were incubated with antibody rabbit anti-human c-erb-2 oncoprotein (1:1000 dilution, DakoCytomation), 2 h incubation. (a) Strong and diffuse membrane c-erb-2 immunostaining (score 3+) in all of the neoplastic cells. (b–d) No c-erb-2 expression is recovered in most of the neoplastic elements, with only a few c-erb-2-positive cells with diffuse (panel b, score 2+) or focal (panels c and d, score 1+) weak pattern of distribution in the tumor at 5 h, 24 h, and 1 week, respectively. Hematoxylin counterstaining, OM 40×.

better reproduces the dynamic behavior of the individual parts of a functioning organism. As each type of tissue from different organs is differently perfused, a broad variability in the intrinsic transverse relaxation should be expected from one organ to another.[27] Hence, to appreciate the impact of TMNC accumulation in a particular tissue, the detected T_2 values were compared with the respective averaged readout signal of the same tissue from untreated mice (control). A relevant amount of TMNC in the MCF-7 tumor at 5 h postinjection was inferred by the increase in $1/T_2$ of this sample, remarkably higher than the control. The gradual increment in $1/T_2$ over time was an index of the progressive accumulation of iron in the tumor and confirmed that TMNC was incorporated by MCF-7 cells and forwarded to the degradation pathways (Figure 3b).

To corroborate our observation that the drop of fluorescence in the tumor was actually due to the degradation of the nanocomplex inside the cells and to obtain a more accurate quantification of nanocrystals in the tumor, we repeated the experiment with perfused mice, where blood supply was absent. Spectrofluorimetric and relaxometric analyses of tumor lysates are reported in Supporting Information (Figure S4).

Active Targeting or Passive Delivery? As a final confirmation that the *in vivo* localization of TMNC in MCF-7 tumors was actually due to an active targeting mediated by its specific interaction with HER2 receptors, we investigated the localization of injected nanocrystals in mice bearing HER2-negative MDA cells. This tumor model was previously validated as a negative control for TMNC specificity in cell cultures.[18] The localization of AF660-TMNC was determined 5 h after injection, which corresponded to the time of maximal fluorescence in

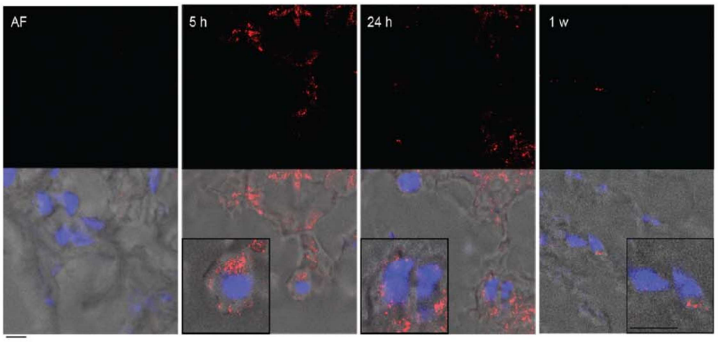

Figure 6. Confocal laser scanning micrographs (single optical sections) of cryosections obtained from MCF-7 tumors at 5 h, 24 h, and 1 week postinjection of AF660-TMNC, and then counterstained with DAPI for nuclei detection. Autofluorescence sample (AF) is a MCF-7 tumor from noninjected mice. The confocal images of nanocrystals (red) have been overlaid on the corresponding bright-field images reporting nuclei (blue). A high magnification of representative cells can be observed in the insets. Scale bars = 10 μm.

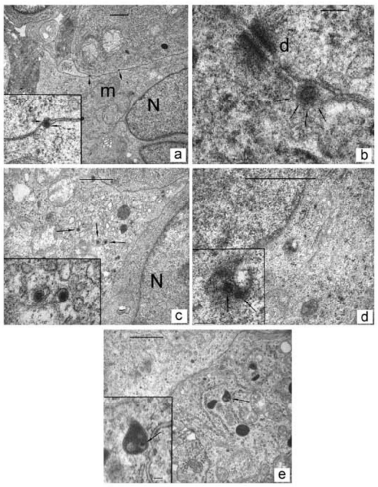

Figure 7. TEM images of MCF-7 tumors isolated at 5 h (a,b), 24 h (c,d), and 1 week (e) postinjection of AF660-TMNC. At 5 h, (a) two nanocrystals (arrows) are interposed between the membranes of two adjacent cells. At a higher magnification (inset), it is evident the close interaction of nanocrystal with membrane (arrows), which invaginates at the binding site level (b). At 24 h, nanocrystals are compartmentalized (arrows) in endosomes (c) and lysosomes (d) and, after 1 week, only in lysosomes (e): m, mitochondria; N, nucleus; d, desmosome. Scale bars = 1 μm (a,c,d,e), 100 nm (b and insets).

MCF-7 tumors. *In vivo* and *ex vivo* CCD camera observations of MDA xenografts (Figure 4a,b) showed a very weak Epf in this cancer model compared to MCF-7, and the averaged Epf intensity of the isolated MDA tumor was significantly lower ($P < 0.05$ by Student's *t*-test) than that measured in MCF-7 tumors, although the biodistribution of TMNC in the two experimental models was comparable (Figures S5 and S6). Moreover, the fluorescence intensity of MDA lysate was one-fifth the value measured in MCF-7 lysates in one of the three tumors analyzed, while in the supplementary two samples was below the detection limit.

Immunohistochemical Analysis of HER2 Expression in Tumor Tissues. Whereas it is well-known that HER2 overexpression is essentially a result of erbB2 gene amplification, it has recently been recognized that erbB2 levels are also regulated on the protein level.[28] To assess the extent of residual receptor expression after treatment of diseased mice with TMNC, we performed an immunohistochemical analysis of tumor tissues drawn at the same time stages of the other experiments. In the absence of TMNC (Figure 5a), we observed a diffuse and strong membrane staining in more than 60% of the neoplastic cells (immunohistochemical score, IHC, +++). At 5 h after TMNC injection (Figure 5b), most of the neoplastic cells were c-erb-2-negative or had a weak and incomplete membrane staining (IHC+). Only a small percentage of the neoplastic elements were scored as c-erb-2 IHC++ (weak yet complete membrane staining). At 24 h and 1 week (Figure 5c,d, respectively), the tumor had a reduced c-erb-2 expression: in these samples, only a minimal residual amount of c-erb-2-positive cells was recovered (IHC+). These results confirm the direct involvement of HER2 in the mechanism of TMNC internalization and suggest a potential application of TMNC in immunoadjuvant or even neoadjuvant therapy exploiting their capability to interfere with HER2-mediated signaling.[29]

Fate of Captured TMNC in MCF-7 Cells. A confocal microscopy examination of tumor cryosections indicated that AF660-TMNC came into contact with the plasma membrane of cells to be subsequently internalized. Figure 6, reporting a single *z*-plane in the cells, in which nuclei are focused, shows that TMNC was interacting with cell surface at 5 h. An intense fluorescence signal

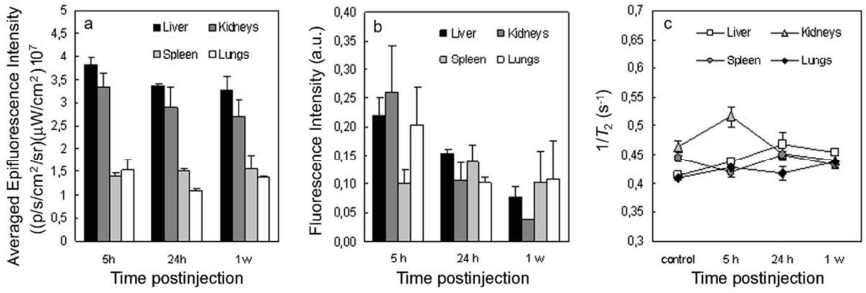

Figure 8. Averaged epifluorescence intensity of isolated liver, kidneys, spleen, and lungs (a), and fluorescence intensity (b) and inverse relaxation time (c) of organ lysates at 5 h, 24 h, and 1 week postinjection of AF660-TMNC. Mean ± SE of three different samples for each experimental time.

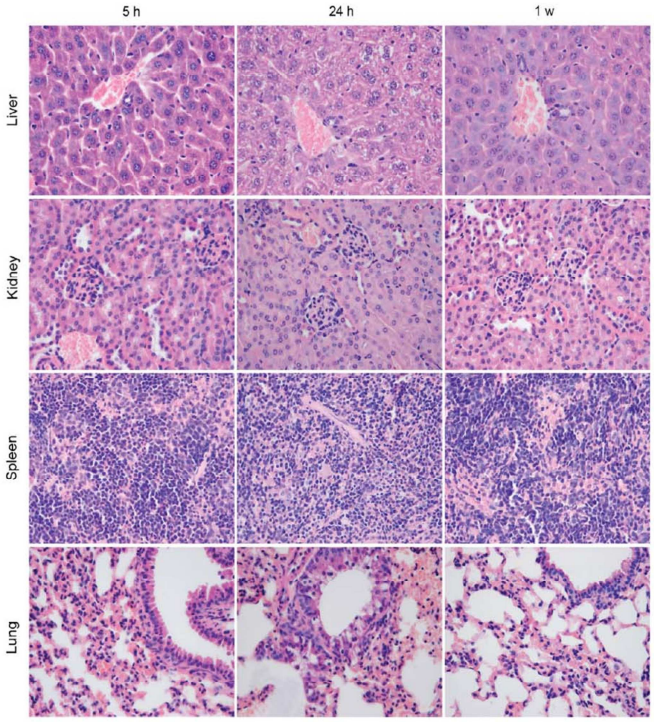

Figure 9. Histopathological analysis of tissue samples. No histological lesions in liver, kidneys, and spleen. A mild inflammatory interstitial infiltrate in all lung samples; a mild hyperplastic reaction of the bronchial epithelium is observed in 24 h lung sample (center of the figure). Hematoxylin-eosin, OM 20×.

was observed in correspondence with the cells, and the staining was mainly localized at the membrane level, as evidenced in the high-magnification image of a single cell cross section. Within 24 h, TMNC was endocytosed by tumor cells, as indicated by the presence of labeled spots deep in the cytoplasm and nearby the nucleus. Fluorescence intensity appeared strongly reduced in tumors isolated after 1 week, where only rare spots were still detectable in close proximity to the nucleus. TEM images provided compelling evidence that TMNC was captured by the plasma membrane of MCF-7 cells within the first 5 h (Figure 7a) followed by membrane invagination, which likely reflects the binding to the target receptors activating the process of

internalization (Figure 7b). After 24 h, TMNC was recovered inside the cytoplasm, compartmentalized in endosomes (Figure 7c) and lysosomes (Figure 7d), suggesting that it was subjected to a typical endocytic pathway upon incorporation by the cell.[30] The presence of TMNC in lysosomes clearly indicates that the degradation of nanocomplexes began within the first 24 h from their injection, thus justifying the drop in fluorescence observed in intact tumors and lysates at this time of exposure. The degradation process progressed over the following days, as indicated by the presence of nanocrystals only in lysosomes after 1 week (Figure 7e).

Analysis of Biodistribution of TMNC in Tumor-Bearing Mice. To evaluate the biodistribution of injected TMNC in mice, some model organs have been monitored by a CCD camera as described above for extracted tumors. The Epf images of liver, kidneys, spleen, and lungs were determined 5 h, 24 h, and 1 week after AF660-TMNC injection. The averaged Epf intensities for each imaged organ (Figure S6) are represented in Figure 8a. Epf intensity was remarkably higher in liver and kidneys, and a detectable tendency to decrease over time in these two organs was apparent.

A more quantitative assessment of TMNC in each individual organ was performed by measuring the fluorescence intensity of lysates. A comparison between the different organs was possible by normalizing the fluorescence values to the total protein content (Figure 8b). The results obtained confirmed a preferential distribution of TMNC in liver and kidneys after 5 h, and an appreciable fluorescence was also recovered in lungs, although no significant labeling was observed in *ex vivo* imaging, probably due to a deeper penetration of labeled nanocrystals in this tissue. Moreover, Figure 8b clearly shows the progressive decrease of intensity in liver and kidneys: after 1 week from TMNC injection, the fluorescence intensity of liver and kidneys was reduced to about one-third and one-fifth, respectively, of the values recorded at 5 h. A relaxometric analysis of the same organ lysates confirmed that nanocrystals were present in liver and kidneys at 5 h postinjection detected as an increase in $1/T_2$ compared to the respective controls (Figure 8c). On one hand, the increase over time in the liver of magnetically active content owed to the metal core combined with the decrease in fluorescence intensity associated with the bioorganic corona suggests that TMNC was internalized and decomposed by this organ exploiting its detoxification role.[31,32] On the other hand, the gradual decrease of $1/T_2$ values in the kidneys follows the drop of Epf intensity in these organs. This effect might be interpreted as the result of TMNC excretion, in contrast with previous observations that a size limit of 5−10 nm is allowed for particle excretion by the kidneys.[33] A possible explanation could be that TMNC were provisionally captured by the kidneys while being delivered down the blood flow, until they reached their final destination at the tumor site or in the liver. Alternatively, the gradual dissolution of the particles could result in another iron phase with different magnetic properties, therefore leading to different NMR contrast. Whatever the actual interpretation, TMNC did not accumulate in the kidneys for a long time. According to the T_2 values measured in spleen and lung lysates (Figure 8c), we can assume that iron content was detectable in lungs at 5 h and exhibited only small variations over the experimental time. This result is in agreement with previous studies describing distribution of intravenously injected nanoparticles in lungs.[34,35] On the other hand, the metal appeared surprisingly undetectable in the spleen.

This behavior was confirmed also with perfused mice, demonstrating that this effect could not be attributed to paramagnetic inhomogeneities from circulating blood (Figure S7).

Assessment of TMNC Toxicity. In order to investigate the possible toxic effects of TMNC on nontarget organs,[36] we performed a histopathological examination of liver, kidneys, spleen, and lungs isolated 5 h, 24 h, and 1 week after TMNC injection (Figure 9). No histological lesions were found in liver, kidneys, and spleen at all observed times. Lung tissues were characterized by a focal and mild inflammatory infiltrate localized at the interstice. Bronchi were spared except for samples at 24 h, in which an early hyperplastic reaction of the epithelium was observed. This acute alteration was transitory and regressed within a few days. Samples at 1 week exhibited no traces of lesions.

TMNC safety has been also verified by investigating liver and kidney functionalities in serum (Table S1). Dosage of aspartate transaminase (AST), alanine transaminase (ALT), urea, and creatinine was performed by specific commercial assay kits (BioAssay Systems, USA). An apparent alteration of renal and hepatic functionality was observed in the first 5 h, but it was completely restored within the following 24 h.

CONCLUSION

In summary, we have synthesized a PEGylated hybrid magnetic nanoparticle functionalized with fluorescently labeled trastuzumab (TMNC) with a control on the antibody orientation on the nanoparticle surface to optimize the targeting efficiency. These nanoparticles proved to be highly effective in selectively targeting HER2-positive breast cancer cells *in vivo* and thus are expected to have potential for monitoring metastatic lymph nodes. A multifaceted bioanalytical approach, combining fluorescence, magnetic relaxivity, transmission electron microscopy, and histological experiments *in vivo* and *ex vivo*, has demonstrated that TMNC (1) prevalently accumulated at the tumor by active targeting and at the liver after an initial broad distribution, (2) was endocytosed by the cells of tumor tissues

following a lysosomal pathway of degradation, and (3) did not result in permanent damage of healthy tissues, although an initial bronchial inflammation was recovered, which will need further investigation in the future. Our results suggest that TMNC is internalized by HER2 receptor-mediated endocytosis, leading to the capture of the TMNC–HER2 complex by lysosomes, followed by rapid degradation of the bioorganic corona, while the inorganic core is expected to be more slowly decomposed. Most importantly, this work highlights the necessity of using different approaches for nanoparticle tracking *in vivo*, as we have demonstrated that organic fluorophores utilized for fluorescent labeling of immobilized biomolecules could be rapidly metabolized upon internalization of the TMNC–HER2 complex, while metal components of nanoparticles kept accumulating in the tumor. Immunohistochemical analysis has provided evidence that TMNC was able to saturate HER2 monomers expressed on cell surface of the tumor tissue, thus eliciting the rapid receptor degradation, which is expected to strongly interfere with signaling processes promoted by this receptor. This behavior paves the way to explore the potential of TMNC as an immunotheranostic agent, which might find application in presurgical neoadjuvant treatments. The *in vivo* molecular approach described here may provide a new perspective in the design of the next generation of multifunctional nanohybrid systems for biomedical application.

MATERIALS AND METHODS

TMNC Production. Magnetic nanocrystals (MNCs) were synthesized and functionalized with an individual B domain of protein A (spaBC3), as described in our previous work with modifications.[18] Briefly, 8 nm iron oxide nanoparticles coated with oleic acid dissolved in chloroform (84 mg, 4.3 mL) were diluted with chloroform (20 mL) and were treated with an aqueous solution of tetramethylammonium hydroxide (TMAOH, 2.4 g in 80 mL) overnight under vigorous stirring at room temperature.[37] The organic solution containing the surfactant was removed by centrifugation at 1000*g* (3 min). The aqueous solution of TMAOH-coated MNC was mixed with 0.1 M *N*-phosphonomethyl iminodiacetic acid phosphonate (PMIDA, 500 mg) dissolved in an aqueous ammonia solution in order to promote ligand exchange. Carboxyl groups onto the surface of the resulting nanoparticles were converted into amine ends by reaction with the bifunctional diamino linker 2,2′-(ethylenedioxy)bisethylamine (EDBE, 284 μL) *via* *N*-(3-dimethylaminopropyl) *N*-ethylcarbodiimide hydrochloride (EDC, 16.2 mg) activation. *N*-Succinimidyl-3-[2-piridyldithio]propionate (SPDP, 4.3 mg) dissolved in dry DMSO (0.75 mL) was conjugated to MNC *via* NHS ester. The resulting thiol-reactive nanoparticles (1 mg) were incubated in the presence of spaBC3 (0.5 mg), obtaining the binding of 0.1 mg of spaBC3. The amount of spaBC3 bound was determined by protein quantification of supernatants. The remaining PDP functional groups were saturated with excess PEG_{500}-SH. Trastuzumab was labeled with AlexaFluor660 dye (Invitrogen, Carlsbad, CA) according to manufacturer's protocol. Trastuzumab conjugation on nanoparticles was performed by incubating nanoparticles (1 mg) at room temperature for 2 h in the presence of labeled Trastuzumab (0.3 mg), obtaining the binding of 0.1 mg of Tz. The amount of Tz bound was determined by protein quantification of supernatants.

Cell Culture and Xenograft Tumor Models. MCF-7 cells were grown in 50% Dulbecco's modified Eagle's medium (DMEM), 50% F12 (EuroClone Celbio, Milan, Italy) supplemented with 10% (v/v) fetal bovine serum (Hyclone Celbio, Milan, Italy), L-glutamine (2 mM), penicillin (50 UI mL^{-1}), and streptomycin (50 mg mL^{-1}) at 37 °C under a humidified 95%:5% (v/v) mixture of air and CO_2. MDA-MD-468 was purchased by ATCC and cultured in Dulbecco's modified Eagle's medium supplemented with 10% (v/v) fetal bovine serum (Hyclone Celbio, Milan, Italy), L-glutamine (2 mM), penicillin (50 UI mL^{-1}), and streptomycin (50 mg mL^{-1}) in the same condition of growth. Eight week old female Balb/c nude mice were anesthetized by i.p. injection of 20 mg mL^{-1} of Avertin, and estrogen pellets were placed s.c. on the back of the mouse's neck by using a trocar. All tumor injections were done 2 days after this procedure. MCF-7 and MDA (10×10^6 cell for each animals) were suspended in growth medium and mixed with Matrigel high factor (BD, Biosciences) in 3:1 ratio and injected into mammary fat pad of Balb/C nude mice (Charles River). Animals were observed at least three times per week, and tumor formation was recorded; tumors were allowed to grow up to 7–10 mm in diameter before nanocomplex injection and imaging.

Magnetic Resonance Imaging. MRI experiments were performed on a 7-T Bruker Biospec 70/30 USR scanner, 30 cm horizontal bore (Bruker BioSpin, Ettlingen, Germany) equipped with a BGA12S (200 mT/m) gradient system and with a 35 mm quadrature volume coil for RF excitation and signal reception. Mice were anaesthetized with 1.5–2% isoflurane (60:40 N_2O/O_2 (vol/vol), flow rate 0.8 L/min). To detect the depth of anesthesia and the animal health condition during the MRI study, the respiratory rate and temperature were monitored by a pneumatic and rectal sensor, respectively. Animals were positioned on an animal bed equipped with a nosecone for gas anesthesia and a three-point-fixation system (tooth-bar and ear-plugs). A 3-orthogonal plane gradient echo tripilot scan was used as a geometric reference to locate the kidneys and the bladder, from which to choose the sections. T_2-weighted images (Coronal; RARE factor = 8, TR = 2 s, TE = 34.8 ms, inter echo time = 11.6 ms, FOV = 4 × 3.4 cm^2, data matrix 300 × 256, slice thickness = 1 mm, trigger on with respiration gate = 2 s, NA = 8) were acquired to visualize anatomical details (liver, kidneys, bladder, tumor). T_2*-weighted images (Coronal, Multi Gradient Echos, flip angle = 30°, TR = 800 ms, numbers of echoes = 4, first TE = 3 ms, echo spacing = 5 ms, FOV = 3 × 3 cm^2, data matrix 256 × 256, slice thickness = 1 mm, trigger on with respiration gate = 800 ms, NA = 1; axial; FLASH flip angle = 30°, TR = 350 ms, TE = 5.4 ms, FOV = 2.2 × 2.2 cm^2, data matrix 256 × 256, slice thickness = 1 mm, NA = 1) were acquired to visualize the susceptibility artifacts due to the presence of iron. To obtain T_2 and T_2* map, MSME and MGE sequences were carried out, respectively (MSME, axial, TR = 3.2 s, numbers of echoes = 20, echo spacing = 10.7 ms, FOV = 2.2 × 2.2 cm^2, data matrix 256 × 256, slice thickness = 1.5 mm, NA = 1; MGE, axial, flip angle = 30°, TR = 1.5 s, numbers of echoes = 18, first TE = 4 ms, echo spacing = 6 ms, FOV = 2.2 × 2.2 cm^2, data matrix 256 × 256, slice thickness = 1.5 mm, NA = 2). From these images, the tumor was manually segmented and maps were computed by the Paravision 5.1 Bruker software.

TMNC Injection and *In Vivo* and *Ex Vivo* Fluorescence Imaging. Mice were immobilized in a restrainer specifically designed for tail vein injections (2 biological instrument, Varese, Italy) and 250 μL of AF660-TMNC, 0.4 mg/mL was injected (5 μg/g body weight). Fluorescence imaging was performed on a IVIS Lumina II CCD camera (Calipers Life Sciences, UK) at 5 h, 24 h, and 1 week postinjection. Animals were anesthetized by i.p. injection of

20 mg mL^{-1} of Avertin and placed in CCD camera at 37 °C. Images were acquired with a Cy5.5 emission filter, while excitation was scanned from 570 to Cy5.5, and mice autofluorescence was removed by spectral unmixing. After *in vivo* acquisitions, mice were sacrificed, and dissected tumors and organs were analyzed with a CCD camera, as described above for the whole animals.

Confocal Microscopy of Cryosections. MCF-7 tumors were isolated and fixed in 4% paraformaldehyde solution for 3 h, washed in PBS, and embedded in OCT for freezing in liquid nitrogen. Ten micrometer thick tumor cryosections were air-dried at room temperature for 1 h, rinsed with PBS, and counterstained with DAPI (diluted 2:1000 in PBS 0.1% Saponin) for 20 min in the dark. After three washes in PBS, sections were mounted in ProLong Gold antifade reagent (Invitrogen) to be observed under a Leica TCS SPE confocal microscope (Leica Microsystems, Wetzlar, Germany). Confocal images were acquired at Fondazione Filarete, Milano, Italia.

Tissue Concentration of AF660-TMNC in Lysates. To obtain tissue samples, mice were sacrificed at different time points after injection with nanoparticles. For fluorescence intensity measurements, liver, spleen, kidney, and lung were excised, weighed, and homogenized with ultraturrax with homogenization buffer (0.32 M sucrose, 100 mM hepes, pH 7.4). The homogenate tissue lysates were centrifuged, and supernatant was resuspended in lysis buffer at a final concentration of 50 mM Tris, pH 7.4, and SDS 1% and incubated for 30 min at 4 °C on a rotator. The supernatant was used for bicinchonic acid (BCA, Pierce, CA) protein assay and for fluorescence measurement with GloMax Multi Detection System (Promega).

T_2 Measurements of Lysates. T_2 relaxation times were performed at a temperature of 313 K using a Bruker Minispec mq20 system (Ettlingen, Gerrmany) working with ^{1}H at 20 MHz magnetic field with the following parameters: Carr-Purcell-Meiboom-Gill pulse sequence, 1000 echoes with a 20 ms echo times and 2 s repetition time. Before T_2 measurements, lysates were diluted at a concentration of 1.5 mg mL^{-1} and introduced using 10 mm NMR spectroscopy tubes prewarmed at 40 °C. T_2 values were acquired after thermal equilibration.

Histopathological Analysis. Liver, kidneys, spleen, and lung samples obtained from Balb/c mice were fixed in 10% buffered formalin for at least 48 h and embedded in paraffin. Three micrometer sections were cut, stained with hematoxylin and eosin, and examined blindly.

Ultrastructural Analysis (TEM). Small portions of MCF-7 tumor samples were fixed in 2.5% glutaraldehyde in 0.1 M phosphate buffer, pH 7.2, for 2 h. After one rinsing with phosphate buffer, specimens were postfixed in 1.5% osmium tetroxide for 2 h, dehydrated by 70, 90, and 100% EtOH, and embedded in epoxy resin (PolyBed 812 Polysciences Inc., USA). Ultrathin sections were stained with uranyl acetate and lead citrate and examined by means of a transmission electron microscope (Zeiss EM109).

Immunohistochemistry. Three micrometer thick paraffin-embedded tissues were cut, deparaffinized in xylene, and rehydrated in ethanol. Microwave oven pretreatment was performed (pH 8.0, EDTA buffer, 2 × 5′). Immunohistochemistry was performed by using a polyclonal antibody rabbit anti-human c-erb-2 oncoprotein (1:1000 dilution, DakoCytomation, 2 h incubation). The reaction was revealed by means of supersensitive nonbiotin detection system (BioGenex) and diaminobenzidine as chromogen.

Acknowledgment. We thank A. Salvadè for help in cell analyses, I. Zucca for acquisition of MR images, E. Pesenti for mice perfusion, and E. Trabucchi for helpful discussions. This work was partly supported by "Assessorato alla Sanità", Regione Lombardia, and Sacco Hospital (NanoMeDia Project), the "Fondazione Romeo ed Enrica Invernizzi", and the Italian Association for Cancer Research. M.C. and S.M. acknowledge "Centro di Microscopia Elettronica per lo sviluppo delle Nanotecnologie applicate alla medicina" (CMENA, University of Milan) for doctoral and postdoctoral fellowships, respectively.

Supporting Information Available: TEM image of nanocrystals, T_2* maps, CCD camera images of organs and epifluorescence distribution. This material is available free of charge *via* the Internet at http://pubs.acs.org.

REFERENCES AND NOTES

1. Weissleder, R.; Pittet, M. J. Imaging in the Era of Molecular Oncology. *Nature* **2008**, *452*, 580–589.
2. de Vries, I. J. M.; Lesterhuis, W. J.; Barentsz, J. O.; Verdijk, P.; van Krieken, J. H.; Boerman, O. C.; Oyen, W. J. G.; Bonenkamp, J. J.; Boezeman, J. B.; Adema, G. J.; *et al.* Magnetic Resonance Tracking of Dendritic Cells in Melanoma Patients for Monitoring of Cellular Therapy. *Nat. Biotechnol.* **2005**, *23*, 1407–1413.
3. Evgenov, N. V.; Medarova, Z.; Dai, G.; Bonner-Weir, S.; Moore, A. *In Vivo* Imaging of Islet Transplantation. *Nat. Med.* **2006**, *12*, 144–148.
4. McMasters, K. M.; Tuttle, T. M.; Carlson, D. J.; Brown, C. M.; Noyes, R. D.; Glaser, R. L.; Vennekotter, D. J.; Turk, P. S.; Tate, P. S.; Sardi, A.; *et al.* Sentinel Lymph Node Biopsy for Breast Cancer: A Suitable Alternative to Routine Axillary Dissection in Multi-institutional Practice when Optimal Technique Is Used. *J. Clin. Oncol.* **2000**, *18*, 2560–2566.
5. Yang, L.; Peng, X.-H.; Wang, Y. A.; Wang, X.; Cao, Z.; Ni, C.; Karna, P.; Zhang, X.; Wood, W. C.; Gao, X.; *et al.* Receptor-Targeted Nanoparticles for *In Vivo* Imaging of Breast Cancer. *Clin. Cancer Res.* **2009**, *15*, 4722–4732.
6. Kim, J.; Piao, Y.; Hyeon, T. Multifunctional Nanostructured Materials for Multimodal Imaging, and Simultaneous Imaging and Therapy. *Chem. Soc. Rev.* **2009**, *38*, 372–390.
7. Riehemann, K.; Schneider, S. W.; Luger, T. A.; Godin, B.; Ferrari, M.; Fuchs, H. Nanomedicine—Challenge and Perspectives. *Angew. Chem., Int. Ed.* **2009**, *48*, 872–897.
8. Lu, A.-H.; Salabas, E. L.; Schüth, F. Magnetic Nanoparticles: Synthesis, Protection, Functionalization, and Application. *Angew. Chem., Int. Ed.* **2007**, *46*, 1222–1244.
9. Pellegrino, T.; Manna, L.; Kudera, S.; Liedl, T.; Koktysh, D.; Rogach, A. L.; Keller, S.; Radler, J.; Natile, G.; Parak, W. J. Hydrophobic Nanocrystals Coated with an Amphiphilic Polymer Shell: A General Route to Water Soluble Nanocrystals. *Nano Lett.* **2004**, *4*, 703–707.
10. Haun, J. B.; Devaraj, N. K.; Hilderbrand, S. A.; Lee, H.; Weissleder, R. Bioorthogonal Chemistry Amplifies Nanoparticle Binding and Enhances the Sensitivity of Cell Detection. *Nat. Nanotechnol.* **2010**, *5*, 660–665.
11. Kampmeier, F.; Ribbert, M.; Nachreiner, T.; Dembski, S.; Beaufils, F.; Brecht, A.; Barth, S. Site-Specific, Covalent Labeling of Recombinant Antibody Fragments *via* Fusion to an Engineered Version of 6-*O*-Alkylguanine DNA Alkyltransferase. *Bioconjugate Chem.* **2009**, *20*, 1010–1015.
12. Kumar, S.; Aaron, J.; Sokolov, K. Directional Conjugation of Antibodies to Nanoparticles for Synthesis of Multiplexed Optical Contrast Agents with Both Delivery and Targeting Moieties. *Nat. Protoc.* **2008**, *3*, 314–320.
13. Harisinghani, M. G.; Barentsz, J.; Hahn, P. F.; Deserno, W. M.; Tabatabaei, S.; van de Kaa, C. H.; de la Rosette, J.; Weissleder, R. Noninvasive Detection of Clinically Occult Lymph Node Metastases in Prostate Cancer. *N. Engl. J. Med.* **2003**, *348*, 2491–2499.
14. Memarsadeghi, M.; Riedl, C. C.; Kaneider, A.; Galid, A.; Rudas, M.; Matzek, W.; Helbich, T. H. Axillary Lymph Node Metastases in Patients with Breast Carcinomas: Assessment with Nonenhanced *versus* USPIO-Enhanced MR Imaging. *Radiology* **2006**, *241*, 367–377.
15. Jiang, W.; Kim, B. Y. S.; Rutka, J. T.; Chan, W. C. W. Nanoparticle-Mediated Cellular Response is Size-Dependent. *Nat. Nanotechnol.* **2008**, *3*, 145–150.
16. Chen, J.; Irudayaraj, J. Quantitative Investigation of Compartmentalized Dynamics of ErbB2 Targeting Gold Nanorods in Live Cells by Single Molecule Spectroscopy. *ACS Nano* **2009**, *3*, 4071–4079.
17. Peer, D.; Karp, J. M.; Hong, S.; Farokhzad, O. C.; Margalit, R.; Langer, R. Nanocarriers as an Emerging Platform for Cancer Therapy. *Nat. Nanotechnol.* **2007**, *2*, 751–760.
18. Mazzucchelli, S.; Colombo, M.; De Palma, C.; Salvadè, A.; Verderio, P.; Coghi, M. D.; Clementi, E.; Tortora, P.; Corsi, F.; Prosperi, D. Single-Domain Protein A-Engineered Magnetic Nanoparticles: Toward a Universal Strategy to Site-Specific Labeling of Antibodies for Targeted Detection of Tumor Cells. *ACS Nano* **2010**, *4*, 5693–5702.

19. Colombo, M.; Corsi, F.; Foschi, D.; Mazzantini, E.; Mazzucchelli, S.; Morasso, C.; Occhipinti, E.; Polito, L.; Prosperi, D.; Ronchi, S.; *et al.* HER2 Targeting as a Two-Sided Strategy for Breast Cancer Diagnosis and Treatment: Outlook and Recent Implications in Nanomedical Approaches. *Pharmacol. Res.* **2010**, *62*, 150–165.
20. Ménard, S.; Tagliabue, E.; Campiglio, M.; Pupe, S. M. Role of HER2 Gene Overexpression in Breast Carcinoma. *J. Cell Physiol.* **2000**, *182*, 150–162.
21. Yezhelyev, M. V.; Gao, X.; Xing, Y.; Al-Hajj, A.; Nie, S.; O'Regan, R. M. Emerging Use of Nanoparticles in Diagnosis and Treatment of Breast Cancer. *Lancet Oncol.* **2006**, *7*, 657–667.
22. Cheon, J.; Lee, J.-H. Synergistically Integrated Nanoparticles as Multimodal Probes for Nanobiotechnology. *Acc. Chem. Res.* **2008**, *41*, 1630–1640.
23. Chari, R. V. J. Targeted Cancer Therapy: Conferring Specificity to Cytotoxic Drugs. *Acc. Chem. Res.* **2008**, *41*, 98–107.
24. Bardhan, R.; Chen, W.; Bartels, M.; Perez-Torres, C.; Botero, M. F.; McAninch, R. W.; Contreras, A.; Schiff, R.; Pautler, R. G.; Halas, N. J.; *et al.* Tracking of Multimodal Therapeutic Nanocomplexes Targeting Breast Cancer *in Vivo*. *Nano Lett.* **2010**, *10*, 4920–4928.
25. Clifford, A.; Hudis, M. D. Trastuzumab—Mechanism of Action and Use in Clinical Practice. *N. Engl. J. Med.* **2007**, *357*, 39–51.
26. Wuang, S. C.; Neoh, K. G.; Kang, E.-T.; Pack, D. W.; Leckband, D. E. HER-2-Mediated Endocytosis of Magnetic Nanospheres and the Implications in Cell Targeting and Particle Magnetization. *Biomaterials* **2008**, *29*, 2270–2279.
27. Mahmoudi, M.; Hosseinkhani, H.; Hosseinkhani, M.; Boutry, S.; Simchi, A.; Journeay, W. S.; Subramani, K.; Laurent, S. Magnetic Resonance Imaging Tracking of Stem Cells *in Vivo* Using Iron Oxide Nanoparticles as a Tool for the Advancement of Clinical Regenerative Medicine. *Chem. Rev.* **2011**, *111*, 253–280.
28. Lam, P. B.; Burga, L. N.; Wu, B. P.; Hofstatter, E. W.; Ping Lu, K.; Wulf, G. M. Prolyl Isomerase Pin1 Is Highly Expressed in Her2-Positive Breast Cancer and Regulates ErbB2 Protein Stability. *Mol. Cancer* **2008**, *7*, 91–102.
29. Mauri, D.; Pavlidis, N.; Ioannidis, J. P. Neoadjuvant *versus* Adjuvant Systemic Treatment in Breast Cancer: A Meta-Analysis. *J. Natl. Cancer Inst.* **2005**, *97*, 188–194.
30. Corsi, F.; De Palma, C.; Colombo, M.; Allevi, R.; Nebuloni, M.; Ronchi, S.; Rizzi, G.; Tosoni, A.; Emilio, T.; Emilio, C.; Prosperi, D. Towards Ideal Magnetofluorescent Nanoparticles for Bimodal Detection of Breast-Cancer Cells. *Small* **2009**, *5*, 2555–2564.
31. Sadauskas, E.; Danscher, G.; Stoltenberg, M.; Vogel, U.; Larsen, A.; Wallin, H. Protracted Elimination of Gold Nanoparticles from Mouse Liver. *Nanomedicine* **2009**, *5*, 162–169.
32. Briley-Saebo, K.; Bjørnerud, A.; Grant, D.; Ahlstrom, H.; Berg, T.; Mørk Kindberg, G. Hepatic Cellular Distribution and Degradation of Iron Oxide Nanoparticles Following Single Intravenous Injection in Rats: Implications for Magnetic Resonance Imaging. *Cell Tissue Res.* **2004**, *316*, 315–23.
33. Choi, H. S.; Liu, W.; Misra, P.; Tanaka, E.; Zimmer, J. P.; Itty Ipe, B.; Bawendi, M. G.; Frangioni, J. V. Renal Clearance of Quantum Dots. *Nat. Biotechnol.* **2007**, *25*, 1165–1170.
34. Lankveld, D. P. K; Oomen, A. G.; Krystek, P.; Neigh, A.; Troost-de Jong, A.; Noorlander, C. W.; Van Eijkeren, J. C. H.; Geertsma, R. E.; De Jong, W. H. The Kinetics of the Tissue Distribution of Silver Nanoparticles of Different Sizes. *Biomaterials* **2010**, *31*, 8350–8361.
35. Cole, A. J.; David, A. E.; Wang, J.; Galban, C. J., Yang, V. C. Magnetic Brain Tumor Targeting and Biodistribution of Long-Circulating PEG-Modified, Cross-Linked Starch-Coated Iron Oxide Nanoparticles. *Biomaterials* **2011**, *32*, 6291–6301.
36. Kim, J. S.; Yoon, T. J.; Yu, K. N.; Kim, B. G.; Park, S. J.; Kim, H. W.; Lee, K. H.; Park, S. B.; Lee, J. K.; Cho, M. H. Toxicity and Tissue Distribution of Magnetic Nanoparticles in Mice. *Toxicol. Sci.* **2006**, *89*, 338–347.
37. Liong, M; Shao, H.; Haun, J. B.; Lee, H.; Weissleder, R. Carboxymethylated Polyvinyl Alcohol Stabilizes Doped Ferrofluids for Biological Applications. *Adv. Mater.* **2010**, *22*, 5168–5172.

ARTICLE 8

Supporting Information

HER2 Expression in Breast Cancer Cells Is Downregulated Upon Active Targeting by Antibody-Engineered Multifunctional Nanoparticles in Mice

Fabio Corsi,[a,] Luisa Fiandra,[a] Clara De Palma,[a] Miriam Colombo,[a,b] Serena Mazzucchelli,[a] Paolo Verderio,[b] Raffaele Allevi,[a] Antonella Tosoni,[a] Manuela Nebuloni,[a] Emilio Clementi,[a,c] Davide Prosperi[b,d,]*

[a]*Dipartimento di Scienze Cliniche "Luigi Sacco", Università di Milano, Ospedale L. Sacco, via G.B. Grassi 74, 20157 Milano, Italy.* [b]*Dipartimento di Biotecnologie e Bioscienze, Università di Milano-Bicocca, piazza della Scienza 2, 20126 Milano, Italy.* [c]*Istituto Scientifico Eugenio Medea, 23842 Bosisio Parini, Italy.* [d]*Laboratorio di Biofisica e Nanomedicina, Polo Tecnologico, Fondazione Don Gnocchi IRCCS-ONLUS, 20148 Milan, Italy.*

* davide.prosperi@unimib.it

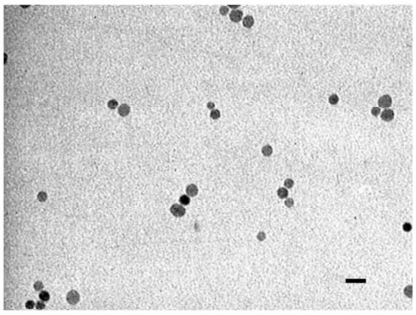

Figure S1. Transmission electron micrograph of TMNC.

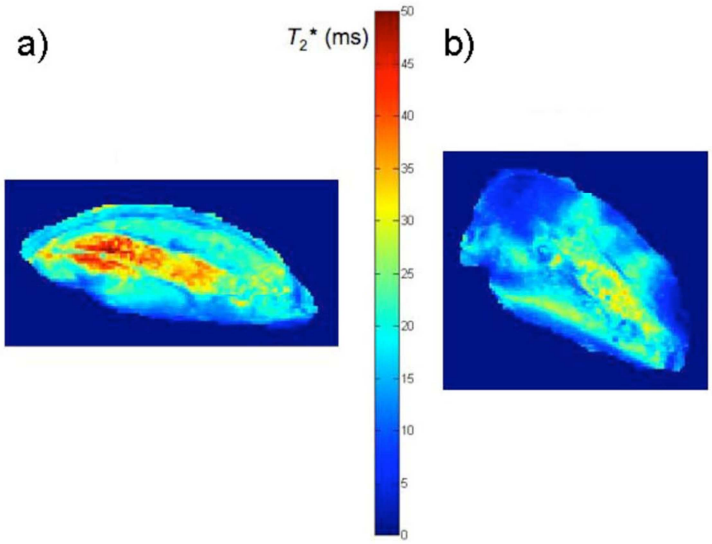

Figure S2. T_2* map of the tumor region of the mouse undergone MRI examination (a) before and (b) 24 h after the TMNC injection.

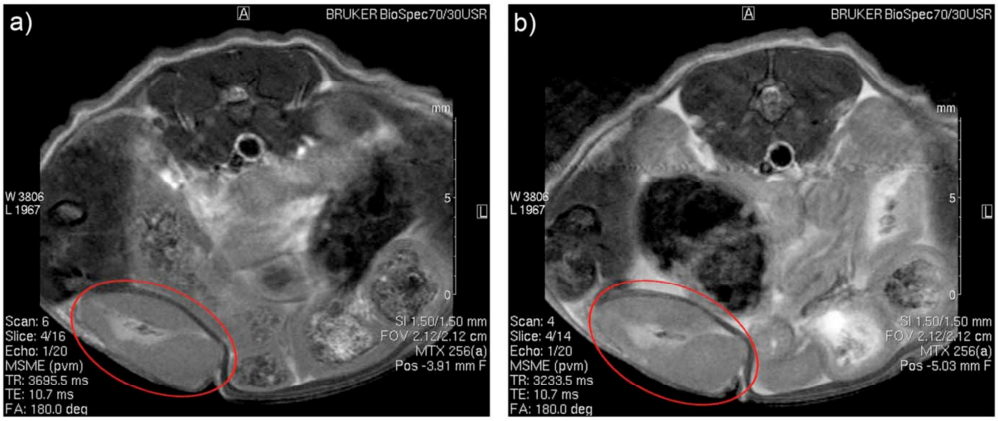

Figure S3. Monitoring of PEG-coated MNCs uptake in vivo by MRI. The axial T_2-weighted MR images have been obtained from a MCF-7 tumor-bearing mice (a) before and (b) 24 h after the injection of nanocrystals. No differences were found in treated mice with respect to control. The images, obtained by a T_2-mapping sequence, were acquired at 10.7 ms echo time.

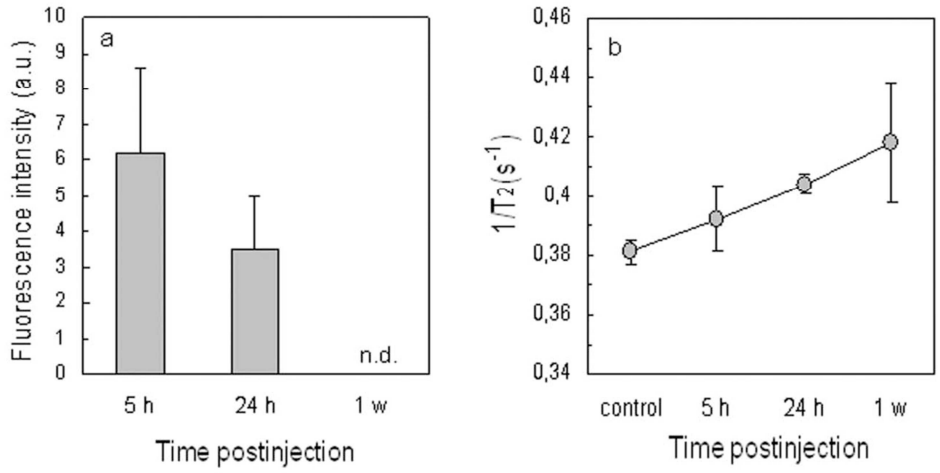

Figure S4. Fluorescence intensity (a) and inverse relaxation time (b) of the lysates of MCF-7 tumor isolated from perfused mice at 5 h, 24 h and 1 week postinjection of AF660-TMNC. Mean ± S.E. of 3 different samples.

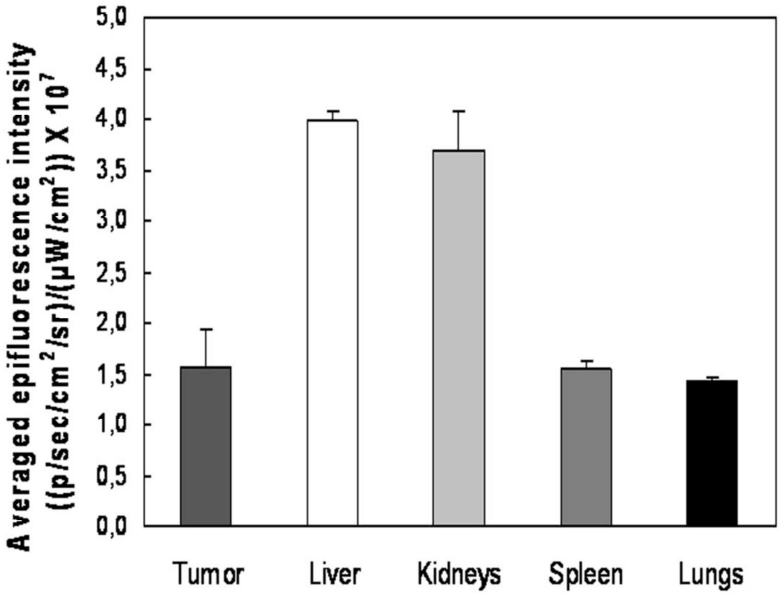

Figure S5. Averaged epifluorescence intensity of isolated tumor, liver, kidneys, spleen and lungs, isolated from MDA bearing mice. Mean ± S.E. of 3 different samples for each experimental model.

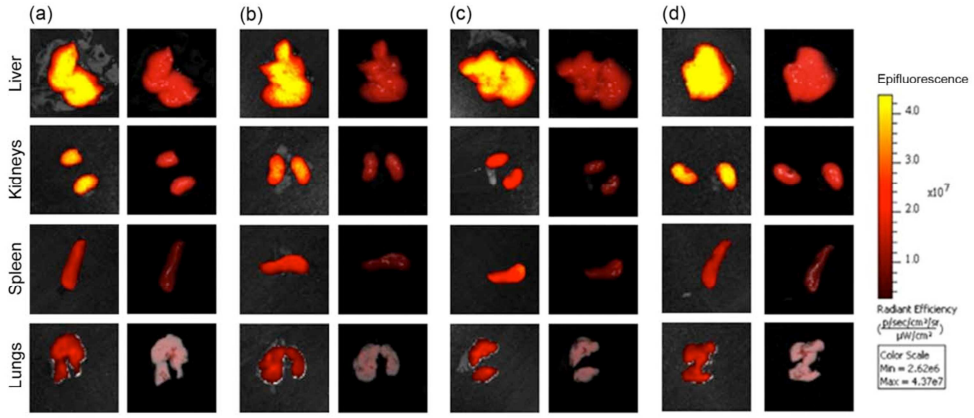

Figure S6. CCD camera images of liver, kidneys, spleen and lungs isolated from MCF-7 bearing mice at 5 h (a), 24 h (b) and 1 week (c), and from a MDA bearing mouse at 5 h (d) postinjection of AF660-TMNC. Epi-fluorescence intensity images and spectrally unmixed fluorescence images are reported on left and right, respectively.

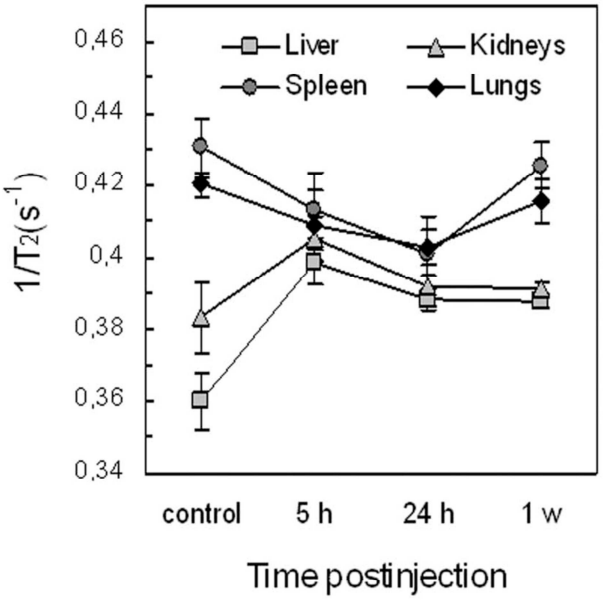

Figure S7. Inverse relaxation time of the lysates of liver, kidneys, spleen and lungs isolated from MCF-7 bearing perfused mice at 5 h, 24 h and 1 week postinjection of AF660-TMNC. Mean ± S.E. of 3 different samples.

Table S1. Effect of AF660-TMNC on the level of aspartate transaminase (AST), alanine transaminase (ALT), urea and creatinine in serum extracted from mice at 5 h, 24 h and 1 week postinjection.

	5 h		24 h		1 w	
	ctrl	**treated**	**ctrl**	**treated**	**ctrl**	**treated**
ALT	7.57±3.38	42.99±14.27	11.97±1.43	24.40±4.89	107.06±43.30	67.71±19.35
AST	52.60±2.43	154.83±25.38*	58.88±8.24	131.98±43.59	315.99±128.39	284.48±54.15
urea	90.45±0.09	175.43±25.36*	113.24±15.08	109.50±12.48	63.80±1.67	83.78±7.70
creatinine	0.23±0.07	0.40±0.01	0.51±0.03	0.52±0.01	1.01±0.06	0.91±0.04

*$P < 0.05$, by Student's *t*-test (Mean ± S.E. of 3 different replicates)

ARTICLE 8

Angewandte International Edition Chemie

DOI: 10.1002/anie.201106775

Protein Nanoconjugation

Site-Specific Conjugation of ScFvs Antibodies to Nanoparticles by Bioorthogonal Strain-Promoted Alkyne–Nitrone Cycloaddition**

*Miriam Colombo, Silvia Sommaruga, Serena Mazzucchelli, Laura Polito, Paolo Verderio, Patrizia Galeffi, Fabio Corsi, Paolo Tortora, and Davide Prosperi**

Hybrid multifunctional nanoparticles (MFN), which combine unique superparamagnetic properties and fluorescence emission, have been envisaged as promising bimodal tracers for noninvasive diagnosis of cancer both in vitro and in vivo.[1–4] The design of ideal targeted MFN (TMFN) needs careful optimization of fundamental features including uniform size and shape,[5] surface charge,[6] optical and magnetic properties,[7,8] and efficient functionalization with suitable homing ligands[9–11] to improve the signal amplification and target selectivity toward malignant cells. When the ligands are complex molecules, such as proteins, their proper orientation on the surface of nanoparticles becomes a crucial factor for maximizing the affinity for their molecular counterparts.[12–14] In this context, copper-catalyzed azide-alkyne cycloaddition (CuAAC), is gaining attention as a versatile strategy for protein immobilization on iron oxide nanoparticles.[15] However, CuAAC requires metal catalysts and these are toxic to cells and unsuited for several kinds of proteins.[16] In light of this severe limitation, the bioorthogonal conjugation, which aims at avoiding the use of unsafe promoters, is rapidly becoming popular.[17–19] The main advantages of this approach are speed, efficiency, and biocompatibility. The strain-promoted azide–alkyne cycloaddition (SPAAC) modification of CuAAC, in which the terminal alkyne is replaced by a highly reactive cyclooctyne, does not require Cu^{I} catalysis and has provided excellent results both in solution and in living cells.[20–22] The kinetics of the reaction can be improved by introducing electron-withdrawing substituents adjacent to the triple bond of the ring-strained cyclooctyne.[23] However, problems still arise when a site-specific attack to a selected amino acid residue under physiological conditions is desired. The attempts so far have mainly followed genetic encoding or metabolic labeling strategies, in which non-natural amino acids bearing an alkyne or azide functionality can be introduced artificially in the peptide sequence.[24,25] However, these methods suffer from poor generality and involve complicated and laborious procedures, which are not accessible in most laboratories.

Recently, an elegant variant to SPAAC has been proposed, which replaces the azido functionality with a nitrone group.[26] Termed strain-promoted azide-nitrone cycloaddition (SPANC), this reaction was fast and high-yielding with several molecular species, including peptides,[27] and entire cells,[28] provided that an accessible nitrone group could be incorporated in the molecular architecture.

We have recently reported the production of a scFv variant (scFv800E6) of the anti-HER2 antibody in *Pichia pastoris*.[29] There is a growing interest for scFvs due to the high target selectivity and reduced immunogenicity compared to whole antibodies.[30] Herein, we explore the potential of the SPANC reaction for site-specific bioengineering of MFN with recombinant scFv bioligands and demonstrate the potential of the resulting targeted MFN (TMFN) in selectively binding to HER2 breast cancer cell receptors.

In principle, the SPANC reaction seems particularly well suited for the immobilization of scFv antibodies on nanoparticles, as 1) it prevents homodimer formation, which is common in thiol-based ligations; 2) the introduction of a serine at the peptide N-terminus, which can be easily accomplished by genetic engineering, leads to one single nitrone species; 3) the conjugation through the N-terminal residue is expected not to interfere with the affinity toward HER2. Indeed, N-terminal serine is located sufficiently far from the antigen-binding site of the peptide. Details on homology modeling of the N-terminal serine mutant of scFv800E6 (scFv1) are included in the Supporting Information. Serine was inserted during gene amplification by the polymerase chain reaction (PCR), cloned in pPICZα and transformed in *P. pastoris*. ScFv1 was obtained with a C-terminal c-myc epitope, 6 × His-tag, and purified by a single-step purification method on a Ni-NTA agarose affinity column in 2.5 $mg\,L^{-1}$ yields.

Ligand **L1** (Scheme 1), containing a 4-dibenzocyclooctynol derivatized with a SH-terminated poly(ethylene glycol) [with a molecular weight of 5000] (PEG_{5000}) carbamate linker, was synthesized in seven steps according to the procedure

[*] M. Colombo,[+] P. Verderio, Prof. P. Tortora, Dr. D. Prosperi
NanoBioLab, Dipartimento di Biotecnologie e Bioscienze
Università di Milano Bicocca
Piazza della Scienza 2, 20126 Milano (Italy)
E-mail: davide.prosperi@unimib.it
Homepage: http://www.nanobiolab.btbs.unimib.it
Dr. L. Polito, Dr. D. Prosperi
Istituto di Scienze e Tecnologie Molecolari, CNR
Via Fantoli 16/15, 20138 Milano (Italy)
Dr. S. Sommaruga,[+] Dr. S. Mazzucchelli, Prof. F. Corsi
Dipartimento di Scienze Cliniche "Luigi Sacco"
Università di Milano, Ospedale L. Sacco
Via G.B. Grassi 74, 20157 Milano (Italy)
Dr. P. Galeffi
UTAGRI-GEN, ENEA, R. C.Casaccia
Via Anguillarese 301, 00123 Roma (Italy)
[+] These authors contributed equally to this work.

[**] M.C. and S.M. acknowledge the research fellowships of CMENA. This work was supported by NanoMeDia Project (Regione Lombardia) and "Fondazione Romeo e Enrica Invernizzi".

Supporting information for this article is available on the WWW under http://dx.doi.org/10.1002/anie.201106775.

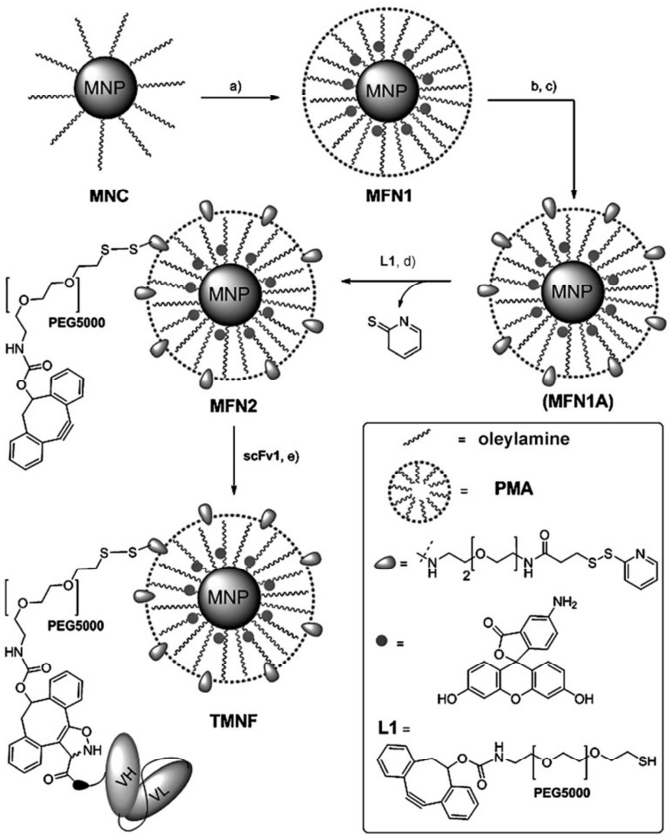

Scheme 1. Synthesis of TMFN, see text for details. a) FITC-PMA; b) EDBE, EDC·HCl, 2 h, room temperature; c) SPDP, 4 h, room temperature; d) **L1**, 2 h, room temperature; e) scFv1, 1 h, room temperature, 14 h at 4 °C. FITC = fluoresceine isothiocyanate, SPDP = *N*-succinimidyl-3-[2-pyridyldithio] propionate, VL = variable light chain, VH = variable heavy chain (VH and VL are variable heavy and light region of IgG molecules, respectively: VH + VL + linker = scFv).

described in the Supporting Information. Highly uniform magnetite nanocrystals (MNC, 7.5 ± 0.5 nm) coated with oleylamine surfactant were obtained by solvothermal decomposition in organic solvents.[31] Nanoparticles were transferred to the water phase by mixing with an amphiphilic polymer, obtained by condensation of poly(isobutylene-*alt*-maleic anhydride) and dodecylamine (PMA),[32] which was previously reacted with fluoresceinamine, resulting in the highly stable, dispersible, and fluorescent MFN1. MFN1 were functionalized with amino groups using the bifunctional linker 2,2-(ethylenedioxy)bis(ethylamine) (EDBE). **L1** was linked to the amines generated on the polymer envelop by activation with thiol-reactive *N*-succinimidyl-3-[2-pyridyldithio] propionate to give MFN2 (Scheme 1). We estimated an average of 20 **L1** molecules per nanoparticle by UV measurement of pyridine-2-thione released upon binding. MFN2 were 60 ± 3 nm in size, as measured by dynamic light scattering (DLS) in phosphate buffer saline (PBS, pH 7.4) at 5 $\mu g\,mL^{-1}$, with a ζ potential of -38 ± 6 mV, and exhibited a maximal fluorescence emission at 515 nm. Even after reaction with **L1**, MFN2 were completely stable in PBS giving a clean solution. MFN2 were subjected to a one-pot SPANC reaction sequence. Unfortunately, the original procedure caused nanoparticle agglomeration, which forced us to adjust the reaction conditions. ScFv1 (2.0 equiv) was diluted 1:1 in 0.1 M ammonium acetate buffer, pH 6.9, and incubated at 25 °C for 1 h with sodium periodate (2.0 equiv), leading to the oxidation of the N-terminal serine. The resulting aldehyde was immediately treated with excess *p*-methoxybenzenethiol (13.0 equiv, 1 h) followed by *p*-anisidine (18.6 equiv, 15 min). Next, MFN2 (1.0 equiv) and *N*-methylhydroxylamine hydrochloride (18.6 equiv) were added, incubated 1 h at room temperature and left overnight at 4 °C, leading to TMFN. The excess scFv1 was removed by centrifuge-assisted dialysis using 100 kDa pore Amicon filters at 3500 rpm. The concentrated TMFN solution was washed two times in the same way, then recovered and diluted to a 7 $mg\,mL^{-1}$ stock solution in PBS. An aliquot was drawn, and the presence of scFv1 on TMFN was cross-checked by dot-blot analysis. The final hydrodynamic size of TMFN in PBS was 158 ± 7 nm with a ζ potential of -47 ± 4 mV, confirming an increase in size after protein conjugation.

TMFN were assessed by flow cytometry to evaluate their affinity and target selectivity in labeling MCF7 breast cancer cells expressing HER2 membrane receptor. TMFN were incubated in parallel for 1 h with HER2-positive ($HER2^+$) MCF7 cells at two different concentrations (20 $\mu g\,mL^{-1}$ and 100 $\mu g\,mL^{-1}$, respectively) and with HER2-negative ($HER2^-$) MDA cells (100 $\mu g\,mL^{-1}$). Flow cytometry showed a remarkable right shift of fluorescence signal for both TMFN concentrations with $HER2^+$ cells, which was not observed with MDA cells (Figure 1). Values in Figure 1 show a remarkable increase in mean fluorescence intensity of 100 $\mu g\,mL^{-1}$ TMFN in comparison with the 20 $\mu g\,mL^{-1}$ sample, while the latter exhibits a population at low intensities, which is accounted for by the presence of residual

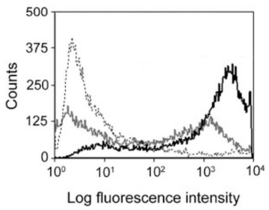

Figure 1. MCF7 cells were incubated 1 h at 37 °C with 20 μg mL^{-1} (gray line) and 100 μg mL^{-1} (black line), respectively, of TMFN. As a negative control, MDA cells were treated with TMFN (dashed line).

unlabeled cells. These results suggest that TMFN accumulate selectively on MCF7 cells and that TMFN-HER2 recognition is concentration dependent. The specificity of binding between TMFN and HER2 was validated by confocal laser scanning microscopy. MCF7 and MDA cells were both treated with TMFN (100 μg mL^{-1}) and, in parallel, with dye-labeled scFv1 (20 μg mL^{-1}). As HER2 is a transmembrane receptor, we observed accumulation of both TMFN and scFv1 at the cell membranes of HER2$^+$ cells only (Figure 2 A and C, respectively, green). Figure 2 panels N and O showed membrane colocalization (orange), which confirmed that nanoparticle capture by cells was actually mediated by specific membrane receptor interaction). HER2$^-$ cells showed only membrane staining (B and D). TMFN bound to MCF7 membrane could not be displaced by free scFv1 even at threefold concentration, confirming our previous evidence that multiple scFv presentation on spherical nanoparticles improves significantly the antigen recognition.[33]

To evaluate the potential of TMFN as magnetic contrast agents in living cells, we performed a set of T_2 relaxation experiments on MCF7 and MDA cells. Two MCF7 and two MDA cell cultures (1 mL) were treated with 20 μg and 100 μg

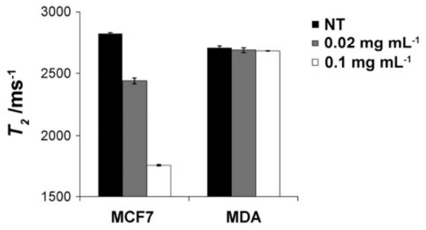

Figure 3. Relaxivity measurements on treated and untreated (NT, controls) MCF7 and MDA cells. Data are the mean ± S.E. (standard error) of three different relaxivity measurements. T_2 values refer to 5×10^5 cells after incubation with different concentrations of TMFN.

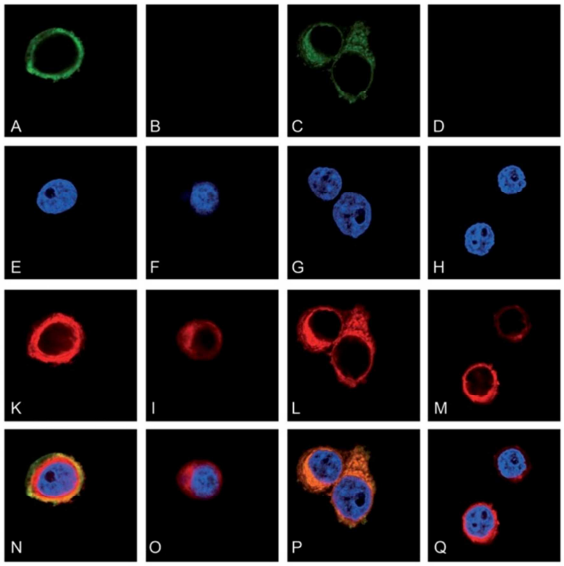

Figure 2. HER2$^+$ cells (MCF7: A, E, K, N) and HER2$^-$ cells (MDA: B, F, I, O) were incubated for 1 h at 37 °C with TMFN (100 μg mL^{-1}). ScFv1 incubation with MCF7 and MDA cells was used as positive (C, G, L, P) and negative controls (D, H, M, Q), respectively. Then cells were fixed and ScFv1 was revealed by a FITC-conjugated antibody to whole murine IgG (C, D). Nuclei were stained with DAPI (blue: E, F, G, H) and membranes were stained with DiD oil (red: K, I, L, M). Merged images are shown in panels N, O, P, and Q. Scale bar = 10 μm.

TMFN, respectively, for 3 h at 37 °C. The cells were washed with PBS, fixed with 2.5 % buffered glutaraldehyde, and eventually resuspended in PBS, at a final concentration of 5×10^5 cells mL^{-1}. The treated samples as well as unlabeled MCF7 and MDA cells (controls) were analyzed by relaxometric measurements. All the treated MCF7 cells exhibited a significant dose-dependent fall in T_2 compared to the control, confirming the capture of paramagnetic iron by cultured cells (Figure 3). As expected, cells treated with 100 μg TMFN exhibited greater fall in T_2 (relaxivity enhancement) compared to 20 μg TMFN, suggesting a dose-dependent nanoparticle capture. In contrast, MDA cells did not provide evidence of T_2 decrease attributable to the interaction with TMFN at all the concentrations tested.

Finally, we investigated the cellular toxicity and cell proliferation of TMFN. TMFN were found to be nontoxic at 20 and 50 μg mL^{-1} in MCF7 after 24 h of exposure, while induced about 15 % mortality at 100 μg mL^{-1}, probably due to the high particulate concentration in suspension. No differences were observed between untreated and TMFN-treated cells in terms of proliferation. Altogether, these experiments suggested a good profile of safety in cultures for TMFN.

In summary, we have demonstrated that strain-promoted azide–nitrone cycloaddition (SPANC) allowed for the rapid and effective conjugation of proteins on nanoparticles functionalized with

cyclooctyne ligands under mild conditions, provided that a N-terminal serine residue was introduced by molecular engineering. In particular, the application of SPANC to a scFv antibody against HER2 tumor marker resulted in its prompt immobilization on multifunctional nanoparticles (MFN), leading to water-stable bioengineered targeted MFN (TMFN), which exhibited a complete conservation of protein effectiveness in selectively targeting HER2 receptor in living cells. As the structural motif of scFv fragments is highly conserved,[34] and other kinds of nanoparticles can be modified identically with the same polymer used herein,[32] this approach is expected to be of general utility and may become a universal strategy for the development of a new generation of targeted nanoparticles.

Received: September 23, 2011
Revised: October 18, 2011
Published online: ■■ ■■, ■■■■

Keywords: bioorthogonal reaction · cell targeting · cycloaddition · nanoparticles · scFv antibody

[1] K. Park, S. Lee, E. Kang, K. Kim, K. Choi, I. C. Kwon, *Adv. Funct. Mater.* **2009**, *19*, 1553 – 1566.
[2] J.-H. Lee, Y.-M. Huh, Y.-w. Jun, J.-w. Seo, J.-t. Jang, H.-T. Song, S. Kim, E.-J. Cho, H.-G. Yoon, J.-S. Suh, J. Cheon, *Nat. Med.* **2007**, *13*, 95 – 99.
[3] J. Kim, S. Park, J. E. Lee, S. M. Jin, J. H. Lee, I. S. Lee, I. Yang, J.-S. Kim, S. K. Kim, M.-H. Cho, T. Hyeon, *Angew. Chem.* **2006**, *118*, 7918 – 7922; *Angew. Chem. Int. Ed.* **2006**, *45*, 7754 – 7758.
[4] F. Corsi, L. Fiandra, C. De Palma, M. Colombo, S. Mazzucchelli, P. Verderio, R. Allevi, A. Tosoni, M. Nebuloni, E. Clementi, D. Prosperi, *ACS Nano* **2011**, *5*, 6383 – 6393.
[5] J. Park, K. An, Y. Hwang, J.-G. Park, H.-J. Noh, J.-Y. Kim, J.-H. Park, N.-M. Hwang, T. Hyeon, *Nat. Mater.* **2004**, *3*, 891 – 895.
[6] F. Corsi, C. De Palma, M. Colombo, R. Allevi, M. Nebuloni, S. Ronchi, G. Rizzi, A. Tosoni, E. Trabucchi, E. Clementi, D. Prosperi, *Small* **2009**, *5*, 2555 – 2564.
[7] J. Yang, E.-K. Lim, H. J. Lee, J. Park, S. C. Lee, K. Lee, H.-G. Yoon, J.-S. Suh, Y.-M. Huh, S. Haam, *Biomaterials* **2008**, *29*, 2548 – 2555.
[8] S. Chen, F. Reynolds, L. Yu, R. Weissleder, L. Josephson, *J. Mater. Chem.* **2009**, *19*, 6387 – 6392.
[9] M. Lewin, N. Carlesso, C.-H. Tung, X.-W. Tang, D. Cory, D. T. Scadden, R. Weissleder, *Nat. Biotechnol.* **2000**, *18*, 410 – 414.
[10] D. Simberg, T. Duza, J. H. Park, M. Essler, J. Pilch, L. Zhang, A. M. Derfus, M. Yang, R. M. Hoffman, S. Bhatia, M. J. Sailor, E. Ruoslahti, *Proc. Natl. Acad. Sci. USA* **2010**, *104*, 932 – 936.
[11] N. T. K. Thanh, L. A. W. Green, *Nano Today* **2010**, *5*, 213 – 230.
[12] E. Occhipinti, P. Verderio, A. Natalello, E. Galbiati, M. Colombo, S. Mazzucchelli, A. Salvadè, P. Tortora, S. Maria Doglia, D. Prosperi, *Nanoscale* **2011**, *3*, 387 – 390.
[13] W. R. Algar, D. E. Prasuhn, M. H. Stewart, T. L. Jennings, J. B. Blanco-Canosa, P. E. Dawson, I. L. Medintz, *Bioconjugate Chem.* **2011**, *22*, 825 – 858.
[14] S. Mazzucchelli, M. Colombo, C. De Palma, A. Salvadè, P. Verderio, M. D. Coghi, E. Clementi, P. Tortora, F. Corsi, D. Prosperi, *ACS Nano* **2010**, *4*, 5693 – 5702.
[15] L. Polito, D. Monti, E. Caneva, E. Delnevo, G. Russo, D. Prosperi, *Chem. Commun.* **2008**, 621 – 623.
[16] L. M. Gaetke, C. K. Chow, *Toxicology* **2003**, *189*, 147 – 163.
[17] E. M. Sletten, C. R. Bertozzi, *Acc. Chem. Res.* **2011**, *44*, 666 – 676.
[18] J. B. Haun, N. K. Devaraj, S. A. Hilderbrand, H. Lee, R. Weissleder, *Nat. Nanotechnol.* **2010**, *5*, 660 – 665.
[19] E. Lallana, R. Riguera, E. Fernandez-Megia, *Angew. Chem.* **2011**, *123*, 8956 – 8966; *Angew. Chem. Int. Ed.* **2011**, *50*, 8794 – 8804.
[20] M. F. Debets, S. S. van Berkel, J. Dommerholt, A. J. Dirks, F. P. J. T. Rutjes, F. L. van Delft, *Acc. Chem. Res.* **2011**, *44*, 805 – 815.
[21] J. C. Jewett, C. R. Bertozzi, *Chem. Soc. Rev.* **2010**, *39*, 1272 – 1279.
[22] P. V. Changa, J. A. Preschera, E. M. Slettena, J. M. Baskina, I. A. Millera, N. J. Agarda, A. Loa, C. R. Bertozzi, *Proc. Natl. Acad. Sci. USA* **2010**, *107*, 1821 – 1826.
[23] X. Ning, J. Guo, M. A. Wolfert, G.-J. Boons, *Angew. Chem.* **2008**, *120*, 2285 – 2287; *Angew. Chem. Int. Ed.* **2008**, *47*, 2253 – 2255.
[24] D. P. Nguyen, H. Lusic, H. Neumann, P. B. Kapadnis, A. Deiters, J. W. Chin, *J. Am. Chem. Soc.* **2009**, *131*, 8720 – 8721.
[25] D. C. Dieterich, J. J. Lee, A. J. Link, J. Graumann, D. A. Tirrell, E. M. Schuman, *Nat. Protoc.* **2007**, *2*, 532 – 540.
[26] C. S. McKay, J. Moran, J. P. Pezacki, *Chem. Commun.* **2010**, *46*, 931 – 933.
[27] X. Ning, R. P. Temming, J. Dommerholt, J. Guo, D. B. Ania, M. F. Debets, M. A. Wolfert, G.-J. Boons, F. L. van Delft, *Angew. Chem.* **2010**, *122*, 3129 – 3132; *Angew. Chem. Int. Ed.* **2010**, *49*, 3065 – 3068.
[28] C. S. McKay, J. A. Blake, J. Cheng, D. C. Danielson, J. P. Pezacki, *Chem. Commun.* **2011**, *47*, 10040 – 10042.
[29] S. Sommaruga, A. Lombardi, A. Salvadè, S. Mazzucchelli, F. Corsi, P. Galeffi, P. Tortora, D. Prosperi, *Appl. Microbiol. Biotechnol.* **2011**, *91*, 613 – 621.
[30] J. Mårlind, M. Kaspar, E. Trachsel, R. Sommavilla, S. Hindle, C. Bacci, L. Giovannoni, D. Neri, *Clin. Cancer Res.* **2008**, *14*, 6515 – 6524.
[31] M. Piazza, M. Colombo, I. Zanoni, F. Granucci, P. Tortora, J. Weiss, T. Gioannini, D. Prosperi, F. Peri, *Angew. Chem.* **2011**, *123*, 648 – 652; *Angew. Chem. Int. Ed.* **2011**, *50*, 622 – 626.
[32] C.-A. J. Lin, R. A. Sperling, J. K. Li, T.-Y. Yang, P.-Y. Li, M. Zanella, W. H. Chang, W. J. Parak, *Small* **2008**, *4*, 334 – 341.
[33] S. Mazzucchelli, P. Verderio, S. Sommaruga, Colombo, A. Salvadè, P. Tortora, F. Corsi, D. Prosperi, *Bioconjugate Chem.* **2011**, *22*, 2296 – 2303
[34] C. Mandal, B. D. Kingery, J. M. Anchin, S. Subramaniam, D. S. Linthicum, *Nat. Biotechnol.* **1996**, *14*, 323 – 328.

Angewandte Chemie
Eine Zeitschrift der Gesellschaft Deutscher Chemiker

Supporting Information

69451 Weinheim, Germany

Site-Specific Conjugation of ScFvs Antibodies to Nanoparticles by Bioorthogonal Strain-Promoted Alkyne–Nitrone Cycloaddition**

*Miriam Colombo, Silvia Sommaruga, Serena Mazzucchelli, Laura Polito, Paolo Verderio, Patrizia Galeffi, Fabio Corsi, Paolo Tortora, and Davide Prosperi**

anie_201106775_sm_miscellaneous_information.pdf

Materials and methods. All chemicals were purchased from Sigma-Aldrich (St. Louis, MO) and used as received. Water was deionized and ultrafiltered by a MilliQ apparatus from Millipore Corporation (Billerica, MA) before use. Transmission electron microscopy (TEM) images were obtained by a Zeiss EM-109 microscope operating at 80 kV, available at the "Centro di Microscopia Elettronica per le Nanotecnologie applicate alla medicina" (CMENA, University of Milan). T_2 relaxation times were acquired at a temperature of 313 K using a Bruker Minispec mq20 system working with 1-H at 20 MHz magnetic field with the following parameters: CMPG sequence, 1000 echoes with a 20 ms echo time and 2 s repetition time. Samples were introduced using 10 mm NMR tubes wormed in a thermostatic bath. Dynamic light scattering (DLS) measurements were performed at 90° with a 90Plus Particle Size Analyzer from Brookhaven Instruments Corporation (Holtsville, NY), working at 15 mW of a solid state laser (λ = 661 nm). Zeta-potential measurements were performed on the same instrument, equipped with a couple of AQ-809 electrodes, and analyses were processed by a ZetaPlus software. Viscosity and refractive index of pure water were used to characterize the solvent. Nanoparticles were dispersed in the solvent and sonicated in a S15H Elmasonic apparatus (Elma, Singen, Germany) before analysis. Final sample concentration used for measurements was typically of 5 $\mu g\ mL^{-1}$.

Synthesis of surfactant-coated Fe_3O_4 nanoparticles (MNC).[1] $Fe(acac)_3$ (4 mmol) was dissolved in a mixture of oleylamine (20 mL) and dibenzyl ether (20 mL). The mixture was heated at 110 °C for 1 h under argon, then refluxed at 300 °C for 2 h, and then cooled to room temperature. Ethanol (100 mL) was added and the black precipitate was centrifuged. The supernatant was discarded and the product washed several times with ethanol to remove the unbound surfactant. The resulting oleylamine-coated magnetite nanocrystals were dispersed in chloroform (MNC).

Synthesis of PMA-coated fluorescent Fe_3O_4 nanoparticles (MFN1). To a 0.5 M PMA[2] in $CHCl_3$ (5 mL) was added 1.0 M fluoresceinamine (0.5 mL in DMSO) and the mixture was left overnight at room temperature. An aliquot of this solution (63 μL) was added to MNC (4.6 mg in $CHCl_3$), the mixture was homogenized and the solvent was then evaporated at reduced pressure. Sodium borate buffer (SBB, pH 12, 10 mL) was added obtaining clean nanoparticle dispersion (MFN1), which was concentrated in Amicon tubes (filter cutoff 100 kDa) by centrifuging at 3500 rpm for 1 h. Finally, MFN1 were washed two times diluting with SBB in the same way and concentrated (each centrifuge cycle was 20 min at 3500 rpm) to a final volume of 200 μL.

Synthesis of L1-functionalized fluorescent Fe_3O_4 nanoparticles (MFN2). The MFN1 solution (200 μL), was reacted with 0.1 M EDC (18 μL) for 2 min, then 0.05 M 2,2-(ethylenedioxy)bis(ethylamine) (EDBE, 9 μL in deionized water) was added and stirred for 2 h. Next, the nanoparticle dispersion was concentrated and washed two additional times with water as described above. Nanoparticles were shaken for 4 h in the presence of *N*-succinimidyl-3-[2-pyridyldithio]-propionate (SPDP, 690 mL, 10 mg mL^{-1} in DMSO), concentrated and washed two times with water. Finally, **L1** (6.75 mg) was added, the mixture was shaken for 2 h at room temperature and the nanoparticle suspension (MFN2) was concentrated at 3500 rpm for 10 min and washed. The supernatants were analyzed by UV and the absorbance was read at 343 nm affording the concentration of released pyridine-2-thione to determine the amount of bound **L1** on MFN2.

Synthesis of TMFN by SPANC reaction of MFN2 and scFv1. ScFv1 (92 nmol in 1 mL PBS) was diluted with 0.1 M ammonium acetate buffer (pH 6.9, 1 mL) and incubated at 25 °C for 1 h with sodium periodate (20 μg, 92 nmol), subsequently treated with *p*-methoxybenzenethiol (84 μg, 598 nmol, 1 h) followed by *p*-anisidine (106 μg, 857 nmol, 15 min). Next, MFN2 (46 nmol) and *N*-methylhydroxylamine hydrochloride (72 μg, 857 nmol) were added, incubated 1 h at room temperature and left overnight at 4 °C (TMFN). The excess scFv1 was removed by concentration at 3500 rpm 100 kDa Amicon filters. The concentrated TMFN solution was washed two times in the same way, then recovered and diluted to a 7 mg mL^{-1} stock solution in PBS.

Procedure for the synthesis of ligand L1.

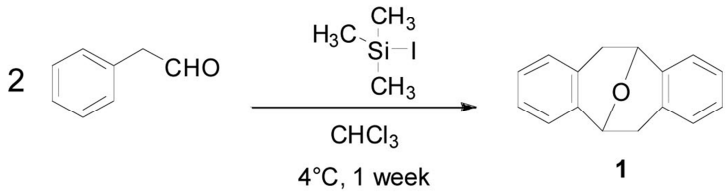

2,3:6,7-Dibenzo-9-oxabicyclo[3.3.1]nona-2,6-diene (1).[3]

In round flask was added phenylacetaldehyde (2.5 g, 20.8 mmol) dissolved in freshly distilled chloroform (10 mL). The flask was keeped under inhert gas atmosphere and cooled in an ice bath. Distilled trimethylsilyl iodide (3.5 mL, 25 mmol) was added to this solution and the reaction was vigorous stirred at 4 °C for 1 week. After warming the reaction to room temperature, the reaction was quenched with 1 M sodium thiosulfate in water (20 mL) and diluted with dichloromethane (20 mL); the two-phase mixture was stirred until the iodine color disappeared. The organic phase was separated and dried over anhydrous Na_2SO_4 and the solvent was evaporated *in vacuo*. The crude product was purified by silica gel column chromatography eluting with chloroform to afford the white crystalline ether **1** (695 mg, 3.16 mmol, 32%). ^{1}H-NMR analyses were consistent with data reported in reference[3].

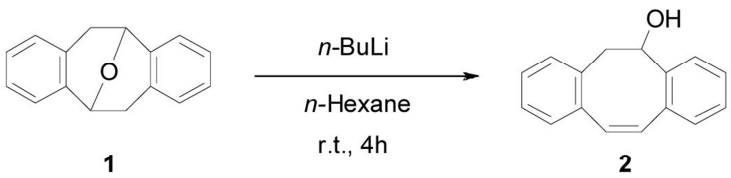

3-Hydroxy-1,2:5,6-dibenzocycloocta-1,5,7-triene (2).[4]

The reaction was keeped under inhert gas atmosphere. To a solution of the ether **1** (2.0 g, 9.0 mmol) in anhydrus THF (60 mL), was added dropwise a solution of *n*-butyllithium 2.44 M in *n*-hexane (7.4 mL, 18 mmol). The reaction was stirred at room temperature for 4 h. Subsequently, the mixture was quenched by slowly addition of water and then extracted with chloroform (2 × 50 mL). The combined organic layers were washed with brine (50 mL), dried over anhydrous Na_2SO_4, and the solvent was evaporated to give the crude product. The compound was purified by silica gel column chromatography, eluting first with chloroform, to remove impurities and later with ethyl acetate to afford the pure alcohol **2** (1.95 g, 8.77 mmol, 97 %). ^{1}H-NMR analyses were consistent with data reported in reference[4].

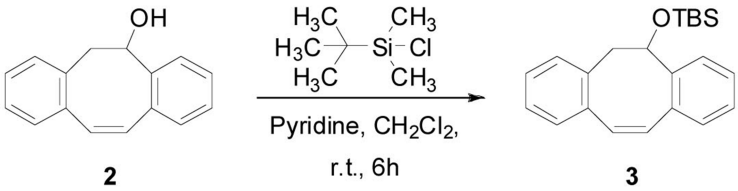

2 **3**

3-*tert*-Butyl-dimethylsilyl-oxy-1,2:5,6-dibenzocycloocta-1,5,7-triene (3).[5]

To a solution of **2** (1.1 g, 5 mmol) in a mixture containing dichloromethane (10 mL) and pyridine 2.5 mL) was added *tert*-Butyl dimethyl silyl chloride (1.5 g, 10 mmol) under vigorous stirring. The mixture were stirred for 6 h at room temperature; later, the reaction was diluted with water (10 mL) and extracted with dichloromethane (20 mL). The organic layer was then washed with water (15 mL) and brine (15 mL) and dried over anhydrous Na_2SO_4. The solvent was evaporated *in vacuo* and the crude product was purified by silica gel column chromatography eluiting with hexane/ethyl acetate, 7:1 v/v, to gain **3** (1.5 g, 4..4 mmol, 87%). ^{1}H-NMR analyses were consistent with data reported in reference[5].

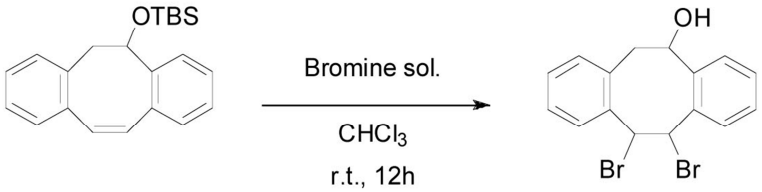

3 **4**

3-Hydroxy-7,8-dibromo-1,2:5,6-dibenzocyclooctene (4).[5]

To a solution of **3** (840 mg, 2.5 mmol) in chloroform (15 mL) was added dropwise at 0 °C a mixture of bromine (400 mg, 2.5 mmol) in the same solvent. The mixture was left under stirring at room temperature for 10 h monitoring the reaction by TLC, hexane/dichloromethane, 7:1 v/v. At the end of the reaction, the organic phase was washed with saturated aqueous sodium thiosulfate solution (8 mL), and dried over anhydrous Na_2SO_4. The organic layer was collected and the solvent was evaporated *in vacuo*; finally, the crude product was purified by silica gel column chromatography eluting with hexane/dichloromethane, 7:1 v/v, to obtain **4** (573 mg, 1.5 mmol, 60%). ^{1}H-NMR analyses were consistent with data reported in reference[5].

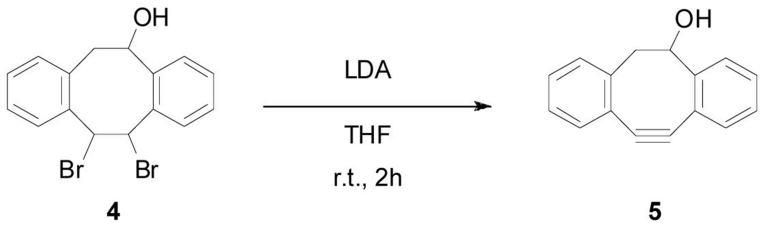

4 **5**

3-Hydroxy-7,8- didehydro-1,2:5,6-dibenzocyclooctene (5).[5]

Under inhert gas atmosphere, **4** (573 mg, 1.5 mmol) was dissolved in tetrahydrofuran (25 mL) and to this solution was added dropwise lithium diisopropylamide 2.0 M in tetrahydrofuran (2.5 mL, 5 mmol). The reaction was vigorous stirred for 3 h at room temperature, after which this solution was poured into ice water (25 mL); the mixture was extracted with dichloromethane (2 × 50 mL) and the combined organic layers were then washed with water (40 mL) and brine (40 mL), then dried over anhydrous Na_2SO_4 and the solvent was eliminated *in vacuo*. The crude product was purified by silica gel column chromatography eluting with hexane/ethyl acetate, 5:1 v/v, to obtain **5** (147 mg, 0.67 mmol, 45%). ^{1}H-NMR analyses were consistent with data reported in reference[5].

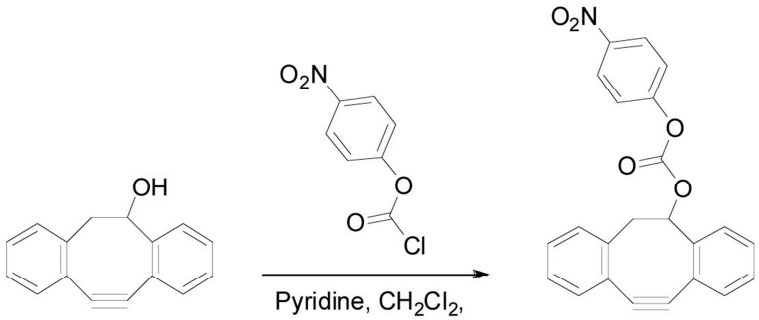

5 **6**

Carbonic acid 7, 8- didehydro-1,2:5,6-dibenzocyclooctene-3-yl ester 4-nitrophenyl ester (6).[5]

The product **5** (110 mg, 0.5 mmol) was dissolved in dichloromethane (15 mL) and then, to this solution, was added 4-nitro-phenyl chloroformiate (0.2 g, 1 mmol) and pyridine (0.2 mL, 2.5 mmol). The reaction was stirred vigorously for 4 h at room temperature and later it was washed with brine (2 × 5 mL); the organic layer was dried over anhydrous Na_2SO_4 and the solvent was evaporated *in vacuo.* The crude product was purified by silica gel column chromatography eluting with hexane/ethyl acetate, 10:1 v/v, to gain **6** (173 mg, 0.45 mmol 89%). ^{1}H-NMR analyses were consistent with data reported in reference[5].

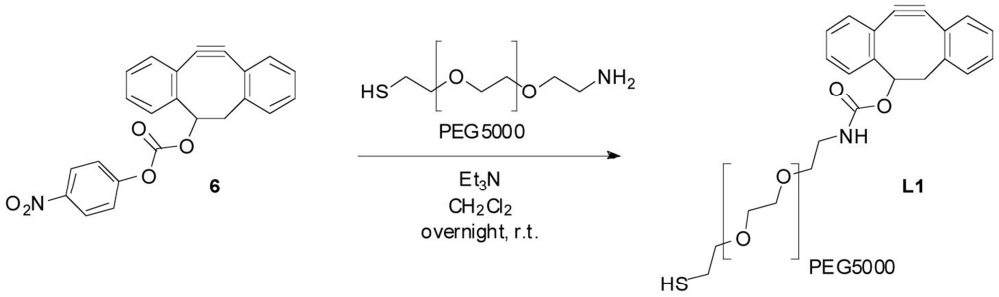

11,12-Didehydro-5,6-dihyrdodibenzo[*a,e*][8]annulen-5-yl thiolPEG_{5000}-1-ylcarbamate (L1). For the synthesis of L1 was followed a procedure reported in literature with minor modification.[6] Briefly, to a solution of **6** (2.3 mg, 6 μmol) in dichloromethane (300 μL), were added Et_3N (1.5 μL, 10 μmol) and HS-PEG_{5000}-NH_2 (10 mg, 2 μmol). The reaction was stirred overnight in the orbital shaker at room temperature; then, the mixture was diluted with dichloromethane (5 mL) and washed with deionized water (1 mL). The organic phase was again washed with HCl 1 M (1 mL), water (1 mL) and brine (1 mL) and then dried over $MgSO_4$. The product was concentrated under reduce pressure and then precipitated with cold Et_2O (10 mL); L1 was washed several times with Et_2O to remove the unreacted reagents and finally dried *in vacuo*. ^{1}H-NMR (400 MHz, $CDCl_3$), δ: 7.53-7.50 (m, 1H), 7.36-7.29 (m, 7H), 5.59 (br s, 1H), 5.47 (br s, 1H), 3.80-3.50 (m, PEG H signals), 3.38 (m, 2H), 2.90 (m, 1H), 2.70 (br. s, 1H).

Dynamic light scattering measurements.

Viscosity and refractive index of water were used to characterize the solvent. MNF2 and TMNF were dispersed in phosphate buffer saline pH = 7.4 (PBS, EuroClone). To avoid the formation of large aggregates, the suspension was filtered through a 0.45 μm cellulose acetate filter. The final sample concentration used for measurements was typically 5 μg mL^{-1} (Figure S1).

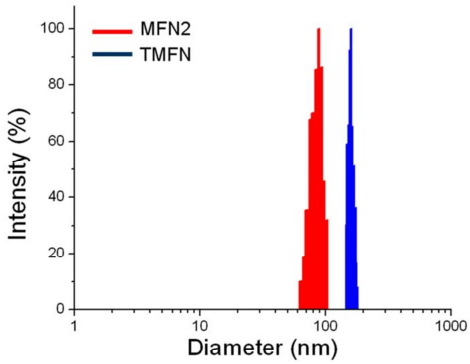

Figure S1. Hydrodynamic size distribution histogram of MFN2 (red) and TMFN (blue) in PBS, pH 7.4. The horizontal scale is semi-logarithmic.

Transmission electron microscopy (TEM) analysis.

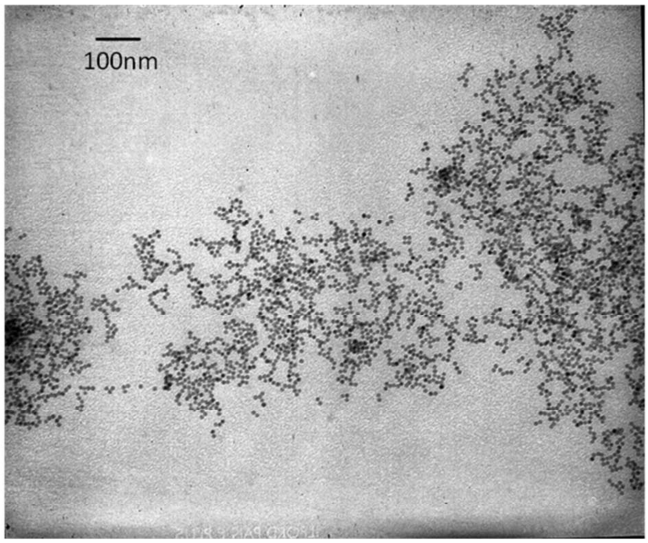

Figure S2. TEM image of MNC synthesized by solvothermal decomposition in organic solvents. For TEM analysis, nanocrystals were dispersed under sonication in hexane (50 μg mL^{-1}) and a drop

of the resulting solution was placed on a formvar/carbon-coated copper grid and air-dried. The image was acquired by Raffaele Allevi from Centro di Microscopia Elettronica per lo sviluppo delle Nanotecnologie applicate alla medicina (CMENA, University of Milan).

Fluorescence analysis

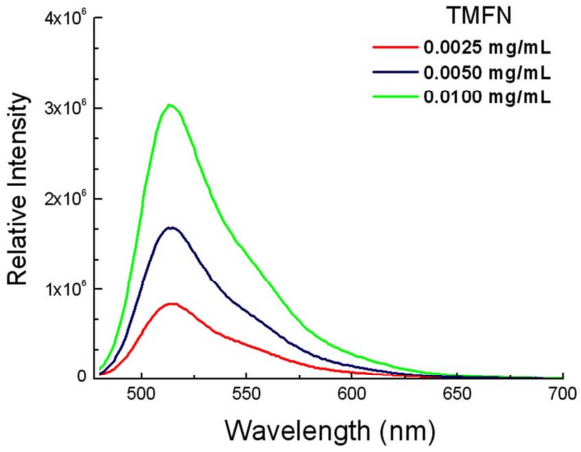

Figure S3. Fluorescence emission spectra at different concentrations of TMFN in PBS, pH 7.4. Spectra were recorded using a Fluoromax®-4P spectrofluorometer from Horiba Scientific (New Jersey, USA). Samples were excited at a fixed wavelength (λ_{ex} = 450 nm) and spectra were recorded in a wavelength range between 480 and 700 nm. The maximum fluorescence intensity of TMNF was at 515 nm.

Cell Cultures. MCF7 and MDA cell lines were used as HER-2 positive and HER-2 negative targets, respectively. Cells were cultured in 50% Dulbecco's Modified Eagle's Medium (DMEM) and 50% F12, supplemented with 10% fetal bovine serum, L-glutamine (2 mM), penicillin (50 UI/mL) and streptomycin (50 mg mL^{-1}) at 37 °C and 5% CO_2 in a humidified atmosphere and subcultured prior to confluence using trypsin/EDTA. Cells culture medium and chemicals were purchased from EuroClone.

Confocal Laser Scanning Microscopy. Cells were cultured on collagene (Sigma) pre-coated coverglass slides until sub-confluence. Cells were incubated 1 h at 37 °C with 0.1 mg mL^{-1} of TMFN or with 0.02 mg mL^{-1} of free scFv1. Then, cells were washed twice with PBS, fixed for 10 min with 4% paraformaldehyde (Sigma) and treated for 10 min with 0.1 M glycine (Sigma) in PBS. A blocking step was performed for 1 h at RT with a solution containing 2% bovine serum albumin (Sigma), 2% goat serum in PBS. ScFv1 was revealed by a FITC-conjugated antibody to whole murine IgG (MP Biomedicals) at a 1:300 dilution by incubating for 2 h at RT in PBS, 2% BSA, 2%

goat serum, 0.1% saponin. Nuclei were stained with DAPI (4',6-diamidino-2-phenylindole, Invitrogen) at 0.2 μg mL^{-1} in PBS with 0.1% Saponin (Sigma) for 20 min at RT. Membranes were stained with DiD oil (Invitrogen) at a 1:300 dilution by incubating 30 min at 37 °C. Microscopy analysis was performed with a Leica SP2 AOBs microscope confocal system. Images were acquired with 63× magnification oil immersion lenses at 1024×1024 pixel resolution (Figure S4).

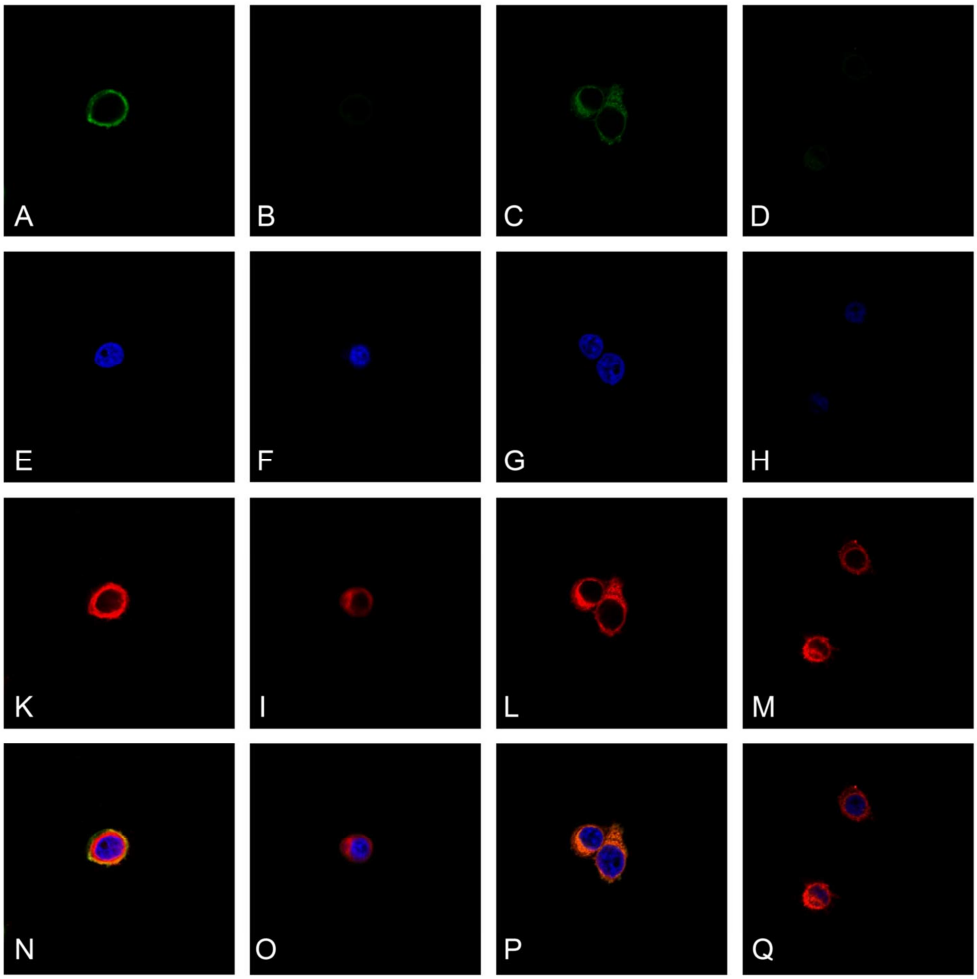

Figure S4. Magnification of Figure 3.

Flow cytometry. Cells were cultured on a multiwell dish until sub-confluence. Then, cells were incubated 1 h at 37 °C in the presence of TMFN (0,02 mg mL^{-1} or 0.1 mg mL^{-1}) or free scFv1 0.02 mg mL^{-1}. Cells were treated for FACS analysis with standard methods. Briefly, cells were incubated for 30 min at 4 °C with the secondary antibodies used for immunofluorescence. Labeled cells were analyzed on a FACS Calibur flow cytometer (Becton Dickinson). 20000 events were acquired for each analysis, after gating on viable cells, and isotype-control antibodies were used to set the appropriate gates.

Cell death analysis. Cells were cultured on a multiwell dish until sub-confluence. Then cells were incubated 24 h at 37 °C in the presence of TMFN (0.02 mg mL^{-1}, 0.05 mg mL^{-1} or 0.1 mg mL^{-1}). After incubation time cells were washed twice with PBS and treated for FACs analysis according to PE Annexin V Apoptosis Detection Kit I manufacturer's protocol (Becton Dickinson Biosciences). Briefly cells were resuspended in Binding Buffer 1× and incubated for 15 min in presence of 0.005 mL of Annexin-PE and 0.005 mL of 7-aminoactinomycin D. After incubation time cells were analyzed within 1 h on a FACS Calibur flow cytometer (Becton Dickinson). 20000 events were acquired for each analysis, after gating on viable cells. Therefore, we consider cell death as the populations positive for Annexin V and for 7AAD staining alone and together. The results are expressed as means ± standard deviation of the mean of 3 individual experiments (Figure S5A).

Cell proliferation assay. Cells were cultured on a 96 multiwell dish at a density of 5000 cells cm^{-1}. Then cells were incubated with TMFN (0.02 mg mL^{-1} and 0.1 mg mL^{-1}). At the indicated time points cells were washed with PBS and then incubated for 3 h at 37 °C with 0.1 mL of 3-(4,5-dimethyl-2-thiazolyl)-2,5-diphenyl-2H-tetrazolium bromide (MTT) stock solution previously diluted 1:10 in DMEM medium without phenol red. At the end of the incubation, 0.1 mL of MTT Solubilizing Solution was added to each well to solubilize the MTT formazan crystals (Sigma-Aldrich). Absorbances were read immediately in a BIORAD Microplate reader using a test wavelength of 570 nm and a reference wavelength of 690 nm. The results are expressed as means ± standard deviation of the mean of 5 individual experiments (Figure S5B).

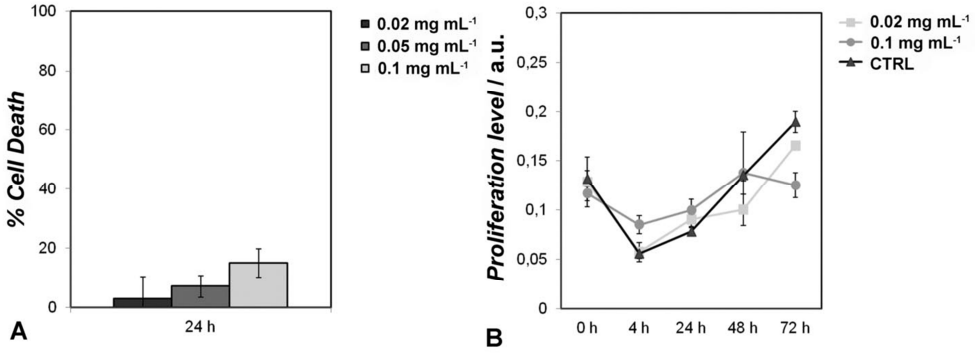

Figure S5. A) Cell death assay with TMFN. MCF7 cells were treated with TMFN (0.02 mg mL^{-1}, 0.05 mg mL^{-1} and 0.1 mg mL^{-1}) for 24 h. Cell death was assessed to measure the exposure of Annexin V and the incorporation of 7-aminoactinomycin D, evaluated by flow cytometry. The percentage of cell death in untreated population was substracted. B) Cell proliferation assay with TMFN. MCF7 cells were treated with TMFN (0.02 mg mL^{-1} and 0.1 mg mL^{-1}) for up to 72 h. Cell proliferation was tested by measuring the conversion of MTT into formazan. CTRL represents untreated control.

Relaxometric analysis of the cells. MCF7 and MDA cells were cultured until sub-confluence. Then cells were treated with TMFN (0.02 mg mL^{-1} and 0.1 mg mL^{-1}) for 3 h at 37 °C. The cells were washed with PBS, fixed with 2.5 % buffered glutaraldehyde and resuspended with PBS at concentration of 5×10^5 cells mL^{-1}. Untreated cells were used as control. T_2 relaxation measurements of the samples were performed at a temperature of 313 K using a Bruker Minispec mq20 system (Ettlingen, Gerrmany) working with 1H at 20 MHz magnetic field with the following parameters: Carr-Purcell-Meiboom-Gill pulse sequence, 10000 echoes with a 20 ms echo times and 2 s repetition time. Samples were introduced using 10 mm NMR spectroscopy tubes prewarmed at 40 °C. T_2 values were acquired after thermal equilibration. The results are expressed as a means ± standard error of the mean.

Bioinformatics. The scFv1 three-dimensional (3D) model was built using the I-TASSER protein structure prediction server.[7,8] The scFv1 sequence was submitted to the I-TASSER online modeling program available at http://zhanglab.ccmb.med.umich.edu/I-TASSER/, which generates three-dimensional structure models by multiple-threading alignments and iterative structural assembly simulations. The scFv1 model was generated by I-TASSER on the template PDB ID: 2ghw_B. In order to identify the hypothetical CDRs regions forming the scFv antigen binding site,

homologs of scFv800E6 with known structures were found using the Blastp program [9] searching the Protein Data Bank database at NCBI (http://www.ncbi.nlm.nih.gov/). Sequence alignments (Figure S6) were generated with ClustalW 2.1[10] using BLOSUM matrix and standard ClustalW parameters (http://www.ebi.ac.uk/Tools/clustalw/index.html). The comparison between scFv800E6 and homologs sequences leads to the identification of hypothetical scFv800E6 CDRs regions.

```
gi|2392474|pdb|1NQB|A       --------------------------QVQLQQSGAELVKPGASVKLSCKA 24
gi|11514087|pdb|1DZB|A      --------------------------QVKLQQSGAELVKPGASVKLSCTA 24
gi|11513786|pdb|1QOK|A      ETVIMKYLLPTAAAGLLLLAAQPAMAQVKLQQSGAELVRSGTSVKLSCTA 50
gi|9257093|pdb|1F3R|B       --------------------------QVQLLESGPGLVRPSETLSLTCTV 24
                                                       **:* :**. **:.. ::.*:*..

gi|2392474|pdb|1NQB|A       SGYTFTSYWMHWVKQRPGRGLEWIGRIDPNSGGTKYNEKFKSKATLTVDK 74
gi|11514087|pdb|1DZB|A      SGFNIKDTYMHWVKQRPEQGLEWIGRIDPANGNTKYDPKFQGKATITADT 74
gi|11513786|pdb|1QOK|A      SGFNIKDSYMHWLRQGPEQGLEWIGWIDPENGDTEYAPKFQGKATFTTDT 100
gi|9257093|pdb|1F3R|B       SGFSLTSFSVSWVRHPSGKGPEWMGRMWYD-GYTAYNSALKSRLSISRDT 73
                            **:.:..  : *::: . :* **:* :    * * *   ::.: ::: *.

gi|2392474|pdb|1NQB|A       PSSTAYMQLSSLTSEDSAVYYCARYDY----YGSSYFDYWGQGTTVTVSS 120
gi|11514087|pdb|1DZB|A      SSNTAYLQLSSLTSEDTAVYYCAR--------WDWYFDVWGQGTTVTVSS 116
gi|11513786|pdb|1QOK|A      SSNTAYLQLSSLTSEDTAVYYCNEGTP----TGPYYFDYWGQGTTVTVSS 146
gi|9257093|pdb|1F3R|B       SKNQVFLKMNSLQTDDTGTYYCTRDLYGGYPLGFWYFDFWGPGTMVTVSS 123
                            ... .:::::** ::*:..*** .          *** ** ** *****

gi|2392474|pdb|1NQB|A       ---------------DIELTQTPLSLPVSLGDQASISCRSSQSIVHSNGN 155
gi|11514087|pdb|1DZB|A      GGGGSGGGGSGGGGSDIELTQSPSSMYTSLGERVTITCKASQDIN----- 161
gi|11513786|pdb|1QOK|A      GGGGSGGGGSGGGGSENVLTQSPAIMSASPGEKVTITCSASSSV------ 190
gi|9257093|pdb|1F3R|B       GGGGSGGGGSGGGGSDIKLTQSPSLLSASVGDRVTLSCKGSQNIN----- 168
                                      :  ***:*  : .* *::.:::* .*..:

gi|2392474|pdb|1NQB|A       TYLEWYLQKPGQSPKLLIYKVSNRFSGVPDRFSGSGSGTDFTLKISRVEA 205
gi|11514087|pdb|1DZB|A      SYLRWFQQKPGKSPKTLIYYATSLADGVPSRFSGSGSGQDYSLTISSLES 211
gi|11513786|pdb|1QOK|A      SYMHWFQQKPGTSPKLWIYSTSNLASGVPARFSGSGSGTSYSLTISRMEA 240
gi|9257093|pdb|1F3R|B       NYLAWYQQKLGEAPKLLIYNTNSLQTGIPSRFSGSGSGTDYTLTISSLQP 218
                            .*: *: ** * :**  ** ...   *:* ******** .::*.** ::.

gi|2392474|pdb|1NQB|A       EDLGVYYCFQGSHVPYTFGGGTKLEIKRAAAEQKLISEEDLNGAAHHHHH 255
gi|11514087|pdb|1DZB|A      DDTTTYYCLQHGESPYTFGGGTKLEIKRAAAEQKLISEEDLN-------- 253
gi|11513786|pdb|1QOK|A      EDAATYYCQQRSSYPLTFGAGTKLELKRAAAEQKLISEEDLN-------- 282
gi|9257093|pdb|1F3R|B       EDVATYFCYQYNN-GYTFGAGTKLELK--AAEQKLISEEDLN-------- 257
                            :*  .*:* * .    ***.*****:*  ************

gi|2392474|pdb|1NQB|A       H 256
gi|11514087|pdb|1DZB|A      -
gi|11513786|pdb|1QOK|A      -
gi|9257093|pdb|1F3R|B       -
```

Figure S6. Multiple sequence alignments of scFv800E6 homologues with known structures. Protein sequences of scFv800E6 homologues with known structures were obtained by BLAST searching the Protein Data Bank (PDB) database at NCBI (http://www.ncbi.nlm.nih.gov/) and aligned by ClustalW (2.1). The CDRs regions of each protein are highlighted in grey. The NCBI accession

number and PDB identification number are indicated for each protein sequence. Symbols: (*) identical residues, (:) conserved and (.) semi-conserved substitutions, respectively.

Strains and plasmid. *E. coli* DH5α was used as a host strain for propagation of the plasmids vector. *P. pastoris* KM71H *(arg4; aox1::ARG4)* (Invitrogen) was used as host for expressing scFv800E6 gene. Plasmid pPICZαA (Invitrogen) was used for constructing plasmid vector. The cDNA coding for scFv800E6 was amplified from pEMBL-scFv800E6 vector.[11] The primers were 5'- CTGCCGCTCGAGAAAAGATCCCAGGTCCAACTGCAGCAGTCTGG -3' (forward primer), which contains a XhoI site (underlined), the sequence coding for Kex2 cleavage site LysArg (highlighted in yellow), the sequence coding for the N-terminal Ser residue (highlighted in green), and 5'-CAGTAGCGGCCGCTTTTATTTCCAGCTTGGTCCC-3' (reverse primer), which contains a NotI site (underlined). The resulting PCR product was digested with XhoI and NotI and ligated to the corresponding site of the expression vector pPICZαA. This strategy leads to the construction of a recombinant expression vector without the Ste13 aminopeptidase cleavage site and thus allow the production of a protein with a native *N*-terminus. The expression vector pPICZαA-scFv1 was confirmed by restriction endonuclease digestion and DNA sequencing.

Protein expression and purification. The linearized plasmid was used to transform *P. pastoris*. Screening of transformants allow the isolation of the best producing clone as described before for KM71H-pPICZαA-scFv800E6.[12] The clone KM71H-pPICZαA-scFv1-6 was grown in 20 mL YPD medium (1% yeast extract, 2% peptone, 2% dextrose) at 30 °C overnight with shaking at 250 rpm. The cultures were centrifuged at 1500 × g for 4 min and then the pellets were resuspended in 400 mL of BMMY (1% yeast extract, 2% peptone, 100 mM potassium phosphate pH 6.0, 1.34% YNB, 0.00004% biotin, 0.5% methanol) with 0.8% glycerol yielding an initial OD 600 value of 10. The culture was induced by daily addition of methanol to a final concentration of 0.5%. After 48 h of methanol treatment, the culture supernatant was filtered through 0.22 μm filters and dialyzed overnight in 50 mM sodium phosphate pH 8.0, 300 mM NaCl. The dialyzed medium was loaded at a flow rate of 0.5 mL min^{-1} onto a Ni-NTA Agarose (Qiagen) column (bed volume 0.5 mL) pre-equilibrated with 50 mM sodium phosphate pH 8.0, 300 mM NaCl, 10 mM imidazole. The column was washed with 50 mM sodium phosphate pH 8.0, 300 mM NaCl, 20 mM imidazole and the protein eluted with a stepwise imidazole gradient, 100 mM to 200 mM, in the same buffer. Fractions were collected and analyzed by SDS-PAGE (Figure S6). SDS-PAGE was performed according to Laemmli using 12% (v/v) polyacrylamide gels.[13] The proteins were detected by Coomassie Brilliant Blue R-250 staining. Protein content was determined both by measuring

absorbance at 280 nm and by using the Coomassie Plus Protein Assay Reagent (Thermo Fisher Scientific) and bovine plasma immunoglobulin G as the standard protein.

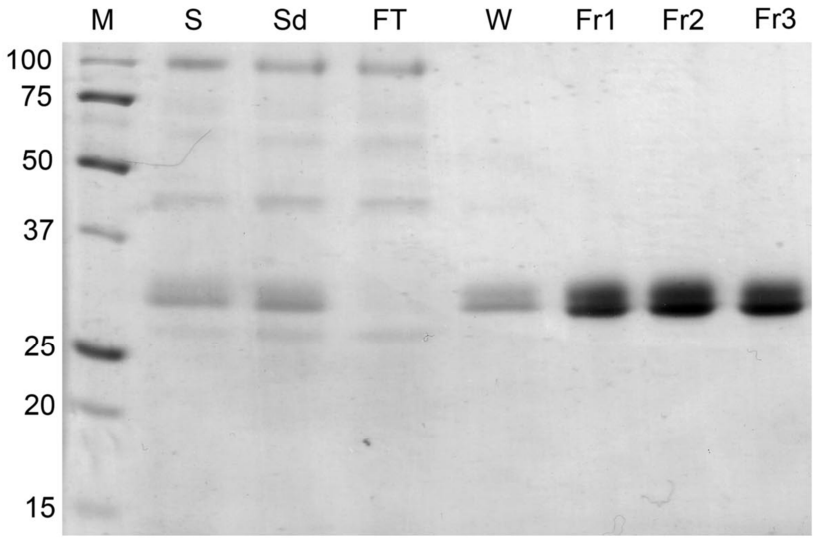

Figure S7. Nickel-affinity purification of scFv1. Proteins from culture supernatant (S), culture supernatant after dialysis (Sd), flow trough (FT), wash (W) and fractions (fr.1, fr.2 and fr.3) obtained by Ni-NTA affinity chromatography were separated by SDS-PAGE and visualized by Commassie staining. M: protein markers (kDa).

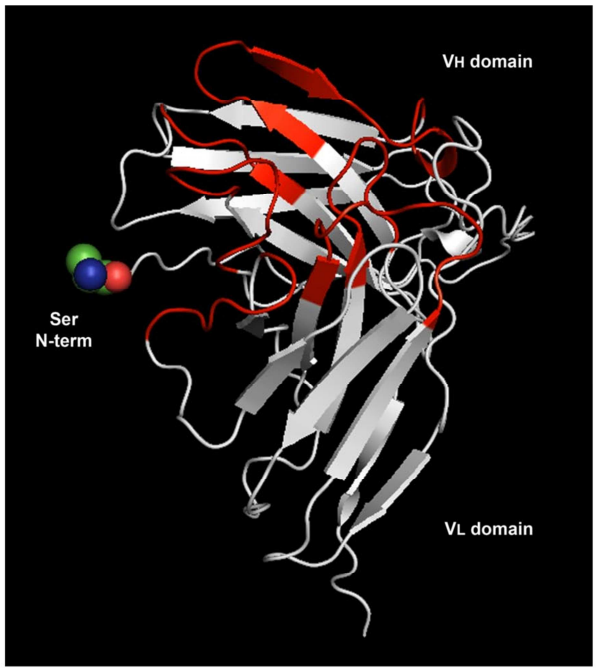

Figure S8. Three-dimensional model of scFv1. The scFv1 protein was modeled using the I-TASSER server. The *N*-terminal Ser residue is indicated with spheres and the scFv1 antigen binding site composed by the six hypothetical CDRs regions is red-colored.

References:

[1] M. Piazza, M. Colombo, I. Zanoni, F. Granucci, P. Tortora, J. Weiss, T. Gioannini, D. Prosperi, F. Peri, *Angew. Chem. Int. Ed.* **2011**, *50*, 622-626.

[2] C.-A. J. Lin, R. A. Sperling, J. K. Li, T.-Y. Yang, P.-Y. Li, M. Zanella, W. H. Chang, W. J. Parak, *Small* **2008**, *4*, 334-341.

[3] M. E. Jung, A. B. Mossman, M. A. Lyster, *J. Org. Chem.* **1978**, *43*, 3698-3701.

[4] M. E. Jung, S. J. Miller, *J. Am. Chem. Soc.* **1981**, *103*, 1984-1992.

[5] X. Ning, J. Guo, M. A. Wolfert, G.-J. Boons. *Angew. Chem. Int. Ed.* **2008**, *47*, 2253-2255.

[6] M. F. Debets, S. S. van Berkel, S. Schoffelen, F. P. J. T. Rutjes, J. C. M. van Hest, F. L. van Delft, *Chem. Commun.* **2010**, *46*, 97-99.

[7] A. Roy, A. Kucukural, Y. Zhang, *Nat. Protoc.* **2010**, *5*, 725-738.

[8] Y. Zhang, *Proteins* **2007**, *69*, 108-117.

[9] S. F. Altschul, T. L. Madden, A. A. Schaffer, J. Zhang, Z. Zhang, W. Miller, D. J. Lipman, *Nucleic Acids Res.* **1997**, *25*, 3389-3402.

[10] J. D. Thompson, D. G. Higgins, T. J. Gibson, *Nucleic Acids Res*. **1994**, *22*, 4673-4680.

[11] P. Galeffi, A. Lombardi, M. D. Donato, A. Latini, M. Sperandei, C. Cantale, P. Giacomini, *Vaccine* **2005**, *23*, 1823-1827.

[12] S. Sommaruga, A. Lombardi, A. Salvadè, S. Mazzucchelli, F. Corsi, P. Galeffi, P. Tortora, D. Prosperi, *Appl. Microbiol. Biotechnol.* **2011**, *91*, 613-621.

[13] U. K. Laemmli, *Nature* **1970**, *227*, 680-685.

ARTICLE 9

Bibliography

1 Kim, B. Y. S.; Rutka, J. T.; Chan, W. C. W. Nanomedicine *N. Engl. J. Med.* **2010**, *363*, 2434–2443.

2 Archakov, A. I.; Ivanov, Y. D.; Analytical nanobiotechnology for medicine diagnostics. *Mol. Bio. Syst.* **2007**, *3*, 336–342.

3 Pautler, M.; Brenner, S. Nanomedicine: promises and challenges for the future of public health. *Int. J. Nanomedicine* **2010**, *5*, 803–809.

4 Bawarski, W. E.; Chidlowsky, E.; Bharali, D. J.; Mousa, S. A. Emerging nanopharmaceuticals. *Nanomedicine* **2008**, *4*, 273–282.

5 Ferrari, M. Cancer nanotechnology: opportunities and challenges. *Nat. Rev. Cancer* **2005**, *5*, 161–171.

6 Alivisatos, A.P. Less is more in Medicine. *Sci. Am.* **2001**, 67–73.

7 Whitesides, G.M. The 'right' size in nanotechnology. *Nat. Biotechnol.* **2003**, *21*, 1161–1165.

8 Council of the Canadian Academies. Small is different: a science perspective on the regulatory challenges of the nanoscale. July 2008. (http://www.nanolawreport.com/)

9 Peer, D.; Karp, J. M.; Hong, S.; Farokhzad, O. C.; Margalit, R.; Langer, R. Nanocarriers as an emerging platform for cancer therapy. *Nat Nanotech.* **2007**, *2*, 751–760.

10 McCarthy, T. D.; Karellas, P.; Henderson, S. A.; Giannis, M.; O'Keefe, D. F.; Heery, G.; Paull, J. R. A.; Matthews, B. R.; Holan, G. Dendrimers as drugs: discovery and preclinical and clinical development of dendrimer-based microbicides for HIV and STI prevention. *Mol. Pharm.* **2005**, *2*, 312–318.

11 Davis, M. E.; Zuckerman, J. E.; Choi, C. H. J.; Seligson, D.; Tolcher, A.; Alabi, C. A.; Yen, Y.; Heidel, J. D.; Ribas, A. Evidence of RNAi in humans from systemically administered siRNA via targeted nanoparticles. *Nature* **2010**, *464*, 1067–70.

12 Resch-Genger, U.; Grabolle, M.; Cavaliere-Jaricot, S.; Nitschke, R.; Nann, T. Quantum dots versus organic dyes as fluorescent labels. *Nat. Methods* **2008**, *5*, 763–775.

13 Sperling, R. A.; Rivera-Gil P.; Zhang, F.; Zanella, M.; Parak, W. J. Biological applications of gold nanoparticles. *Chem. Soc. Rev.* **2008**, *37*, 1896–1908.

14. Liu, Z. A.; Li, X. L.; Tabakman, S. M.; Jiang, K. L.; Fan, S. S.; Dai, H. J. Multiplexed multicolor Raman imaging of live cells with isotopically modified single walled carbon nanotubes. *J. Am. Chem. Soc.* **2008**, *130*, 13540–13541.

15 Hobbs, S. K.; Monsky, W. L.; Yuan, F.; Roberts, G.; Griffith, L.; Torchilin, V. P.; Jain, R. K. Regulation of transport pathways in tumor vessels: role of tumor type and microenvironment. *Proc. Natl. Acad. Sci. U.S.A.* **1998**, *95*, 4607–4612.

16 Prencipe, G.; Tabakman, S. M.; Welsher, K.; Liu, Z.; Goodwin, A. P.; Zhang, L.; Henry, J.; Dai, H. PEG branched polymer for functionalization of nanomaterials with ultralong blood circulation. *J. Am. Chem. Soc.* **2009**, *131*, 4783–4787.

17 Alexis, F.; Pridgen, E.; Molnar, L. K.; Farokhzad, O. C. Factors affecting the clearance and biodistribution of polymeric nanoparticles. *Mol. Pharm.* **2008**, *5*, 505–515.

18 Harisinghani, M. G.; Barentsz, J.; Hahn, P. F.; Deserno, W. M.; Tabatabaei, S.; van de Kaa C. H.; de la Rosette, J.; Weissleder, R. Noninvasive detection of clinically occult lymph-node metastases in prostate cancer. *N. Engl. J. Med.* **2003**, *348*, 2491–2499.

19 Kho, K.W.; Shen, Z.X.; Zeng, H.C.; Soo, K.C.; Olivo, M. Deposition method for preparing SERS-active gold nanoparticle substrates. *Anal. Chem.* 2005, 77, 7462–7471.

20 Posthuma-Trumpie, G. A.; Korf, J.; van Amerongen, A. V. Lateral flow (immuno)assay: its strengths, weaknesses, opportunities and threats: a literature survey. *Anal. Bioanal. Chem.* **2009**, *393*, 569–582.

21 Nam, J. M.; Thaxton, C. S.; Mirkin, C. A. Nanoparticle-based bio-bar codes for the ultrasensitive detection of proteins. *Science* **2003**, *301*, 1884–1886.

22 Thaxton, C. S.; Elghanian, R.; Thomas, A. D.; Stoeva, S. I.; Lee, J. S.; Smith, N. D.; Schaeffer, A. J.; Klocker, H.; Horninger, W.; Bartsch, G.; Mirkin, C.A. Nanoparticle-based bio-barcode assay redefines "undetectable" PSA and biochemical recurrence after radical prostatectomy. *Proc. Natl. Acad. Sci. U.S.A.* **2009**, *106*, 18437–18442.

23 Lammers, T.; Aime, S.; Hennink, W. E.; Storm, G.; Kiessling, F. Theranostic nanomedicine. *Acc. Chem. Res*. DOI:10.1021/ar200019c

24 Gupta, A. K.; Gupta, M. Synthesis and surface engineering of iron oxide nanoparticles for biomedical applications *Biomaterials* **2005**, *26*, 3995–4021.

25 Babincova, M.; Babinec, P.; Bergemann, C. High-gradient magnetic capture of ferrofluids implications for drug targeting and tumor immobilization *Z. Naturforsch. (Sect. C)* **2001**, *56*, 909–911.

26 Wang, Y. X.; Hussain, S. M.; Krestin, G. P. Superparamagnetic iron oxide contrast agents: physicochemical characteristics and applications in MR imaging. *Eur. Radiol.* **2001**, *11*, 2319–2331.

27 Goya, G. F.; Berquo, T. S.; Fonseca, F. C. Static and dynamic magnetic properties of spherical magnetite nanoparticles. *J. Appl. Phys.* **2003**, *94*, 3520–3528.

28 Berry, C. C.; Curtis, A. S. G. Functionalisation of magnetic nanoparticles for applications in biomedicine *J. Phys. D: Appl. Phys.* **2003**, *36*, R198–206.

29 Jordan, A.; Scholz, R.; Maier-Hauff, K.; Johannsen, M.; Wust, P.; Nadobny, J.; Schirra, H.; Schmidt, H.; Deger, S.; Loening, S.; Lanksch, W.; Felix, R. Presentation of a new magnetic field therapy system for the treatment of human solid tumors with magnetic fluid hyperthermia *J. Magn. Magn. Mater.* **2001**, *225*,118–126.

30 Tartaj, P.; Morales, M. P.; Veintemillas-Verdaguer, S.; Gonzalez-Carreno, T.; Serna, C. J.; The preparation of magneticnanopartic les for applications in biomedicine *J. Phys. D: Appl. Phys.* **2003**, *36*, R182–197.

31 Ito, A.; Hibino, E.; Kobayashi, C.; Terasaki, H.; Kagami, H.; Ueda, M.; Kobayashi, T.; Honda, H. Construction and delivery of tissue-engineering human retinal pigment epithelial cell sheets using magnetite nanoparticles and magnetic force. *Tissue Eng.* **2005**, *11*, 489–496.

32 Hofmann, A.; Thierbach, S.; Semisch, A.; Hartwig, A.; Taupitz, M.; Rühl, E.; Graf, C. Highly monodisperse water-dispersable iron oxide nanoparticles for biomedical applications. *J. Mater. Chem.* **2010**, *20*, 7842–7853.

33 Dacoata, G. M.; Degrave, E.; Debakker, P. M. A.; Vandenberghe, R. E. Synthesis and characterization of some iron oxides by sol-gel method. *J. Solid State Chem.* **1994**, *113*, 405–412.

34 Deng, Y.; Wang, L.; Yang, W.; Fu, S.; Elaissari, A. Preparation of magnetic polymeric particles via inverse microemulsion polymerization process. *J. Magn. Magn. Mater.* **2003**, *257*, 69–78.

35 Mukh-Qasem, R. A.; Gedanken, A. Sonochemical synthesis of stable hydrosol of Fe_3O_4 nanoparticles. *J. Colloid Interface Sci.* **2005**, *284*, 489–494.

36 Chen, D.; Xu, R. Hydrothermal synthesis and characterization of nanocrystalline Fe_3O_4 powders. *Mater. Res. Bull.* **1998**, *33*, 1015–1021.

37 Hyeon, T.; Lee, S. S.; Park, J.; Chung, Y.; Na, H. B. Synthesis of highly crystalline and monodisperse maghemite nanocrystallites without a size-selection process. *J. Am. Chem. Soc.* **2001**, *123*, 12798–12801.

38 Basak, S.; Chen, D. R.; Biswas, P. Electrospray of ionic precursor solutions to synthesize iron oxide nanoparticles: modified scaling law. *Chem. Eng. Sci.* **2007**, *62*, 1263–1268.

39 Veintemillas-Verdaguer, S.; Morales, M. P.; Serna, C. J. Continuous production of γ-Fe_2O_3 ultrafine powders by laser pyrolysis. *Mater. Lett.* **1998**, *35*, 227–231.

40 Lee, C. S.; Lee, H.; Westervelt, R. M. Microelectromagnets for the control of magnetic nanoparticles. *Appl. Phys. Lett.* **2001**, *79*, 3308–3310.

41 Gupta, A. K.; Wells, S. Surface modified superparamagnetic nanoparticles for drug delivery: preparation, characterisation and cytotoxicity studies. *IEEE Trans Nanobiosci.* **2004**, *3*, 66–73.

42 Sun, S.; Zeng, H. Size-controlled synthesis of magnetite nanoparticles *J. Am. Chem. Soc.* **2002**, *124*, 8204–8205.

43 Rockenberger, J.; Scher, E. C.; Alivisatos, A. P. A new nonhydrolytic single-precursor approach to surfactant-capped nanocrystals of transition metal oxides. *J. Am. Chem. Soc.* **1999**, *121*, 11595–11596.

44 Lu, A. H.; Salabas, E. L.; Schuth, F. Magnetic nanoparticles: synthesis, protection, functionalization, and application *Angew. Chem. Int. Ed.* **2007**, *46*, 1222–1244.

45 Gupta, A. K.; Curtis, A. S. G. Lactoferrin and ceruloplasmin derivatized superparamagneticiron oxide nanoparticles for targeting cell surface receptors. *Biomaterials* **2004**, *25*, 3029–3040.

46 Hamley, I. W. Nanotechnology with soft materials. *Angew. Chem. Int. Ed.* **2003**, *42*, 1692–1712.

47 Hao, R.; Xing, R.; Xu, Z.; Hou, Y.; Gao, S.; Sun, S. Synthesis, functionalization, and biomedical applications of multifunctional magnetic nanoparticles. *Adv. Mater.* **2010**, *22*, 2729–2742.

48 Mendenhall, G. D.; Geng, Y.; Hwang, J. Optimization of long-term stability of magneticfluids from magnetite and synthetic polyelectrolytes *J. Coll. Interf. Sci.* **1996**, *184*, 2, 519–526.

49 Liz-Marza´n, L. M.; Kamat, P. V. *Nanoscale materials*. Boston: Kluwer Academic Publishers; **2003**.

50 Lu, A. H.; Salabas, E. L.; Schüth, F. Magnetic nanoparticles: synthesis, protection, functionalization, and application. *Angew. Chem. Int. Ed.* **2007**, *46*, 1222–1244.

51 Lee, H.; Dellatore, S. M.; Miller, W. M.; Messersmith, P. B. Mussel-inspired surface chemistry for multifunctional coatings. *Science* **2007**, *318*, 426–430.

52 Moghimi, S. M.; Hunter, A. C.; Murray, J. C. Long-circulating and target-specific nanoparticles: theory to practice. *Pharmacol. Rev.* **2001**, *53*, 283–318.

53 Moghimi, S. M.; Hunter, A. C. Poloxamers and poloxamines in nanoparticle engineering and experimental medicine. *Trends. Biotechnol*, **2000**, *18*, 412–420.

54 Mornet, S.; Vasseur, S.; Grasset, F.; Duguet, E. Hyperthermia in combined treatment of cancer. *J. Mater. Chem.* **2004**, *14*, 2161–2175.

55 Corot, C.; Robert, P.; Idée, J. M.; Port, M. Recent advances in iron oxide nanocrystal technology for medical imaging. *Adv. Drug. Delivery Rev.* **2006**, *58*, 1471–1504.

56 Weissleder, R.; Mahmood, U. Molecular imaging. *Radiology*, **2001**, *219*, 316–333.

57 Mendonca Dias, M. H.; Lauterbur, P. C. Ferromagnetic particles as contrast agents for magnetic resonance imaging of liver and spleen. *Magn. Reson. Med.* **1986**, *3*, 328–330.

58 Semelka, R. C.; Helmberger, T. K. Contrast agents for MR Imaging of the liver. *Radiology* **2001**, *218*, 27–38.

59 Morawski, A. M.; Winter, P. M.; Crowder, K. C.; Caruthers, S. D.; Fuhrhop, R. W.; Scott, M. J.; Robertson, J. D.; Abendschein, D. R.; Lanza, G. M.; Wickline, S. A. Targeted nanoparticles for quantitative imaging of sparse molecular epitopes with MRI. *Magn. Reson. Med.* **2004**, *51*, 480–486.

60 Weissman, I. L. Translating stem and progenitor cell biology to the clinic: barriers and opportunities. *Science* **2000**, *287*, 1442–1446.

61 Bulte, J. W. M.; Douglas, T.; Witwer, B.; Zhang, S.; Strable, E.; Lewis, B. K.; Zywicke, H.; Miller, B.; van Gelderen, P.; Moskowitz, B. M.;

Duncan, I. D.; Frank, J. A. Magnetodendrimers allow endosomal magnetic labeling and in vivo tracking of stem cells. *Nature Biotech.* **2001**, *19*, 1141–1147.

62 Choi, H. S.; Liu, W.; Liu, F.; Nasr, K.; Misra, P.; Bawendi, M. G.; Frangioni, J. V.; Design considerations for tumour-targeted nanoparticles. *Nat. Nanotechnol*, **2010**, *5*, 42–47.

63 Chomoucka, J.; Drbohlavova, J.; Huska, D.; Adam, V.; Kizek, R.; Hubalek, J. Magnetic nanoparticles and targeted drug delivering. *Pharmacol. Res.* **2010**. *62*, 144–149.

64 Mornet, S.; Vasseur, S.; Grasset, F.; Duguet, E. Magnetic nanoparticle design for medical diagnosis and therapy. *J. Mater. Chem.* **2004**, *14*, 2161–2175.

65 Small Times http://www.smalltimes.com/

66 Heath, J. R.; Phelps, M. E.; Hood L. NanoSystems biology. *Mol. Imaging Biol.* **2003**, *5*, 312–325.

67 Shellman, Y. ; Howe, W. R.; Miller, L. A.; Goldstein, N. B.; Pacheco, T. R.; Mahajan, R. L.; LaRue, S. M.; Norris, D. A. Hyperthermia induces endoplasmic reticulum-mediated apoptosis in melanoma and non-melanoma skin cancer cells. *J. Invest .Dermatol.* **2008**, *128*, 949–956.

68 Wust, P.; Hildebrandt, B.; Sreenivasa, G.; Rau, B.; Gellermann, J.; Riess, H.; Felix, R.; Schlag, P. M. Hyperthermia in combined treatment of cancer. *Lancet Oncol.* **2002**, *3*, 487–497.

69 Yanase, M.; Shinhai, M.; Honda, H.; Wahabayashi, T.; Yoshida, J.; Kobayashi, T. Antitumor immunity induction by intracellular hyperthermia using magnetite cationic liposomes. *Jpn. J. Cancer Res.* **1998**, *89*, 775–782.

70 Maier-Hauff, K.; Rothe, R.; Scholz, R.; Gneveckow, U.; Wust, P.; Thiesen, B.; Feussner, A.; Von Deimling, A.; Waldoefner, N.; Felix, R.; Jordan, A. Intracranial thermotherapy using magnetic nanoparticles combined with external beam radiotherapy: results of a feasability study

on patients with glioblastoma multiforme. *J. Neuro-Oncol.* **2007**, *81*, 53–60.

71 Jordan, A.; Scholz, R.; Maier-Hauff, K.; Van Landeghem, F. K. H.; Waldoefner, N.; Teichgraeber, U.; Pinkernelle, J.; Bruhn, H.; Neumann, F.; Thiesen, B.; von Deimling, A.; Felix, R. The effect of thermotherapy using magnetic nanoparticles on rat malignant glioma. *J. Neuro-Oncol.* **2006**, *78*, 7–14.

72 Johannsen, M.; Gneveckow, U.; Eckelt, L.; Feussner, A.; Waldofner, N.; Scholz, R.; Deger, S.; Wust, P.; Loening, S. A.; Jordan, A. Clinical hyperthermia of prostate cancer using magnetic nanoparticles: presentation of a New Interstitial Technique. *Int. J. Hyperthermia* **2005**, *21*, 637–647.

73 Johannsen, M.; Gnevekow, U.; Thisen, B.; Taymoorian, K.; Cho, C. H.; Waldofner, N.; Scholz, R.; Jordan, A.; Loening, S. A.; Wust, P. Thermotherapy of prostate cancer using magnetic nanoparticles: feasability, imaging, and three-dimensional temperature distribution. *Int. J. Hyperthermia* 2007, 52, 1653–1662.

74 Kawai, N.; Ito, A.; Futakuchi Yoshida, T.; Ito, A.; Sato, S.; Naiki, T. M.; Honda, H.; Shirai, T.; Kohri, K. Effect of heat therapy using magnetic nanoparticles conjugated with cationic liposomes on prostate tumor in bone. *The Prostate* **2008**, *68*, 784–792.

75 DeNardo, S. J.; De Nardo G. L.; Miers, L. A.; Natarajan, A.; Foreman, A. R.; Gruettner, C.; Adamson, G. N.; Ivkov, R. Development of tumor targeting bioprobes (^{111}In-chimeric L6monoclonal antibody nanoparticles) for alternating magnetic field cancer therapy. *Clin. Cancer Res.* **2005**, *11*, 7087s–7092s.

76 These companies are Sirtex (an Australian company), Magforce (a German company), and Aspen Medisys (an American company, previously Aduro Biotech and Triton Biosystem).

77 The patents submitted by the companies mentioned in ref 17 are for Sirtex US2006167313 or WO 2004/064921, for Triton Biosystems nowAspen Medisys,

78 Frangioni, J. V. New technologies for human cancer imaging. *J. Clin. Oncol.*, **2008**, *26*, 4012–4021.

79 Park, J.; An, K.; Hwang, Y.; Park, J. G.; Noh, H. J.; Kim, J. Y.; Park, J. H.; Hwang, N. M.; Hyeon, T. Ultra-large-scale syntheses of monodisperse nanocrystals. *Nat. Mater.* **2004**, *3*, 891–895.

80 Tabner, B. J.; Turnbull, S.; El-Agnaf, O.; Allsop, D. Production of reaction oxygen species from aggregating proteins implicated in Alzheimer's disease, Parkinson's disease, and other neurodegenerative disease, *Curr. Top. Med. Chem.* **2001**, *1*, 507–517.

81 Rasheed, Z.; Ali, R. Reactive oxygen species damaged human serum albumin in patients with type 1 diabetes mellitus: biochemical and immunological studies *Life Sci.* **2006**, *79*, 2320–2328.

82 Susi, H.; Byler, D. M., Resolution-enhanced fourier transform infrared spectroscopy of enzymes. *Methods Enzymol.* **1986**, *130*, 290–311.

83 Arrondo, J. L. R.; Goni, F. M. Structure and dynamics of membrane proteins as studied by infrared spectroscopy. *Prog. Biophys. Mol. Biol.* **1999**, *72*, 367–405.

84 Wittel, U. A.; Jain, M.; Goel, A.; Chauhan, S. C.; Colcherand, D.; Batra, S. K. The in vivo characteristics of genetically engineered divalent and tetravalent single-chain antibody constructs. *Nucl. Med. Biol.* **2005**, *32*, 157−164.

85 Polito, L.; Monti, D.; Caneva, E; Delnevo, E.; Russo, G.; Prosperi, D. One-step bioengineering of magnetic nanoparticles via a surface diazo transfer/azide-alkyne click reaction sequence *Chem. Commun.*, **2008**, 621−623.

86 Gaetke, L. M.; Chow, C. K. Copper toxicity, oxidative stress, and antioxidant nutrients. *Toxicology* **2003**, *189*, 147−163.